

**THE INFLUENCE OF PHYSICOCHEMICAL REACTION
PARAMETERS ON THE SYNTHESIS OF MULTI-WALLED
CARBON NANOTUBES FOR USE AS CATALYST
SUPPORTS**

by

Rachel Suzanne Oosthuizen

Submitted in fulfillment of the academic requirements for the degree of Master of Science
in the School of Chemistry, University of KwaZulu-Natal, Durban.

December 2012

ABSTRACT

Multi-walled carbon nanotubes (MWCNTs) and other shaped carbon nanomaterials (SCNMs) were synthesized by the floating catalyst chemical vapour deposition (CVD) method, using either ferrocene **[1]** as the catalyst at 2.5 or 5 wt.%, or a synthesized heteroatom-containing ferrocene derivative, in toluene, in the range 750 to 950 °C. The derivatives used were ferrocenoyl imidazolidine **[3]** (a source of N and O) at 2.5 and 5 wt.%, (*N*-phenylcarbamoyl)ferrocene **[4]** (a source of N and O) at 1.25 wt.% and *S,S*-bis(ferrocenylmethyl)dithiocarbonate **[5]** (a source of S and O) at 2.5 wt.%, which was synthesized from ferrocenylmethanol **[2]**. These were characterized by melting point, ¹H- and ¹³C-NMR spectroscopy, IR spectroscopy and mass spectrometry (MS). The effects of variations in the CVD physicochemical reaction parameters, namely temperature, catalyst employed (and the effect of its heteroatoms, where applicable) and catalyst concentration, on the CVD products were investigated. These materials were characterized by transmission electron microscopy (TEM), scanning electron microscopy (SEM), energy dispersive X-ray spectroscopy (EDX), Raman spectroscopy, thermogravimetric analysis (TGA) and some by the Brunauer, Emmett and Teller method (BET).

The best temperature range, in terms of high yields of MWCNTs with relatively high thermal stabilities and surface areas, in general, was identified as being 800 to 900 °C, from results obtained with **[1]**. This temperature range was used for further experiments. Among other results, it was shown that **[1]** and **[3]**, at 2.5 wt.%, and at 800 and 850 °C respectively, produced the best materials. Catalysts **[4]** and **[5]** produced primarily carbon spheres, however, in general, all experiments using N-containing catalysts produced bamboo-shaped MWCNTs. For **[3]**, at 2.5 wt.%, smaller bamboo compartment lengths correlated with decreasing temperature and decreasing crystallinity, suggesting a larger incorporation of nitrogen with lowered temperature. Catalyst **[3]** at 2.5 wt.% also produced very “clean” MWCNTs and this was attributed to optimal levels of oxygen being able to convert amorphous carbons to gas. Certain MWCNT properties were shown to be dependent on the combined, or synergistic, effects of catalyst concentration and temperature.

The best undoped MWCNTs that were synthesized and commercially produced MWCNTs were loaded with Pd nanoparticles using a metal organic CVD (MOCVD) method. Results revealed well dispersed metal nanoparticles of narrow size distribution.

PREFACE

The experimental work described in this dissertation was carried out in the School of Chemistry and Physics, University of KwaZulu-Natal, Durban, from January 2009 to June 2012, under the supervision of Dr Vincent O. Nyamori.

These studies represent original work by the author and have not otherwise been submitted in any form for any degree or diploma to any tertiary institution. Where use has been made of the work of others it is duly acknowledged in the text.

DECLARATION 1 - PLAGIARISM

I, Rachel Suzanne Oosthuizen, declare that

1. The research reported in this dissertation, except where otherwise indicated, is my original research.
2. This dissertation has not been submitted for any degree or examination at any other university.
3. This dissertation does not contain other persons' data, pictures, graphs or other information, unless specifically acknowledged as being sourced from other persons.
4. This dissertation does not contain other persons' writing, unless specifically acknowledged as being sourced from other researchers. Where other written sources have been quoted, then:
 - a. Their words have been re-written but the general information attributed to them has been referenced.
 - b. Where their exact words have been used, then their writing has been placed in italics and inside quotation marks, and referenced.
5. This dissertation does not contain text, graphics or tables copied and pasted from the Internet, unless specifically acknowledged, and the source being detailed in the dissertation in the References sections.

Signed:



DECLARATION 2 - PRESENTATIONS AND PUBLICATIONS

Details of contribution to publications that form part and/or include research presented in this dissertation:

Publications

- (a) R. S. Oosthuizen and V. O. Nyamori, "Carbon nanotubes as supports for palladium catalysts for use in hydrogenation reactions", *Platinum Metals Rev.*, 2011, **55**, (3), 154.
- (b) R. S. Oosthuizen and V. O. Nyamori, "Heteroatom-containing ferrocene derivatives as catalysts for MWCNTs and other shaped carbon nanomaterials", *Appl. Organomet. Chem.*, 2012, (accepted for publication 11 June 2012), DOI 10.1002/aoc.2897.
- (c) R. S. Oosthuizen and V. O. Nyamori, "Pd/MWCNTs as catalysts for use in hydrogenation reactions", *Mater. Chem. Phys.*, (manuscript in preparation).

Oral Presentations

- (a) R. S. Oosthuizen and V. O. Nyamori, "Studies of physicochemical reaction parameters on the synthesis of MWCNTs and its investigation as a catalyst support", at a presentation day of the members of the Nanotechnology Flagship Programme "Nano-architecture in the Beneficiation of Platinum Group Metals", at the University of the Western Cape, 6 July 2009.
- (b) R. S. Oosthuizen and V. O. Nyamori, "Studies of physicochemical reaction parameters on the synthesis of MWCNTs and its investigation as a catalyst support", at the second, update, presentation day of the members of the Nanotechnology Flagship Programme "Nano-architecture in the Beneficiation of Platinum Group Metals", at the University of the Western Cape, 20 September 2010.
- (c) V. O. Nyamori and R. S. Oosthuizen, "Ferrocenyl derivatives as catalysts for shaped carbon nanomaterials (SCNMs)", at Egerton University, Kenya, 17 December 2010.
- (d) R. S. Oosthuizen and V. O. Nyamori, "Heteroatom-containing ferrocene derivatives for the synthesis of nitrogen-doped carbon nanotubes", at the International Conference on Pure and Applied Chemistry, Flic en Flac, Mauritius, 2 to 6 July 2012.

Poster Presentations

- (a) R. S. Oosthuizen and V. O. Nyamori, "Ferrocenyl imidazolide as catalyst precursor in the CVD synthesis of N-doped MWCNTs", at the 40th Convention of the South African Chemical Institute, University of the Witwatersrand, 16 to 21 January 2011.
- (b) V. O. Nyamori, R. S. Oosthuizen and S. M. Zulu, "Ferrocenyl derivatives and their salts as catalysts for synthesizing nitrogen-doped carbon nanotubes (N-CNTs)", at the International Conference on Pure and Applied Chemistry, Flic en Flac, Mauritius, 2 to 6 July 2012.

Signed:



CONTENTS

	Page
Abstract	ii
Preface	iii
Declaration 1 – Plagiarism	iv
Declaration 2 – Presentations and Publications	v
Contents	vi
Acknowledgements	xiv
Glossary of Compounds	xv
List of Abbreviations and Symbols	xvi

CHAPTER 1 LITERATURE REVIEW OF CARBON NANOTUBES

1.1	Introduction	1
1.2	Discovery of carbon nanotubes (CNTs)	1
1.3	Structural characteristics of CNTs	2
	1.3.1 Single-walled carbon nanotubes (SWCNTs)	3
	1.3.2 Multi-walled carbon nanotubes (MWCNTs)	4
1.4	Properties of CNTs	5
	1.4.1 Mechanical properties	5
	1.4.2 Thermal properties	6
	1.4.3 Electronic properties	6
	1.4.4 Optical properties	7
1.5	CNTs and other shaped carbon nanomaterials (SCNMs)	7
1.6	Synthesis of CNTs and other SCNMs	9
	1.6.1 Arc-discharge method	9
	1.6.2 Laser ablation/Laser furnace technique	10
	1.6.3 Chemical vapour deposition (CVD) method	10
	1.6.3.1 Supported catalyst method	12
	1.6.3.2 Floating catalyst method	12
	1.6.3.3 Confined space method	14
1.7	Variables that affect CNT growth in CVD synthesis	14
	1.7.1 Catalyst and its concentration	15

1.7.1.1	Organometallic compounds as catalysts	15
1.7.2	Carbon source	18
1.7.3	Temperature	19
1.7.4	Reducing agent and its concentration	20
1.7.5	Gas flow rate	21
1.7.6	Gas pressure	21
1.7.7	Injection rate	22
1.8	Growth mechanisms of CNTs	22
1.9	Effect of introducing heteroatoms	24
1.9.1	Nitrogen and N-doped CNTs	25
1.9.2	Promoting and cleaning agents for CNT growth	26
1.9.2.1	Phosphorus	26
1.9.2.2	Sulfur	26
1.9.2.3	Oxygen	27
1.10	Purification methods for CNTs	27
1.11	Structural and morphological characterization of CNTs	28
1.11.1	Transmission electron microscopy (TEM)	28
1.11.2	Scanning electron microscopy (SEM)	28
1.11.3	Thermogravimetric analysis (TGA)	28
1.11.4	Energy dispersive X-ray spectroscopy (EDX)	29
1.11.5	Brunauer, Emmett and Teller (BET) analysis	29
1.11.6	Raman spectroscopy	29
1.12	Applications of CNTs	29
1.12.1	Field emission devices	30
1.12.2	Storage of hydrogen gas	30
1.12.3	Fuel cells	30
1.12.4	Composites	30
1.12.5	Nanoelectronics	31
1.12.6	Catalyst supports	31
	References	32

CHAPTER 2 CNTs AS SUPPORTS FOR Pd AND BIMETALLIC CATALYSTS FOR USE IN HYDROGENATION REACTIONS

2.1	Introduction	39
2.2	The advantages of CNTs as catalyst supports	41
2.2.1	Introduction to types of supports	41
2.2.2	Electronic properties of CNTs <i>versus</i> graphite sheets	41
2.2.3	Mechanical strength of CNTs <i>versus</i> traditional supports	42
2.2.4	Reactivity and stability of CNTs <i>versus</i> traditional supports	42
2.2.5	Surface area and selectivity of CNTs <i>versus</i> traditional supports	43
2.2.6	Recovery and recycling of precious metals from CNTs <i>versus</i> traditional supports	45
2.3	Loading techniques and considerations	45
2.4	Modified CNTs as supports	47
2.5	Bimetallic catalysts – effect of secondary metal	49
2.6	Hydrogenation on Pd/CNT catalysts	51
2.6.1	Alkene and alkyne hydrogenation	51
2.6.2	Conversion of nitro ($-\text{NO}_2$) to amino ($-\text{NH}_2$) group <i>via</i> hydrogenation	51
2.6.3	Hydrogenation of nitric oxide (NO)	52
2.7	Conclusions	53
	References	54

CHAPTER 3 MOTIVATION, OBJECTIVES AND OUTLINE

3.1	Motivation for this study	57
3.2	Objectives	57
3.3	Outline of this dissertation	58
	References	59

CHAPTER 4 SYNTHESIS OF CATALYSTS

4.1	Introduction to the catalysts chosen for MWCNT and other SCNM synthesis	60
4.1.1	Ferrocene [1] and its derivatives	60
4.1.2	Ferrocenoyl imidazolidine [3]	61
4.1.3	(<i>N</i> -Phenylcarbamoyl)ferrocene [4]	62

4.1.4	<i>S,S</i> -Bis(ferrocenylmethyl)dithiocarbonate [5]	64
4.2	General procedures	65
4.2.1	Cleaning of glassware	65
4.2.2	Drying of solvents	65
4.2.2.1	Preparation of anhydrous diethyl ether	65
4.2.2.2	Preparation of anhydrous hexane	65
4.2.2.3	Preparation of anhydrous dichloromethane	65
4.2.2.4	Preparation of anhydrous tetrahydrofuran (THF)	65
4.3	Common laboratory chemicals, reagents, solvents and gases	66
4.4	Characterization of catalyst compounds	67
4.4.1	Melting point (m.p.) determination	67
4.4.2	Infrared spectroscopy (IR)	67
4.4.3	Nuclear magnetic resonance spectroscopy (NMR)	67
4.4.4	Mass spectrometry (MS)	67
4.4.5	Elemental analysis	68
4.4.6	X-ray diffraction (XRD) studies	68
4.5	Catalyst synthesis and characterization	68
4.5.1	Recrystallization of ferrocene [1]	69
4.5.2	Ferrocenylmethanol [2]	69
4.5.3	Ferrocenoyl imidazolide [3]	70
4.5.4	(<i>N</i> -Phenylcarbamoyl)ferrocene [4]	70
4.5.5	<i>S,S</i> -Bis(ferrocenylmethyl)dithiocarbonate [5]	71
4.6	Results and discussion	72
4.6.1	Ferrocenylmethanol [2]	72
4.6.2	Ferrocenoyl imidazolide [3]	73
4.6.3	(<i>N</i> -Phenylcarbamoyl)ferrocene [4]	75
4.6.4	<i>S,S</i> -Bis(ferrocenylmethyl)dithiocarbonate [5]	78
4.7	Conclusions	79
	References	79

CHAPTER 5 SYNTHESIS AND CHARACTERIZATION OF MWCNTs AND OTHER SCNMs USING FERROCENE AS A CATALYST

5.1	General procedures	81
	5.1.1 Cleaning of quartz reactor and glass apparatus	81
	5.1.2 Preparation of anhydrous toluene	81
5.2	Common laboratory chemicals, reagents, solvents and gases	81
5.3	Reactor design and setup	82
5.4	General procedure for synthesis and recovery of MWCNTs and other SCNMs from reactor	83
	5.4.1 General synthesis method	83
	5.4.1.1 Experiment 1	84
	5.4.1.2 Experiment 2	84
	5.4.2 Recovery of MWCNTs and other SCNMs from reactor	85
5.5	Purification methods	86
5.6	Characterization of MWCNTs and other SCNMs: Instrumentation and techniques	87
	5.6.1 Transmission electron microscopy (TEM)	87
	5.6.2 Scanning electron microscopy (SEM)	89
	5.6.3 Electron dispersive X-ray spectroscopy (EDX)	89
	5.6.4 Thermogravimetric analysis (TGA)	89
	5.6.5 Brunauer, Emmett and Teller (BET) analysis	90
	5.6.6 Raman spectroscopy	90
5.7	Results and discussion of Experiment 1 – Effect of temperature	90
	5.7.1 Experimental challenges, modifications and raw yields	90
	5.7.2 Products obtained at 950 °C	92
	5.7.3 Products obtained at 900 °C	93
	5.7.4 Products obtained at 850 °C	95
	5.7.5 Products obtained at 800 °C	96
	5.7.6 Products obtained at 750 °C	98
	5.7.7 General trends from the effect of temperature	99
	5.7.7.1 SCNMs formed	99
	5.7.7.2 ID and OD of MWCNTs	101
	5.7.7.3 Length of MWCNTs	103
	5.7.7.4 Alignment of MWCNTs	104

5.7.7.5	Size of spheres	104
5.7.7.6	Elemental composition (by EDX) of products	105
5.7.7.7	Crystallinity and thermal stability of products	105
5.7.7.8	Surface area of products	108
5.7.8	Anomalous structures	109
5.7.9	Conclusions from Experiment 1	110
5.8	Results and discussion of purified MWCNTs from Experiment 1	111
5.9	Results and discussion of Experiment 2 – Effect of temperature and concentration	114
5.9.1	Raw yields	114
5.9.2	SCNMs formed	114
5.9.3	ID and OD of MWCNTs	116
5.9.4	Length of MWCNTs	118
5.9.5	Alignment of MWCNTs	119
5.9.6	Crystallinity and thermal stability of products	119
5.10	Conclusions from Experiment 2	121
5.11	Summary of Experiments 1 and 2	121
	References	122

CHAPTER 6 INFLUENCE OF HETEROATOMS (N, O AND S) ON THE SYNTHESIS OF MWCNTs AND OTHER SCNMs

6.1	Results and discussion of Experiments 3, 4 and 5 – Effect of the introduction of N and O	124
6.1.1	Reaction parameters and raw yields	124
6.1.2	SCNMs formed	125
6.1.3	ID and OD of MWCNTs	134
6.1.4	Length of MWCNTs	139
6.1.5	Alignment of MWCNTs	140
6.1.6	Size of spheres	141
6.1.7	Crystallinity and thermal stability of products	141
6.2	Conclusions from Experiments 3, 4 and 5	146
6.3	Results and discussion of Experiment 6 – Effect of the introduction of S and O	148
6.3.1	Reaction parameters and raw yields	148
6.3.2	SCNMs formed	148
6.3.3	Size of spheres	149

6.3.4	Crystallinity and thermal stability of products	150
6.4	Conclusions from Experiment 6	152
6.5	Summary of Experiments 3 to 6	152
References		152

CHAPTER 7 LOADING Pd ONTO MWCNTs BY MOCVD

7.1	Introduction to MOCVD	154
7.2	Instrumentation – The MOCVD apparatus	156
7.3	Laboratory chemicals, reagents, solvents and gases	157
7.4	General procedure	158
7.4.1	Surface functionalization of the chosen supports	158
7.4.2	Deposition of Pd by MOCVD	158
7.5	Characterization of Pd/MWCNTs: Instrumentation and techniques	159
7.5.1	Inductively coupled plasma-optical emission spectroscopy (ICP-OES)	159
7.5.2	Scanning electron microscopy (SEM)	160
7.6	Results and discussion of oxyacid functionalization of supports	160
7.6.1	TEM and SEM analysis	160
7.6.2	TGA results	161
7.6.3	BET analysis	162
7.7	Results and discussion of the deposition of Pd onto supports	163
7.7.1	Raw yields	163
7.7.2	TEM and SEM analysis	164
7.7.3	BET analysis	167
7.7.4	ICP-OES analysis	168
7.8	Conclusions	168
References		169

CHAPTER 8 CONCLUSIONS AND FUTURE WORK

8.1	Conclusions	170
8.2	Future work	171

APPENDICES	173
A ^1H -NMR spectra	174
B ^{13}C -NMR spectra	176
C FTIR spectra	178
D Mass spectra	181
E Selected SEM, TEM and HRTEM images of MWCNTs and SCNMs	186
F EDX results	190
G Raman results	193
H TGA derivative curves	194
I Bamboo compartment lengths	197
J ICP-OES calibration curve	198

ACKNOWLEDGEMENTS

I would like to warmly thank and acknowledge the help, time and effort that Dr Vincent Nyamori, my supervisor, put into training me during the course of this study. His enthusiasm and interest in both nanochemistry as well as in me as his student is much appreciated. I am grateful for his mentorship role in furthering my education in chemistry.

Thanks are also due to the University of KwaZulu-Natal, School of Chemistry and Physics, for the opportunity to do a Master of Science and the space to do my research.

I also extend grateful appreciation to my colleagues:

- Fulufhelo Sithole, Nonkululeko Mote and Hezekiel Kumalo for helping me scale-up reactions in the lab,
- Rajshekhar Karpoormath, Sicelo Sithole, Monisola Ikhile, Michael Pillay and Dennis Mkhize for their practical advice and help, but especially Dennis whose interest in his project inspired me in mine,
- Dilip Jagjivan for his expertise in NMR analysis,
- Dr James Wesley-Smith, Priscilla Maartens, Sharon Eggers and Phillip Christopher in the Electron Microscope Unit for their efforts in training and assisting me,
- Neal Broomhead and Anita Naidoo for endless patience and willingness to train me on various instruments and for solving and fixing instrument problems,
- Dr Thavendran Govender and Sibonelo Bhengu for their advice on the running of and interpretation of certain mass spectra,
- Manoko Maubane (University of the Witwatersrand) who uncomplainingly ran some of my TGA samples when the TGA instrument at UKZN was undergoing repairs,
- Dr Patrick Ndungu who shared his expertise on MOCVD with me,
- Prof. Bice Martincigh who assisted in editing some of my work,
- Dr Bernard Owaga for the XRD work and his advice concerning crystal structures.

Funding was provided by the National Research Foundation (NRF) *via* the grant-holder Dr Leslie Petrik at the University of the Western Cape, under the Nanotechnology Flagship Programme “Nano-architecture in the Beneficiation of Platinum Group Metals”. I thank both the NRF and Dr Petrik for this support.

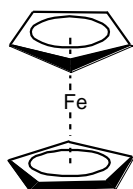
I am most grateful to Prof. Neil Coville (University of the Witwatersrand) for his advice in the construction of Chapter 2, the review paper, and Prof. Bice Martincigh (University of KwaZulu-Natal) for assisting in proof-reading and comments during the development of the manuscripts for journal publication as well as in proof-reading this dissertation. Prof. Martincigh also gave me helpful direction in Chapter 6.

I extend a heartfelt thank you to my husband, my parents and my brother. Their continuing encouragement and support in my efforts to tackle this project part-time has made it all the more worthwhile.

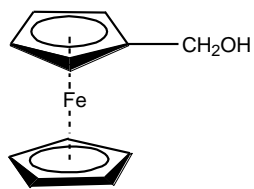
And finally, I thank the Lord for His constant presence and encouragement in my studies. His strength has lifted me up and enabled me to complete this interesting work.

GLOSSARY OF COMPOUNDS

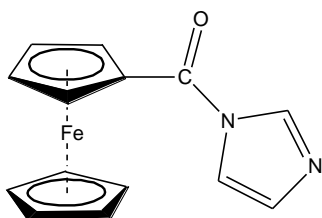
Compound structure and number



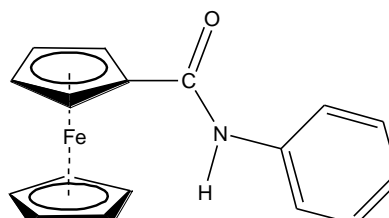
[1]
ferrocene



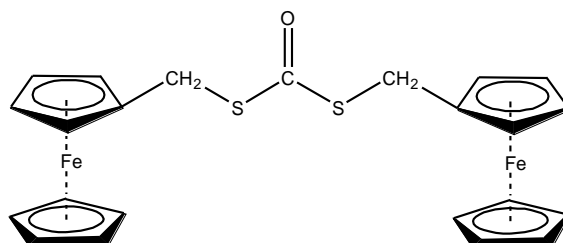
[2]
ferrocenylmethanol



[3]
ferrocenoyl imidazolidide



[4]
N-phenylcarbamoylferrocene



[5]
S,S-bis(ferrocenylmethyl)dithiocarbonate

LIST OF ABBREVIATIONS AND SYMBOLS

Full name	Abbreviation
Acetyl acetate	acac
Activated carbon	AC
Analytical reagent	AR
Angstrom	Å
Approximately	<i>ca.</i> or approx.
Arbitrary unit	a.u.
Atmospheres	atm
Attenuated total reflectance Fourier transform infrared spectroscopy	ATR or ATR-FTIR
Average	Ave.
Brunauer Emmett and Teller (method)	BET
Carbon nanofibre(s)	CNF(s)
Carbon nanotube(s)	CNT(s)
Carbon thirteen nuclear magnetic resonance	¹³ C-NMR
Catalyst	cat.
Centimetre	cm
Chemically pure	CP
Chemical vapour deposition	CVD
Commercial multi-walled carbon nanotubes	com-MWCNTs
Concentration	conc.
Cubic centimetre	cm ³
Degrees Celsius	°C
Dichloromethane	DCM
Diethyl ether	Et ₂ O
Double-walled carbon nanotube(s)	DWCNT(s)
Electron impact ionization	EI
Electrospray ionization	ESI
Elemental analysis	CHN
Energy dispersive X-ray spectroscopy	EDX
Ethyl acetate	EtOAc
Experiment	Exp.
Ferrocenyl moiety	Fc
Field emission gun scanning electron microscopy	FEG SEM
Fourier-transform infrared spectroscopy	FTIR
Functionalized commercial multi-walled carbon nanotubes	<i>f</i> -com-MWCNTs
Functionalized synthesized multi-walled carbon nanotubes	<i>f</i> -syn-MWCNTs
Gram	g
Hertz	Hz
Hexafluoroacetylacetate	hfa
High angle annular dark field microscopy	HAADF
High pressure carbon monoxide [process]	HiPCO
High resolution electrospray ionization	HRESI

High resolution scanning transmission electron microscopy	HRSTEM
High resolution transmission electron microscopy	HRTEM
Hour	h
Ionic liquid	IL
Inductively coupled plasma optical emission spectroscopy	ICP-OES
Infrared	IR
Inner diameter	ID
Kelvin	K
Kiloelectron volts	keV
Kilopascals	kPa
Kilovolts	kV
Lithium aluminium hydride	LAH
Litres	L
Macherey Nagel	MN
Mass-to-charge ratio	m/z
Mass spectrometry	MS
Maximum	max.
Melting point	m.p.
Metal organic chemical vapour deposition	MOCVD
Methanol	MeOH
Metres squared	m ²
Microlitre	μL
Micrometre	μm
Millibars	mbar
Milligrams	mg
Millilitres	mL
Millimetres	mm
Moles	mol
Millimoles	mmol
Minimum	min.
Minutes	min
Molar concentration	M
Moles	mol
Mole percent	mol%
Multi-walled carbon nanotube(s)	MWCNT(s)
Nanometres	nm
Nanoparticle(s)	NP(s)
Nitrogen-doped carbon nanotube(s)	N-CNT(s)
Nitrogen-doped multi-walled carbon nanotube(s)	N-MWCNT(s)
Nuclear magnetic resonance	NMR
Outer diameter	OD
Palladium-loaded functionalized commercial multi-walled carbon nanotubes	Pd- <i>f</i> -com-MWCNTs
Palladium-loaded functionalized synthesized multi-walled carbon nanotubes	Pd- <i>f</i> -syn-MWCNTs
Parts per million concentration	ppm

Phenyl ring	Ph
Picoamperes	pA
Proton nuclear magnetic resonance	$^1\text{H-NMR}$
Radial breathing mode	RBM
Ratio of D-band intensity to G-band intensity in Raman spectroscopy	I_D/I_G
Room temperature	RT
Scanning electron microscopy	SEM
Seconds	s
Shaped carbon nanomaterials	SCNMs
Single-walled carbon nanotube(s)	SWCNT(s)
Sodium bis(2-hexylethyl)sulfosuccinate	AOT
Sodium dodecyl sulfate	SDS
Standard cubic centimetres per minute	sccm
Synthesized multi-walled carbon nanotubes	syn-MWCNTs
Temperature of constant temperature zone in CVD furnace	T_{\max}
Tetrahydrofuran	THF
Tetramethylsilane	TMS
Thermal gravimetric analysis	TGA
Thin layer chromatography	TLC
Transmission electron microscopy	TEM
Turnover frequency	TOF
Volts	V
Volume-by-volume concentration	v/v
Watts	W
Watts per meter Kelvin	W/mK
Wavenumber	cm^{-1}
Weight-by-weight concentration	w/w
Weight percent	wt.%
X-ray photoelectron spectroscopy	XPS
X-ray diffraction	XRD

CHAPTER 1

LITERATURE REVIEW OF CARBON NANOTUBES

1.1 Introduction

The history of mankind has been broadly categorized and defined by major scientific advances; from the beginnings of steel forging with its influence on agriculture and society in the Iron Age, through to the electronic and information age of the mid to late 1900s, which is still pervading our entire society, and finally to the nanotechnology age of the present. Nanotechnology was aptly described by Ando *et al.* as “*the creation of functional materials, devices, and systems through control of matter on the nanometer scale and the exploitation of novel phenomena and properties of matter (physical, chemical, biological, electrical, etc.) at that length scale*”.¹ The authors went on to say that, “*Carbon nanotubes are supposed to be a key component of nanotechnology*”. Indeed, the discovery of carbon nanotubes (CNTs), with their unique properties, has been a major turning point in the direction of scientific research, with growing numbers of scientists shifting their focus towards nano-scale studies.

1.2 Discovery of carbon nanotubes (CNTs)

For over two centuries, man has been aware of the growth of very small, even micro-sized carbon filaments on iron crucibles from carbonaceous gases.² In the latter part of the 1960s nanofibres of carbon were grown over a metal support.³ Then in 1985, the synthesis of C₆₀, or buckminsterfullerene, was first reported.⁴ This nano-sized carbon structure was so named after Richard Buckminster Fuller, an architect who designed the geodesic dome, since the structure of this allotrope of carbon resembles two geodesic domes joined into a sphere. This new form of carbon, other than the known diamond and graphite, started a move towards the study of other possible carbon allotropes and compounds.

In 1991 Iijima was using arc evaporation techniques to produce C₆₀ of high purity.⁵ TEM studies showed the existence of tubular carbon structures in the product. The tubes were closed at each end and consisted of outer diameters ranging from 4 to 30 nm. This was perhaps the first observation of nano-sized carbon tubes, or CNTs. However, a report by Monthieux and Kuznetsov⁶ suggests that perhaps the discovery of CNTs should be credited to Oberlin *et al.*⁷ The latter authors published a report in 1976 which contained images resembling very thin CNTs. Further research ensued as scientists began to reproduce this material *via* different techniques and interest in CNTs has grown considerably.

CNTs have been found to display unique and surprising properties. A broadening scope of potential applications for CNTs exists due to these properties. These particular aspects will be discussed later in this chapter, while a discussion on CNT structure follows.

1.3 Structural characteristics of CNTs

CNTs can be considered to be sheets of sp^2 hybridized carbon atoms, essentially graphene, rolled up into a cylinder with carbon atoms on the perimeter bonding seamlessly to form a tube. On either end could be half a fullerene molecule (bucky ball).⁸ Two mechanisms for CNT formation are commonly considered. The predominant understanding is that CNTs derive from half a bucky ball growing lengthways. However, others suggest that the encapsulation of Pd nanoparticles (NPs) inside CNTs, synthesized from an arc-discharge method, suggests that perhaps graphene sheets do indeed curl up.⁹ Such growth mechanisms will be discussed in **Section 1.8**.

CNTs are classified very broadly into single-walled carbon nanotubes (SWCNTs), double-walled carbon nanotubes (DWCNTs) and multi-walled carbon nanotubes (MWCNTs), depending on the number of concentric, coaxial cylinders present in the structure. Some authors refer to such hollow tubular structures as carbon nanofibres (CNFs) or filaments,¹⁰ while some consider those structures without hollow centres as CNFs. Still others call those CNTs which are wider in diameter than 100 nm to be CNFs. **Figure 1.1** depicts how a graphene sheet could roll up, to form a SWCNT. **Figure 1.2** shows the structure of tubes, one containing a single concentric cylinder (SWCNT) and the other containing more than one cylinder (MWCNT).

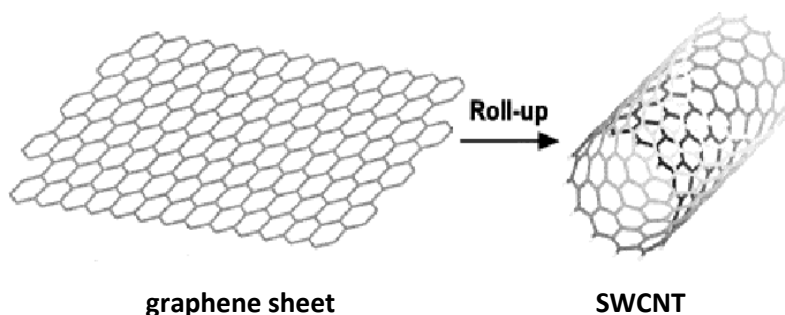


Figure 1.1 Diagram showing the manner in which a SWCNT resembles a rolled up graphene sheet.¹¹

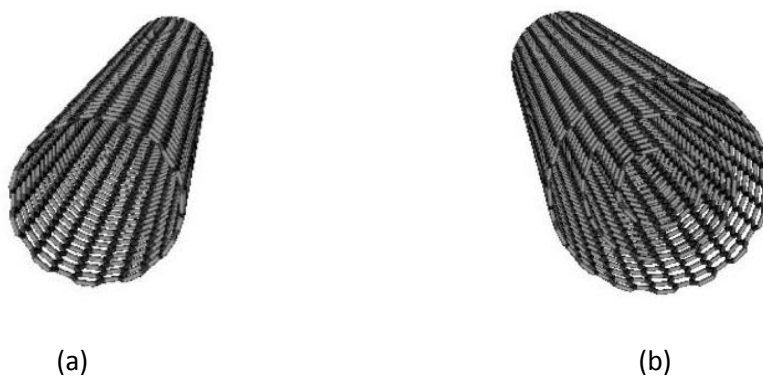


Figure 1.2 Diagram showing the lone cylinder of a (a) SWCNT versus the multiple concentric cylinders of a (b) MWCNT.¹²

Typically SWCNTs have diameters as small as 0.4 nm and MWCNTs range widely in diameter up to 100 nm.¹³ The typical diameters of these structures are given in **Table 1.1**. CNT and CNF lengths vary considerably in the literature, and can be proportionately much larger than their diameters, with the aspect ratio reaching, in some cases, over 10^9 for SWCNTs.^{14,15}

Table 1.1 The typical diameters of SWCNTs, MWCNTs and CNFs.

	SWCNTs	MWCNTs	CNFs
typical diameter (nm)	> 0.4 ¹³	5 - 100 ¹³	> 100

These straight cylinder-type structures can be modified in their shape when heteroatoms, such as nitrogen and boron, are incorporated into their structure (doping), effectively replacing some carbon atoms. Doping of CNTs will be discussed in **Section 1.9**.

1.3.1 Single-walled carbon nanotubes (SWCNTs)

The manner in which a graphene sheet is curled up into a tubular structure is defined by **equation (1)**:

$$C_h = na_1 + ma_2, \quad (1)$$

where C_h is the chiral vector, n and m are integer values, and a_1 and a_2 are lattice vectors.^{16,17}

Figure 1.3 shows the chiral vector.

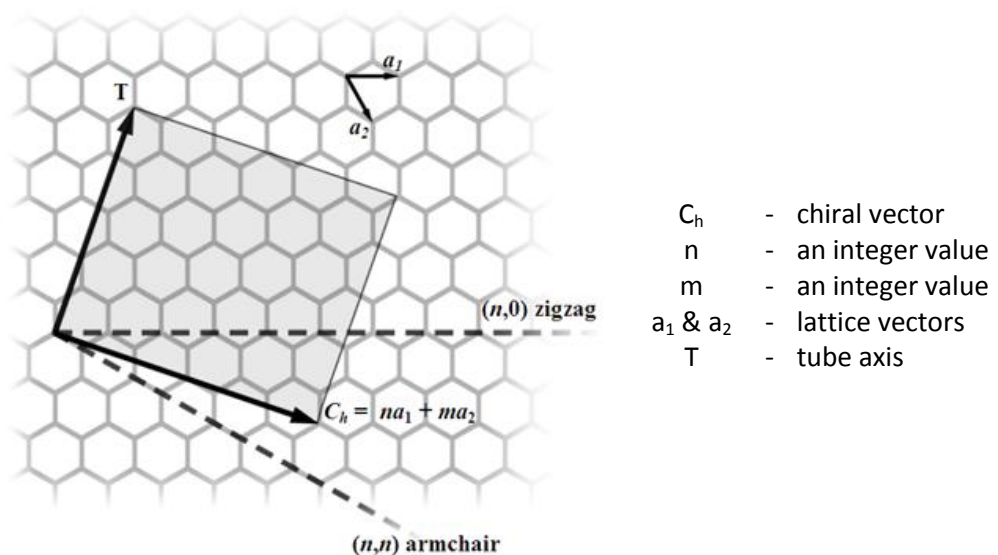


Figure 1.3 The chiral vector, C_h , which describes different manners in which a graphene sheet can roll up into a CNT.¹⁸

Helicity of CNTs can exist in one of three forms: the armchair structure, when the chiral angle is 30° and $n = m$; the zigzag structure, formed when the chiral angle is 0° and either n or m is equal to 0; and the chiral type nanotubes where the chiral angle is between 0° and 30° . The distance between two adjacent bonded carbon atoms is 1.44 \AA which is slightly larger than the 1.42 \AA of graphite.¹⁹ Presumably the curvature of the graphene layer results in the altered bond lengths. **Figure 1.4** shows the three helicities graphically.

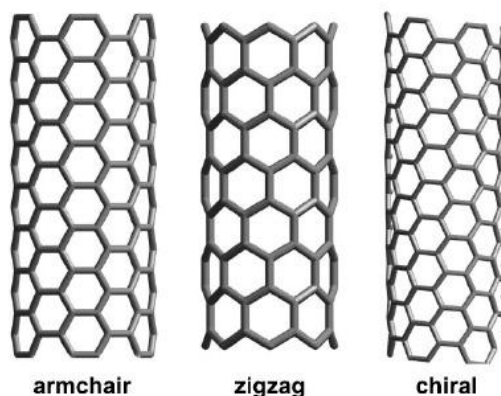


Figure 1.4 Diagram of the three helicities of SWCNTs.²⁰

The metallic or semi-conducting nature of SWCNTs is determined by the way in which the hexagonal rings are arranged, i.e. by their helicity.²¹

1.3.2 Multi-walled carbon nanotubes (MWCNTs)

Two models exist which describe the structure of MWCNTs. These models are the Russian Doll Model where concentric SWCNTs of different diameters are combined one inside the other concentrically⁵ like a Russian Doll, and the Parchment or Scroll Model where only one graphene sheet exists rolled up on itself like a scroll.⁹ Most authors understand MWCNT structure in terms of the former model. The distance between the individual layers in MWCNTs approximates the distance between graphite layers which is 3.4 \AA .²²

When concentric cylinders of carbon nanotubes make up the MWCNT, the resulting structure can be referred to as parallel-fibres. When the layers appear to look like fishbones the structure is referred to as a fish- or herringbone fibre.²³ Both structures have been synthesized under similar conditions. **Figure 1.5** shows a schematic diagram of these structures. The simplest MWCNTs are the DWCNTs.

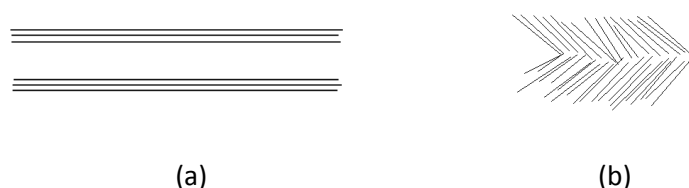


Figure 1.5 Schematic diagram of (a) MWCNTs or parallel-fibres and (b) herringbone fibres.

1.4 Properties of CNTs

This section discusses some properties of CNTs in a general and brief manner. However, **Chapter 2, Section 2.2** looks at a comparative discussion of those properties that are specifically important when considering CNTs, and other materials, as supports for catalysts.

1.4.1 Mechanical properties

CNTs are the stiffest and strongest material known. Their stiffness, measured as a Young's modulus, can reach into the terapascal range for ropes of SWCNTs – the strongest man-made material.²⁴ A MWCNT was tested in 2000 for tensile strength. Results generated a value of 63 gigapascals.²⁵ The mechanical strength of CNTs arises from the carbon-carbon covalent sp^2 bonds and the resulting honeycomb lattice structure. The larger the diameter of CNTs, the less is the degree of curvature. This results in a lower strain on the carbon-carbon bonds, and hence the more the strength of the material will be similar to that of graphite.²⁶ This explains why MWCNTs have a Young's modulus closer to graphite than do SWCNTs. (Graphite has a Young's modulus of approximately 9 to 14 gigapascals.)²⁷

CNTs are flexible and are known to be highly elastic in nature. However, MWCNTs are not as elastic as SWCNTs. Amongst many studies on the elasticity of CNTs, Cheng *et al.* showed this property anecdotally.²⁸ They synthesized SWCNTs and then analyzed them by means of transmission electron microscopy (TEM). One particular image revealed a CNT bent into a “z” shape, without the tube breaking. The bending of the CNT into a “z” shape was considered a simple piece of evidence suggesting that the tube was indeed a SWCNT. It is the hexagonal structure of CNT units which allows for the relaxation of stress on bending, hence, an elastic deformation.

The number and placement of defects in CNTs also largely determines their strength.²⁹ Salvetat *et al.* explain that the individual bonding of atoms, across the length of CNTs affects the overall “cohesion” of the CNTs and hence the Young's modulus.²⁶ These authors grew CNTs by arc-discharge and a catalytic method. Their arc-discharge grown CNTs had a Young's modulus of approximately an order of magnitude higher than those grown catalytically. Arc-discharge CNTs are also generally lower in defects than those grown by catalytic methods. This makes arc-discharge CNTs more suitable for applications where higher strength is needed. Whether bulk materials, such as composites, would differ greatly in terms of strength when the synthesis methods of their component CNTs differ, is a consideration, although it is unlikely that a significant difference, on the bulk-scale would be observed. On the nanoscale it would perhaps be marked. Salvetat *et al.* also discussed the fact that the strength of a material is also affected by the pressure, temperature and chemical environment.²⁶ Thus all these factors ultimately influence the overall strength of the material, with very few materials acting according to theoretical predictions. For example, CNTs at low temperature act as typical covalent materials, with brittleness increasing at lower temperatures. Hence, the application environments of CNTs for strength purposes are not inconsequential, but will influence the ultimate strength properties.

An interesting paper by Shenderova *et al.* compared SWCNTs with “diamond nanorods” by computational methods.³⁰ Diamond has been acclaimed as the most superior material for strength and hardness on the bulk scale. However, the authors found that the nanoscale diamond structures are less strong than small diameter SWCNTs, since SWCNTs have stronger carbon-carbon double bonds compared to the carbon-carbon single bonds in diamond. With an increase in diameter the diamond nanorods, however, were increasingly stronger than the SWCNTs.

1.4.2 Thermal properties

The thermal conductivity of CNTs is high, with up to 3000 W/mK being reached for MWCNTs.³¹ Copper is considered a good thermal conductor and transmits heat energy at a much lower rate, specifically 385 W/mK. CNTs are also thermally stable. For more on their thermal properties, see **Chapter 2, Section 2.2** where CNTs are compared and contrasted with the more traditional catalyst supports.

1.4.3 Electronic properties

Literature has shown that the electrical properties of CNTs are determined by a variety of factors, from the chemical composition, to the helicity, and even to the way in which they bend.

The helicity of CNTs is perhaps the primary factor in determining the electronic nature. Theoretical calculations showed that SWCNT armchair nanotubes are metallic in nature, while the chiral and zigzag forms are either conducting or semiconducting.³² Because it is challenging to isolate individual SWCNTs, SWCNTs are often treated theoretically for electrical behaviour. The challenge is in getting large bundles with predictable properties, since a bundle may be composed of tubes which are both more conducting (metallic) and more insulating (semi-metallic). Despite the experimental challenges, in 2001, the first intramolecular logic gate was made from a single SWCNT bundle.³³

SWCNTs act like quantum wires, confining the electrons to the axis of the tube. However, MWCNTs resemble graphite in their conductivity. Since the helicities of the individual tubes in a MWCNT can vary, this causes the overall electronic properties of different MWCNTs difficult to determine. Coupled with this is the increased opportunity for structural defects as the number of walls increases, and because structure and helicity affect electrical properties, it is logical to conclude that defects thus influence the electrical properties.

In other studies it was shown that the chemical environment and bending of CNTs greatly influences their electronic properties. With respect to chemical environment, air and oxygen were shown to affect the electrical resistance of SWCNTs.³⁴ It was suggested that “tuning” the conductivity of the SWCNTs can be done by the adsorption of selected gases onto the surfaces. This would have impact on the electronic applications of the SWCNTs. In terms of bending, a change in electrical properties is caused by the change in carbon-carbon bond lengths.³⁵

Problems in controlling the electrical nature can arise, since CNTs, with their high aspect ratio, bend readily. Thus bending is an important factor when using CNTs in electrical applications.

Another factor controlling the electrical nature of CNTs is their chemical composition. Doping of CNTs with heteroatoms such as nitrogen and boron can increase the metallic nature of the CNTs. Doping and its effects will be discussed further in **Section 1.9**.

Like any electrical conductor, external electrical fields will interact with the conductor's electrical field, essentially altering it and producing a new, net effect. This was demonstrated in a first principles computational study, where the effect of a transverse electric field on SWCNTs was studied.³⁶ Zigzag and armchair CNTs were found to behave very differently in the field. The field was able to reduce the band gap in zigzag CNTs, but had little effect on the armchair CNTs which remained metallic. This type of research should thus inform the design and placement of SWCNTs in nano-scale electrical devices.

1.4.4 Optical properties

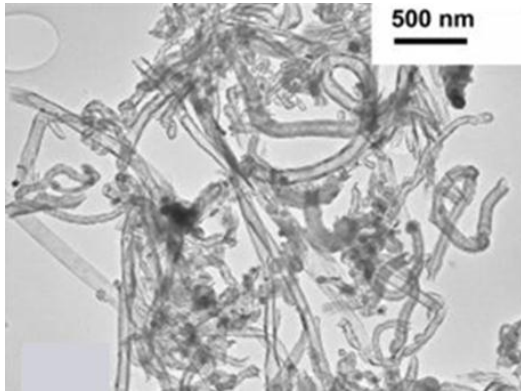
Optical properties of CNTs are those interactions that CNTs have and display when irradiated with light. Optical analysis methods include Raman, ultraviolet, infrared and visible spectroscopy and combinations of these. Typically the information collected from such analyses is used to characterize the structure and properties of CNTs. Raman spectroscopy, for example, which collects reflected laser light from CNTs, is useful in determining the crystallinity of CNTs and the relative diameter of SWCNTs. Kataura *et al.* compared TEM images and Raman data with results from another optical technique, photothermal deflection spectroscopy.³⁷ They showed that the information from the latter can be used in a similar manner to the former two methods – namely to indicate tube diameters.

The optical property related applications of CNTs have not advanced as much as those applications which rely on their mechanical and chemical properties. Nevertheless, research continues in this area, with some emerging applications being their use in light-emitting devices³⁸ and photo-detectors.³⁹ (Other applications of CNTs will be discussed in **Section 1.12**.)

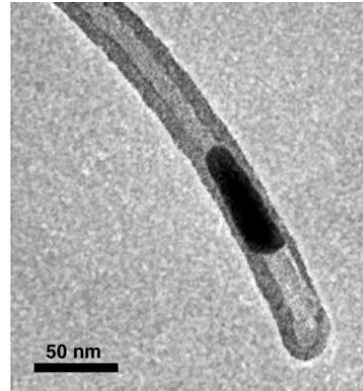
The next section deals with impurities and other materials formed during certain CNT synthesis techniques.

1.5 CNTs and other shaped carbon nanomaterials (SCNMs)

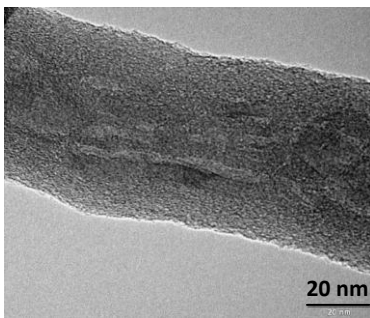
Though high yields of CNTs can be produced^{19,40-43} in certain synthesis techniques, the reaction conditions employed can dictate the formation of a range of possible structural morphologies. These substances include carbon nanotubes – hollow⁴⁴ or metal filled,⁹ carbon nanofibres,⁴⁵ carbon nano- and microspheres – hollow^{46,47} or filled,⁴⁷⁻⁵⁰ horns,⁵¹ onions,⁵² core-shell spheres/nodules,^{53,54} cages,⁵⁵ polygon structures and amorphous carbon. **Figure 1.6** shows selected TEM images of such structures. As research into the field of nanostructures progresses, so the range of carbon nanostructures is being added to.



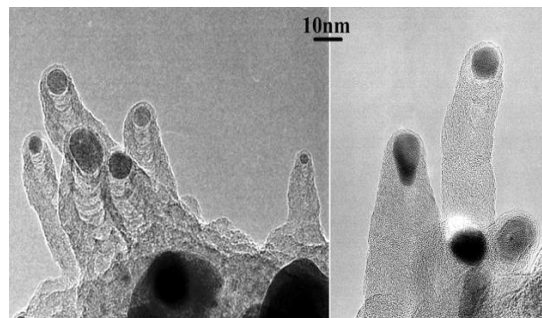
Carbon nanotubes (hollow)⁴⁴



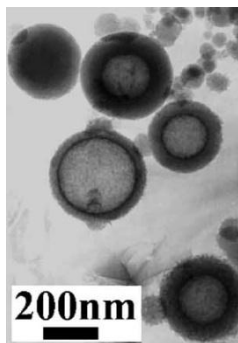
Carbon nanotube
(containing encapsulated metal particle)⁵⁶



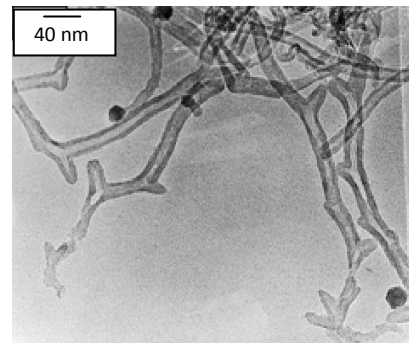
Carbon nanofibres⁴⁵



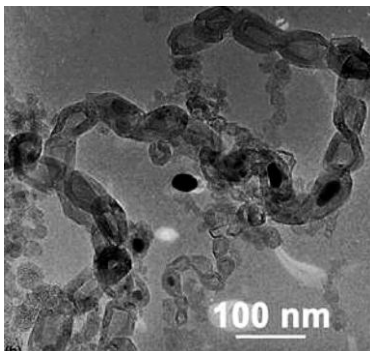
Carbon nanohorns⁵¹



Carbon nanospheres (hollow and filled)⁴⁷



Carbon nanotubes with Y-junctions⁵⁷



Carbon nano-onions⁵⁸



Carbon nanocoils⁵⁹

Figure 1.6 Representative TEM images of some shaped carbon nanomaterials (SCNMs).

Other examples include, for example, the carbon nano-“necklaces” – actually stacked multi-walled carbon spheres resembling cups which were produced *via* a thermal plasma method,⁶⁰ and tapered CNTs made from CdS/SnO/activated carbon mixtures.⁶¹

At the nanoscale, structural morphology is of vital concern, because particles of nanodimension have significantly enhanced or even different properties as compared to the same material on a scale orders of magnitude larger than the nanoscale.⁶² The next section deals with the techniques used to synthesize nanoscale carbon structures.

1.6 Synthesis of CNTs and other SCNMs

The three most common techniques used to synthesize CNTs and other SCNMs have been used and modified over approximately the last two decades.⁶³ These methods are the arc-discharge method, laser ablation method and chemical vapour deposition (CVD) method. Each technique has its own set of benefits and limitations. All techniques require a carbon source, high temperatures to decompose the carbon source and an inert atmosphere to prevent gasification of the carbon material. All techniques involve the collection of the products off the surface onto which they have been deposited.

1.6.1 Arc-discharge method

When an electric arc is generated between two graphite electrodes the energy can be sufficient to produce CNTs on the surface of the cathode, chamber walls or in the sooty gaseous atmosphere.^{64,65} Temperatures can reach up to 3000 °C in this process and thus an inert atmosphere is used to prevent the oxidation of the graphite rods. These high temperatures create a plasma. Sometimes a powdered metal catalyst is a constituent of one of the electrodes.⁶⁵ Co and Ni are common examples of such metal catalysts. Vapourization of carbon (and the metal if present) occurs, hence producing SWCNTs and other SCNMs⁶⁶⁻⁶⁸ with the metal often filling the structures. Secondary metals have been shown to influence the activity of the base metal.⁶⁹ Ar/CH₄ atmospheres are conducive to the synthesis of SWCNTs with iron as the catalyst and produce SWCNTs predominantly. Disadvantages of this method include low yields of short (< 1 μm) SWCNTs. Subsequent purification methods are necessary to remove the unwanted components – soot and metal catalyst residual particles. Although this technique is a costly one, it has simplicity as an attractive feature.^{70,71} Highly ordered (crystalline) products are usually the primary advantage of such a technique. **Figure 1.7** shows the basic setup of the arc-discharge instrumentation.

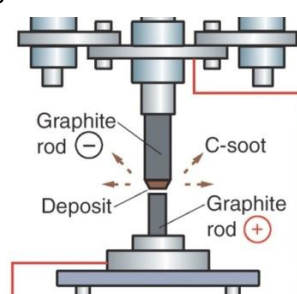


Figure 1.7

Diagram of a typical setup in the arc-discharge apparatus.¹

As mentioned, other SCNMs, besides SWCNTs, can be formed using arc-discharge. For example, Qiu *et al.* synthesized fairly uniform, micrometre-range diameter (10-20 μm), highly graphitized carbon spheres with this method, by using a Ni catalyst and coal as the carbon source.⁷²

1.6.2 Laser ablation/Laser furnace technique

Kroto *et al.* were the first to report the synthesis of fullerenes in the gas phase by means of a laser ablation technique.⁴ **Figure 1.8** shows the general instrumentation used in the laser ablation synthesis of carbon materials. A laser can be used to ablate a graphite target, which is filled with a metal powder catalyst, into a vapour form.^{73,74} Co and Ni are common examples of catalysts. An inert atmosphere is necessary to prevent oxidation of the carbonaceous material. Cooling of the vapour occurs as it expands, followed by subsequent condensation of the carbonaceous species. High furnace temperatures promote annealing of the products, thereby increasing their crystallinity. The interaction of the species can result in clusters of carbon which are moved downstream by an inert carrier gas, and deposited on a cold finger where further growth of the particles may occur. The end-products are carbon allotropes such as CNTs and other SCNMs.⁷³⁻⁷⁶ Typically the CNTs are SWCNTs. These SWCNTs are typically found in “ropes” consisting of up to several tens of SWCNTs aligned and held together by van der Waal’s forces.⁷⁶

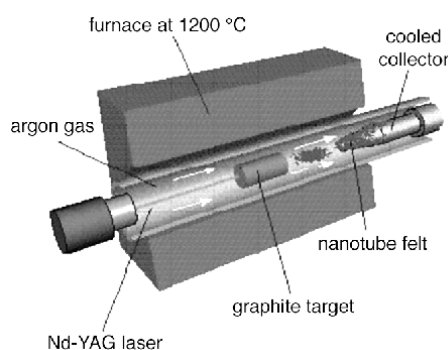


Figure 1.8 Diagram of the laser ablation apparatus.⁷⁷

The laser ablation method usually produces high yields of high quality SWCNTs. Bandow *et al.* used microfiltration techniques to separate SWCNTs from other SCNMs formed by this method, thereby increasing the purity of the products.⁷⁸ However, despite high percentage yields of CNTs, arc and laser techniques are not yet industrially viable for the production of large quantities of materials.

1.6.3 Chemical vapour deposition (CVD) method

Chemical vapour deposition (CVD), sometimes called thermal or catalytic vapour deposition, is a technique which has been employed for decades for the production of carbon filaments and

fibres.⁷⁹ CVD can produce both SWCNTs and MWCNTs, as well as other SCNMs such as carbon nanospheres, depending on the reaction conditions. Usually high temperatures, from 300 to 1000 °C, are used to decompose an organometallic compound/complex and a carbon source.^{44,80} (However, Matveev *et al.* successfully grew CNTs at temperatures below room temperature.⁸¹) The carbon source can be in the solid, liquid or gas phase and is either introduced into the hot zone of a furnace under a controlled carrier gas flow rate, by injection or aerosol, or held in the zone while heating, decomposition and CNT growth occurs. The catalyst is usually finely divided – either as a solid on a surface or in the gaseous phase (see **Sections 1.6.3.1 to 1.6.3.3**). Systems can be open (see **Sections 1.6.3.1 and 1.6.3.2**) or closed (see **Section 1.6.3.3**).

The organometallic compound/complex is used as a source of metal atoms. The catalytically active component is the zero oxidation state liquid metal nanoparticle (NP) and not the organometallic compound itself. Strictly speaking, the organometallic compound should thus be called a *catalyst precursor*, although in the literature the term *catalyst* is used interchangeably for both the initial compound and the metallic NP formed after compound decomposition and reduction. In this dissertation the word *catalyst* will be used.

The organometallic compound/complex can itself act as a source of carbon. The individual carbon atoms, from compound decomposition, dissolve in the metal NP and, on cooling, precipitate out on the curved metal particle surfaces. (Refer to **Figure 1.9**.) As more atoms precipitate out, so the carbon structure is lifted off the surface and the tube grows.

The tailoring of the catalyst NP diameter will in turn affect the inner diameter (ID) and outer diameter (OD) of the resultant CNT as in **Figure 1.9 (a)**. Temperature, reaction time, carbon source and gas flow rate are controllable factors influencing the diameter of the metal NP and thus the CNTs. **Figure 1.9 (b)**, however, shows a growing CNT whose diameter is much smaller than the metal NP. The former method (**Figure 1.9 (a)**) is generally accepted.¹⁰

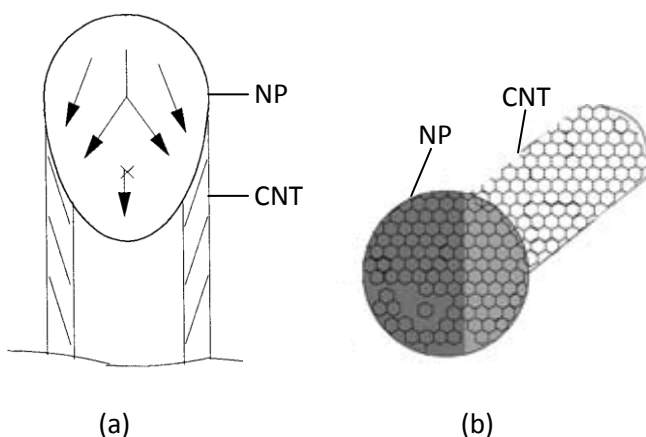


Figure 1.9

Diagram showing how carbon atoms precipitate off the metal NP surface forming a CNT (a) in proportion with the diameter of the metal NP¹⁰ versus (b) out of proportion with the diameter of the metal NP.⁸²

CVD allows for both scale-up and fairly acceptable purity^{19,40-42} making it a more industrially viable approach. This method also has the advantage that it can be adapted to form powders, films of varying thicknesses, CNT networks or aligned CNTs grown on substrates. Controlling the placement of catalytic particles on a surface can be used to control the site of formation of CNTs.

The maximum temperature needed for growth in this method is lower than for arc-discharge or laser ablation.²⁸ A limitation of this method, however, is that the CNTs formed are often less crystalline in nature than the former two methods. There are a few variations of the CVD method. These are discussed in the **Sections 1.6.3.1 to 1.6.3.3**, which now follow.

1.6.3.1 Supported catalyst method

Here the metal catalyst can be a metal surface, a metal compound or an organometallic compound/complex on a variety of substrates – from CaCO_3 ⁴², to silica⁸³ to Al_2O_3 ⁸⁴ substrates. As mentioned, control of catalyst deposition will determine at which sites the CNTs are formed. This is an advantage in terms of the number of steps involved in specific applications, since the CNTs can be grown directly on the surface on which they are to be used.

Harsh conditions are often used to recover the CNTs in this method. HF is usually used to wash away zeolites and concentrated NaOH used to wash away the SiO_2 and Al_2O_3 after CNT synthesis. This poses a health and environmental hazard. In an interesting experiment, Co supported on NaCl was used to grow CNTs by CVD.⁸⁵ Afterwards the NaCl was washed away using distilled water. This method is considered to be a “greener” approach to such syntheses.

1.6.3.2 Floating catalyst method

In this technique both the catalyst and carbon source are introduced into the main reactor hot zone as vapour. Typically there are three ways in which to do this, i.e. *via* the injection method,⁸⁶ nebulizer or aerosol method^{87,88} or sealed container synthesis. (The latter will be discussed separately in **Section 1.6.3.3**).

In the injection method the catalyst and carbon source are injected into a hot furnace at a predetermined rate and in the aerosol assisted method, they are added in atomized form with a carrier gas. Volatilization occurs in the furnace. For this reason volatile organometallic compounds are generally used for the floating catalyst method. Decomposition occurs under high temperatures. Metal ions released from the organometallic complex are then reduced to the zero oxidation state by a reducing agent, commonly hydrogen gas. Individual metal atoms coalesce into nanosized liquid droplets in the gas stream. Carbon atoms from the carbon source dissolve in the liquid metal NP until the carbon-metal solution is saturated. Once the solubility point of carbon in the liquid metal droplet is exceeded, carbon atoms precipitate out of the liquid metal droplet onto the surface as filaments/CNTs.¹⁰ In other words, CNT nucleation is driven by the supersaturation of the metal with carbon. (Although some authors believe that in carbon filament growth it is the concentration gradient of carbon, in the form of metal carbides, within the metal droplet and at its surface that causes the growth of the structures.⁸⁹) At this point stabilization of the free atoms/radicals occurs through the formation of bonds. As precipitation proceeds, so the tube length grows.

Typically CVD in the floating catalyst method is carried out in either a horizontal or a vertical furnace. (See **Figure 1.10**.) In the horizontal furnace approach, the CNTs fall under the

influence of gravity onto the sides of the tube, or form by interaction with metal particles clinging to the tube walls. **Figure 1.10 (a)** shows a horizontal *two-phase* furnace system. The catalyst is supported on a “boat”. The gas-phase carbon source, in this example acetylene, and the carrier gas, enter the first furnace. The temperature in the first furnace is suitable for the organometallic catalyst compound to sublime. All chemicals are then passed into the second furnace whose temperature is suitable for compound decomposition and CNT formation. In **Figure 1.10 (b)** the catalyst compound is introduced into a *single-phase* furnace by, in this example, atomization/nebulisation into the gas stream. In the vertical set-up the reactants are introduced at one end of the reactor tube and collected at the other, with products falling to the exhaust end under gravity [see **Figure 1.10 (c)**] or being transported up to the exhaust end by a carrier gas.⁹⁰

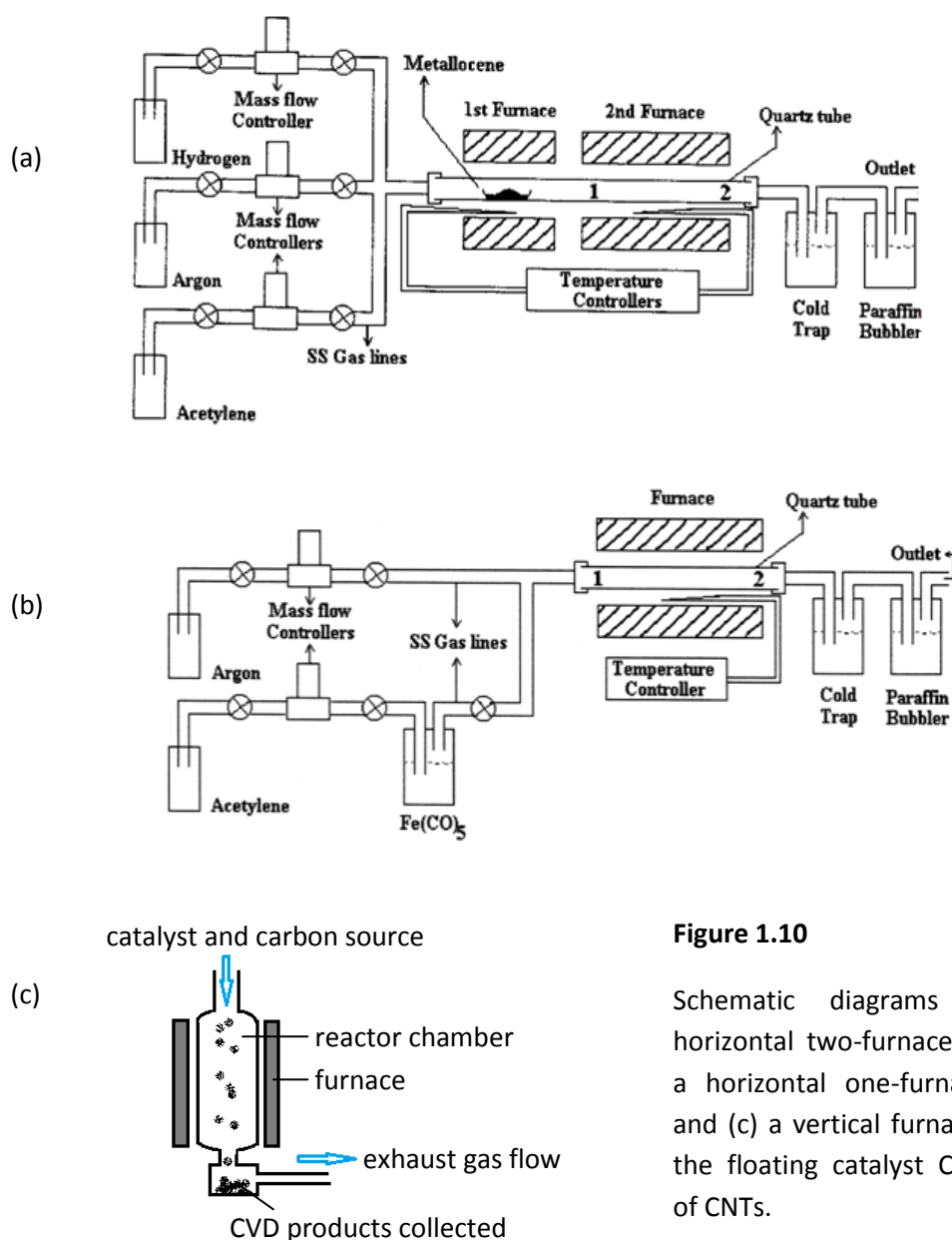


Figure 1.10

Schematic diagrams of (a) a horizontal two-furnace system⁹¹ (b) a horizontal one-furnace system⁹¹ and (c) a vertical furnace set-up for the floating catalyst CVD synthesis of CNTs.

The floating catalyst CVD method is a continuous process and thus large scale production is possible from this process. Material can be collected directly from the effluent/waste stream as well as that deposited on the inner sides of the reactor. Other authors have used a differential electrical mobility system, to detect the presence of SWCNTs on-line, rather than collect and analyze product.⁹² A related CVD method uses a hot wire generator to produce a vapour of metal NPs instead of the injection of metal-containing solutions.^{88,92}

1.6.3.3 Confined space method

A less used technique for the synthesis of CNTs is the use of a sealed container, typically metal reactors under high pressures or sealed quartz vials.^{44,46,93,94} **Figure 1.11** is a photograph of such a vial. This technique looks promising for the synthesis of CNTs, but thus far little research has been done using this method.

In most cases the organometallic compound/complex acts as both the catalyst and the carbon source. Advantages of this method include simplicity of equipment needed and the ability to control the catalyst:carbon ratio exactly.⁴⁴ An example of SCNMs produced in a sealed system, without a catalyst, are the multishell carbon microspheres, with diameters about 1 μm , which were synthesized in an autoclave from Hg_2Cl_2 and CS_2 .⁹⁵



Figure 1.11

Photograph of sealed quartz containers for CNT synthesis.⁹⁶

For the purposes of this project, CVD synthesis by the floating catalyst method was chosen, owing to the simplicity of the set-up, the ability to scale-up products and the relative cost effectiveness compared to some other techniques. Also, CVD provides a method that is easy to compare with the many literature examples and variables in CVD will now be discussed.

1.7 Variables that affect CNT growth in CVD synthesis

Synthesis parameters influence CNT (and other SCNM) size and morphology and ultimately properties. Much research has been performed into modifying reactor design and reaction parameters, but comparatively little has been done on the choice of catalyst and its effects. The carbon source used, the metal catalyst employed, as well as the temperature during which tube growth occurs, are perhaps the most important factors in the synthesis of CNTs.

An example of a study which investigated a variety of reaction parameters and their effects is that of Mohlala *et al.*⁹⁷ They produced MWCNTs and CNFs from ferrocene (either 5 or 10 wt.%)

in toluene) and a variety of substituted ferrocene compounds. Other parameters were 5% H₂ in Ar at a flow rate of 100 mL/min, a temperature of 800 – 1000 °C and an injection rate of 0.2 and 0.8 mL/min. They found that the concentration of the catalyst, the temperature of pyrolysis, as well as the injection rate, were factors influencing both the form of carbon material produced and the amount of this material. Further examples of parameter effects follow.

1.7.1 Catalyst and its concentration

CNT synthesis usually requires the presence of a catalyst and without a metal catalyst carbon spheres are the primary product.^{48,98,99}

The floating catalyst method requires that the metal catalyst exist as separate particles in the gas phase, hence the common use of volatile organometallic compounds. Indeed each formula unit or molecule delivers individual metal ions or atoms into the gas stream.

1.7.1.1 Organometallic compounds as catalysts

Ferrocene and iron pentacarbonyl as catalysts

Since the discovery of dicyclopentadienyl iron(II), commonly known as ferrocene, the field of organometallic chemistry has exploded. This compound was first discovered in 1951¹⁰⁰ and in 1993 the first report of ferrocene-catalyzed growth of carbon fibres was published.¹⁰¹ Today ferrocene, as well as iron pentacarbonyl, are commonly used organometallic compounds in many applications and are also excellent catalysts for the synthesis of CNTs. The latter compound is often used with CO¹⁰² and is the choice of catalyst in the industrial high pressure carbon monoxide (HiPCO) process. **Figure 1.12** shows the structure of these organometallic compounds.

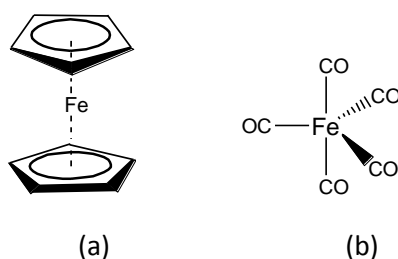
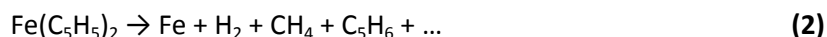


Figure 1.12 The chemical structures of (a) ferrocene, Fe(C₅H₅)₂, and (b) iron pentacarbonyl, Fe(CO)₅.

One reason for their popularity as SCNM catalysts, especially in the floating catalyst CVD method, is their volatility which is relatively lower than for other organometallic compounds. Literature gives different temperatures for ferrocene sublimation and decomposition, since these processes are pressure dependant. For example, ferrocene has been reported to decompose above 400 °C and vapourize at 185 °C²⁸ and decomposes at 190 °C and sublimes at

140 °C¹⁰³ although in both cases the pressure was not given. The decomposition of ferrocene is spontaneous and has been shown to follow the reaction in **equation (2)**:¹⁰⁴



Again, these compounds have the inherent ability to supply individual metal atoms to the gas phase in the floating catalyst technique and because ferrocene itself contains carbon, it can act as the carbon source itself, alone,¹⁰⁵ or along with other carbon source(s). Also, ferrocene is stable in air for relatively long periods of time, and is readily available, whereas many other organometallic compounds are unstable. However, other compounds may yet prove to be more suitable than ferrocene.

Other organometallic compounds as catalysts

The ability of iron from ferrocene to catalyze such syntheses prompted researchers to test other relatives – ruthenocene,¹⁰⁶ cobaltocene and nickelocene.¹⁰⁷ The latter two catalysts were successful for MWCNT synthesis.

A narrow range of research articles have appeared on the use and effect of substituted ferrocene and other organometallic complexes on SCNM synthesis and morphology.^{80,97,108-115} Ligands bound to ferrocene (or other organometallic compounds) can modify both the chemical properties of the compound as well as physical properties, such as the volatility. In turn, the morphology, diameter and electronic properties, amongst others, of the resulting SCNMs are also modified. For example, diameters of CNTs have been shown to be narrower when produced from dimethylferrocene than with unfunctionalized ferrocene.⁹⁷ Often the morphology is altered as a result of the incorporation of heteroatoms into the carbon nanotube backbone.

A recent review by Nyamori *et al.* summarizes much of the literature on organometallic transition metal complexes as catalysts in the floating catalyst CVD synthesis of CNTs and other SCNMs.⁸⁰ They discuss ferrocene and other metallocenes, Fe-, Co- and Ni-phthalocyanines, as well as some ferrocenyl derivatives, as successful catalysts for CNT synthesis.

The influence of the type of metal in the catalyst has been investigated. Since transition metals have been successful as catalysts for CNT production in arc-discharge, laser ablation and CVD methods, Deck and Vecchio chose a range of transition and lanthanide metals (Fe, Co, Ni, Cr, Mn, Zn, Cd, Ti, Zr, La, Cu, V, Gd), in the form of either metallocenes or chlorides, to study for suitability as CNT catalysts.⁵⁶ Only three metal elements, of 13, were catalytically active for the synthesis of CNTs, namely Fe, Co and Ni. This confirmed other studies which showed Fe, Co and Ni to be active for CNT formation. Soot was the product in all runs for the CNT-catalytically-inactive metals, while, interestingly, three metals produced no product at all, namely Ti, Cu and Gd. The active metals were successful in producing CNTs whether their precursors were metallocenes or chlorides, showing that metallocenes are not necessary, but that it is indeed the metal which is important for CNT formation. (Nevertheless iodine was shown to poison or hinder the formation of CNTs.¹¹⁵) Deck and Vecchio performed Mossbauer

spectroscopy, a spectroscopic technique that uses gamma rays, on the iron-synthesized CNTs.⁵⁶ Results showed that iron carbides were present. It was shown that elements which form multiple phases of carbides are not suitable as CNT catalysts in CVD. The authors went on to study the carbon-catalyst binary phase diagrams for more than 70 potentially catalytic elements. Interestingly, they showed that the lanthanides, platinum metals, and a few other transition metals, may be capable of catalyzing CNT growth at very high temperatures or from their carbide form. Titanium carbide was then tested and was experimentally shown to catalyze the formation of CNTs. Qiu *et al.* showed from X-ray diffraction (XRD) studies that iron carbides are the main form of catalysts in the system.¹¹⁶ Iron carbide (Fe_3C) was shown to be an intermediate in the formation and growth of CNTs by selected area electron diffraction pattern studies.¹¹⁷

Effects of catalyst concentration on morphology, size and growth rate of MWCNTs and the influence of the support and a secondary metal on the catalyst

Controlling the catalyst:carbon ratio is an advantage of the CVD process. The choice of catalyst, and its concentration relative to the carbon source, influences the crystallinity of the products, their diameters and the type of SCNM formed. Chaisitsak *et al.* found that at 700 °C and a flow rate of Ar of 1.0 L/min, an optimal ferrocene:ethanol ratio of 1-1.5 wt.% was necessary to produce optimally graphitized SWCNTs.¹¹⁸ On either side of this limited range the degree of crystallinity, as defined by the ratio of intensity of Raman graphitic and disorder peaks (see **Section 1.11.6**), became smaller. Singh *et al.* showed that a larger concentration of ferrocene results in both larger yields of carbonaceous product and larger diameter CNTs.¹¹⁹ However, Chaisitsak *et al.* did not find a clear correlation between increasing ferrocene concentration and CNT diameter in the concentration range they used (0.1 to 3 wt.% ferrocene in ethanol), but rather they believe that the manner in which the catalyst is introduced into the system affects the diameter of the CNTs, though they did not expound on this in their paper.¹¹⁸ Nevertheless, the logical argument is that the higher the concentration of catalyst NPs, the more likely they will collide in the CVD gas stream, increasing the rate of coalescence and thereby providing larger catalyst NPs. This in turn increases the diameter of the CNTs, or nanospheres, which grow from them, specifically the ID. Changes in the Fe:C ratio (from ferrocene and anthracene) *via* solid state synthesis in a sealed quartz container were shown to influence the type of SCNM formed.⁴⁴ MWCNTs, spheres and amorphous carbon were formed. It was found that lower Fe:C ratios favoured CNT formation. However, very low ratios, of 0.033 and lower (approximating zero percent Fe), favoured sphere formation. Sphere radius was shown to be influenced by the quantity of Fe present (no Fe gave bigger spheres). However, for CNTs, the average diameter and diameter distribution increased with increasing Fe content. Yields of CNTs were highest at 800 °C (they measured at 700, 800 and 900 °C). At 700 °C the production of amorphous carbon was attributed to the decomposition of carbonaceous reactants without Fe involvement. Temperature had little effect on the size of the spheres.

The OD of CNTs is influenced by the volatility and decomposition temperature of catalysts. SWCNTs have been produced from CO at ambient pressure, rather than at high pressure as in the HiPCO process, by the thermal decomposition of ferrocene or iron pentacarbonyl.¹²⁰ Since

iron pentacarbonyl has a lower decomposition temperature than does ferrocene, it can form larger metal NPs and thus forms larger diameter CNTs than ferrocene at the same temperature.

The use of organometallic compounds merely to initiate, but not sustain CNT growth, was investigated by Cao *et al.*¹⁰³ Short aligned CNTs, grown in the form of a thin film from ferrocene and xylene vapour, were shown to continue in growth even after no further catalyst (ferrocene) was introduced into the system. Only a continuous supply of carbon source (xylene) was necessary though the authors suggest that the rate of growth in the absence of a continual supply of catalyst will decline. The authors suggest that catalyst quantities in CVD synthesis can thus be reduced as only an initial small amount is needed.

In other experiments the substrate interfered with the catalyst's performance and, ultimately, affected the products. For example, MWCNTs were grown on a substrate of silicon carbide whiskers using xylene/ferrocene by CVD.¹²¹ The silicon in this substrate poisoned the iron catalyst particles by forming iron-silicon compounds under elevated temperatures. The silicon carbide substrate was thus treated and oxidized to form silicon dioxide. This resulted in the formation of more CNTs since the layer of silicon dioxide could prevent the iron catalyst particles coming into contact with the silicon carbide, and hence, they were available to catalyze the formation of MWCNTs.

Bimetallic catalysts have also been used in the CVD synthesis of CNTs. Bimetallic catalysts often increase the solubility of carbon in the catalyst NP, and hence produce an enhanced reaction yield. Alternatively bimetallic catalysts can promote reactions in the carbon source. Notably, Cassell *et al.* showed that an Fe-Mo catalyst caused a higher yield of SWCNTs than an Fe catalyst alone, as did an Fe-Ru catalyst.¹²² Herrera *et al.* used Co-Mo/SiO₂ catalysts and produced SWCNTs by a CO disproportionation reaction.¹²³ The production of Mo carbide species promoted smaller clusters of Co, and thus promoted the synthesis of SWCNTs. When ferrocene was mixed with cobaltocene or nickelocene, higher yields of CNTs were produced compared to monometallic ferrocene.¹²⁴ A trimetallic catalyst consisting of Co, Zn and Al was used to synthesize MWCNTs by CVD.¹²⁵

1.7.2 Carbon source

Research studies often use organic solvents, typically hydrocarbons, as the carbon source in the CVD floating catalyst method, since many organometallic catalyst compounds dissolve readily in them. Examples include xylene¹²⁶ and toluene.^{97,112,127} Gaseous hydrocarbons can also be used, for example methane¹²⁸ and acetylene.¹²⁹

Another common carbon source in CNT production is CO.^{88,92,130-132} The disproportionation reaction which occurs is given in **equation (3)**:



where $C_{(s)}$ is the CNT. The HiPCO process, as mentioned in **Section 1.7.1**, is the method of choice for the industrial preparation of industrial quantities of CNTs to date. An iron pentacarbonyl catalyst is used under approximately 3 atmospheres and high temperatures to convert CO to SWCNTs. The high pressure increases the rate at which CO disproportionation occurs, thereby increasing the rate of SWCNT formation.¹³³

Morphology, distribution and SCNM size are influenced by the carbon source. For example, Ci *et al.* used the floating catalyst CVD method, under identical reaction conditions except for a difference in the carbon source (benzene or hexane), and yielded CNTs double the size when benzene was the carbon source.¹³⁴ No explanation for this was suggested. However, the results clearly show that the nature of the carbon source influences the product formation. This is shown in other examples in the literature. For example, thermal decomposition of dolomite yielded carbon “calabashes”¹³⁵ primarily, instead of CNTs.

Species from carbon source decomposition can affect the products directly or can interfere with the action of the catalyst. In turn, the products are affected. For example, DWCNTs were produced with ferrocene as the catalyst and tetraethoxysilane as the carbon source in an H_2/Ar environment.¹³⁶ It was suggested that the decomposition of the carbon source formed a CHO compound and SiO_2 . A very large $SiO_2:Fe$ ratio resulted in less collision of Fe NPs, thus Fe NPs did not grow large. Consequently, only DWCNTs were formed. In another example, pyrolytic carbon on CNTs was suggested to be formed primarily from the deposition of liquid hydrocarbons from the vapour phase.¹³⁷ This phenomenon was first reported by Grisdale in 1953.¹³⁸ Interestingly, it was shown by Ci *et al.* that a carbon support is not a very good support for growing CNTs.¹²¹ The authors state that carbon from the substrate may diffuse into the Fe NPs under high temperatures and prevent the formation of CNTs, effectively poisoning the metal NPs towards CNT formation.

As was mentioned previously, when a carbon source is not accompanied by a catalyst, in most reported cases, carbon spheres were primarily formed.⁹⁹ However, in other studies, CNTs were produced without an additional or external carbon source because the carbon atoms derived from the catalyst were sufficient for CNT formation.¹⁰⁷

It is generally understood that a variety of carbon species arise from the deposition of carbon sources and carbon-containing catalysts. These include neutral species and ions/radicals of varying sizes. The manner in which compounds decompose is thus also a factor in determining the results of CVD synthesis.¹³⁹

1.7.3 Temperature

The temperature chosen for CVD processes will affect the kinetic energy of liquid metal NPs in the floating catalyst method. Hence, the rate of metal NP collision and coalescence is influenced too. As was discussed in **Section 1.6.3**, the metal NPs act as a template for CNT nucleation and growth. Thus, CNT diameter is influenced as well. This temperature-diameter relationship was shown through modelling by Kuwana and Saito.¹⁴⁰ and experimentally by Singh *et al.*¹¹⁹

An optimal temperature must be carefully considered, depending on the other reaction conditions. Liu *et al.* showed that 800 °C is a more suitable temperature for the synthesis of MWCNTs from pentane and Fe(CO)₅ than are temperatures at least one hundred degrees lower or higher than this optimum.⁵⁰ In other words, the temperature affects the SCNTs formed. Temperature also affects yields. Higher temperatures, in the range 500 to 800 °C, gave larger yields of carbonaceous product with a slight tailing off at 900 °C in the CVD synthesis from ferrocene and xylene with 5% H₂ in Ar.⁹⁰ In general, in the literature, MWCNTs form preferentially between 600 to 900 °C and SWCNTs between 900 and 1200 °C. However, depending on the reaction conditions, CNTs can form at much lower temperatures.

Temperature affects the rate of collision and dissolution of carbon species (atoms, radicals and larger neutrals) with metal NPs, hence affecting the rate of nucleation and growth. It has been shown that the wider the metal catalyst NPs, the slower the growth rate of carbon filaments.¹⁴¹ It was suggested that this is because the time taken for carbon to diffuse through larger metal particles is longer than through smaller particles. Bichler *et al.* showed that the higher the temperature, with other parameters being held constant, the greater the supersaturation of metal catalyst particles with carbon.¹⁴² Neumayer and Haubner reported that because supersaturation and thus growth rates are very high at higher temperatures, more spherical particles are often produced than tubular structures.⁹⁰ The authors did not expound on this, but presumably excessively high growth rates lead to “uncontrolled” carbon-carbon bond formation, which spread more quickly around metal particles than the tip or root growth mechanisms can lift growing carbons off metal surfaces. Bai *et al.* showed that preheating temperature in a two-phase CVD system also influences growth rate of CNTs since the way in which the catalyst itself decomposes influences how carbon products form.¹⁴³

Temperature choice in CVD methods also influences the levels of amorphous carbon. Su *et al.*, who used a floating catalyst method with ferrocene and an alcohol carbon source, saw that more amorphous carbon was produced at temperatures higher than 1100 °C.¹⁴⁴ This showed that temperature plays a role in the resultant “cleanness” of products, through its influence on the decomposition of the carbon source. Also, temperatures lower than 900 °C yielded fewer SWCNTs, due to a presumed incomplete decomposition of the alcohol. Clearly the effect of temperature on the yield of CNTs is not an isolated phenomenon, but one combined with the effects of other system components and parameters.

1.7.4 Reducing agent and its concentration

Reducing agents, such as H₂, were shown to be necessary for the growth of CNTs from ferrocene.⁹⁰ The Fe²⁺ ion needs to be reduced to a zero oxidation state for catalytic activity as was mentioned before. (Iron pentacarbonyl, on the other hand, is an example of a catalyst with a zero-valent Fe particle, in other words, an atom of Fe.) Nasibulin *et al.* described how SWCNT formation is dependent on the presence of H₂ during synthesis.⁸⁸ They used an on-line detection system and showed that when the H₂/N₂ gas was replaced by N₂ alone, CNT synthesis ceased. They suggested that the small quantities of oxygen in the nitrogen (≤ 0.0003% O₂) are sufficient to oxidize the metal catalyst NPs and thus hinder or stop the

formation of CNTs. Prior to this it was shown that oxides of metal NPs do not produce CNTs, but that if the oxide is reduced they can be catalytically active.¹⁴⁵

H₂ also affects the types of radicals which form from the decomposition of the catalyst and carbon source, and thus ultimately the products. Reilly *et al.* described how radical condensates, not just the metal catalyst, need H₂ to form CNT walls on the growing tube.¹³⁹

Moisala *et al.* suggested that, coupled with the ability of H₂ to remove amorphous carbon from metal particle surfaces, as well as its larger heat conductivity and diffusion coefficient than commonly used carrier gases, H₂ may actually promote the agglomeration and sintering of iron particles at a faster rate than usual, resulting in even larger iron NPs.¹²⁰ These authors found that the presence of H₂ actually prevented the formation of any SWCNTs in experiments using iron pentacarbonyl or ferrocene with CO (at 1 atm, 600 to 1300 °C). This confirmed what Wong *et al.* found, although they used a supported catalyst.¹⁴⁶ Also, carrier gas composition, in other words the percentage of H₂ in the gas stream, has been shown to influence the diameters of the carbon spheres.⁹⁹

1.7.5 Gas flow rate

Gas flow rate is yet another factor influencing the type(s) of SCNMs formed from CVD, their length, diameter and their rate of formation. Fast flow rates of carrier gas favoured the formation of SWCNTs as these flow rates prevent agglomeration of iron NPs which would then be too big for SWCNT formation.¹⁴⁴ Gas flow rate is directly related to residence time of components that are suspended in the system, and residence time in the constant temperature zone/zone of maximum temperature. This was reported by Qiu *et al.*¹¹⁶ The higher the flow rate of the coal gas, the higher was the rate of formation of the SWCNTs from ferrocene in CVD. Moisala *et al.* also saw that the length of SWCNT bundles decreased at higher flow rates explaining that less carbon is available to metal NPs at higher flow rates.¹²⁰ Chaisitsak *et al.*'s results are in agreement with this, i.e. that higher flow rates produced shortened lengths of CNTs.¹¹⁸ They used ferrocene and ethanol in an argon environment and did tests at 650 to 800 °C. Interestingly, very high flow rates (2.5 L/min) yielded only iron particles. Nevertheless, parameters were different in their experiments, again confirming the idea that one cannot predict the results of CVD by looking at one parameter alone, but perhaps all work together in an integrated manner. In another experiment, gas flow rate was shown to influence SWCNT diameter. When gas flow rates were increased from 300 sccm (standard cubic centimetres) to 1500 sccm, at intervals of 300, and other parameters of the CVD process were kept constant, the SWCNT diameters decreased.¹⁴⁷

1.7.6 Gas pressure

The pressure of gas in a CVD reactor will influence the rate of collision of: (1) metal NPs with other metal NPs, (2) metal NPs with carbon species and (3) metal ions with reducing agent. Thus, it is logical to conclude that gas pressure would ultimately influence both the rate of CNT nucleation and growth as well as the final diameter of CNTs.

Neumayer *et al.* explained that the pressure of the gas will influence both the retention time of the reacting species in the reactor as well as the amount of carbon *versus* metal NPs in the gas phase, according to thermodynamics.⁹⁰ Usually atmospheric pressure is used in floating catalyst CVD. However, Chen *et al.* successfully produced CNTs at low reactor pressures (8, 10, 15 and 21 kPa) for $T_{\max} = 650$ °C, H_2 flow rate = 60 sccm and 4.9×10^{-3} mole ratio of thiophene/cyclohexane with ferrocene as the catalyst.¹⁴⁸ The longest and straightest CNTs were formed at 15 kPa. Results from Raman studies indicated that pressure also influences the crystallinity of the products. The authors did not expound on this, but presumably a lower pressure makes for long retention times. A longer time in the high temperature zone of the furnace, in the presence of inert gases, would make for a longer annealing period. This is a logical explanation of how crystallinity could be increased.

CNT diameters, too, were demonstrated to be correlated to pressure. Optical absorption spectroscopy studies revealed that very narrow CNTs were produced under elevated pressures in the floating catalyst CVD method with ferrocene as both catalyst and carbon source.¹⁰⁵

Ci *et al.* selectively produced large yields of DWCNTs by controlling the carbon partial pressure.¹⁴⁹ Thus yield of a desired SCNM material is another end result of pressure choice.

1.7.7 Injection rate

Yet another controllable parameter in the CVD floating catalyst method is the rate of introduction of catalyst/carbon source/(catalyst + carbon source) into the maximum temperature zone of a furnace. In the injection method, injection rate plays a role in both the reaction rate and product size. Reaction rates increase when injection rate is high since the partial pressure of components in the gas phase is higher. Secondly, diameters would be larger from the increased rate of metal NP collision and coalescence. However, Mohlala *et al.* showed that injection rate seemed to have no effect on the size and morphology of CNTs when they compared injection rates (0.2 *versus* 0.8 mL/min).¹¹⁵ However, the yield of carbon products was influenced, with more products forming at the lower injection rate.

Following this discussion on CVD variables is a discussion on growth mechanisms of CNTs, followed by the effects of heteroatoms in CVD processes.

1.8 Growth mechanisms of CNTs

It is generally accepted that two mechanisms exist by which CNTs form, although this topic needs further research. One method is the root or base growth mechanism whereby it is thought that metal catalyst particles attached to a support remain in place while the CNTs grow outward away from the support/substrate.¹⁵⁰ This type of growth would predominate where the catalyst particles are attached strongly to a surface. Conversely, when the interaction between the metal NP and the support is weak, the tip growth mechanism predominates. In the tip growth mechanism the metal particles are thought to move with the growing end of the nanotubes.^{151,152} In other words, the support-catalyst interaction

influences the mode of growth. The base/root growth mechanism is primarily used to describe CNT growth on a surface, but is still considered simple enough for floating catalyst methods. Refer to **Figure 1.13** for a visual representation of these mechanisms.

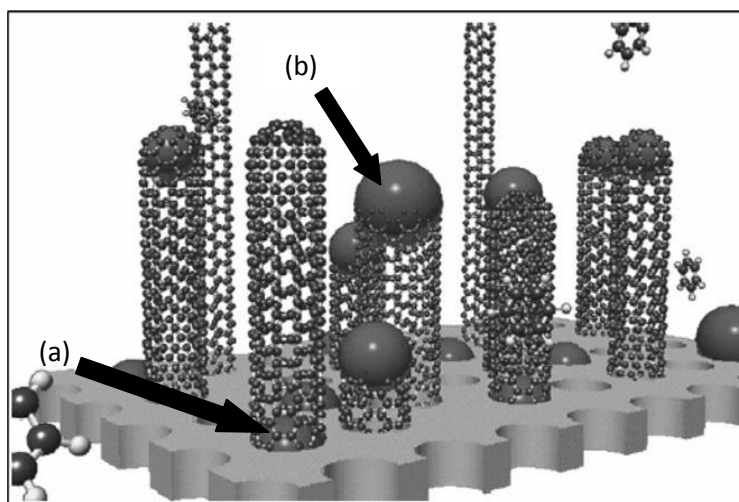


Figure 1.13 Schematic diagram of the (a) root-growth and (b) tip-growth mechanisms.¹⁵³

Some supporting evidence for the “Scroll Model” of CNT growth, as discussed in **Section 1.3.2**, makes use of a study of potassium-graphite intercalation compounds (a host graphite substance which allows the intercalation of guest substances in between layers) and hydrocarbon vapours.¹⁵⁴ These substances were reacted at room temperature and produced small amounts of CNTs. The authors suggested that when the unsaturated hydrocarbon entered the spaces between the graphite layers, this resulted in the graphite layers moving apart and no longer being perfectly parallel. Long exposure to solvent separates the components leaving isolated graphene sheets which roll up much like a scroll. They suggest that these “scrolled CNTs” are what were evidenced in their TEM images.

Deck and Vecchio studied the mechanism of CNT “carpet”/“mat” formation.¹⁵⁵ They proposed a mechanism for why CNTs grow in an aligned manner on the surfaces of a CVD reactor in the floating catalyst method. They suggested “embryo” CNTs deposit on the surface of CVD reactor. Their tight packing, and subsequent growth, causes or forces the tubes to grow in an aligned manner.

As a carbon filament grows, so the metal particle is deformed if the rate of tube growth far outweighs that of movement of carbon through liquefied metal NPs. This was proposed by Snoeck *et al.* who suggested that at low temperatures, the rate of filament/CNT nucleation is small compared to the rate at which the carbon diffuses through the metal catalyst particle.¹⁰ This results in nucleation occurring at a fairly uniform rate on the metal surface and thus little deformation or “stretching” of the metal particle. However, under higher temperatures, the rate of precipitation and nucleation is much faster than diffusion. The difference in these rates results in a deformed metal particle. **Figure 1.14** shows this visually.

An alternative growth mechanism was proposed by Reilly *et al.*¹³⁹ They believe that radical condensates, rather than only elemental carbon, react together to form the growing tube

walls. They suggested that because the radical condensates are different, the manner in which they react causes constant variation in the state of the tube at the growing point. Hence, they suggest that the argument about the open or closed state of tips during growth is unnecessary.

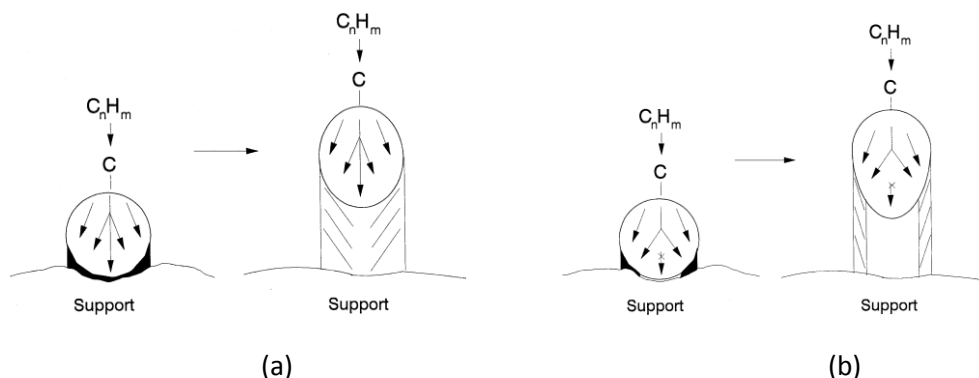


Figure 1.14 Particle deformation at (a) low and (b) high temperatures.¹⁰

1.9 Effect of introducing heteroatoms

CNTs can be modified in two ways – by the incorporation of heteroatoms in the CNT backbone structure (doping), or by the attachment of particles or side groups to the surfaces. Doping can be done during CNT synthesis, or after.¹⁵⁶ Post-doping methods make use of a precursor containing the element to be inserted.

Regarding doping, in 1994 CNTs were doped for the first time by Stephan *et al.*⁶⁶ F and K-doped CNTs were later studied by theoretical calculations.¹⁵⁷ Interestingly, it was shown that F-doped CNTs have the ability to extract charge from a diamond surface, while potassium, with a very low electronegativity, cannot. It was suggested that this may open new fields of research for doped-CNTs on diamond as gas sensors.

An example of the addition of chemical side groups is the functionalization of CNTs with ester groups and amide groups *via* oxidized carbon atoms on the surfaces, specifically COOH groups.¹⁵⁸ Solubility of CNTs is altered by such functional groups, and optical properties change. Advantages of doing this include solubilizing CNTs in polymer composites for enhanced properties or in aqueous systems for biological applications.

When the carbon source, or the catalyst, contain heteroatoms such as nitrogen¹⁵⁹ or boron¹⁶⁰, the heteroatoms become incorporated into the CNT backbone. The heteroatom replaces a carbon atom, often resulting in a different ring structure at the site of the heteroatom depending on its valency. The modified ring structure, in turn, affects the surface and bulk morphology of the CNT. Doping can also affect the resulting size of SCNMs. For example, average microsphere diameters correlated strongly with the presence or absence of boron in CVD reactions.¹⁶¹ Crystallinity and length of CNTs have been shown to be affected by doping too. For example, B-C-N nanotubes and B-CNTs were produced by an arc-discharge method using a graphite cathode and a BC_4N anode.¹⁶² Both tube lengths and graphitic nature were increased as a result of the presence of boron. In other studies B-doping decreased the

graphitic nature by disordering the CNT structure, and did not have much influence on the electrical conductivity of the CNTs.¹⁶³ In the same study it was found, from Raman spectroscopy data, that the degree of disorder was proportional to the concentration of boron.

1.9.1 Nitrogen and N-doped CNTs

Studies have shown that nitrogen incorporation into the backbone typically generates “bamboo-shaped” CNTs with discrete cross walls within the tubes.⁹⁶ Bamboo-type cross walls are also sometimes seen in undoped CNTs and have been reported to have formed from fluctuations in the carbon concentration in the metal catalyst NPs.¹⁶⁴ Jung *et al.* also reported bamboo-type CNTs produced without nitrogen.¹⁶⁵ Presumably this effect is bigger in the presence of nitrogen. **Figure 1.15** shows the typical bamboo-shaped compartments found in N-CNTs.

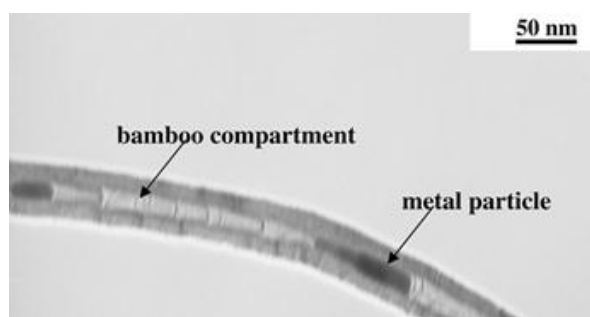


Figure 1.15 TEM image of a “bamboo”-shaped CNT as a result of N-doping.¹⁶⁶

Syntheses of SCNMs with inherent nitrogen have been performed by arc-discharge methods,^{58,167,168} CVD¹⁶⁹ (floating catalyst^{166,170} and pyrolysis¹⁷¹) and solvothermal^{172,173} techniques.

The nitrogen source in *in-situ* doping can be a ligand on the catalyst compound or the carbon source. Post-doping carbon materials with nitrogen often is done under high temperature in a N-containing atmosphere such as NH_3 .^{174,175}

The degree with which nitrogen is incorporated into CNTs is an area of interest because if doping levels can be controlled and fine-tuned, better control of desirable electronic properties can be achieved. Doping with elements such as nitrogen provides electrons which can alter the electrical conductivity of CNTs.¹⁷⁶ Indeed it has been shown that the conductivity of N-CNTs may be higher than the undoped versions.¹⁷⁷ In fact, certain N-CNTs can be metallic in nature.¹⁷⁸ Chemical reactivity would then also be altered. Thus, N-CNTs could be tailored for specific applications. Other properties, such as solubility in water, could also be altered by the formation of N-containing groups on CNT walls.

As was mentioned previously, doping can influence the physical characteristics of CNTs. Nxumalo *et al.* used sealed quartz containers in which N-CNTs were synthesized from ferrocenylmethylimidazole or a ferrocene/methylimidazole mixture at 800 °C.⁹⁶ Bamboo-type CNTs had an average OD of 70 nm from the former catalyst, which is smaller than for

underivatized ferrocene. They also showed that the morphology of the products can be quite different according to the nitrogen source used. They attributed this to the manner in which the N-containing starting materials decomposed. Also, the closer the nitrogen atom was to the iron particle of the ferrocene moiety, the higher the incorporation of nitrogen into the resulting SCNM(s). The higher the amount of nitrogen present, the lower was the yield of CNTs, although more bamboo-type CNTs were produced.

N-CNTs have been shown to be excellent supports for NPs of Pt-Ru in fuel cells, due to the altered properties from the inclusion of nitrogen.¹⁷⁹ Applications of doped and pristine CNTs will be discussed later in this chapter.

1.9.2 Promoting and cleaning agents for CNT growth

Introduction of heteroatoms into the system can result in promotion of the growth of or “cleaning” of CNTs, rather than doping. Such heteroatoms include phosphorous, sulfur and oxygen. The promoting action of these three examples will now be discussed in more detail.

1.9.2.1 Phosphorus

Phosphorus has been shown to promote the growth of CNTs in the floating catalyst CVD method.¹⁸⁰ Ferrocene was used as the catalyst in benzene, with H₂ as the reducing gas at a flow rate of 100 mL/min, with reaction temperatures of 1100 – 1200 °C. A small amount of PPh₃ was added to the catalyst solution in several runs. Without the phosphorus-containing compound, carbon spheres were formed and with PPh₃ CNTs were produced. It was shown that under the reaction conditions an optimal concentration of phosphorus is needed to result in the growth of the CNTs. They suggest that phosphorus forms a Fe-P eutectic when the concentration of phosphorus is just right, thereby improving the fluidity of the molten metal catalyst particles and the diffusion of the carbon atoms, and hence enhance their arrival at the surface of the catalyst particle for incorporation into the growing CNT. The authors went on to say that phosphorus particles attach to the surface of iron, and in that state they increase the activity of the iron, but that if the catalyst surface is entirely covered, no hydrocarbon or carbon atoms can diffuse into the catalyst particle, and hence the catalyst is poisoned.

1.9.2.2 Sulfur

The addition of sulfur can be done by using this element as part of the catalyst or carbon source or as separate sulfur -containing compounds (for example thiophene). Under the right conditions elemental sulfur can be used.

Sulfur influences the morphology of the products. For example, studies with thiophene yielded Y-junction CNTs.⁵⁷ Product quality is also a function of the presence of sulfur. Lower doses of thiophene (in the range 0.5 to 5 wt.%) gave rise to fewer, but higher quality, SWCNTs from the CVD synthesis of CNTs using benzene, ferrocene and H₂.²⁸ Doses higher than 5 wt.%

thiophene predominantly gave rise to MWCNTs. Tibbetts *et al.* suggested earlier that a Fe-S eutectic forms when sulfur is present, causing a decrease in the melting point of iron, hence improving the nucleation of carbon filaments in much the same way as phosphorus does.¹⁸¹ They showed that sulfur also affects the quality of the fibres produced. Ci *et al.* disagreed with this theory stating that Tibbetts *et al.* did not have sufficient sulfur to form a eutectic, although the data and evidence for this argument was not published at the time of their rebuttal.¹⁸⁰

1.9.2.3 Oxygen

Oxygen can act as a system “cleanser” effectively converting the would-be amorphous carbons to CO₂, thereby improving the smoothness of CNT surfaces. Although, as mentioned in **Section 1.7.4**, even low levels of oxygen can oxidize the catalyst. This lowers its catalytic activity. Oxidation of the bulk of metal NPs retards the growth of CNTs.¹⁸² Controlling the amount of oxygen in the system is thus an important factor and must be carefully controlled. Oxygen introduced in small amounts as CO₂ and H₂O caused etching of carbon off catalysts in a CVD synthesis method.¹⁸³

The first production of SWCNTs by the floating catalyst CVD method, using ferrocene in alcohol solution, was reported by Su *et al.*¹⁴⁴ Purity of SWCNTs was high (little amorphous carbon). They suggest that the OH radicals from the alcohol remove the amorphous carbon. The OH radical is decomposed at the catalyst and carbon atoms with dangling bonds react with the oxygen species to form CO, essentially suppressing the formation of amorphous carbon, as well as MWCNTs. They go on to say that if the concentration of ferrocene is too low then there would be less iron to remove amorphous carbon in this manner, so the concentration of the catalyst is also important in controlling the formation of pure SWCNTs. A discussion on post-synthesis purification follows.

1.10 Purification methods for CNTs

Most methods by which CNTs are produced result in an impure product – in terms of the heterogeneity of the SCNMs formed (often forming nanospheres and amorphous carbon too),¹⁸⁴ SCNM sizes and the chemical composition of these structures. Purification methods are commonly used to remove metal catalyst NPs, which could interfere with further applications of CNTs, and amorphous carbon. Such methods include acid or base treatment and annealing, usually in an inert atmosphere. Thermal oxidation in an oven at slightly elevated temperatures (≈ 350 °C) can also be used to burn off amorphous carbon. Residual iron catalyst particles are commonly found trapped inside CNTs and other SCNMs, as can be evidenced by TEM imaging or energy dispersive X-ray spectroscopy (EDX) studies. This regularly occurs in CNTs grown by the CVD method due to the peculiar growth mechanism of this technique. When metal catalyst NPs are trapped in closed-ended CNTs, the metal remains separated from purification media. Also, the metal will not be able to act directly as a reactant or catalyst itself while isolated within a sealed CNT. However, many purification methods employ strong acids or bases, or mixtures of acids, to remove exposed residual metal.

Oxidizing acids, which are preferred, can fragment closed CNTs into shorter tubes. The “cutting” action exposes the metal particles to the purification medium, thus removing the metal. This is often accompanied by sonication to disperse CNTs which tend to agglomerate. Grinding methods can break bundles apart to expose more surfaces to purification media. Non-oxidizing, or reducing acids, such as HCl, can be used. Acid-washed CNTs are then usually filtered and rinsed with distilled water until the filtrate attains a neutral pH. Acid washing can damage the surface of CNTs creating defects. Thermal annealing (> 1000 °C) under an inert atmosphere or under vacuum can improve the graphitic nature of the CNTs. (The types of oxy-groups produced on CNTs as a result of acid washing, as well as the usefulness and applications of such purification techniques, are discussed further in **Chapter 2, Section 2.3.**)

1.11 Structural and morphological characterization of CNTs

Typical techniques used to study the morphology of CNTs and other SCNMs include transmission electron microscopy, scanning electron microscopy, thermogravimetric analysis, Raman spectroscopy, infrared spectroscopy, energy dispersive X-ray spectroscopy and X-ray diffraction. This will now be discussed in a bit more depth.

1.11.1 Transmission electron microscopy (TEM)

TEM studies yield two dimensional images of a sample. These include the shapes of CNTs and other SCNMs and their approximate quantitative ratios. Their IDs and ODs can be measured and the number of walls in MWCNTs, their lengths, apex structure and the presence of impurities in the structures, such as iron, can be studied.

Interestingly, Mølhave *et al.* showed that severe damage to CNTs can occur under the electron beam during TEM or other electron microscopy techniques, even with the commonly used 100 keV electron beam potentials and below.¹⁸⁵ Specifically the outer shells can become damaged, while the inner tube remains intact. They suggest that water vapour may etch the outer tubes. For the purposes of most lower-magnification studies, however, such damage is not critical to the results.

1.11.2 Scanning electron microscopy (SEM)

Scanning electron microscope (SEM) imaging yields three-dimensional images of the topographical morphology of micro- and nanoscopic structures. CNT alignment is better studied using this method than TEM.

1.11.3 Thermogravimetric analysis (TGA)

Thermogravimetric analysis (TGA) techniques use a small sample of CNTs or SCNMs under an oxidizing or inert atmosphere and increasing temperatures to study the thermal stability of the

nanostructures. Thermal stability is closely related to the graphitic nature of CNTs and SCNMs. Thus, TGA results give an indication as to the relative purity of samples and the relative proportions of CNTs and other SCNMs in different materials. TGA can also be used to determine the amounts of residual metal catalyst (after CNT combustion), i.e. the purity of a material.

1.11.4 Energy dispersive X-ray spectroscopy (EDX)

EDX spectroscopy allows for the determination of the approximate elemental composition of a small scanned region of a CNT(s) or other SCNM(s). However, because only a small region is analyzed, the results need to be used with caution as this is not necessarily the global composition.

1.11.5 Brunauer, Emmett and Teller (BET) analysis

The Brunauer, Emmett and Teller (BET) method is used to determine the surface area and porosity of CNTs. This is particularly important when studying CNTs as potential supports for catalysts. Both the inner cavities of CNTs and the outer, exposed surfaces form the total surface area. (In CNT bundles, some portions of the outer surfaces are not exposed, depending on the tightness of packing.) Nitrogen is the gas typically adsorbed on the surface for these studies.

1.11.6 Raman spectroscopy

This analysis technique is useful in that it gives a “signature” spectrum from the collected reflected laser light from a sample. Monochromatic light changes frequency when interacting with a sample and this shift in frequency can be used to identify transitions in molecules which are indicative of the types of functional groups the molecules contain. With respect to CNTs and other SCNMs specifically, peaks around 1350 and 1500 cm^{-1} are of interest. The “D” band around 1350 cm^{-1} arises from poorly ordered or disordered graphite. Peaks near 1500 cm^{-1} are associated with the E_{2g} in-plane stretching mode of graphite, and hence describe the graphitic nature of bonds. The literature often compares the intensity of these two peaks as a ratio: I_D/I_G or I_G/I_D . The ratio indicates the overall crystallinity or graphicity of the sample. The radial breathing mode (RBM), or A_{1g} breathing mode, whose peak is found near a wavenumber of 200 cm^{-1} , is specifically associated with SWCNT diameter, with the frequency of this vibration being determined by the diameter.

1.12 Applications of CNTs

The flexibility, high strength and high electrical conductivity of CNTs, amongst other properties, open up a range of possible applications for this unique material. The electrical properties of CNTs, coupled with their chemical stability and high surface area, for example,

allow CNTs to be used in electrical applications such as lithium-ion batteries, solar cells, supercapacitors and gas sensors to name a few. Indeed nanotechnological CNT applications have reached into many spheres of science, with CNTs finding use in areas such as materials engineering to biological applications. CNTs even find applications in the medical field. For example, “gadonanotubes” (Gd^{3+} ions trapped inside SWCNTs), have the ability to enhance the contrast in Magnetic Resonance Imaging.¹⁸⁶ Several tens to hundreds of metric tons of CNTs are synthesized per annum^{187,188} with figures expected to rise as CNTs find more applications.

Much research has gone into the functionalization of CNTs to tailor their properties for specific applications. CNTs are inherently unreactive since all the carbon atoms have four occupied valence orbitals by bonding to other carbon atoms. Modification of the tube walls with functional groups can allow for improved solubility and dispersion in both water and organic solvents,¹⁸⁹ which allows for use in otherwise unsuitable applications. Incidentally, the high curvature and thus high strain on the ends of closed CNTs makes these parts of the tubes more reactive. Some examples of progressive research fields for pristine and functionalized CNTs follow.

1.12.1 Field emission devices

The electrical properties of CNTs make them useful in field emission devices. For example, aligned CNTs were grown on a tungsten field emitter tip.¹⁹⁰ Studies indicated that these CNTs were potentially good field emitters. Arrays of CNTs have been used in flat panel displays.¹⁹¹ The field emission capabilities of CNTs are enhanced when doped with nitrogen,¹⁹² while theoretical calculations show the opposite effect for B-CNTs.¹⁹³ Tips for atomic force microscopy have been made from single CNTs.¹⁹⁴

1.12.2 Storage of hydrogen gas

CNTs make ideal vessels for hydrogen storage.¹⁹⁵ The amount of hydrogen that can be stored is very high compared to that of other carbon materials due to the large surface area of CNTs.

1.12.3 Fuel cells

CNT systems are advantageous over traditional amorphous carbon electrodes in fuel cells because of their high surface-to-volume and surface-to-weight ratios, as well as their higher conductivity.¹⁹⁶ They are also lightweight and, thus, are beneficial in power supplies which are becoming increasing lighter and smaller as technological devices get smaller.

1.12.4 Composites

Small quantities (0.5 to 5 wt.%) of CNTs added to a normal material can result in a matrix of significantly different properties since the NP properties affect the bulk material when evenly

dispersed. Mechanical strength, electrical conductivity and thermal conductivity are examples of such properties. Velasco-Santos *et al.* compared the storage modulus and tensile strength of polymers embedded with pristine CNTs or functionalized CNTs.¹⁹⁷ Results showed, among others, that the functionalized version had improved tensile strength. They attributed this to the increased chemical bonding by cross-links between the CNTs in the composite with the matrix substance, hence an improved load sharing. Adhesion between CNTs and the matrix into which they are embedded must be sufficiently high to ensure the tensile strength of CNTs is fully harnessed when loads are applied to a CNT-containing composite. Salvetat *et al.* suggest that adhesion can be improved by functionalizing CNTs to roughen their surfaces.²⁶ This would effectively create a larger surface area for adhesion. They point out that functionalization must not come at the cost of tube integrity. Disorder in tubes can be increased with increased functionalization. More on tube functionalization is discussed in **Chapter 2, Section 2.4**. Another example of CNTs improving the strength of other materials is that of fluorinated SWCNTs composited with polyacrylonitrile. The new material was shown to have a larger tensile strength than the same composite with unfunctionalized CNTs.¹⁹⁸ However, the latter material-type was a better conductor than the fluorinated version. The addition of CNTs to composites has been shown to improve the thermal conductivity and mechanical properties of the material.¹⁹⁹ Applications of such nanocomposite materials from such research are growing²⁰⁰ and a host of nanocomposite materials exist. Because the tensile strength of CNTs far outweighs that of other known materials it makes this new material ideal in composites that need strengthening and reinforcement. Such composites have been used in bullet-proof vests, bicycle frames and the like. Also, CNTs are low in density since they are composed of a light element and have hollow inner tubes. This “lightweight factor” is advantageous in materials where strength but low density is required, for example in aircraft materials.

1.12.5 Nanoelectronics

CNTs, and especially SWCNTs because of their more predictable properties, are perhaps the quintessential molecular wires. For this reason research into their use in nanoelectronics is moving forward rapidly. Two examples include branched CNTs and gold-“loving” thiolated SWCNTs. With regards to the former, mixtures of metal containing compounds such as ferrocene, cobaltocene, nickel-phthalocyanines, iron-phthalocyanines, or iron pentacarbonyl, with thiophene, produce Y-junction CNTs.⁵⁷ With respect to the latter, SWCNTs have been thiolated directly by mixing them with sulfur and placing this mixture in a plasma of argon and hydrogen.²⁰¹ These thiolated-SWCNTs were shown to self-assemble onto gold electrodes, for use in nanoelectric circuits.

1.12.6 Catalyst supports

Coupled with a need for research into the improvement of the methods for manufacturing CNTs, is the usefulness of such materials as supports for catalysts. Palladium is possibly one of the most versatile and widely used metals for organic catalysis. However, catalysts achieve a

much greater catalytic potential when supported. Supports provide not only access by the substrate to a larger surface area of the catalyst (supports can help prevent agglomeration which decreases the available surface of the catalyst), but the nature of the support also influences the catalytic properties of the metal catalyst. CNTs have both an inherently high surface area (compared to other traditional supports), and interesting influences on palladium when it is loaded onto CNTs. Not only this, but CNTs have other advantages as supports over the more conventional ones, making Pd/CNT hybrids a viable research area for use in, for example, industrial reactions and fuel cells.

The literature shows clearly the usefulness of CNTs as materials in a range of applications, based on their inherent and tuneable properties. Indeed tens of thousands of reports on these nanostructures in terms of morphology, synthesis, properties and applications have been published. A consideration of the broad trends in the literature has shaped the course of this study. In particular, the main areas of focus in this study are: (1) the synthesis of CNTs and other SCNMs through the CVD method of synthesis, due to its simplicity and advantages, (2) research on ferrocene derivatives as catalysts and their effects, and (3) the preparation of Pd nanoparticles on CNTs (Pd/CNTs) as emerging carbonaceous supports for heterogeneous catalysis. **Chapter 2** is dedicated to the topic of Pd/CNTs.

References

- 1 Y. Ando, X. Zhao, T. Sugai and M. Kumar, *Mater. Today*, 2004, **7**, 22
- 2 W. R. Davis, R. J. Slawson and G. R. Rigby, *Nature*, 1953, **171**, 756
- 3 P. C. M. van Stiphout, D. E. Stobbe, F. J. H. van der Scheur and J. W. Geus, *Appl. Catal.*, 1998, **40**, 219
- 4 H. W. Kroto, J. R. Heath, S. C. O'Brien, R. F. Curl and R. E. Smalley, *Nature*, 1985, **318**, 162
- 5 S. Iijima, *Nature*, 1991, **354**, 56
- 6 M. Monthioux and V. L. Kuznetsov, *Carbon*, 2006, **44**, 1621
- 7 A. Oberlin, M. Endo and T. Koyama, *J. Cryst. Growth*, 1976, **32**, 335
- 8 N. Grobert, *Mater. Today*, 2007, **10**, 28
- 9 D. Bera, S. C. Kuiry, M. McCutchen, A. Kruize, H. Heinrich, M. Meyyappan and S. Seal, *Chem. Phys. Lett.*, 2004, **386**, 364
- 10 J.-W. Snoeck, G. F. Froment and M. Fowles, *J. Catal.*, 1997, **169**, 240
- 11 T. W. Odom, J.-L. Huang, P. Kim and C. M. Lieber, *J. Phys. Chem. B*, 2000, **104**, 2794
- 12 <http://itech.dickinson.edu/chemistry/?cat=74> (accessed 8 March 2011)
- 13 M. Endo, T. Hayashi, Y. A. Kim, M. S. Dresselhaus and M. Terrones, *Phil. Trans. R. Soc. Lond. A*, 2004, **362**, 2223
- 14 H. W. Zhu, C. L. Xu, D. H. Wu, B. Q. Wei, R. Vajtai and P. M. Ajayan, *Science*, 2002, **296**, 884
- 15 X. Wang, Q. Li, J. Xie, Z. Jin, J. Wang, Y. Li, K. Jiang and S. Fan, *Nano Lett.*, 2009, **9**, 3137
- 16 M. S. Dresselhaus, G. Dresselhaus and R. Saito, *Carbon*, 1995, **33**, 883
- 17 N. Hamada, S. Sawada and A. Oshiyama, *Phys. Rev. Lett.*, 1992, **68**, 1579
- 18 Image is granted to the public domain
- 19 M. L. Terranova, V. Sessa and M. Rossi, *Chem. Vap. Deposition*, 2006, **12**, 315
- 20 <http://coecs.ou.edu/Brian.P.Grady/nanotube.html> (accessed 28 June 2010)
- 21 D. Tasis, N. Tagmatarchis, A. Bianco and M. Prato, *Chem. Rev.*, 2006, **106**, 1105

- 22 M. S. Dresselhaus and M. Endo, in *Carbon Nanotubes: Synthesis, Structure, Properties and Applications, Topics Appl. Phys.*, eds. M. S. Dresselhaus, G. Dresselhaus and P. Avouris, Springer-Verlag, Berlin, 2001, vol. **80**, pp. 11-28
- 23 N. M. Rodriguez, A. Chambers and R. T. K. Baker, *Langmuir*, 1995, **11**, 3862
- 24 J.-P. Salvetat, G. A. D. Briggs, J.-M. Bonard, R. R. Bacsa, A. J. Kulik, T. Stöckli, N. A. Burnham and L. Forró, *Phys. Rev. Lett.*, 1999, **82**, 944
- 25 M.-F. Yu, O. Lourie, M. J. Dyer, K. Moloni, T. F. Kelly and R. S. Ruoff, *Science*, 2000, **287**, 637
- 26 J.-P. Salvetat, J.-M. Bonard, N. H. Thomson, A. J. Kulik, L. Forró, W. Benoit and L. Zuppiroli, *Appl. Phys. A*, 1999, **69**, 255
- 27 http://www.ceramisis.com/carbons_graphites_specs.htm (accessed 8 March 2011)
- 28 H. M. Cheng, F. Li, G. Su, H. Y. Pan, L. L. He, X. Sun and M. S. Dresselhaus, *Appl. Phys. Lett.*, 1998, **72**, 3282
- 29 D. Qian, G. J. Wagner, W. K. Liu, M.-F. Yu and R. S. Ruoff, *Appl. Mech. Rev.*, 2002, **55**, 495
- 30 O. Shenderova, D. Brenner and R. S. Ruoff, *Nano Lett.*, 2003, **3**, 805
- 31 P. Kim, L. Shi, A. Majumdar and P. L. McEuen, *Phys. Rev. Lett.*, 2001, **87**, 215502
- 32 T. W. Odom, J. H. Hafner and C. M. Lieber, in *Carbon Nanotubes: Synthesis, Structure, Properties and Applications, Topics Appl. Phys.*, eds. M. S. Dresselhaus, G. Dresselhaus and P. Avouris, Springer-Verlag, Berlin, 2001, vol. **80**, pp. 173-211
- 33 V. Derycke, R. Martel, J. Appenzeller and Ph. Avouris, *Nano Lett.*, 2001, **1**, 453
- 34 P. G. Collins, K. Bradley, M. Ishigami and A. Zettl, *Science*, 2000, **287**, 1801
- 35 P. Koskinen, *Phys. Rev. B*, 2010, **82**, 193409
- 36 T. H. Cho, W. S. Su, T. C. Leung, W. Ren and C. T. Chan, *Phys. Rev. B*, 2009, **79**, 235123
- 37 H. Kataura, Y. Kumazawa, Y. Maniwa, I. Umezumi, S. Suzuki, Y. Ohtsuka and Y. Achiba, *Synth. Met.*, 1999, **103**, 2555
- 38 J. A. Misewich, R. Martel, Ph. Avouris, J. C. Tsang, S. Heinze and J. Tersoff, *Science*, 2003, **300**, 783
- 39 M. Freitag, Y. Martin, J. A. Misewich, R. Martel and Ph. Avouris, *Nano Lett.*, 2003, **3**, 1067
- 40 R. Andrews, D. Jacques, D. Qian and T. Rantell, *Acc. Chem. Res.*, 2002, **35**, 1008
- 41 Y. Yang, Z. Hu, Y. J. Tian, Y. N. Lü, X. Z. Wang and Y. Chen, *Nanotechnol.*, 2003, **14**, 733
- 42 E. Couteau, K. Hernadi, J. W. Seo, L. Thiên-Nga, C. Mikó, R. Gaál and L. Forró, *Chem. Phys. Lett.*, 2003, **378**, 9
- 43 R. Guzmán de Villoria, A. J. Hart and B. L. Wardle, *ACS Nano*, 2011, **5**, 4850
- 44 V. O. Nyamori and N. J. Coville, *Organometallics*, 2007, **26**, 4083
- 45 I. Martin-Gullon, J. Vera, J. A. Conesa, J. L. González and C. Merino, *Carbon*, 2006, **44**, 1572
- 46 C. Wu, X. Zhu, L. Ye, C. OuYang, S. Hu, L. Lei and Y. Xie, *Inorg. Chem.*, 2006, **45**, 8543
- 47 L. Xu, W. Zhang, Q. Yang, Y. Ding, W. Yu and Y. Qian, *Carbon*, 2005, **43**, 1090
- 48 Y. Z. Jin, C. Gao, W. K. Hsu, Y. Zhu, A. Huczko, M. Bystrzejewski, M. Roe, C. Y. Lee, S. Acquah, H. Kroto and D. R. M. Walton, *Carbon*, 2005, **43**, 1944
- 49 P. Serp, R. Feurer, P. Kalck, Y. Kihn, J. L. Faria and J. L. Figueiredo, *Carbon*, 2001, **39**, 621
- 50 X.-Y. Liu, B.-C. Huang and N. J. Coville, *Carbon*, 2002, **40**, 2791
- 51 J. Geng, C. Ducati, D. S. Shephard, M. Chhowalla, B. F. G. Johnson and J. Robertson, *Chem. Commun.*, 2002, 1112
- 52 M. C. Schnitzler, M. M. Oliveira, D. Ugarte and A. J. G. Zarbin, *Chem. Phys. Lett.*, 2003, **381**, 541
- 53 S. Liu and R. J. Wehmschulte, *Carbon*, 2005, **43**, 1550
- 54 Y. Lu, Z. Zhu and Z. Liu, *Carbon*, 2005, **43**, 369
- 55 J. Liu, L. Xu, W. Zhang, W. J. Lin, X. Chen, Z. Wang and Y. Qian, *J. Phys. Chem. B*, 2004, **108**, 20090
- 56 C. P. Deck and K. Vecchio, *Carbon*, 2006, **44**, 267

- 57 F. L. Deepak, A. Govindaraj and C. N. R. Rao, *Chem. Phys. Lett.*, 2001, **345**, 5
- 58 M. Glerup, J. Steinmetz, D. Samaille, O. Stéphan, S. Enouz, A. Loiseau, S. Roth and P. Bernier, *Chem. Phys. Lett.*, 2004, **387**, 193
- 59 N. Grobert, M. Terrones, S. Trasobares, K. Kordatos, H. Terrones, J. Olivares, J. P. Zhang, Ph. Redlich, W. K. Hsu, C. L. Reeves, D. J. Wallis, Y. Q. Zhu, J. P. Hare, A. J. Pidduck, H. W. Kroto and D. R. M. Walton, *Appl. Phys. A*, 2000, **70**, 175
- 60 H. Okuno, E. Grivei, F. Fabry, T. M. Gruenberger, J. Gonzalez-Aguilar, A. Palnichenko, L. Fulcheri, N. Probst and J. C. Charlier, *Carbon*, 2004, **42**, 2543
- 61 J. Hu, Y. Bando, J. Zhan, C. Zhi, F. Xu and D. Golberg, *Adv. Mater.*, 2006, **18**, 197
- 62 R. Schlögl and S. B. A. Hamid, *Angew. Chem. Int. Ed.*, 2004, **43**, 1628
- 63 K. K. Kar, *Carbon Nanotubes: Synthesis, Characterization and Applications*, Research Publishing, Kanpur, India, 2011
- 64 T. W. Ebbesen and P. M. Ajayan, *Nature*, 1992, **358**, 220
- 65 H. Huang, H. Kajiura, S. Tsutsui, Y. Hirano, M. Miyakoshi, A. Yamada and M. Ata, *Chem. Phys. Lett.*, 2001, **343**, 7
- 66 O. Stephan, P. M. Ajayan, C. Colliex, Ph. Redlich, J. M. Lambert, P. Bernier and P. Lefin, *Science*, 1994, **266**, 1683
- 67 S. Iijima and T. Ichihashi, *Nature*, 1993, **363**, 603
- 68 Y. Saito, T. Yoshikawa, M. Okuda, N. Fujimoto, K. Sumiyama, K. Suzuki, A. Kasuya and Y. Nishina, *J. Phys. Chem. Solids*, 1993, **54**, 1849
- 69 C.-H. Kiang, W. A. Goddard III, R. Beyers, J. R. Salem and D. S. Bethune, *J. Phys. Chem. Solids*, 1996, **57**, 35
- 70 X. Zhao, M. Ohkohchi, H. Shimoyama and Y. Ando, *J. Cryst. Growth*, 1999, **198/199**, 934
- 71 Z. Shi, Y. Lian, X. Zhou, Z. Gu, Y. Zhang, S. Iijima, L. Zhou, K. T. Yue and S. Zhang, *Carbon*, 1999, **37**, 1449
- 72 J. Qiu, Y. Li, Y. Wang, C. Liang, T. Wang and D. Wang, *Carbon*, 2003, **41**, 767
- 73 E. Muñoz, W. K. Maser, A. M. Benito, M. T. Martínez, G. F. de la Fuente, Y. Maniette, A. Righi, E. Anglaret and J. L. Sauvajol, *Carbon*, 2000, **38**, 1445
- 74 W. K. Maser, E. Muñoz, A. M. Benito, M. T. Martínez, G. F. de la Fuente, Y. Maniette, E. Anglaret and J. L. Sauvajol, *Chem. Phys. Lett.*, 1998, **292**, 587
- 75 A. Thess, R. Lee, P. Nikolaev, H. Dai, P. Petit, J. Robert, C. Xu, Y. H. Lee, S. G. Kim, A. G. Rinzler, D. T. Colbert, G. E. Scuseria, D. Tománek, J. E. Fischer and R. E. Smalley, *Science*, 1996, **273**, 483
- 76 H. Dai, in *Carbon Nanotubes: Synthesis, Structure, Properties and Applications, Topics Appl. Phys.*, eds. M. S. Dresselhaus, G. Dresselhaus and P. Avouris, Springer-Verlag, Berlin, 2001, vol. **80**, pp. 29-53
- 77 B. I. Yakobson and R. E. Smalley, *Am. Sci.*, 1997, **85**, 324
- 78 S. Bandow, A. M. Rao, K. A. Williams, A. Thess, R. E. Smalley, and P. C. Eklund, *J. Phys. Chem. B*, 1997, **101**, 8839
- 79 P. L. Walker Jr, J. F. Rakszawski and G. R. Imperial, *J. Phys. Chem.*, 1959, **63**, 133
- 80 V. O. Nyamori, S. D. Mhlanga and N. J. Coville, *J. Organomet. Chem.*, 2008, **693**, 2205
- 81 A. T. Matveev, D. Golberg, V. P. Novikov, L. L. Klimkovich and Y. Bando, *Carbon*, 2001, **39**, 155
- 82 A. G. Nasibulin, P. V. Pikhitsa, H. Jiang and E. I. Kauppinen, *Carbon*, 2005, **43**, 2251
- 83 S. Chaisitsak, A. Yamada and M. Konagai, *Diamond Relat. Mater.*, 2004, **13**, 438
- 84 M. R. Aguiar, C. Verissimo, A. C. Ramos, S. A. Moshkalev and J. W. Swart, *J. Nanosci. Nanotechnol.*, 2009, **9**, 4143
- 85 A. Szabó, D. Méhn, Z. Kónya, A. Fonseca and J. B. Nagy, *Phys. Chem. Comm.*, 2003, **6**, 40
- 86 G. S. B. McKee, C. P. Deck and K. S. Vecchio, *Carbon*, 2009, **47**, 2085

- 87 H. J. Jeong, H. K. Choi, G. Y. Kim, Y. I. Song, Y. Tong, S. C. Lim and Y. H. Lee, *Carbon*, 2006, **44**, 2689
- 88 A. G. Nasibulin, A. Moisala, D. P. Brown, H. Jiang and E. I. Kauppinen, *Chem. Phys. Lett.*, 2005, **402**, 227
- 89 A. J. H. M. Kock, P. K. de Bokx, E. Boellaard, W. Klop and J. W. Geus, *J. Catal.*, 1985, **96**, 468
- 90 H. Neumayer and R. Haubner, *Diamond Relat. Mater.*, 2004, **13**, 1191
- 91 B. C. Satishkumar, A. Govindaraj, R. Sen and C. N. R. Rao, *Chem. Phys. Lett.*, 1998, **293**, 47
- 92 A. Moisala, A. G. Nasibulin, S. D. Shandakov, H. Jiang and E. I. Kauppinen, *Carbon*, 2005, **43**, 2066
- 93 D. Jain, A. Winkel and R. Wilhelm, *Small*, 2006, **2**, 752
- 94 J. Liu, M. Shao, Q. Xie, L. Kong, W. Yu and Y. Qian, *Carbon*, 2003, **41**, 2101
- 95 J. Shen, J. Li, Q. Chen, T. Luo, W. Yu and Y. Qian, *Carbon*, 2006, **44**, 190
- 96 E. N. Nxumalo, V. P. Chabalala, V. O. Nyamori, M. J. Witcomb and N. J. Coville, *J. Organomet. Chem.*, 2010, **695**, 1451
- 97 M. S. Mohlala, X.-Y. Liu and N. J. Coville, *J. Organomet. Chem.*, 2006, **691**, 4768
- 98 J. Chen, N. Xia, T. Zhou, S. Tan, F. Jiang and D. Yuan, *Int. J. Electrochem. Sci.*, 2009, **4**, 1063
- 99 H.-s. Qian, F.-m. Han, B. Zhang, Y.-c. Guo, J. Yue and B.-x. Peng, *Carbon*, 2004, **42**, 761
- 100 P. L. Pauson, *J. Organomet. Chem.*, 2001, **637-639**, 3
- 101 G. G. Tibbets, D. W. Gorkiewicz and R. L. Alig, *Carbon*, 1993, **31**, 809
- 102 P. Nikolaev, M. J. Bronikowski, R. K. Bradley, F. Rohmund, D. T. Colbert, K. A. Smith and R. E. Smalley, *Chem. Phys. Lett.*, 1999, **313**, 91
- 103 A. Cao, L. Ci, G. Wu, B. Wei, C. Xu, J. Liang and D. Wu, *Carbon*, 2001, **39**, 152
- 104 A. Leonhardt, S. Hampel, C. Müller, I. Mönch, R. Koseva, M. Ritschel, D. Elefant, K. Biedermann and B. Büchner, *Chem. Vap. Deposition*, 2006, **12**, 380
- 105 A. Barreiro, S. Hampel, M. H. Rummeli, C. Kramberger, A. Grüneis, K. Biedermann, A. Leonhardt, T. Gemming, B. Büchner, A. Bachtold and T. Pichler, *J. Phys. Chem. B*, 2006, **110**, 20973
- 106 L. S. Panchakarla and A. Govindaraj, *Bull. Mater. Sci.*, 2007, **30**, 23
- 107 R. Sen, A. Govindaraj and C. N. R. Rao, *Chem. Phys. Lett.*, 1997, **267**, 276
- 108 T. M. Keller, M. Laskoski and S. B. Qadri, *J. Phys. Chem. C*, 2007, **111**, 2514
- 109 M. Laskoski, T. M. Keller and S. B. Qadri, *Carbon*, 2007, **45**, 443
- 110 T. M. Keller and S. B. Qadri, *Chem. Mater.*, 2004, **16**, 1091
- 111 M. S. Mohlala, X.-Y. Liu, J. M. Robinson and N. J. Coville, *Organometallics*, 2005, **24**, 972
- 112 M. S. Mohlala, X.-Y. Liu, M. J. Witcomb and N. J. Coville, *Appl. Organomet. Chem.*, 2007, **21**, 275
- 113 A. Govindaraj and C. N. R. Rao, *Pure Appl. Chem.*, 2002, **74**, 1571
- 114 J. D. Harris, R. P. Raffaele, T. Gennett, B. J. Landi and A. F. Hepp, *Mater. Sci. Eng. B*, 2005, **116**, 369
- 115 M. S. Mohlala and N. J. Coville, *J. Organomet. Chem.*, 2007, **692**, 2965
- 116 J. Qiu, Y. An, Z. Zhao, Y. Li and Y. Zhou, *Fuel Process. Technol.*, 2004, **85**, 913
- 117 A. K. Schaper, H. Hou, A. Greiner and F. Phillipp, *J. Catal.*, 2004, **222**, 250
- 118 S. Chaisitsak, J. Nukeaw and A. Tuantranont, *Diamond Relat. Mater.*, 2007, **16**, 1958
- 119 C. Singh, M. S. P. Shaffer and A. H. Windle, *Carbon*, 2003, **41**, 359
- 120 A. Moisala, A. G. Nasibulin, D. P. Brown, H. Jiang, L. Khriachtchev and E. I. Kauppinen, *Chem. Eng. Sci.*, 2006, **61**, 4393
- 121 L. Ci, Z. Ryu, N. Y. Jin-Phillipp and M. Rühle, *Diamond Relat. Mater.*, 2007, **16**, 531
- 122 A. M. Cassell, J. A. Raymakers, J. Kong and H. Dai, *J. Phys. Chem. B*, 1999, **103**, 6484
- 123 J. E. Herrera, L. Balzano, A. Borgna, W. E. Alvarez and D. E. Resasco, *J. Catal.*, 2001, **204**, 129
- 124 Z. E. Horváth, K. Kertész, L. Pethő, A. A. Koós, L. Tapasztó, Z. Vértesy, Z. Osváth, Al. Darabont, P. Nemes-Incze, Zs. Sárközi and L. P. Biró, *Curr. Appl. Phys.*, 2006, **6**, 135

- 125 E. D. Dikio, F. T. Thema, C. W. Dikio and F. M. Mtunzi, *Int. J. Nanotech. Applica.*, 2010, **4**, 117
- 126 A. Cao, X. Zhang, J. Wei, Y. Li, C. Xu, J. Liang, D. Wu and B. Wei, *J. Phys. Chem. B*, 2001, **105**, 11937
- 127 E. N. Nxumalo, P. J. Letsoalo, L. M. Cele and N. J. Coville, *J. Organomet. Chem.*, 2010, **695**, 2596
- 128 J.-M. Ting, T.-P. Li and C.-C. Chang, *Carbon*, 2004, **42**, 2997
- 129 Y. T. Lee, N. S. Kim, J. Park, J. B. Han, Y. S. Choi, H. Ryu and H. J. Lee, *Chem. Phys. Lett.*, 2003, **372**, 853
- 130 J. Jiao and S. Seraphin, *J. Phys. Chem. Solids*, 2000, **61**, 1055
- 131 A. G. Nasibulin, A. Moisala, D. P. Brown and E. I. Kauppinen, *Carbon*, 2003, **41**, 2711
- 132 H. Dai, A. G. Rinzler, P. Nikolaev, A. Thess, D. T. Colbert and R. E. Smalley, *Chem. Phys. Lett.*, 1996, **260**, 471
- 133 M. J. Bronikowski, P. A. Willis, D. T. Colbert, K. A. Smith and R. E. Smalley, *J. Vac. Sci. Technol. A*, 2001, **19**, 1800
- 134 L. Ci, B. Wei, J. Liang, C. Xu and D. Wu, *J. Mater. Sci. Lett.*, 1999, **18**, 797
- 135 F. J. M. Rietmeijer, P. H. Schultz and T. E. Bunch, *Chem. Phys. Lett.*, 2003, **374**, 464
- 136 Y.-F. Shi, H.-J. Quan, G.-B. Zheng, H. Sano and Y. Uchiyama, *Carbon*, 2002, **411**, 1674
- 137 M. Monthieux, H. Allouche and R. L. Jacobsen, *Carbon*, 2006, **44**, 3183
- 138 R. O. Grisdale, *J. Appl. Phys.*, 1953, **24**, 1082
- 139 P. T. A. Reilly and W. B. Whitten, *Carbon*, 2006, **44**, 1653
- 140 K. Kuwana and K. Saito, *Carbon*, 2005, **43**, 2088
- 141 R. T. K. Baker, P. S. Harris, R. B. Thomas and R. J. Waite, *J. Catal.*, 1973, **30**, 86
- 142 R. Bichler, R. Hauber and B. Lux, 6th Euro CVD Conference, Jerusalem, 1987, 413-422
- 143 X. Bai, D. Li, Y. Wang and J. Liang, *Tsinghua Sci. Technol.*, 2005, **10**, 729
- 144 L. F. Su, J. N. Wang, F. Yu, Z. M. Sheng, H. Chang and C. Pak, *Chem. Phys. Lett.*, 2006, **420**, 421
- 145 A. Moisala, A. G. Nasibulin and E. I. Kauppinen, *J. Phys.: Condens. Matter*, 2003, **15**, S3011
- 146 E. W. Wong, M. J. Bronikowski, M. E. Hoenk, R. S. Kowalczyk and B. D. Hunt, *Chem. Mater.*, 2005, **17**, 237
- 147 A. Barreiro, C. Kramberger, M. H. Rummeli, A. Grüneis, D. Grimm, S. Hampel, T. Gemming, B. Büchner, A. Bachtold and T. Pichler, *Carbon*, 2007, **45**, 55
- 148 Y. Chen, Z. Sun, Y. N. Li and B. K. Tay, *Mater. Chem. Phys.*, 2006, **98**, 256
- 149 L. Ci, Z. Zhou, D. Tang, X. Yan, Y. Liang, D. Liu, H. Yuan, W. Zhou, G. Wang and S. Xie, *Chem. Vap. Deposition*, 2003, **9**, 119
- 150 A. Yasuda, N. Kawase and W. Mizutani, *J. Phys. Chem. B*, 2002, **106**, 13294
- 151 S. B. Sinnott, R. Andrews, D. Qian, A. M. Rao, Z. Mao, E. C. Dickey and F. Derbyshire, *Chem. Phys. Lett.*, 1999, **315**, 25
- 152 S. Huang, M. Woodson, R. Smalley and J. Liu, *Nano Lett.*, 2004, **4**, 1025
- 153 T. Hayashi, Y. A. Kim, T. Matoba, M. Esaka, K. Nishimura, T. Tsukada, M. Endo, and M. S. Dresselhaus, *Nano Lett.*, 2003, **3**, 887
- 154 H. Shioyama and T. Akita, *Carbon*, 2003, **41**, 179
- 155 C. P. Deck and K. Vecchio, *Carbon*, 2005, **43**, 2608
- 156 Y. Shao, J. Sui, G. Yin and Y. Gao, *Appl. Catal. B: Environ.*, 2008, **79**, 89
- 157 S. J. Sque, C. P. Ewels, R. Jones and P. R. Briddon, *Phys. Stat. Sol. (a)*, 2007, **204**, 2898
- 158 Y.-P. Sun, K. Fu, Y. Lin and W. Huang, *Acc. Chem. Res.*, 2002, **35**, 1096
- 159 C.-L. Sun, H.-W. Wang, M. Hayashi, L.-C. Chen and K.-H. Chen, *J. Am. Chem. Soc.*, 2006, **128**, 8368
- 160 Z. Xu, W. Lu, W. Wang, C. Gu, K. Liu, X. Bai, E. Wang and H. Dai, *Adv. Mater.*, 2008, **20**, 3615
- 161 K. C. Mondal, A. M. Strydom, Z. Tetana, S. D. Mhlanga, M. J. Witcomb, J. Havel, R. M. Erasmus and N. J. Coville, *Mater. Chem. Phys.*, 2009, **114**, 973

- 162 Ph. Redlich, J. Loeffler, P. M. Ajayan, J. Bill, F. Aldinger and M. Rühle, *Chem. Phys. Lett.*, 1996, **260**, 465
- 163 K. C. Mondal, A. M. Strydom, R. M. Erasmus, J. M. Keartland and N. J. Coville, *Mater. Chem. Phys.*, 2008, **111**, 386
- 164 V. Jourdain, H. Kanzow, M. Castignolles, A. Loiseau and P. Bernier, *Chem. Phys. Lett.*, 2002, **364**, 27
- 165 M. Jung, K. Y. Eun, J.-K. Lee, Y.-J. Baik, K.-R. Lee and J. W. Park, *Diamond Relat. Mater.*, 2001, **10**, 1235
- 166 E. N. Nxumalo, V. O. Nyamori and N. J. Coville, *J. Organomet. Chem.*, 2008, **693**, 2942
- 167 R. Droppa Jr, P. Hammer, A. C. M. Carvalho, M. C. dos Santos and F. Alvarez, *J. Non-Cryst. Solids*, 2002, **299-302**, 874
- 168 S. Glenis, S. Cooke, X. Chen and M. M. Labes, *Chem. Mater.*, 1994, **6**, 1850
- 169 M. Yudasaka, R. Kikuchi, Y. Ohki and S. Yoshimura, *Carbon*, 1997, **35**, 195
- 170 S. Maldonado, S. Morin and K. J. Stevenson, *Carbon*, 2006, **44**, 1429
- 171 C. Tang, Y. Bando, D. Golberg and F. Xu, *Carbon*, 2004, **42**, 2625
- 172 Q. Guo, Y. Xie, X. Wang, S. Zhang, T. Hou and S. Lv, *Chem. Commun.*, 2004, 26
- 173 C. Cao, F. Huang, C. Cao, J. Li and H. Zhu, *Chem. Mater.*, 2004, **16**, 5213
- 174 R. A. Sidik, A. B. Anderson, N. P. Subramanian, S. P. Kumaraguru and B. N. Popov, *J. Phys. Chem. B*, 2006, **110**, 1787
- 175 L. Jiang and L. Gao, *Carbon*, 2003, **41**, 2923
- 176 Y. Huang, J. Gao and R. Liu, *Synth. Met.*, 2000, **113**, 251
- 177 X. Sun and M. S. Saha, in *PEM Fuel Cell Electrocatalysts and Catalyst Layers: Fundamentals and Applications*, ed. J. Zhang, Springer-Verlag, London, 2008, pp. 655-704
- 178 Y. Miyamoto, M. L. Cohen and S. G. Louie, *Solid State Commun.*, 1997, **102**, 605
- 179 R. Chetty, S. Kundu, W. Xia, M. Bron, W. Schuhmann, V. Chirila, W. Brandl, T. Reinecke and M. Muhler, *Electrochim. Acta*, 2009, **54**, 4208
- 180 L. Ci, H. Zhu, B. Wei, J. Liang, C. Xu and D. Wu, *Carbon*, 1999, **37**, 1652
- 181 G. G. Tibbetts, C. A. Bernardo, D. W. Gorkiewicz and R. L. Alig, *Carbon*, 1994, **32**, 569
- 182 T. M. Minea, S. Point, A. Gohier, A. Granier, C. Godon and F. Alvarez, *Surf. Coat. Technol.*, 2005, **200**, 1101
- 183 A. G. Nasibulin, D. P. Brown, P. Queipo, D. Gonzalez, H. Jiang and E. I. Kauppinen, *Chem. Phys. Lett.*, 2006, **417**, 179
- 184 T.-J. Park, S. Banerjee, T. Hemraj-Benny and S. S. Wong, *J. Mater. Chem.*, 2006, **16**, 141
- 185 K. Mølhav, S. B. Gudnason, A. T. Pedersen, C. H. Clausen, A. Horsewell and P. Bøggild, *Ultramicroscopy*, 2007, **108**, 52
- 186 M. L. Matson and L. J. Wilson, *Future Med. Chem.*, 2010, **2**, 491
- 187 <http://www.nanotube-suppliers.com/node/10> (accessed 1 September 2011)
- 188 D. Lekas, "Analysis of Nanotechnology from an Industrial Ecology Perspective Part II: Substance Flow Analysis Study of Carbon Nanotubes", Master of Environmental Management Revised Draft paper, November, 2005
- 189 B. Yu, F. Zhou, G. Liu, Y. Liang, W. T. S. Huck and W. Liu, *Chem. Commun.*, 2006, 2356
- 190 R. B. Sharma, V. N. Tondare, D. S. Joag, A. Govindaraj and C. N. R. Rao, *Chem. Phys. Lett.*, 2001, **344**, 283
- 191 N. S. Lee, D. S. Chung, I. T. Han, J. H. Kang, Y. S. Choi, H. Y. Kim, S. H. Park, Y. W. Jin, W. K. Yi, M. J. Yun, J. E. Jung, C. J. Lee, J. H. You, S. H. Jo, C. G. Lee and J. M. Kim, *Diamond Relat. Mater.*, 2001, **10**, 265
- 192 K.-Y. Chun, H. S. Lee and C. J. Lee, *Carbon*, 2009, **47**, 169

- 193 L. Qiao, C. Wang, C. Q. Qu, Y. Zeng, S. S. Yu, X. Y. Hu, W. T. Zheng and Q. Jiang, *Diamond Relat. Mater.*, 2009, **18**, 657
- 194 S. S. Wong, E. Joselevich, A. T. Woolley, C. L. Cheung and C. M. Lieber, *Nature*, 1998, **394**, 52
- 195 A. C. Dillon, K. M. Jones, T. A. Bekkedahl, C. H. Kiang, D. S. Bethune and M. J. Heben, *Nature*, 1997, **386**, 377
- 196 M. Kaempgen, M. Lebert, N. Nicoloso and S. Roth, *Appl. Phys. Lett.*, 2008, **92**, 094103
- 197 C. Velasco-Santos, A. L. Martínez-Hernández, F. T. Fisher, R. Ruoff and V. M. Castaño, *Chem. Mater.*, 2003, **15**, 4470
- 198 F. J. Owens, *Mater. Lett.*, 2005, **59**, 3720
- 199 M. J. Biercuk, M. C. Llaguno, M. Radosavljevic, J. K. Hyun, A. T. Johnson and J. E. Fischer, *Appl. Phys. Lett.*, 2002, **80**, 2767
- 200 P. Ajayan and O. Z. Zhou, in *Carbon Nanotubes: Synthesis, Structure, Properties and Applications, Topics Appl. Phys.*, eds. M. S. Dresselhaus, G. Dresselhaus and P. Avouris, Springer-Verlag, Berlin, 2001, vol. 80, pp. 391-425
- 201 N. O. V. Plank, R. Cheung and R. J. Andrews, *Appl. Phys. Lett.*, 2004, **85**, 3229

CHAPTER 2*

CNTs AS SUPPORTS FOR Pd AND BIMETALLIC CATALYSTS FOR USE IN HYDROGENATION REACTIONS

2.1 Introduction

The need to optimize industrially important processes and new technologies, and to create a sustainable society and environment, drives the search for better energy sources and better materials. Coupled with this, is the need for economic development and competitiveness in the global market. Worldwide trends are towards greener chemistry, greener energy and a decrease of our reliance on fossil fuels. Catalysis plays an important role in this and two recent papers have discussed how it has shaped, and will continue to shape, society.^{1,2} Progressive research into novel catalytic systems is a part of this endeavour.

Palladium is one of the most versatile metal catalysts used in industry. Two of the main reasons for its importance are its ability to catalyze the formation of carbon-carbon bonds and the insensitivity of many palladium catalysts to water or oxygen. Palladium is particularly efficient as a catalyst in hydrogenation reactions. Metal catalysts reach a much greater potential when supported. This is because metal catalyst particles can be dispersed to a greater degree, and therefore are exposed to a larger number of substrate molecules. Up to 75% of hydrogenation reactions are currently carried out over Pd/C catalysts.

A variety of carbon supports for precious metal catalysts have, for several decades, been used in heterogeneous catalysis.³ Emerging carbonaceous supports, such as the newly discovered carbon allotropes and SCNMs, including CNTs⁴ [see **Figure 2.1 (a)**], carbon microspheres⁵ [see **Figure 2.1 (b)**] and CNFs⁶ [see **Figure 2.1 (c)**] are gaining more interest. The remarkable properties of CNTs, as discussed in **Chapter 1, Section 1.4**, make them worthwhile to investigate as supports for palladium metal catalysts.

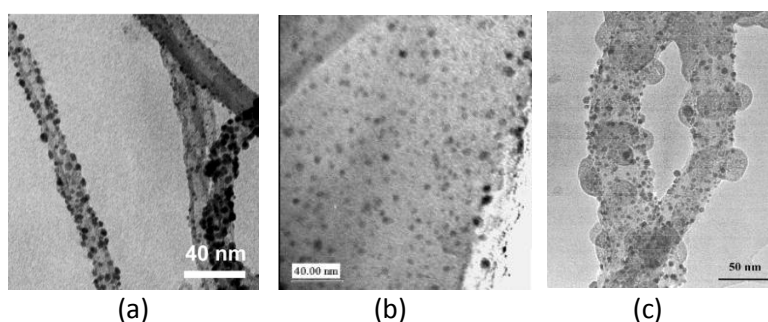


Figure 2.1 TEM image of (a) Pd/MWCNTs used for heterogeneous hydrogenation of *trans*-stilbene;⁴² (b) Pd/microspheres before a hydrogenation reaction;⁵ (c) Pd/CNFs used for the heterogeneous hydrogenation of cinnamaldehyde.⁶

*This chapter is taken from the review paper: R. S. Oosthuizen and V. O. Nyamori, *Platinum Metals Rev.*, 2011, **55**, 154. Minor changes and deletions have been made to maintain the flow of this dissertation, prevent repetitions and keep constant formatting.

Trends in technological and scientific progress in catalysis lean towards the production of more efficient catalysts, smaller particle sizes and more finely dispersed particles to optimize yields and decrease reaction times. For this reason, nanosized catalytic particles have received much attention and they are known to display higher catalytic activity.⁷ Hybrid metal-CNT systems have been shown by theoretical calculations to have altered properties compared to unmodified CNTs.⁸ The results of hydrogenation reactions on various supports suggest that the interaction between the metal catalyst and the support greatly influences the catalytic activity in a hydrogenation reaction.⁹⁻¹¹ Hence, this chapter addresses the issue of support use with the aim of broadly answering the following questions:

- How do CNTs compare with other traditional carbonaceous supports for catalysts and in what cases are CNTs superior as palladium supports in hydrogenation reactions?
- How do chemically modified CNTs influence the activity of palladium NPs, especially in hydrogenation reactions?
- What effect does a secondary metal have on the catalytic activity of the Pd/CNT system?

Lastly, a few literature examples involving the use of Pd/CNT hybrids in hydrogenation reactions are given.

This chapter covers a wide range of literature on Pd/CNT systems. The examples chosen for this review mainly involve some current studies of Pd/CNT systems for hydrogenation reactions. Specifically, examples based on cinnamaldehyde [Figure 2.2 (a)], which has useful applications such as a flavouring, fungicide, antimicrobial agent or anticancer agent among others, are provided. The reduction of this organic compound is interesting because it has more than one functional group that can be reduced. The useful products that are obtained include cinnamyl alcohol [Figure 2.2 (b)], 3-phenylpropionaldehyde [Figure 2.2 (c)] and 3-phenylpropan-1-ol [Figure 2.2 (d)], among others, depending on chemoselectivity. Hence, this compound, as an example, could form the basis for the comparison of conversions and the effect or influence of the support on palladium chemoselectivity.

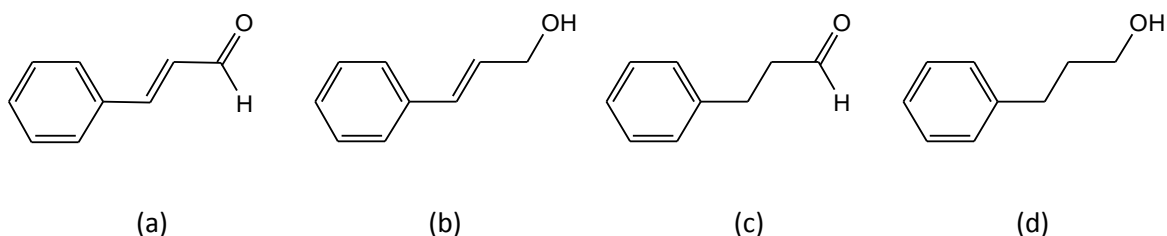


Figure 2.2 Structures of (a) cinnamaldehyde; (b) cinnamyl alcohol; (c) 3-phenylpropionaldehyde (hydrocinnamaldehyde) and (d) 3-phenylpropan-1-ol.

2.2 The advantages of CNTs as catalyst supports

2.2.1 Introduction to types of supports

A host of supports for palladium catalysts are available, from metal oxide supports such as alumina, silica and zeolites, to the traditional carbonaceous supports such as activated charcoal or activated carbon (AC), carbon blacks, graphites and the emerging carbon nanomaterials.³

Oxide supports are often mechanically and thermally unstable. In the case of alumina, under high temperatures the ions of the catalytically active phase can interact with the support in such a manner as to lower the catalyst availability and catalytic activity.¹² In transition aluminas, conversion to α -alumina at temperatures near 1100 °C can occur, resulting in a lowered surface area.¹³ Heat dispersion in certain oxide supports, such as alumina, is not always uniform, due to the insulating nature of this material. Thus, under oxidizing conditions, so called “hot-spots” can form, resulting in alteration of both the support and metal catalyst.¹⁴

There are a variety of AC products that differ in certain key properties such as porosity, pore size and particle size distribution, surface area, resistance to attrition and the content of ash, depending on the process of manufacture. AC is commonly used in liquid phase processes and remains the popular choice of support for hydrogenation reactions. This is due to its ease of separation from the reaction mixture, resistance towards aggressive media such as high pH, and the relative ease of metal recovery after use. Carbon black, which is produced from acetylene under high temperatures, is more suitable for use as a support than conventional carbon black made from other petroleum fractions. However, carbon black in general has relatively very low ash content.³

In order to overcome some of the disadvantages of the common commercial supports, there is a need to research and develop new nanodimensional supports such as CNTs or CNFs. These nanostructured carbon-based materials display good physical and chemical properties which are ideal for catalyst supports.

2.2.2 Electronic properties of CNTs *versus* graphite sheets

The arrangement of carbon atoms determines the surface and electronic properties as discussed in **Chapter 1, Section 1.4**. The metallic or semi-metallic nature of CNTs naturally has an effect on the properties of metals loaded onto the support. Duca *et al.* studied the combined properties of graphite *versus* SWCNTs with Pd₉ clusters by means of computational methods.¹⁵ Their findings showed that Pd₉ clusters may have a stronger interaction with a CNT than with traditional flat graphite sheet bilayers due to the curvature of the nanotube which has an effect on metallic properties. The following sections compare and contrast the properties of CNTs as supports with the more traditional supports.

2.2.3 Mechanical strength of CNTs *versus* traditional supports

The high mechanical strength of CNTs makes them not only favourable in composites,^{14,16} but also in mechanically taxing catalytic environments such as vigorously stirred liquid phase reactions. On more conventional supports high levels of friction may lead to attrition, effectively altering the surface area of the exposed metal catalyst.¹⁴ Moreover, the relatively lower mechanical stability of common commercial carbon-based supports initiates the formation of fine particulates during operation. The existence of a large amount of micropores can reduce the full accessibility of the reactants to the active site.

2.2.4 Reactivity and stability of CNTs *versus* traditional supports

Carbon supports are often unreactive and stable in many acidic and basic media, and consequently find use in a wide range of industrial applications^{3,17} while many other supports are rendered useless after reaction. However, traditional carbon-based supports have limitations not only when it comes to mechanical stability but also in terms of resistance to oxidizing atmospheres at high temperatures.¹⁴ Oxidation and hydrogenation processes can result in gasification when the temperature is above 500 °C and approximately 700 °C, respectively.⁵ The order of ease of oxidation is: amorphous carbon > MWCNTs > SWCNTs. The SWCNTs are generally more structured and have fewer surface defects than MWCNTs, and hence are more stable under most conditions.⁴

AC is more easily oxidized than CNTs,⁴ and CNTs are more easily oxidized than graphite. Chiang *et al.* showed by thermogravimetric analysis (TGA) that acid oxidized MWCNTs were more thermally stable than AC fibres or C₆₀ fullerene.¹⁸ However, impurities in carbonaceous supports, such as metal residues from CVD processes, as well as defects in the structure, may not only limit the temperature at which hydrogenation takes place, but may also poison the active metal catalyst, such as palladium, and lower the temperature at which carbon oxidizes.⁴ CNTs have good thermal conductivity and therefore reactions catalyzed by metal/carbon systems need to be carefully controlled, especially if they are exothermic. Temperature can affect the performance of the catalyst on the carbon support and more research is needed to explore this aspect.

The effect of microwave irradiation on MWCNTs has been studied by Olivier *et al.*¹⁹ The authors prepared 10 wt.% palladium on MWCNTs with the metal particles located only on the outer walls. Microwave irradiation was used to drive hydrogenation of cinnamate esters with ammonium formate as a reductant. Chemoselective C=C bond hydrogenation occurred for all substrates and the catalyst could be recycled more than five times without loss of activity. The same reaction carried out under the same conditions with Pd/AC generated a variety of other products due to microwave degradation of chemical species, demonstrating that Pd/AC is less regio- and stereoselective than 10 wt.% Pd on MWCNTs.

Liang *et al.* investigated the hydrogenation of CO₂ catalyzed by supported Pd/ZnO catalysts.²⁰ Pd/ZnO on MWCNTs proved more favourable than Pd/ZnO on either alumina or AC, with the MWCNTs providing a promoting effect. Also, herringbone-type CNTs had a greater promoting

activity than parallel-type CNTs in these studies. The high conversion and selective formation of methanol from CO₂ by the MWCNT-supported catalysts was due to their favourable ability to reversibly adsorb a greater amount of hydrogen, thus increasing the rate of surface hydrogenation reactions.

2.2.5 Surface area and selectivity of CNTs *versus* traditional supports

SWCNTs, which are inherently microporous, are considered by some to be very suitable supports for metal catalysts. One reason for this is the high surface-to-volume ratio of SWCNTs compared to other supports. They also have high surface areas, 1587 m² g⁻¹²¹ (see **Table 2.1**) after purification and tube-end opening. The SWCNT structure is such that every atom is exposed to not one but two surfaces – both the inner and outer surfaces of the nanotube. **Table 2.1** shows the approximate surface areas of various carbon supports. In the case of AC, the micropores are large in quantity and their size may actually slow the progress of substrate molecules into the pores.¹⁴ The ACs can have macro-, meso- and micropores, which can decrease the reproducibility of metal loading. Surface areas can range from 800-1200 m² g⁻¹.³ However, loading of palladium on SWCNTs has been found to be lower than that obtained on MAXSORB® AC for hydrogen sorption studies.²² The authors of that study suggest that this is due to the larger pore volumes and surface area of the AC, and thus the correspondingly larger number of sites on which nucleation can occur. However, smaller palladium crystallites were formed on SWCNTs than on AC.

Table 2.1 Comparison of the surface areas of carbon-based supports.

Support		Typical surface area (m ² g ⁻¹)	Reference	
activated carbon		800-1200	3	
carbon black	conventional	100-1500	3	
	graphitized	60-300	3	
graphite		10-50	3	
shaped carbon nanomaterials	CNTs	SWCNTs	1587 ^y	21
		MWCNTs	400 ^δ	26
	other	carbon nano- & microspheres	10	83

^yafter (i) debundling with dimethylformamide/ethylene diamine mixture, (ii) acid treatment, (iii) wet oxidation

^δafter basic treatment

It has also been shown that the activity of palladium for the hydrogenation of α - β -unsaturated aldehydes is high, but its selectivity remains challenging and many times it has been boosted by the addition of promoters.²³ A much researched model compound of this class of aldehydes is cinnamaldehyde. The selectivity of palladium for cinnamyl alcohol is low when compared to platinum or ruthenium, however, using CNTs as supports seems to provide advances in overcoming this challenge. Corma *et al.* compared Pd/SWCNTs with Pd/AC prepared by the

same method.²⁴ They showed that Pd/AC had a higher activity for the hydrogenation of cinnamaldehyde to 3-phenylpropionaldehyde than Pd/SWCNTs. However, there was a wider range of particle sizes for Pd/AC than for Pd/SWCNTs. This was thought to be due to the larger variety of functional groups on AC. This may cause Pd²⁺ ions not to be uniformly deposited in the beginning stages of deposition, resulting in bigger agglomerates over time, and hence a larger range of sizes.

MWCNTs are inherently mesoporous structures. The pore sizes of MWCNTs allow for diffusion, reaction and desorption of chemical species and thus are good supports for catalysts.²⁵ They also possess high surface areas, reaching up to approximately 400 m² g⁻¹ after basic treatments.²⁶ These supports sometimes give better activity than microporous supports such as AC. Janowska *et al.* showed that selectivity for the C=C bond hydrogenation product of cinnamaldehyde can exceed 80% when performed over Pd/CNTs.²⁷ The explanation given was the lack of micropores as well as the high surface area of the CNTs. Lack of micropores affects the time spent by reactants and products on the support surface as well as affecting the manner in which desorption occurs. Also, palladium crystallites and CNTs may interact to alter the adsorption and selectivity properties. In other research, palladium NPs inside MWCNTs and on AC both achieved complete conversion of cinnamaldehyde, although the completion times for the former were slightly faster.²⁸ In this work it was shown that at a higher hydrogen flow rate, the rate of hydrogenation increased, but more so for the AC support than for the MWCNTs. The MWCNT-supported catalyst hydrogenated predominantly the C=C bond, rather than the C=O bond, with only about 10% of the totally hydrogenated product forming. The AC-supported catalyst showed an equal selectivity for both products, namely 3-phenylpropan-1-ol and hydrocinnamaldehyde. Neither catalyst showed any selectivity for cinnamyl alcohol. It was concluded that the MWCNT-supported catalyst was superior in terms of selectivity for hydrocinnamaldehyde and that the MWCNTs had a higher surface area (some micropores on the traditional support being inaccessible to some substrates) resulting in a higher catalytic activity.

Zhang *et al.* used MWCNTs with different palladium loadings for benzene hydrogenation.²⁹ They then compared the results with those from Pd/zeolite (SiO₂/Al₂O₃ = 5.1) and Pd/AC prepared under the same conditions. They showed that the conversion of benzene to cyclohexane was approximately 100% at the highest loading (12.0 wt.%) of Pd/MWCNT. An intermediate loading (8.0 wt.%) yielded nearly double the conversion of benzene compared to that achieved using the AC- or zeolite-supported catalysts. This was despite the fact that the specific surface area of the MWCNTs was lower than that of the zeolite and AC as determined after acid treatment. It was also shown that diluted palladium salt solutions yielded smaller palladium particles inside tubes and more concentrated solutions yielded larger particles, which would influence catalytic rates.

In a study on the partial hydrogenation of phenylacetylene, CNTs, AC and carbon black were used as supports for palladium.³⁰ Although all active phases achieved over 95% conversion to styrene, the selectivity was highest for the Pd/CNT catalyst, with five runs maintaining the activity and selectivity. The AC support showed agglomeration of the palladium NPs.

Pd/CNFs (5 wt.% Pd) and Pd/AC were used in the liquid-phase hydrogenation of the C=C bond in cinnamaldehyde by Pham-Huu *et al.*⁶ Both the surface area:volume ratio and thus catalytic activity were higher for the CNF-supported catalyst. This was assumed to be due to the large number of micropores on AC leading to diffusion problems which affects the catalytic rate. This cannot occur in CNFs because they have no micropores. Pd/CNFs produced almost exclusively (98%) hydrocinnamaldehyde and negligible amounts of cinnamyl alcohol and 3-phenylpropanol, showing that the selectivity of the catalyst for C=C hydrogenation under these conditions is good. The AC catalyst produced a mixture of all products. However, the nature of the carbon support was shown to have negligible effect on the hydrogenation of a variety of polar aromatic compounds in a recent article by Anderson *et al.*³¹ They showed that the nature of the solvent is a bigger factor in the selectivity.

Graphite has a comparatively low surface area (10 to 50 m² g⁻¹), although grinding processes can increase it to approximately 300 m² g⁻¹.³ The capacity for adsorption of volatile organic compounds onto MWCNTs and CNFs is lower than for high surface area graphite.³²

2.2.6 Recovery and recycling of precious metals from CNTs *versus* traditional supports

The high price of precious metals makes the recovery and reuse of such catalysts economically important. Carbon supports make recovery more economical compared to metal oxide supports as they can be burnt off the metal catalyst and the catalyst recovered from a small volume of ash. The solid waste is minimal. The metal can then be dissolved and recovered from acidic solutions.

Oxidation of AC over long periods of time can decrease its usefulness as a support.³ The inertness of CNTs, on the other hand, enables them to resist oxidation over long periods of time and allows them to be recycled many times. CNT-metal hybrids can be dispersed to a fairly uniform degree by stirring in organic solvents. After use, the hybrid CNT-NPs can be recovered by gravitational sedimentation. Hence, as a support, CNTs are economical and stable when it comes to processes of recovery and reuse of catalysts.

2.3 Loading techniques and considerations

A fair amount of research has gone into mechanisms suitable for attaching palladium NPs to the walls of SWCNTs and MWCNTs.³³ Common loading techniques for palladium include impregnation,^{28,29,34} deposition precipitation,³⁵ electroless deposition^{36,37} and electrochemical deposition.^{38,39} Less commonly used methods include CVD⁴⁰ and microemulsion techniques.⁴¹ Supercritical CO₂ has been used instead of conventional solvents to effect a greener approach to palladium loading techniques.⁴² However, the palladium NP size, crystal structure and distribution cannot be accurately manipulated by many of these processes.

Considerations for choosing a loading technique include the desired level of loading, required particle size and/or size distribution ranges, and the macroscopic distribution of particles on

the support. The higher the palladium loading, in general, the greater the rate of product formation, since more palladium catalyst particles are exposed to substrate molecules. Most methods yield heterogeneously dispersed particle sizes, although controlling the size of metal particles is still being investigated. Typically, the smaller the particle size, the larger the surface area of palladium metal and the higher the catalytic activity. Pore structure and accessibility of the substrate to the metal in the pores also influences the macroscopic distribution. The common types of supported catalyst structure are egg-shell, uniform distributions or intermediates of the two.³ Typically, uniform distribution of small metal NPs is ideal for hydrogenations. However, uniformly impregnated catalysts are also more likely to lose a part of the precious palladium metal loading through leaching.³ This can be minimized by improving the availability of hydrogen in the liquid reaction medium and by either using less catalyst for the reaction or decreasing the palladium metal loading.

Pristine CNTs are considered to be relatively inert allowing for only low levels of palladium deposition⁴ at defect sites such as Stone-Wales defects, dangling bonds at open tips and vacancies.⁴³ The CNTs do not contain many functional groups on their surfaces and thus need to be activated to create anchoring sites for better palladium metal deposition. Many of these techniques are similar to the pretreatment of other carbon supports and are primarily used to remove metallic impurities, such as iron derived from the CNT synthesis, and generate surface groups in the process. Functionalization can be done through ball-milling⁴⁴ or by chemical or electrochemical means. Chemical means often incorporate the use of highly oxidizing conditions such as H₂SO₄ or HNO₃⁴⁵⁻⁴⁷ or molecular oxygen.⁴⁵ Sometimes sonication is used in conjunction with a chemical means.⁴⁸ Plasmas can also be employed.^{45,49,50} Covalent functional groups such as alcohols (-OH), carbonyl groups (-C=O) and carboxylic acids (-COOH) form.

In general, more oxygen groups aid higher dispersion of palladium, although some authors maintain that oxygen-containing groups are not sites onto which the metals anchor, but rather that they merely increase wetting. Enhanced wetting allows for better dispersion in aqueous deposition solutions. Unger *et al.* achieved very low loadings of palladium (1 wt.%) on pre-oxidized CNTs.⁵¹ They suggested that covalent bonding does not occur between the oxide groups and the metal, and that palladium therefore cannot attach in large quantities. However, Guo and Li suggested that more palladium particles form at positions where -COOH groups would preferably form, for example at the end of SWCNTs.⁵²

Most reports discuss palladium NPs decorated on the exterior of CNT surfaces. However, some state that certain palladium metal catalysts loaded on the inside of nanotubes exhibit a higher catalytic activity than the same amount on more conventional supports.^{53,54} **Figure 2.3** shows a TEM image of such a system. The supposition is that the partial pressure of the substrates inside the tubes is increased, altering the rate of catalysis. Factors affecting the placing of palladium particles inside tubes include hydrophobicity of tubes, inner diameter, the concentration of palladium in the precursor solution and surface tension of the palladium deposition solution. Palladium particles found near the tips of tubes were probably deposited there due to the fast rate of evaporation of water out of the tubes. The strong interaction between palladium particles and the tube could give rise to the faceted nature of the catalyst

particles.⁵⁴ It has been suggested that this interaction may affect dispersion.²⁹ Tessonier *et al.* suggested that the morphology of the inner wall may alter the electronic nature of the adsorbed metal and thus modify the adsorption of the substrate and selectivity for the product.²⁸ They stated that the nature of the precursor solution seemed to have a negligible effect on dispersion.

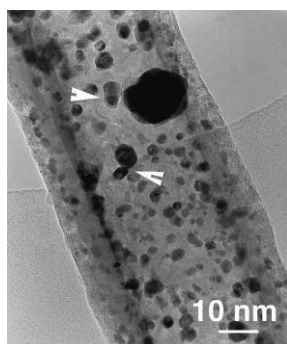


Figure 2.3 TEM image of palladium NPs located primarily on the inside of MWCNTs with the arrowheads indicating the presence of some highly faceted palladium particles.⁵⁴

Factors influencing the properties of the nanometallic particles include size, shape and the crystalline geometry.⁵⁵ Computational calculations indicated that CNT-supported Pd₉ clusters would have a higher activity than the unsupported cluster for H₂ bond breaking in hydrogenation reactions.⁵⁶ Franklin *et al.* reported the first controlled decoration of SWCNTs with palladium particles of a consistent morphology,⁵⁷ and Ansón *et al.* found that the mass ratios of the Pd:support (SWCNTs or MAXSORB® AC) directly determined the percentage of palladium loaded.²² These latter authors suggested, from their results, that a threshold for palladium saturation is reached when the mass ratio of support:Pd is 1:4. Also, the crystallite size was larger at higher palladium loadings. These authors demonstrated that the quantity of palladium loaded onto the SWCNTs was not altered in runs that used oxidative pretreatments, although their palladium wt.% loading values decreased slightly after a nitric acid treatment in the case of Pd(PPh₃)₄ as the palladium source. Different precursor palladium compounds were also found to influence the loading on CNTs and AC in the same studies.

2.4 Modified CNTs as supports

Besides modification with oxide groups, other means of functionalization can produce further benefits. Functionalization can be covalent⁵⁸ or noncovalent.⁵⁹ CNTs have the ability to attach a wide range of chemical species at active sites, such as their sidewalls, tubular tips or defect areas. The exohedral and endohedral functionalization can also provide an opportunity to create unique catalyst supports for palladium.

Agglomeration of NPs reduces the surface area of catalytically active metal particles. Some loading techniques, such as modification of the support with a surfactant or ionic liquid (IL) before metal deposition, can be employed to control the formation of larger nanoclusters on the surface of CNTs. Surface moieties are thought to aid stabilization of the crystallites during

sintering.³ Chun *et al.* functionalized MWCNTs with an imidazolium bromide followed by palladium.⁶⁰ They effectively formed an IL catalytic system rendering the functionalized MWCNTs soluble in water, and thereby successfully prevented CNT agglomeration and aided dispersion in the aqueous phase ready for palladium deposition. Following this, hydrogenation of *trans*-stilbene was performed with turnover frequency (TOF) values up to 2820 mol h⁻¹, which is considered to be high. Varying the anion was shown to influence the catalytic activity in this hydrogenation reaction. Pd/IL-*f*-MWCNTs (where *f* indicates functionalized; IL is [1-butyl-3-methyl-imidazolium][hexafluoroantimonate]) remained active after 10 cycles and were then used in olefin hydrogenations. Only after 50 runs did the activity significantly decrease.

Sodium dodecyl sulfate (SDS)⁶¹ and sodium bis(2-hexylethyl)sulfosuccinate (AOT)⁴¹ also aid in the homogenous distribution of palladium particles on the support by acting as surfactants. Agglomeration of palladium particles is prevented. **Figures 2.4 (a) and (b)** show Pd/CNTs prepared with and without AOT, respectively.⁴¹ The fairly even distribution of NPs in **Figure 2.4 (a)** is apparent, whereas **Figure 2.4 (b)** shows significant agglomeration. SDS⁶² and sodium *n*-tetradecyl sulfate (SC₁₄S)⁶³ also induce reduction of the palladium precursor. Karousis *et al.* used Pd/MWCNTs with SDS to hydrogenate a variety of olefins.⁶⁴ Four olefins were successfully hydrogenated. The Pd/MWCNTs were then compared to Pd/AC for the hydrogenation of methyl-9-octadecenoate and 2-methyl-2-pentenal. The molar ratio of Pd:substrate was kept constant. TOF values for Pd/MWCNTs for both compounds were three to five times higher than for Pd/AC. Large amounts of the palladium precursor also cause agglomeration. Thus it is important to control the amounts of both the precursor and the SDS added to the reaction mixture for optimal dispersion.⁶¹

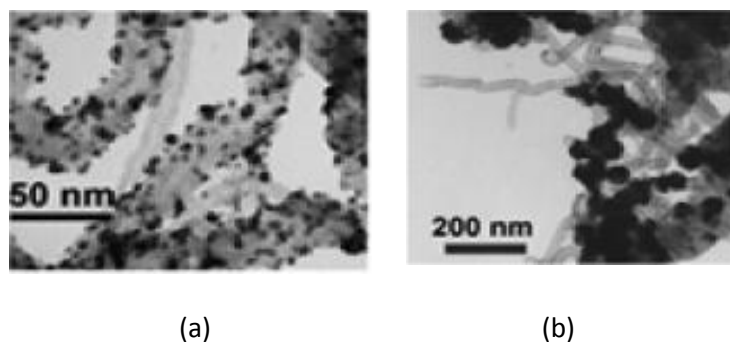


Figure 2.4 TEM image of Pd/MWCNTs prepared (a) with a surfactant, showing fairly uniform distribution of palladium NPs and (b) without a surfactant, resulting in agglomeration of palladium NPs.⁴¹

In another paper palladium was loaded onto SDS-stabilized MWCNTs and SWCNTs and then used in successful hydrogenations of the same four olefins as well as 3-phenyl-2-propenal,⁶⁵ although a detailed comparison of the two supports was not given. The Pd/MWCNTs were then compared with Pd/AC for the hydrogenation of methyl-9-octadecenoate and 2-methyl-2-pentenal. TOF values for Pd/MWCNTs approximated three to five times higher than for the conventional catalyst. Even after seven cycles of the Pd/MWCNTs there was little to no leaching of palladium off the support.

Doping of CNTs and other carbon materials has been fairly extensively researched for N- and B-dopants⁶⁶⁻⁶⁸ resulting in modified properties. Many properties such as electronic properties⁶⁹ and even strength with which other species adsorb⁷⁰ are affected by doping. Most doping studies for CNTs are for MWCNTs, with a few on SWCNTs for applications such as field emission devices. (Refer to **Chapter 1, Section 1.9** for more on doping.) Generally, CNTs are inert, but the incorporation of heteroatoms into their structure can give rise to a more chemically active material. Disadvantages include the fact that often N-doped counterparts are less thermally stable and more prone to oxidation.⁷¹

An and Turner studied the binding between transition metals and CNTs by making use of density functional theory calculations for individual metal atoms on N- or B-doped SWCNTs at chosen sites.⁷⁰ These initial studies showed, among other things, that a range of commercially important transition metals, including palladium, undergo higher chemisorption with doped SWCNTs as opposed to pristine SWCNTs. B-doped CNTs gave the most enhanced binding. Amadou *et al.* carried out experiments in which the dispersion of palladium was found not to be significantly different on doped or undoped tubes.³⁴ However, it was interesting to note that no palladium NPs were found inside the N-doped tubes. This was thought to be due to compartmentalization as shown in **Figure 2.5**. The Pd/N-doped CNTs were compared with Pd/CNTs and Pd/AC for the liquid-phase hydrogenation of cinnamaldehyde. Pd/AC, with the highest specific surface area, displayed the highest activity. Pd/N-doped CNTs had an activity nearly equal to that of Pd/AC, but almost double that of the undoped Pd/CNTs. This indicated a significant influence of the N incorporation on the activity for C=C bond hydrogenation. In terms of selectivity, the doped support was best for hydrocinnamaldehyde production while the Pd/AC catalyst was the least selective.

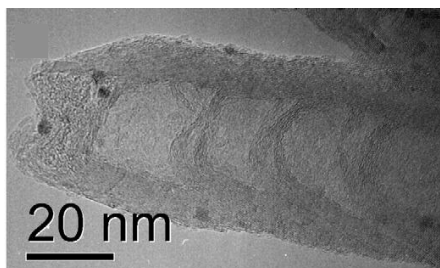


Figure 2.5 TEM showing the “bamboo” cross-structures in a palladium loaded N-doped MWCNT without palladium NPs incorporated inside the cavities.³⁴

2.5 Bimetallic catalysts – effect of secondary metal

Research has shown that bimetallic catalysts can influence the catalytic activity of a system⁷² and sometimes have higher catalytic performance in certain reactions than a single metal catalyst.⁷³ The additional metal(s) can improve the size and morphology of active particles as well as the catalyst selectivity.⁷³

The activity of Pd-Pt is superior to that of other commercial bimetallic catalysts in the hydrogenation of aromatic compounds, a pre-step in the desulfurization of fuels. Noble metals are susceptible to poisoning by sulfur. Use of acidic supports or bimetallic Pd-Pt catalysts has

proven to enhance the resistance to poisoning by sulfur.⁷⁴ Pawelec *et al.* studied Pd-Pt/MWCNTs in the hydrogenation of toluene and naphthalene in the presence of dibenzothiophene in the gas phase to monitor, simultaneously, the hydrodesulfurization of the sulfur-containing compound.⁷⁵ A Pd-Pt/zirconium phosphate-silica zeolite and a Pd-Pt/amorphous SiO₂-Al₂O₃ (ASA) catalyst were also prepared for comparison although different loading techniques were used. Results suggested that all catalysts are more active for toluene hydrogenation than for the polyaromatic compound. Pd-Pt/MWCNTs had the lowest loading and BET specific areas but the highest activity for toluene hydrogenation. However, Pd-Pt/ASA was the best catalyst for naphthalene hydrogenation and the hydrodesulfurization of dibenzothiophene. The combined effect of the Pd-Pt alloy may be a factor, coupled with the location of these NPs on the MWCNTs, since a marked lack of steric hindrance for the substrate would be found on the outer surfaces of MWCNTs as compared to the other catalysts. However, the bimetallic effect is still not yet well understood.

Qiu *et al.* observed that the conversion and selectivity towards cinnamyl alcohol was highest for a Pd-Ru bimetallic catalyst on CNTs than for either of the two monometallic catalysts under identical conditions.⁷⁶ This finding was attributed either to the promoting effect of ruthenium on palladium or to a synergistic effect from Pd-Ru together.

Arene hydrogenation is important in industry, for example, for diesel fuels with low aromatic contents. Heterogeneous catalysis with metals at high temperatures is the traditional method for arene hydrogenation. Yoon *et al.* hydrogenated benzene at room temperature under 1-20 atm over Pd-Rh/CNTs.⁷⁷ A high activity for benzene reduction, with no solvent, was found. Commercially available Pd/C and Rh/C cannot do this under these conditions yet. Pd/CNT had very low or no activity at room temperature, whereas the Pd-Rh/CNT had a catalytic activity much higher than either of the monometallic systems. A conversion of 98% of benzene at room temperature to cyclohexane occurred after 24 h at room temperature and 10 atm. Pd/CNT needed 24 h at 50 °C and 10 atm to achieve a near 50% conversion of benzene to the saturated product. Pd-Rh/CNT was shown to be recyclable multiple times.

Functionalized MWCNTs in a water-in-hexane microemulsion as a surfactant were loaded with Pd, Rh or Pd-Rh.⁴¹ Arene hydrogenation tests revealed that Pd-Rh/CNTs (see **Figure 2.6**) were more active than the monometallic systems for anthracene hydrogenation. However, the detailed morphology of this bimetallic catalyst system was not studied or confirmed.

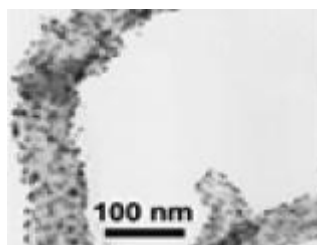


Figure 2.6 TEM image of Pd-Rh/MWCNTs.⁴¹

It has also been shown that the molar ratio of the two metals in a bimetallic oxide catalyst, such as Pd/ZnO, influences the catalytic activity of CO₂ hydrogenation.²⁰

2.6 Hydrogenation on Pd/CNT catalysts

Palladium on CNT supports is effective as a catalyst for the reduction of a variety of functional groups. Following this are specific examples for carbon-carbon multi-bond and nitrogen-containing group hydrogenations.

2.6.1 Alkene and alkyne hydrogenation

Pd/CNTs grown and supported on carbon microfibers were used as catalysts in the gas phase hydrogenation of cyclooctene.⁴⁰ Initial studies showed the system to be active for reduction of this alkene.

The first report on the use of Pd/CNT to hydrogenate $C\equiv C$ discussed the successful hydrogenation of tolane, phenylacetylene and 1-heptyne with 5% palladium on CNTs.⁷⁸ The results showed that only 0.02 mol% Pd/CNT was needed to convert all the starting materials to products, indicating that this catalytic system had a high activity towards $C\equiv C$ hydrogenation. This catalytic activity was higher than that found in earlier work by the same authors for the hydrogenation of tolane over palladium complexes supported on fullerenes.⁷⁹ The ratio of the two reaction products was found to be determined largely by the temperature and length of time of hydrogenation. The lower the hydrogenation time, or the higher the temperature (within the range 22–60 °C), the greater the conversion to a saturated product. Further reactions with the Pd/CNT catalyst showed the same catalytic performance. All three acetylenic hydrocarbons underwent complete conversion to a mixture of ethylenic and saturated compounds. Reapplication of the catalyst at 60 °C for 7 h yielded 100% selectivity for the saturated product.

Jung *et al.* studied Pt on CNFs and CNTs for cinnamaldehyde hydrogenation and palladium on CNFs for 1-octyne hydrogenation.⁸⁰ They used a colloidal microwave process to load metals onto supports. This method makes pretreatment unnecessary and yields a high dispersion of the catalyst. Unloaded supports (CNFs, CNTs, AC and Al_2O_3) were tested for cinnamaldehyde catalysis but no activity was found. Palladium is possibly the most selective catalyst for the semi-hydrogenation of alkynes. Previous studies had shown the hydrogenation of cinnamaldehyde over Pt/CNTs to be poorer than over Pt/CNFs, thus only CNFs were used in the 1-octyne studies. Conversion of 1-octyne by palladium on two types of CNFs yielded the semi-hydrogenated product 1-octene, which had a slow conversion to the saturated product.

2.6.2 Conversion of nitro ($-NO_2$) to amino ($-NH_2$) group *via* hydrogenation

Pd/AC is a common catalyst for the selective hydrogenation of nitrobenzene and derivatives thereof. In one study, nitrobenzene was hydrogenated in the liquid phase by using palladium deposited on the inside of MWCNTs.⁵⁴ This reaction was compared with a Pd/AC system. The activity of the Pd/MWCNT catalyst hybrid was superior to that of the Pd/AC catalyst system, even though the surface area of the AC was higher than that of the MWCNTs. The observed

results were explained in terms of the lack of micropores in the MWCNTs. It was also suggested that convection in the liquid phase in the MWCNTs increased the rate of substrate collision with H₂ molecules and thereby increased the activity.

Jiang *et al.* hydrogenated the nitro- group of *o*-chloronitrobenzene to provide an amine derivative using palladium supported on three different supports: CNTs, γ -Al₂O₃ and SiO₂.⁸¹ Both the activity and selectivity for the formation of the amine product were favoured by the CNT-based catalyst. These results may be influenced by the geometric and electronic effects of CNTs on the catalysis process as well as the textures and properties of the CNTs.

2.6.3 Hydrogenation of nitric oxide (NO)

Wang *et al.* used pre-hydrogenated Pd/CNTs to reduce NO.⁸² The reducing action of the hydrogenated Pd/CNT showed that such systems can take up hydrogen effectively in significant amounts. This may be of interest to the hydrogen storage industry. CNTs without a metal additive were hydrogenated to a far lesser extent. Subsequent addition of NO caused reduction of this gas in only the Pd-hydrogenated/CNTs.

There are a fair amount of examples of Pd/CNTs and bimetallic platinum-group-metal-CNTs as hydrogenation catalysts in the literature. **Table 2.2** summarizes some of this research.

Table 2.2 Examples of Pd/CNTs used in hydrogenation reactions.

	Metal-catalyst system		Substrate for hydrogenation	Reference	
As synthesized CNTs	mono-metallic catalyst	Pd/CNTs	Pd/SWCNTs ^ξ	cinnamaldehyde	24
			Pd/MWCNTs ^ρ	NO	82
		benzene		29	
		cinnamaldehyde		14,27	
		<i>trans</i> -stilbene		42	
		cyclooctene		40	
		nitrobenzene		54	
		phenylacetylene		30	
		cinnamate esters	19		
	tolane, phenylacetylene, 1-heptyne	78			
<i>o</i> -chloronitrobenzene	81				
bimetallic catalyst	Pd/CNFs ^π		cinnamaldehyde	6	
			1-octyne	80	
			benzoic acid, benzaldehyde, acetophenone, benzamide, phenyl acetic acid, cinnamic acid, 4-hydroxy benzoic acid	31	
	Pd/ZnO- <i>h</i> ^λ -MWCNTs		CO ₂	20	
	Pd/ZnO- <i>p</i> ^θ -MWCNTs				

Table 2.2 cont...

	Metal-catalyst system		Substrate for hydrogenation	Reference
As synth. CNTs	bimetallic catalyst	Pd-Ru/CNTs	cinnamaldehyde	76
		Pd-Pt/MWCNTs	toluene/naphthalene/ dibenzothiophene	75
		Pd-Rh/MWCNTs	benzene	77
Modified CNTs	side-group addition with mono-metallic catalyst	Pd/SDS [§] -MWCNTs	methyl-9-octadecenoate, 2-methyl-3-buten-2-ol, 3,7-dimethyl-2,6-octadien-1-ol, 2-methyl-2-pentenal	64
			methyl-9-octadecenoate, 2-methyl-3-buten-2-ol, 3,7-dimethyl-2,6-octadien-1-ol, 2-methyl-2-pentenal, 3-phenyl-2-propenal	65
		Pd/SDS-SWCNTs	methyl-9-octadecenoate, 2-methyl-3-buten-2-ol, 3,7-dimethyl-2,6-octadien-1-ol, 2-methyl-2-pentenal, 3-phenyl-2-propenal	65
		Pd/imidazolium salt-MWCNTs	<i>trans</i> -stilbene	60
	bimetallic & surfactant composite	Pd-Rh/sodium bis(2-hexylethyl)sulfosuccinate-MWCNTs	anthracene	41
doped	Pd/N-MWCNTs	cinnamaldehyde	34	

^PMWCNTs – multi-walled carbon nanotubes; ^SSWCNTs – single-walled carbon nanotubes; ^TCNFs- carbon nanofibres; ^λ*h*- herringbone type; ^ϑ*p*- parallel type; [§]SDS – sodium dodecyl sulfate

2.7 Conclusions

This survey of the literature has shown that the catalytic activity of nanosized palladium metal particles in hydrogenation reactions is greatly influenced by the support on which this metal is loaded. CNTs may be highly advantageous as supports compared with the more traditional carbonaceous supports. CNTs do not display many of the disadvantages that the more common commercial supports possess. In particular, CNTs have very high mechanical strength and thus are preferable over other supports in mechanically taxing stirred batch reactions. In terms of surface area, SWCNTs, in particular, have very high surface areas and are inherently microporous. Their high surface areas also allow for more reproducible loading compared to some of the currently used ACs. CNTs lower the rate of metal NP agglomeration, due to the

strong metal-support interaction arising from the unique curvature of the CNTs, thereby enhancing the lifespan of the catalyst and ensuring its high level of activity. The chemical stability of CNTs makes them less easily oxidized than ACs, and they are economical and stable when it comes to processes of recovery and reuse of catalysts.

In many cases the chemoselectivity of Pd/CNTs in hydrogenation reactions has been shown to be superior to Pd/AC systems. One study showed that surfactant-modified Pd/MWCNTs gave higher TOF values for hydrogenation than the equivalent Pd/AC hybrids. Almost double the activity and a superior selectivity for a specific product was found for Pd/N-CNTs compared to undoped Pd/CNTs and a Pd/AC catalyst, respectively, in a study on hydrogenation reactions.

Studies of bimetallic palladium systems on CNTs revealed that selectivity and conversion for the hydrogenation of selected bonds, as well as activity towards hydrogenation of certain substrates, is enhanced by the presence of a secondary metal.

In summary, evidence exists for the superior activity and selectivity of Pd/CNTs in a range of hydrogenation reactions. There is also evidence for improved catalytic performance in certain cases by the use of modified or bimetallic Pd/CNT systems. Such findings will, hopefully, spur research in this field. However, ACs are still widely chosen as hydrogenation supports due to their ease of preparation and low cost. The challenge remains of improving the cost-effectiveness of CNT synthesis to make them an economically viable alternative to ACs as palladium supports for hydrogenation reactions.

References

- 1 C. Adams, *Top. Catal.*, 2009, **52**, 924
- 2 G. Centi and S. Perathoner, *Catal. Today*, 2008, **138**, 69
- 3 E. Auer, A. Freund, J. Pietsch and T. Tacke, *Appl. Catal. A: Gen.*, 1998, **173**, 259
- 4 P. Serp, M. Corrias and P. Kalck, *Appl. Catal. A: Gen.*, 2003, **253**, 337
- 5 K. C. Mondal, L. M. Cele, M. J. Witcomb and N. J. Coville, *Catal. Commun.*, 2008, **9**, 494
- 6 C. Pham-Huu, N. Keller, L. J. Charbonniere, R. Ziessel and M. J. Ledoux, *Chem. Commun.*, 2000, 1871
- 7 R. Schlögl and S. B. Abd Hamid, *Angew. Chem. Int. Ed.*, 2004, **43**, 1628
- 8 E. Durgun, S. Dag, S. Ciraci and O Gülseren, *J. Phys. Chem. B*, 2004, **108**, 575
- 9 A. Yu Stakeev and L. M. Kustov, *Appl. Catal. A: Gen.*, 1999, **188**, 3
- 10 A. Chambers, T. Nemes, N. M. Rodriguez and R. T. K. Baker, *J. Phys. Chem. B*, 1998, **102**, 2251
- 11 C. Park and R. T. K. Baker, *J. Phys. Chem. B*, 1998, **102**, 5168
- 12 A. B. Stiles, in *Catalyst Supports and Supported Catalysts: Theoretical and Applied Concepts*, ed. A. B. Stiles, Butterworth-Heinemann, Stoneham, Massachusetts, 1987, pp.1-9
- 13 M. Inoue, H. Otsu, H. Kominami and T. Inui, *Ind. Eng. Chem. Res.*, 1996, **35**, 295
- 14 J.-M. Nhut, R. Vieira, L. Pesant, J.-P. Tessonnier, N. Keller, G. Ehret, C. Pham-Huu and M. J. Ledoux, *Catal. Today*, 2002, **76**, 11
- 15 D. Duca, F. Ferrante and G. La Manna, *J. Phys. Chem. C*, 2007, **111**, 5402
- 16 P. Delhaès, J. P. Issi, S. Bonnamy and P. Launois, in *Understanding Carbon Nanotubes: From Basics to Applications, Lect. Notes Phys.*, eds. A. Loiseau, P. Launois, P. Petit, S. Roche and J.-P. Salvetat, Springer-Verlag, Berlin, 2006, vol. **677**, pp. 1-47

- 17 M. L. Toebes, J. A. van Dillen and K. P. de Jong, *J. Mol. Catal. A: Chem.*, 2001, **173**, 75
- 18 Y.-C. Chiang, C.-C. Lee and C.-Y. Lee, *Toxicol. Environ. Chem.*, 2009, **91**, 1413
- 19 J.-H. Olivier, F. Camerel, R. Ziessel, P. Retailleau, J. Amadou and C. Pham-Huu, *New J. Chem.*, 2008, **32**, 920
- 20 X.-L. Liang, X. Dong, G.-D. Lin and H.-B. Zhang, *Appl. Catal. B: Environ.*, 2009, **88**, 315
- 21 M. Cinke, J. Li, B. Chen, A. Cassell, L. Delzeit, J. Han and M. Meyyappan, *Chem. Phys. Lett.*, 2002, **365**, 69
- 22 A. Ansón, E. Lafuente, E. Urriolabeitia, R. Navarro, A. M. Benito, W. K. Maser and M. T. Martínez, *J. Alloys Compd.*, 2007, **436**, 294
- 23 V. Ponec, *Appl. Catal. A: Gen.*, 1997, **149**, 27
- 24 A. Corma, H. Garcia and A. Leyva, *J. Mol. Catal. A: Chem.*, 2005, **230**, 97
- 25 Q.-H. Yang, P.-X. Hou, S. Bai, M.-Z. Wang and H.-M. Cheng, *Chem. Phys. Lett.*, 2001, **345**, 18
- 26 S. Musso, S. Porro, M. Vinante, L. Vanzetti, R. Ploeger, M. Giorcelli, B. Possetti, F. Trotta, C. Pederzoli and A. Tagliaferro, *Diamond Relat. Mater.*, 2007, **16**, 1183
- 27 I. Janowska, G. Winé, M.-J. Ledoux and C. Pham-Huu, *J. Mol. Catal. A: Chem.*, 2007, **267**, 92
- 28 J.-P. Tessonnier, L. Pesant, G. Ehret, M. J. Ledoux and C. Pham-Huu, *Appl. Catal. A: Gen.*, 2005, **288**, 203
- 29 A. M. Zhang, J. L. Dong, Q. H. Xu, H. K. Rhee and X. L. Li, *Catal. Today*, 2004, **93-95**, 347
- 30 S. Domínguez-Domínguez, Á. Berenguer-Murcia, B. K. Pradhan, Á. Linares-Solano and D. Cazorla-Amorós, *J. Phys. Chem. C*, 2008, **112**, 3827
- 31 J. A. Anderson, A. Athawale, F. E. Imrie, F.-M. M^cKenna, A. M^cCue, D. Molyneux, K. Power, M. Shand and R. P. K. Wells, *J. Catal.*, 2010, **270**, 9
- 32 E. Díaz, S. Ordóñez and A. Vega, *J. Colloid Interface Sci.*, 2007, **305**, 7
- 33 P. Serp and J. L. Figueiredo (eds.), *Carbon Materials for Catalysis*, John Wiley and Sons, Hoboken, New Jersey, 2009
- 34 J. Amadou, K. Chizari, M. Houllé, I. Janowska, O. Ersen, D. Bégin and C. Pham-Huu, *Catal. Today*, 2008, **138**, 62
- 35 E. van Steen and F. F. Prinsloo, *Catal. Today*, 2002, **71**, 327
- 36 L.-M. Ang, T. S. A. Hor, G.-Q. Xu, C.-h. Tung, S. Zhao and J. L. S. Wang, *Chem. Mater.*, 1999, **11**, 2115
- 37 L. Qu and L. Dai, *J. Am. Chem. Soc.*, 2005, **127**, 10806
- 38 T. M. Day, P. R. Unwin and J. V. Macpherson, *Nano Lett.*, 2007, **7**, 51
- 39 B. M. Quinn, C. Dekker and S. G. Lemay, *J. Am. Chem. Soc.*, 2005, **127**, 6146
- 40 W. Xia, O. F.-K. Schlüter, C. Liang, M. W. E. van den Berg, M. Guraya and M. Muhler, *Catal. Today*, 2005, **102-103**, 34
- 41 B. Yoon and C. M. Wai, *J. Am. Chem. Soc.*, 2005, **127**, 17174
- 42 X. R. Ye, Y. Lin and C. M. Wai, *Chem. Commun.*, 2003, 642
- 43 J.-C. Charlier, *Acc. Chem. Res.*, 2002, **35**, 1063
- 44 K. Niesz, A. Siska, I. Vesselényi, K. Hernadi, D. Méhn, G. Galbács, Z. Kónya and I. Kiricsi, *Catal. Today*, 2002, **76**, 3
- 45 H. Ago, T. Kugler, F. Cacialli, W. R. Salaneck, M. S. P. Shaffer, A. H. Windle and R. H. Friend, *J. Phys. Chem. B*, 1999, **103**, 8116
- 46 M. S. P. Shaffer, X. Fan and A. H. Windle, *Carbon*, 1998, **36**, 1603
- 47 S. Porro, S. Musso, M. Vinante, L. Vanzetti, M. Anderle, F. Trotta and A. Tagliaferro, *Physica E*, 2007, **37**, 58-61
- 48 Y. Xing, L. Li, C. C. Chusuei and R. V. Hull, *Langmuir*, 2005, **21**, 4185
- 49 J. Chen, Z. H. Zhu, Q. Ma, L. Li, V. Rudolph and G. Q. Lu, *Catal. Today*, 2009, **148**, 97

- 50 J. Yang, X. Wang, X. Wang, R. Jia and J. Huang, *J. Phys. Chem. Solids*, 2010, doi:10.1016/j.jpcs.2009.12.008
- 51 E. Unger, G. S. Duesberg, M. Liebau, A. P. Graham, R. Seidel, F. Kreupl and W. Hoenlein, *Appl. Phys. A*, 2003, **77**, 735
- 52 D.-J. Guo and H.-L. Li, *J. Colloid Interface Sci.*, 2005, **286**, 274
- 53 P. I. Dosa, C. Erben, V. S. Iyer, K. P. C. Vollhardt and I. M. Wasse, *J. Am. Chem. Soc.*, 1999, **121**, 10430
- 54 J.-M. Nhut, L. Pesant, J.-P. Tessonnier, G. Winé, J. Guille, C. Pham-Huu and M.-J. Ledoux, *Appl. Catal. A: Gen.*, 2003, **254**, 345
- 55 B. Wiley, Y. Sun, B. Mayers and Y. Xia, *Chem. Eur. J.*, 2005, **11**, 454
- 56 V. D'Anna, D. Duca, F. Ferrante and G. La Manna, *Phys. Chem. Chem. Phys.*, 2009, **11**, 4077
- 57 A. D. Franklin, J. T. Smith, T. Sands, T. S. Fisher, K-S. Choi and D. B. Janes, *J. Phys. Chem. C*, 2007, **111**, 13756
- 58 C. A. Dyke and J. M. Tour, *J. Phys. Chem. A*, 2004, **108**, 11151
- 59 R. J. Chen, Y. Zhang, D. Wang and H. Dai, *J. Am. Chem. Soc.*, 2001, **123**, 3838
- 60 Y. S. Chun, J. Y. Shin, C. E. Song and S.-g. Lee, *Chem. Commun.*, 2008, 942
- 61 X. Chen, Y. Hou, H. Wang, Y. Cao and J. He, *J. Phys. Chem. C*, 2008, **112**, 8172
- 62 C.-L. Lee, C.-C. Wan and Y.-Y. Wang, *Adv. Funct. Mater.*, 2001, **11**, 344
- 63 C.-L. Lee, Y.-C. Huang, L.-C. Kuo and Y.-W. Lin, *Carbon*, 2007, **45**, 203
- 64 N. Karousis, G.-E. Tsotsou, N. Ragoussis and N. Tagmatarchis, *Diamond Relat. Mater.*, 2008, **17**, 1582
- 65 N. Karousis, G.-E. Tsotsou, F. Evangelista, P. Rudolf, N. Ragoussis and N. Tagmatarchis, *J. Phys. Chem. C*, 2008, **112**, 13463
- 66 Y. Zhang, H. Gu, K. Suenaga and S. Iijima, *Chem. Phys. Lett.*, 1997, **279**, 264
- 67 D. Golberg, Y. Bando, W. Han, K. Kurashima and T. Sato, *Chem. Phys. Lett.*, 1999, **308**, 337
- 68 S. Maldonado, S. Morin and K. J. Stevenson, *Carbon*, 2006, **44**, 1429
- 69 D.-P. Kim, C. L. Lin, T. Mihalisin, P. Heiney and M. M. Labes, *Chem. Mater.*, 1991, **3**, 686
- 70 W. An and C. H. Turner, *J. Phys. Chem. C*, 2009, **113**, 7069
- 71 C. J. Lee, S. C. Lyu, H.-W. Kim, J. H. Lee and K. I. Cho, *Chem. Phys. Lett.*, 2002, **359**, 115
- 72 J. R. Croy, S. Mostafa, L. Hickman, H. Heinrich and B. R. Cuenya, *Appl. Catal. A: Gen.*, 2008, **350**, 207
- 73 M. H. Jordão, V. Simões and D. Cardoso, *Appl. Catal. A: Gen.*, 2007, **319**, 1
- 74 T. Fujikawa, K. Idei, T. Ebihara, H. Mizuguchi and K. Usui, *Appl. Catal. A: Gen.*, 2000, **192**, 253
- 75 B. Pawelec, V. La Parola, R. M. Navarro, S. Murcia-Mascarós and J. L. G. Fierro, *Carbon*, 2006, **44**, 84
- 76 J. Qiu, H. Zhang, X. Wang, H. Han, C. Liang and C. Li, *React. Kinet. Catal. Lett.*, 2006, **88**, 269
- 77 B. Yoon, H.-B. Pan and C. M. Wai, *J. Phys. Chem. C*, 2009, **113**, 1520
- 78 E. V. Starodubtseva, M. G. Vinogradov, O. V. Turova, N. A. Bumagin, E. G. Rakov and V. I. Sokolov, *Catal. Commun.*, 2009, **10**, 1441
- 79 E. V. Starodubtseva, V. I. Sokolov, V. V. Bashilov, Y. N. Novikov, E. V. Martynova, M. G. Vinogradov and O. V. Turova, *Mendeleev Commun.*, 2008, **18**, 209
- 80 A. Jung, A. Jess, T. Schubert and W. Schütz, *Appl. Catal. A: Gen.*, 2009, **362**, 95
- 81 L. Jiang, H. Gu, X. Xu and X. Yan, *J. Mol. Catal. A: Chem.*, 2009, **310**, 144
- 82 S. J. Wang, W. X. Zhu, D. W. Liao, C. F. Ng and C. T. Au, *Catal. Today*, 2004, **93-95**, 711

CHAPTER 3

MOTIVATION, OBJECTIVES AND OUTLINE

3.1 Motivation for this study

Although much research has gone into the CVD floating catalyst synthesis of SCNMs, specifically MWCNTs, comparatively little study into the effect of different organometallic catalysts on the morphology, size, and purity of the products has been performed. Thus, the synthesis and characterization of MWCNTs, and the effects produced by different catalysts, was the focus of this project. For this reason, more attention was given to MWCNTs in terms of the literature review.

Having mentioned that, some catalysts and reaction parameters produce carbon nano- or microspheres primarily. Although carbon spheres were not the focus of this project, the spheres were characterized in the same way as CNTs and were useful to compare with MWCNTs in terms of yield, graphiticity, and thermal stability amongst other properties. Deshmukh *et al.* reviewed carbon spheres extensively in 2010.¹ This review paper is useful for background information of carbon spheres. Hence, not much background information on carbon spheres will be given in this dissertation.

3.2 Objectives

The main goals of this research can be phrased as questions, specifically:

1. What effect does altering experimental parameters, specifically temperature, catalyst and catalyst concentration, in the CVD floating catalyst injection method, have on the raw yield, purity, size and shape distribution of SCNMs, in particular multi-walled carbon nanotubes (MWCNTs)?
2. What are the optimal conditions (in terms of the three parameters described in 1. above) to produce the best quality MWCNTs?
3. What are the effects of introducing various heteroatoms as part of the organometallic catalyst or ferrocenyl derivative on MWCNT synthesis?
4. How effective are selected purification techniques for the removal of catalyst metal particles and amorphous carbon?
5. Can palladium be effectively loaded at approximately 5 and 10 wt.% onto synthesized MWCNTs *via* a metal organic chemical vapour deposition (MOCVD) method?
6. What is the distribution of palladium NPs on the loaded MWCNTs?

Suitable experiments designed to answer these questions were performed. They all involved the use of the CVD method for the synthesis of carbon nanomaterials. Variations in catalyst (ferrocene or ferrocene derivatives), catalyst concentration and temperature variation were investigated, with other parameters being held constant. Thereafter, the products were characterized and compared by a variety of techniques. The best undoped MWCNT samples were then scaled-up and purified. Commercially bought MWCNTs were also purified. These purified materials were then loaded with palladium using a MOCVD method at two different loading concentrations. These products were characterized and compared by TEM, SEM, EDX, BET and inductively coupled plasma optical emission spectroscopy (ICP-OES).

3.3 Outline of this dissertation

This dissertation has been structured as follows:

Chapter 1

A review of the background, synthesis, properties and applications of CNTs is given.

Chapter 2

The background, synthesis, properties and use of Pd/CNTs and bimetallic catalysts in hydrogenation reactions is discussed in this chapter.

Chapter 3

This chapter contains a motivation for this study, the objectives and the outline for the project.

Chapter 4

This chapter includes the reagents, gases and chemicals used for catalyst synthesis. A description of the equipment and the methodology for catalyst synthesis and the catalyst characterization techniques used are also given.

Chapter 5

A description of the reagents, gases and chemicals used, the equipment and reactor design and the methodology for the synthesis of undoped MWCNTs and SCNMs with ferrocene as the catalyst are given in this chapter. The chapter also includes characterization techniques used on synthesized MWCNTs/SCNMs and the results collected from the analyses, as well as a discussion of the effects of temperature and concentration on the synthesized materials. Three purification methods are also compared.

Chapter 6

Unlike Chapter 5 (which discusses MWCNTs and other SCNMs synthesized from ferrocene), this chapter looks at the introduction of heteroatoms in the catalysts and their effects on MWCNT/SCNM synthesis. A discussion of the results obtained from the variation of temperature and concentration of catalysts is also given.

Chapter 7

This chapter describes the reagents and chemicals used, the equipment and reactor design, and the methodology for the MOCVD preparation of Pd/CNTs from as-synthesized and commercial MWCNTs at 5 and 10 wt.% loadings. A comparative discussion for these products is also given.

Chapter 8

The Conclusions section discusses the fulfilment of the stated objectives.

Finally, the Future Work section briefly discusses the scope of possible research avenues stemming from this research.

References

- 1 A. A. Deshmukh, S. D. Mhlanga and N. J. Coville, *Mat. Sci. Eng. R*, 2010, **70**, 1

CHAPTER 4

SYNTHESIS OF CATALYSTS

This chapter includes a brief background on the catalysts chosen for this project and their experimental synthesis, as well as their characterization techniques. Lastly, spectral evidence for the formation of these catalysts is provided and plausible mechanisms for some of these reactions are proposed.

4.1 Introduction to the catalysts chosen for MWCNT and other SCNM synthesis

Derivatives of ferrocene, or even ferrocene itself, have a wide range of applications. These include antiknock agents in petrol combustion engines,¹ anticancer medicines² and even polymers containing the ferrocenyl moiety.³ Some of these polymers are useful in biosensors, immunosensors and sensors for CO₂ gas.⁴ As was discussed in **Chapter 1, Section 1.7.1.1**, ferrocene and related compounds have been found to be excellent catalysts for the formation of MWCNTs and other SCNMs. However, derivatized ferrocene compounds, as CNT-formation catalysts, are markedly poorly found in the literature. For this reason ferrocene itself and, for comparison, three other ferrocene derivatives were chosen for this project. Notably, two of these derivative compounds are nitrogen-containing and one is sulfur-containing. After a thorough literature search, it has been concluded, to the best of our knowledge, that none of the three ferrocene derivative compounds have yet been reported as CNT-formation catalysts, or CNT catalysts as they will be referred to from here on, to date.

4.1.1 Ferrocene [1] and its derivatives

The two five-membered rings in ferrocene are aromatic, and thus ferrocene can react in a very similar manner to other aromatic compounds. Such reactions include electrophilic and nucleophilic substitutions.⁵ An example of the former is the reaction of ferrocene with an electrophile such as the acetyl group from compounds such as acetyl chloride and acetic anhydride. An example of the latter is the reaction with a nucleophile such as the iodo-group in methyl iodide. Iodoferrocene is useful in Suzuki cross-coupling reactions. Sometimes such reactions are performed by prior-lithiation of ferrocene, and thus compounds such as butyl lithium, give lithiated ferrocenes⁶ which are intermediates in Suzuki cross-coupling reactions.

Oxidation of ferrocene can result in salts of $[\text{Fe}(\text{C}_5\text{H}_5)_2]^+$, depending on the oxidizing agent(s). For example, when ferrocene is oxidised by nitrosonium tetrafluoroborate, ferrocenium tetrafluoroborate, $[\text{Fe}(\text{C}_5\text{H}_5)_2]\text{BF}_4$, is produced.⁷ This compound is commonly used as part of a redox pair, or a ferrocene/ferrocenium couple, and is commonly used as a reference electrode in electrochemistry in the place of the standard hydrogen electrode. Ferrocenyl imidazolium

salts can be ionic liquids,⁸ as well as precursors to *N*-heterocyclic carbenes for use in homogeneous catalysis.⁹

Phosphorous derivatives of ferrocene, such as 1,1'-bis(diphenylphosphino)ferrocene, which is commercially available, can be prepared by first lithiating ferrocene in the presence of tetramethylethylenediamine, a compound with an affinity for lithium ions, and then reacting it with chlorodiphenylphosphine.¹⁰

The three derivatives of ferrocene that were chosen for this project are ferrocenoyl imidazolid (compound [3]), (*N*-phenylcarbamoyl)ferrocene (compound [4]) and *S,S*-bis(ferrocenylmethyl)dithiocarbonate (compound [5]). The structure of each of these three compounds is shown in **Figure 4.1** as well as that of ferrocene (compound [1]) and a precursor compound (compound [2]). Individual compounds will be discussed in the subsequent sections that follow.

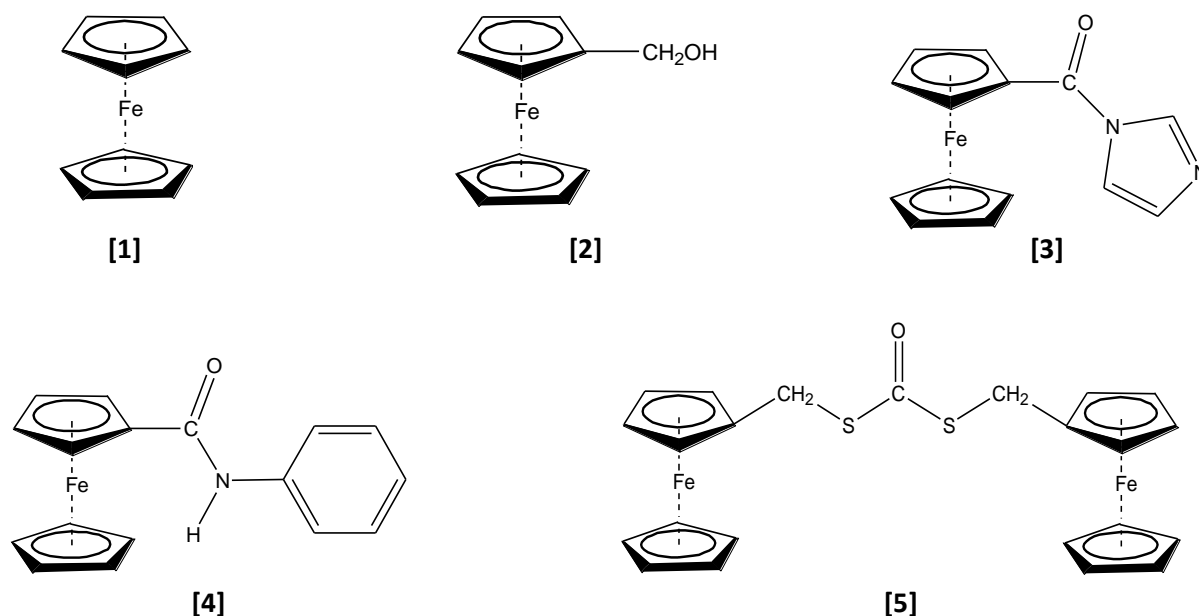


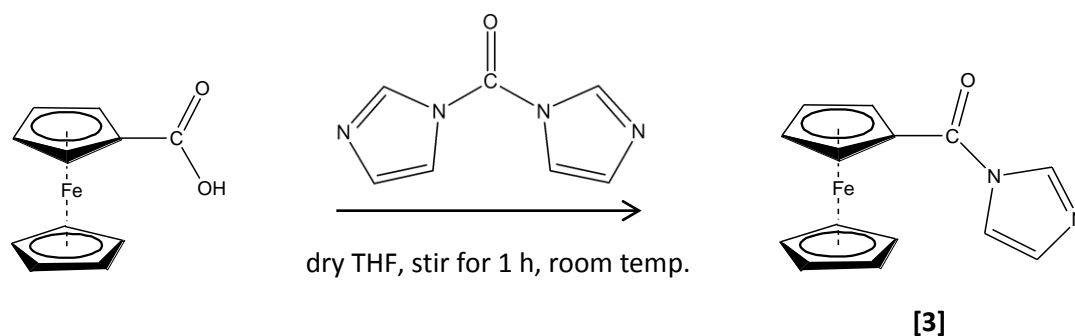
Figure 4.1 The structures of compounds [1] to [5].

4.1.2 Ferrocenoyl imidazolid [3]

Ferrocenoyl imidazolid, a red solid at room temperature, was first synthesized by Imrie *et al.*¹¹ This compound, when pure, is stable at temperatures below 5 °C in air. The same authors used ferrocenoyl imidazolid as a source of the ferrocenoyl moiety in other reactions. Such reactions include the synthesis of esters, and the reaction of thiophenolate salts with the ferrocenoyl moiety to yield ferrocenoyl phenyl sulfide. The ferrocenoyl moiety has applications in derivatives for liquid crystals¹² and possible medical^{13,14} applications.

Ferrocenoyl imidazolid is relatively easy to prepare in high yield, following the reaction given in **Scheme 4.1**. The reaction time mentioned in the literature was only 1 h, and this gave a yield over 60%. Coupled with its stability, this compound is an excellent precursor in other

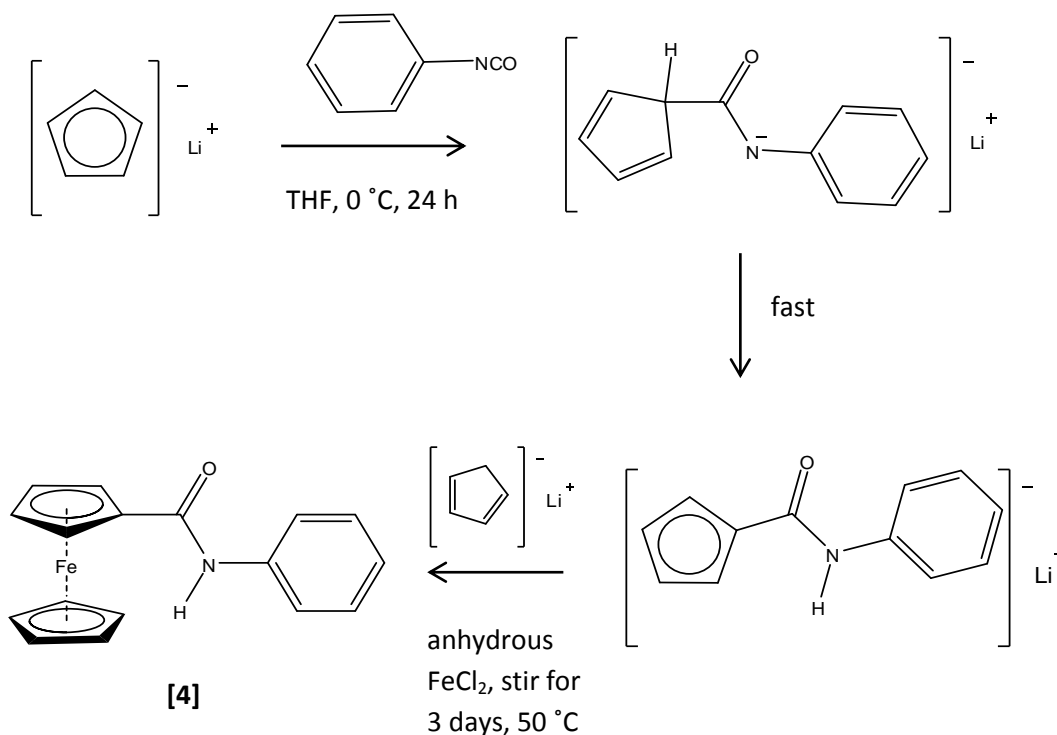
reactions. For the purposes of this project, this compound was used to study the effects of heteroatoms (oxygen and nitrogen) in CNT synthesis and also as a starting material in the synthesis of compound [4].



Scheme 4.1 The reaction involved in the synthesis of compound [3].¹¹

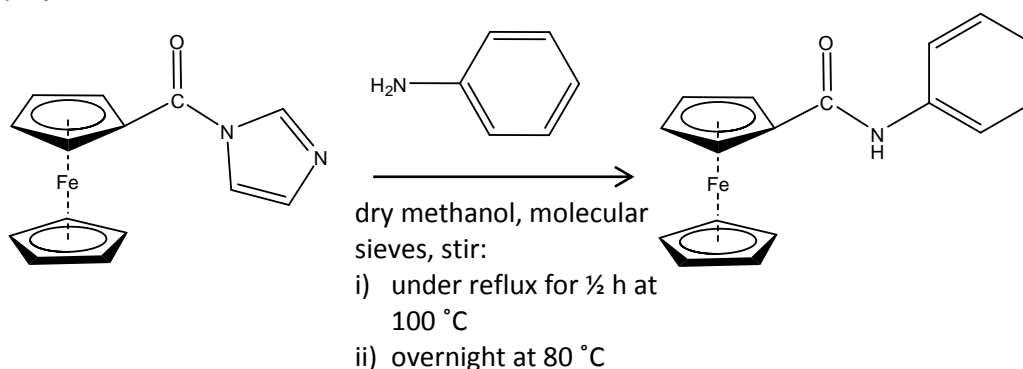
4.1.3 (*N*-Phenylcarbamoyl)ferrocene [4]

Compound [4] was first synthesized by Oberhoff *et al.*, who reported their findings in 1996.¹⁵ They synthesized this compound using the reactions shown in **Scheme 4.2**.



Scheme 4.2 The reaction involved in the synthesis of compound [4].¹⁵

The refluxing of compound **[3]** with aniline in anhydrous methanol is a more facile method for producing compound **[4]** than that in **Scheme 4.2** and, hence, it was decided to use this alternative synthesis method. Also, this method is less time-consuming than the one shown in **Scheme 4.2**. **Scheme 4.3** shows the reaction involved for the synthesis of compound **[4]** in this project.



Scheme 4.3 The reaction involved in the synthesis of compound **[4]** in this project.

This compound was characterized and the results compared well with those of Oberhoff *et al.*¹⁵ It is interesting to note, however, that several compounds have this structure as part of a larger compound¹⁶⁻²⁰ (**Figure 4.2**) with the phenylamide side group appearing twice on the bisferrocenyl moiety¹⁵ as seen in **Figure 4.2 (a)**, or in a more complex structure such as the ring structure created from ether groups in **(b)**.¹⁹

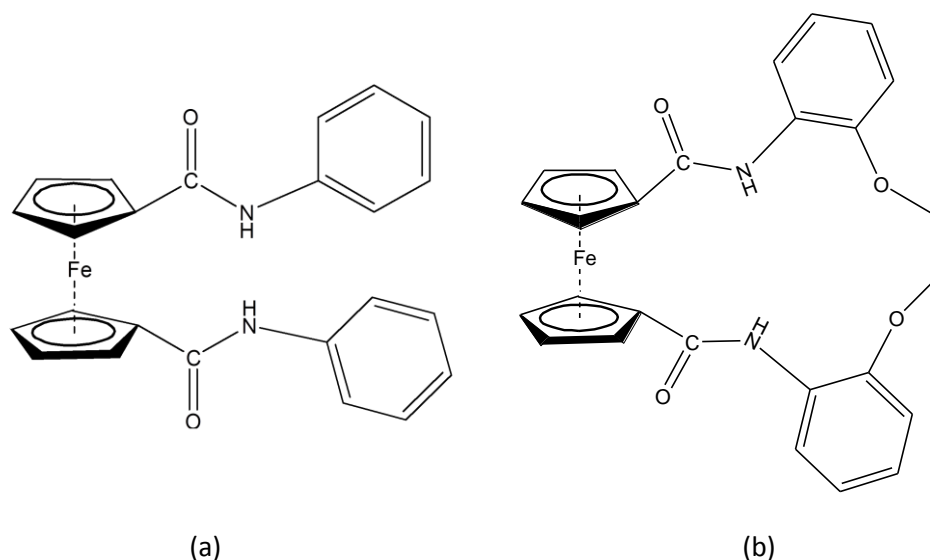


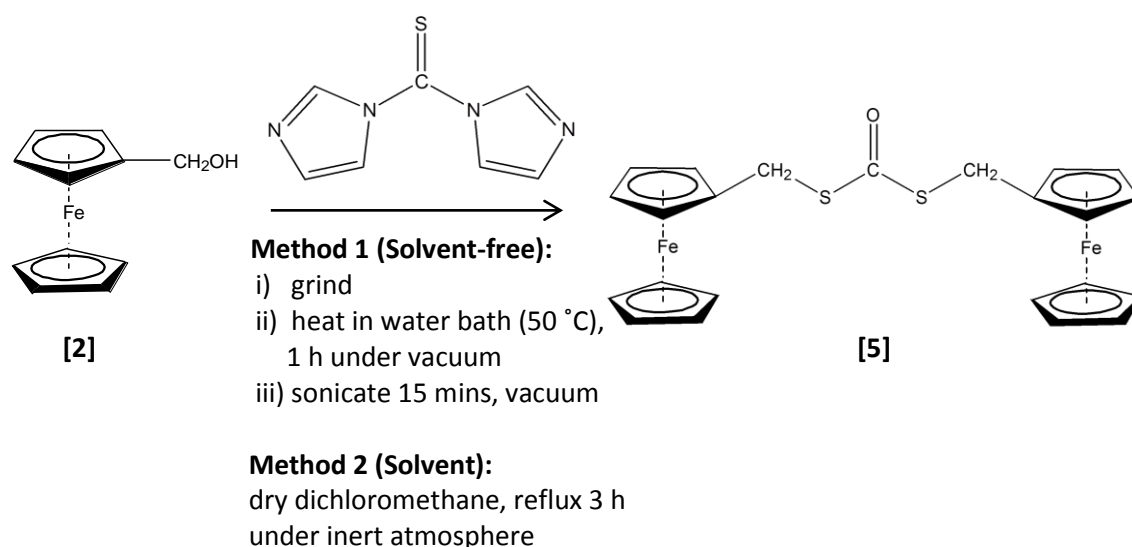
Figure 4.2 The structures of two ferrocene compounds known to contain the phenylamide moiety where (a) is 1,1'-bis(*N*-phenylcarbamoyl)ferrocene¹⁵ and (b) is 1,1'-[1,2-ethanediylbis(oxy-2,1-phenyleneiminocarbonyl)]ferrocene.¹⁹

The crystal structures for different conformations of the diphenylamide compounds, also known as bis(phenylamido)ferrocenes, are known.¹⁶ Compounds containing moieties of ferrocene coupled to a secondary phenyl amide have been shown to act as anion sensors in organic solvents and this topic has been reviewed.¹⁷

Compound [4] is comparable to compound [3] in terms of the types of heteroatoms (nitrogen and oxygen) present. The effect of different catalyst sources, containing the same types of heteroatoms, on the synthesis of MWCNTs, was investigated. Also, [3] contains two nitrogen atoms, whereas [4] contains only one. The effects from this difference was also investigated. Since sulfur is another heteroatom which is known to influence CNT and other SCNM formation, catalyst [5] was also investigated and will now be discussed.

4.1.4 *S,S*-Bis(ferrocenylmethyl)dithiocarbonate [5]

This compound was first reported by Onyancha *et al.*²¹ They synthesized it by using solvent-free and conventional solvent methods, the importance was that the former gave double the yield. Compounds of this nature, derivatives of the reaction between thiocarbonyl imidazoles and alcohols, have been used as reagents for alcohol deoxygenation.²² *N,N'*-Thiocarbonyldiimidazole and alcohols have also been reported in the synthesis of natural products.²² Compound [5] provides both oxygen and sulfur which makes it interesting to study in terms of the heteroatom effects on CNTs. Also, the effect of two Fe ions per compound is worth studying. When pure, the compound is fairly stable; however, it is synthesized in low yields when made by the reaction shown in **Scheme 4.4**. This same procedure was followed to synthesize compound [5] in this project. Ferrocenylmethanol (compound [2]), in the reaction in **Scheme 4.4**, was prepared from ferrocenecarboxaldehyde by using a reducing agent (LiAlH_4). In this project both a solvent and solvent-free approach to the synthesis of compound [5] was used, just as Onyancha *et al.* did.²¹ In the solvent approach compound [2] was refluxed with *N,N'*-thiocarbonyldiimidazole in anhydrous dichloromethane and in the solvent-free approach these same two reactants were ground together and then heated and sonicated under vacuum to maximize reactant particle interaction.



Scheme 4.4 The reactions involved in the synthesis of compound [5].²¹

The general procedures, chemicals, reagents, solvents and gases used in the synthesis of compounds [2] to [5] are discussed in the next section.

4.2 General procedures

4.2.1 Cleaning of glassware

Common laboratory glassware was washed in soapy water with scrubbing, rinsed with tap water, followed by acetone and water again. A final rinse with a small portion of distilled water and heating in air in an oven at 110 to 120 °C for at least half an hour ensured an adequate level of dryness for many procedures. In the case of water-sensitive reagents, such as lithium aluminium hydride, glassware was left to dry in the oven for a minimum of an hour before cooling and use. Acetone-rinsed and oven-dried glassware was also used for hygroscopic solvents such as freshly dried THF.

4.2.2 Drying of solvents

Solvents used in catalyst synthesis were distilled before use in all cases where necessary. However, occasionally crude solvent was used when a high level of purity was not required, for example, for isolating and purifying products by column chromatography.

4.2.2.1 Preparation of anhydrous diethyl ether

Crude diethyl ether was stored over sodium wire²³ for approximately a week to dry, and then freshly distilled over CaH₂ when needed.

4.2.2.2 Preparation of anhydrous hexane²⁴

Crude hexane was stored over sodium wire for approximately a week to dry, and then freshly distilled over CaH₂ when needed.

4.2.2.3 Preparation of anhydrous dichloromethane²³

Dichloromethane was distilled under an inert atmosphere (dry N₂) from CaH₂ at 40-41 °C, tapped into an oven-dried glass container with a glass stopper and was used immediately. Excess CH₂Cl₂ was stored over activated 3 Å molecular sieves.

4.2.2.4 Preparation of anhydrous tetrahydrofuran (THF)²⁵

THF was stored over sodium wire for approximately a week. Benzophenone was then added to the THF and refluxed under an inert atmosphere (dry N₂) until the reaction mixture turned a dark blue colour. At this point THF was distilled off under dry N₂, collected and stored in a glass stoppered flask for immediate use.

4.3 Common laboratory chemicals, reagents, solvents and gases

Chemicals (non-solvent/reagent)

- anhydrous magnesium sulfate (Saarchem, Merck, South Africa, 62-70%)
- benzophenone (BDH Laboratory Reagents, England, min. 99%)
- Na wire (Riedel-de Häen, Germany, 99.5%)
- silica gel self-indicating (Merck, South Africa, CP grade, particle size < 2.5 mm max. 10%, > 6.3 mm max. 10%)
- calcium chloride (Sigma-Aldrich, Germany, -4+30 mesh, technical grade)
- molecular sieves (Acros Organics, USA, mixture of 3Å and 4 to 8 mesh)

Reagents

- ferrocene (Merck, Germany, > 98%)
- ferrocenecarboxaldehyde (Aldrich, Germany, 98%)
- lithium aluminium hydride (LAH) (Aldrich, Germany, 95%)
- ethyl acetate (Rochelle Chemicals, South Africa, 99%)
- *N,N'*-thiocarbonyldiimidazole (also called 1,1-thiocarbonyldiimidazole), (Fluka, Sigma-Aldrich, Switzerland, ≥ 95.0%)
- ferrocene monocarboxylic acid (Fluka, USA, ≥ 97.0%)
- *N,N'*-carbonyldiimidazole (Fluka, Japan, ≥ 97.0%)
- aniline (Saarchem, South Africa, min. 99%)

Solvents

The solvents listed below were used either as crude, CP or AR grade, depending on the application. Crude solvents were used for column elution, TLC analysis and washing. Where possible distilled and dried CP grade, or higher grade, was used for reaction mixtures and recrystallization techniques.

- diethyl ether (Associated Chemical Enterprises, South Africa, min. 99.5%)
- dichloromethane (Shalom Lab. Supplies c.c., South Africa, crude)
- hexane (Merck, UniLab, CP grade)
- tetrahydrofuran (Merck, South Africa, min. 99.5%)
- deuterated chloroform (Aldrich, USA, 99.8 atom % D)
- acetone (Protea Chemicals, South Africa, crude)
- acetonitrile (Merck, Germany, > 99.9%)
- methanol (BDH Chemicals Ltd, England, 99.8%)

Gases

- ultra high purity Ar (Afrox, South Africa, 99.999-100%, O₂ ≤ 3 ppm, moisture ≤ 2 ppm)
- ultra high purity N₂ (Afrox, South Africa, 99.999-100%, O₂ ≤ 3 ppm, moisture ≤ 3 ppm)

A dry N₂ or Ar atmosphere was used for the synthesis of catalysts where possible. When an inert atmosphere was not used, this is mentioned.

All reagents and gases were used as supplied by the manufacturer, unless otherwise stated. Recrystallizations were all performed under ambient conditions.

For column chromatography silica gel 60 (Merck, Germany, 0.040-0.063 mm) or aluminium oxide 90 active neutral (Merck, Germany, 70-239 mesh ASTM) was used. Thin layer chromatography (TLC) was performed on aluminium-backed silica gel 60 (Merck, Germany, F₂₅₄) plates.

4.4 Characterization of catalyst compounds

4.4.1 Melting point (m.p.) determination

Melting points were determined on a Gallenkamp melting point apparatus (England) and are uncorrected.

4.4.2 Infrared spectroscopy (IR)

Attenuated total reflectance (ATR) is a Fourier transform infrared (FTIR) method requiring little to no sample preparation – for example, solids, liquids and gases can be analyzed directly and thus it is a solventless method. This method involves the passage of infrared waves into the sample and changes in the totally internally reflected beam are monitored and measured. Total internal reflection produces an evanescent wave in a crystal which acts as a platform for the sample. This wave also extends into the sample on the crystal “platform”. This wave is altered where it is absorbed by the sample. Such studies were carried out by using a Perkin Elmer Spectrum 100 spectrometer. The Perkin Elmer Spectrum Multimedia software was used to manipulate the spectra obtained.

4.4.3 Nuclear magnetic resonance spectroscopy (NMR)

An automated Bruker 400 MHz B-ACS-60 nuclear magnetic resonance spectrometer was used to measure ¹H- and ¹³C-NMR spectra in deuterated chloroform (CDCl₃). The number of scans, by default, was 16 and 1024 respectively, depending on the concentration of the sample solution. Bruker TOPSPIN 2.1 software was used to manipulate the data and spectra generated. No external addition of tetramethylsilane (TMS) was used as internal standard; however, chemical shift values were calibrated by using the solvent peak values relative to TMS. *J*-values are expressed in hertz (Hz).

4.4.4 Mass spectrometry (MS)

Electron ionization, a hard ionization, i.e. fragmentation of the mother compound and its daughter fragments, by the removal of an electron(s), i.e. the negative mode, was performed for compounds [2] to [5]. Firstly the compounds were subjected to gas chromatography by use of an Agilent 6890 series gas chromatograph (HP 19091J-433 HP-55% phenylmethylsiloxane column of dimensions 30.0 m x 250 μm x 0.25 μm, split ratio of 20.0:1

injection, with a He flow rate maintained at 1.0 mL/min). For each compound, a small sample was dissolved in a suitable solvent and a 1 μ L injection volume introduced to the column at 250 °C, passed into the column which was held at 70 °C for 1 minute, ramped to 260 °C at a rate of 10 °C/min and then held at the maximum temperature for 10 minutes. This column was coupled to an Agilent 5973 Network Mass Selective Detector, run at a voltage of 1835 V. Instrument parameters were controlled by using the Agilent Chem Station software and the Enhanced Data Analysis software was employed to generate mass spectra.

High resolution electrospray ionization, a soft ionization technique where protonation of the mother compound occurs to yield a mass +1 greater than the compound under analysis, i.e. the positive mode, without fragmentation, was done for compound [4]. This compound was analyzed at the University of the Witwatersrand by using a Thermo Electron DFM instrument in the positive mode and data viewed using Thermo Xcalibur software. Compound [5] was analyzed by a technician at the University of KwaZulu-Natal by using a Bruker micrOTOF Q II mass spectrometer in the positive mode. Programmes were set and results viewed using micrOTOF control software.

4.4.5 Elemental analysis

The chemical composition of catalyst [4] was determined on a LECO CHNS-932 elemental analyzer, standardized with acetanilide.

4.4.6 X-ray diffraction (XRD) studies

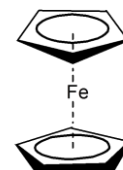
Crystals of compound [4] were grown in toluene and analyzed using a Bruker Smart Apex II CCD diffractometer with graphite-monochromated Mo K α radiation. Data reduction was performed by using the SAINT-Plus program, version 7.34A and XPREP.²⁷ The program SADABS was used to perform multiscan adsorption corrections. Direct methods were used to solve the structure by using the SHELXS-97 program. Non-hydrogen atoms were refined isotropically and then anisotropically using a full-matrix least-squares calculation. All hydrogen atoms were placed geometrically, then refined subject to geometrical restraints and finally allowed to ride on the host carbon. The program ORTEP3 was used to compute the graphics of the molecule.²⁸

4.5 Catalyst synthesis and characterization

Detailed synthesis of catalysts is described in **Sections 4.5.1 to 4.5.5**. Characterization of these products was carried out by using melting point determination, ¹H-NMR, ¹³C-NMR, IR studies, and mass spectrometry. (See **Appendices A, B, C and D** respectively for spectra from the latter four techniques.) Compound [4] was also characterized by elemental analysis and XRD. Since ferrocene was itself a catalyst, and since it is readily available, the report in **Section 4.5.1** merely discusses the recrystallization of ferrocene to ensure high purity.

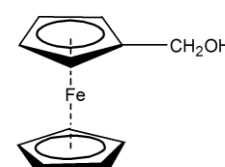
4.5.1 Recrystallization of ferrocene [1]

Approximately 5.00 g of ferrocene was dissolved in toluene, heated with stirring until complete dissolution was achieved, and then filtered under gravity to remove insoluble contaminants. Further evaporation of solvent, and then cooling, afforded orange crystals of pure ferrocene in solution. These were filtered through a Büchner funnel *in vacuo* and allowed to dry under vacuum for approximately 45 minutes. NMR and m.p. (174 °C) results are consistent with those in literature.²⁶

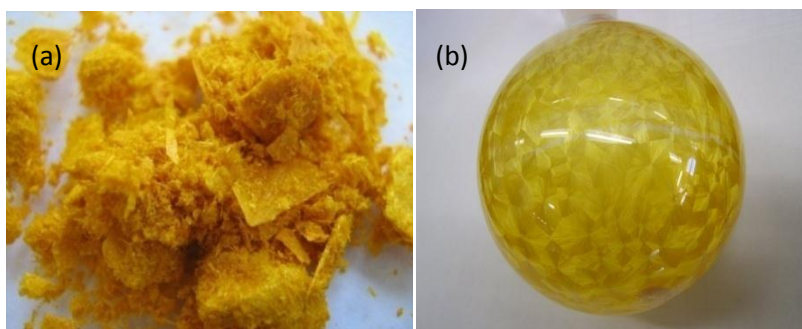


4.5.2 Ferrocenylmethanol [2]²⁹ - a starting product for *S,S*-bis(ferrocenylmethyl)-dithiocarbonate

Ferrocenecarboxaldehyde (16.00 g, 74.75 mmol) was dissolved in anhydrous diethyl ether (Et₂O) (100 cm³) and this solution was then transferred into a pressure-equalizing separating funnel. This separating funnel was stoppered and attached to a two-necked round-bottomed flask,

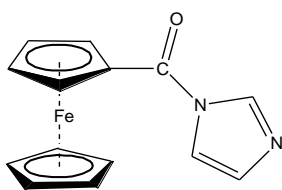


to which was also attached a condenser. A CaCl₂ drying-tube was fitted to the condenser. The ferrocenecarboxaldehyde solution was added drop-wise, while stirring, to a mixture of excess lithium aluminium hydride (LAH) and approximately 100 cm³ of anhydrous Et₂O in the round-bottomed flask. After the complete addition of the solution, heat was applied to provide a gentle reflux, which was allowed to occur for 2 h after which the heat was switched off and the solution left to stir overnight. The round-bottomed flask was then placed in an ice-water bath. Crude ethyl acetate (EtOAc) was slowly added to the reaction mixture to destroy excess LAH, followed by the careful drop-wise addition of ice-cold water. The resulting mixture was then washed with H₂O (6 x *ca.* 200 cm³) in a separating funnel and the bottom aqueous layer discarded along with some decomposed material. The organic layer was left in a closed container with a generous portion of drying agent (anhydrous MgSO₄) before being filtered under gravity. The filtrate was then concentrated *in vacuo* and subjected to column chromatography on silica gel. Six yellow-orange solutions were collected by eluting with hexane: Et₂O (80:20) and gradually increasing the Et₂O concentration to 100%. TLC revealed that solution one contained unreacted ferrocenecarboxaldehyde and solution six had a R_f value different to ferrocenecarboxaldehyde and ferrocenylmethanol. This compound was not identified. However, solutions two to five were identical in terms of R_f value. Thus, these solutions were combined and concentrated *in vacuo* until long, fine needles of yellow, crystalline product formed (see **Figure 4.3**). The product was left to dry further overnight under vacuum and gave IR, ¹H- and ¹³C-NMR data similar to literature.²⁹ Yield (11.26 g, 70%); m.p. 73-76 °C (lit.²⁹ 76 °C); IR (cm⁻¹) 3226, 2930, 1104; ¹H-NMR (CDCl₃) 4.31 (2H, d, *J* 5.8, CH₂), 4.22 (2H, t, *J* 1.7, C₅H₄), 4.16 (5H, s, C₅H₅), 4.15-4.16 (7H, m, *J* 1.9, C₅H₅ and C₅H₄); ¹³C-NMR (CDCl₃) 88.65; 68.51; 68.49; 68.08; 60.93; m/z (EI) 216 (M⁺, 87%), 138 (100), 73 (18), 121 (13), 56 (11), 186 (6).

**Figure 4.3**

Photographs of ferrocenylmethanol **[2]** (a) on filter paper and (b) in a round-bottomed flask.

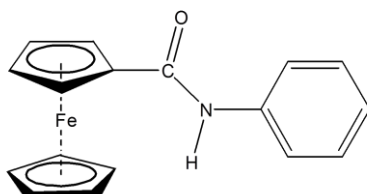
4.5.3 Ferrocenoyl imidazole **[3]**¹¹

**Figure 4.4**

Photograph of ferrocenyl imidazole **[3]** in powdered form.

N,N'-Carbonyldiimidazole (1.50 g, 9.25 mmol) was dissolved in anhydrous THF (70 cm³) and this solution was added to a solution of ferrocene monocarboxylic acid (2.00 g, 8.70 mmol) in anhydrous THF (30 cm³). The mixture was stirred at room temperature (RT) for 24 h under an inert Ar atmosphere, followed by concentration to approximately 10 cm³ on a rotavapour. The concentrated solution was then rapidly eluted (by vacuum) with Et₂O through a column of silica gel, leaving a green-black layer of decomposed material at the top of the column. This was followed by concentration to dryness and vacuum drying. Red-orange crystals were obtained (see **Figure 4.4**). Yield (2.02 g, 83%); m.p. 120-121 °C (lit.¹¹ 121-122 °C); IR (cm⁻¹) 3123, 3079, 2722, 1677, 1525, 1378, 1360, 1299, 1200, 1097, 1073, 1048, 1019, 1000, 818, 747, 655; ¹H-NMR (CDCl₃) 8.38 (1H, s, NCH), 7.65 (1H, s, NCH), 7.11 (1H, s, NCH), 4.92 (2H, t, *J* 1.7, C₅H₄), 4.63 (2H, t, *J* 1.7, C₅H₄), 4.27 (5H, s, C₅H₅); ¹³C-NMR (CDCl₃), 169.15, 137.39, 130.36, 117.78, 73.11, 72.09, 71.83, 70.85; *m/z* (EI) 280 (M⁺, 100%), 213 (48), 185 (61), 129 (34), 119 (29), 56 (20), 161 (7).

4.5.4 (*N*-Phenylcarbamoyl)ferrocene **[4]** - also known as *N*-phenylferrocenyl-imidic acid or *N*-phenylferrocenylamide or *N*-phenylferrocenecarboxamide



Ferrocenoyl imidazole, compound **[3]**, (0.500 g, 1.79 mmol) and freshly distilled excess aniline were placed in a round-bottomed flask. To ensure complete dissolution of the solid reactant, approximately 1.5 cm³ of freshly dried and distilled methanol (MeOH) was added. The mixture was left to reflux at 105 °C for 30 minutes over 220 mg activated molecular sieves (mixture of 3Å and 4 to 8 mesh) and dried under Ar to drive off any H₂O. A further 1 cm³ of MeOH was added



Figure 4.5

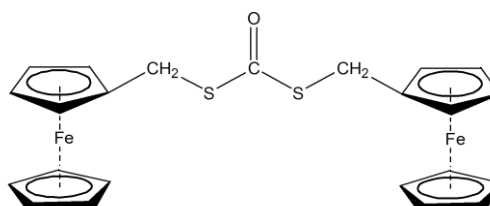
Photograph of compound [4] in a glass vial.

and the solution left to stir overnight under gentle heating in the inert atmosphere. The following day excess and unreacted aniline and black, polymerized aniline and black decomposed ferrocenyl imidazolidine was decanted after a third addition of *ca.* 0.5 cm³ MeOH. The solid left behind was allowed to dry *in vacuo* overnight. A pale orange-yellow powder formed (refer to **Figure 4.5**) and was identified as the amide derivative of compound [3]. Yield (0.151 g, 28%); m.p. 208–210 °C (lit.¹⁵ 208 °C); IR (cm⁻¹) 3293, 1639, 1595; ¹H-NMR (CDCl₃) 7.57 (2H, d, *J* 7.8, Ph), 7.34 (2H, t, *J* 7.9, Ph), 7.11 (1H, t, *J* 7.3, Ph), 4.76 (2H, t, *J* 1.8, C₅H₄), 4.41 (2H, t, *J* 1.9, C₅H₄), 4.24 (5H, s, C₅H₅); ¹³C-NMR (CDCl₃) 168.80, 138.33, 129.32, 124.26, 119.98, 76.46, 71.13, 70.10, 68.48; m/z (EI) 305 (M⁺, 100 %), 213 (72), 185 (35), 129 (24), 119 (19), 56 (10), (HR-ESI) Calc. 306.05813 for C₁₇H₁₆OFeN, Found. 306.05814 C₁₇H₁₆OFeN; CHN (mass %) Found (Calc.) C 65.81 (66.91), H 5.06 (4.95), N 4.36 (4.59).

4.5.5 *S,S*-Bis(ferrocenylmethyl)dithiocarbonate [5]²¹ - also known as *S,S*-bis(ferrocenylmethyl)carbonodithioate

Method 1 – solvent free

Ferrocenylmethanol (2.00 g, 9.26 mmol) and *N,N'*-thiocarbonyldiimidazole (2.00 g, 11.2 mmol) were ground together, at RT, using a glass rod in a Pyrex[®] tube fitted with a ground glass joint. The grinding action resulted in an orange-brown melt.



The reaction mixture was then placed under vacuum and left to heat gently in a constant temperature water bath at 50 °C for about 1 h.

The Pyrex[®] tube was then stoppered and placed in a sonicator for *ca.* 15 minutes at RT. The resulting reaction mixture was placed under a high vacuum overnight and the next day loaded onto silica gel by first mixing the crude reaction mixture rapidly with a small volume of dichloromethane (DCM) and silica gel and evaporating the solvent off quickly with compressed air and then loading the resultant reactant mixture/silica powder onto a silica gel column. Hexane/Et₂O (9:1) was eluted through the column, gradually increasing the polarity until 100% Et₂O. Nine yellow-orange solutions were collected sequentially in different flasks by elution with hexane/Et₂O (9:1). TLC revealed that the solutions in flasks three through to eight contained a compound identical in terms of R_f value and so were combined and the compound identified as the product *S,S*-bis(ferrocenylmethyl)dithiocarbonate after concentration and drying under vacuum. (Unreacted ferrocenylmethanol was recovered from the top of the column by washing the used silica gel with DCM and concentrating under vacuum. Prior to this, a brown oil was also collected from the column although this was not characterized. Some of the loaded mixture decomposed at the top of the column and could be seen as a brown-green immovable layer.)

The *S,S*-bis(ferrocenylmethyl)dithiocarbonate product (see **Figure 4.6**) was isolated as a yellow solid with similar spectral data to Onyancha *et al.*²¹ Yield (0.299 g, 13%); m.p. 163-164 °C (lit.²¹ 165 °C); IR (cm⁻¹) 3092, 2931, 1694, 1634, 1466, 1406, 1243, 1211, 1104, 1037, 1024, 998, 924, 872, 807, 684, 568; ¹H-NMR (CDCl₃) 4.17 (4H, t, *J* 1.7, C₅H₄), 4.14 (10H, s, 2 x C₅H₅), 4.10 (4H, t, *J* 1.7, C₅H₄), 4.03 (4H, s, 2 x CH₂); ¹³C-NMR (CDCl₃) 189.45, 83.69, 69.04, 68.95, 68.46, 31.12; *m/z* (ESI) Found. 490.98843 (M⁺, 100%) for C₂₃Fe₂H₂₂O₁S₂, Calc. 489.98109 for C₂₃Fe₂H₂₂O₁S₂.



Figure 4.6

Photograph of compound [5] on filter paper.

Method 2 – with solvent

Ferrocenylmethanol (8.02 g, 37.1 mmol) and *N,N'*-thiocarbonyldiimidazole (8.10 g, 45.5 mmol) were added to anhydrous DCM (40 cm³) in a 250 cm³ two-necked round-bottomed flask. The solution was heated and allowed to reflux for 3 h under dry N₂. A dark orange solution formed. The reaction mixture was concentrated and subjected to column chromatography over silica gel. Hexane/Et₂O (9:1) was used as the eluting solvent, with a gradual increase to 100% Et₂O. Seven successive solutions were collected separately, the first yielding a yellow oily substance, the next five consecutive solutions yielding orange/yellow crystals, and the last a brown oil. Unreacted ferrocenylmethanol was recovered from the top of the column by washing the used silica gel with DCM and concentrating under vacuum. Solutions 2 to 5 were combined after TLC studies revealed that they had the same R_f value, and concentrated and dried under vacuum to give the yellow solid *S,S*-bis(ferrocenylmethyl)dithiocarbonate. Characterization of this compound is as for **Method 1** of **Section 4.5.5**. Yield (1.49 g, 15%).

4.6 Results and discussion

A brief discussion of selected spectra, and the most plausible mechanisms by which compounds [3], [4] and [5] form, is provided in the following **Sections 4.6.1** to **4.6.4**.

4.6.1 Ferrocenylmethanol [2]

An IR spectrum was run for the starting material of compound [2]. The prominent R₂C=O peak at 1684 cm⁻¹ for the aldehyde starting material was not evident in the IR spectrum of the methanol product, but a broad band between 3000 and 3400 cm⁻¹ appeared, with the maximum transmittance value at a wavenumber of 3226 cm⁻¹. [Refer to **Appendix C.1 (a)** and **(b)**.] This broad band corresponds to the stretching mode of the OH group while, on the other hand, there is the disappearance of the carbonyl group in the aldehyde and hence this confirms the formation of the product.

4.6.2 Ferrocenoyl imidazolid [3]

The $^1\text{H-NMR}$ spectrum of compound **[3]** shows a peak far downfield at 8.38 ppm (**Figure 4.7**). This peak corresponds to the most deshielded proton, which is bonded to the carbon atom between the two electronegative nitrogen atoms. This peak was assigned to H_a . Similarly, the peaks at 7.65 and 7.11 ppm were assigned to H_b and H_c respectively, since these protons are also both in the vicinity of an electron-withdrawing nitrogen atom. The five H_f , two H_e and two H_d protons fall within the range 4-5 ppm, giving the classic pattern of monosubstituted ferrocenyl moiety protons. The most downfield carbon peak, however, in **Figure 4.8**, was not attributed to C_b , but C_a , since C_a sits at a chemical shift typical of carbonyl carbons, as well as being attached to a nitrogen atom. Oxygen is more electronegative than nitrogen, and, typically, carbonyl carbon signals fall between 160 and 180 ppm for R-CONR_2 compounds.

Scheme 4.5 shows a plausible mechanism for the formation of compound **[3]** from its starting materials, as described in **Section 4.5.3**. The first step of the reaction involves the conjugate base of the ferrocene monocarboxylic acid behaving as a nucleophile, while the carbonyl group of the carbonyldiimidazole behaves as an electrophile. The nucleophile thus attacks the electrophilic centre. This nucleophilic addition is followed by a series of rearrangements. The preferential formation of CO_2 and the imidazole by-product drives the reaction, since these two substances are thermodynamically stable. Also, the desired product, ferrocenoyl imidazolid **[3]**, is fairly stable itself. Thus, the reaction achieves a high yield of 83%.

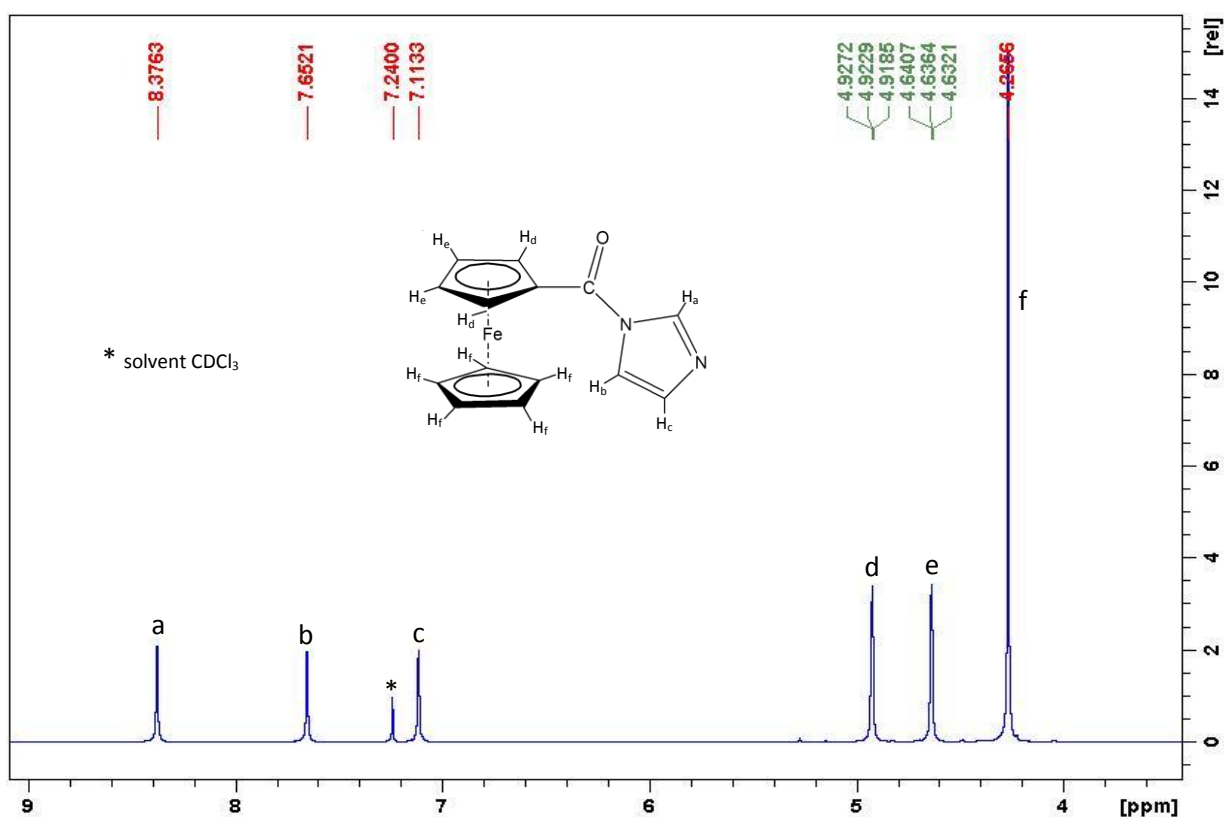


Figure 4.7 $^1\text{H-NMR}$ spectrum of compound **[3]**.

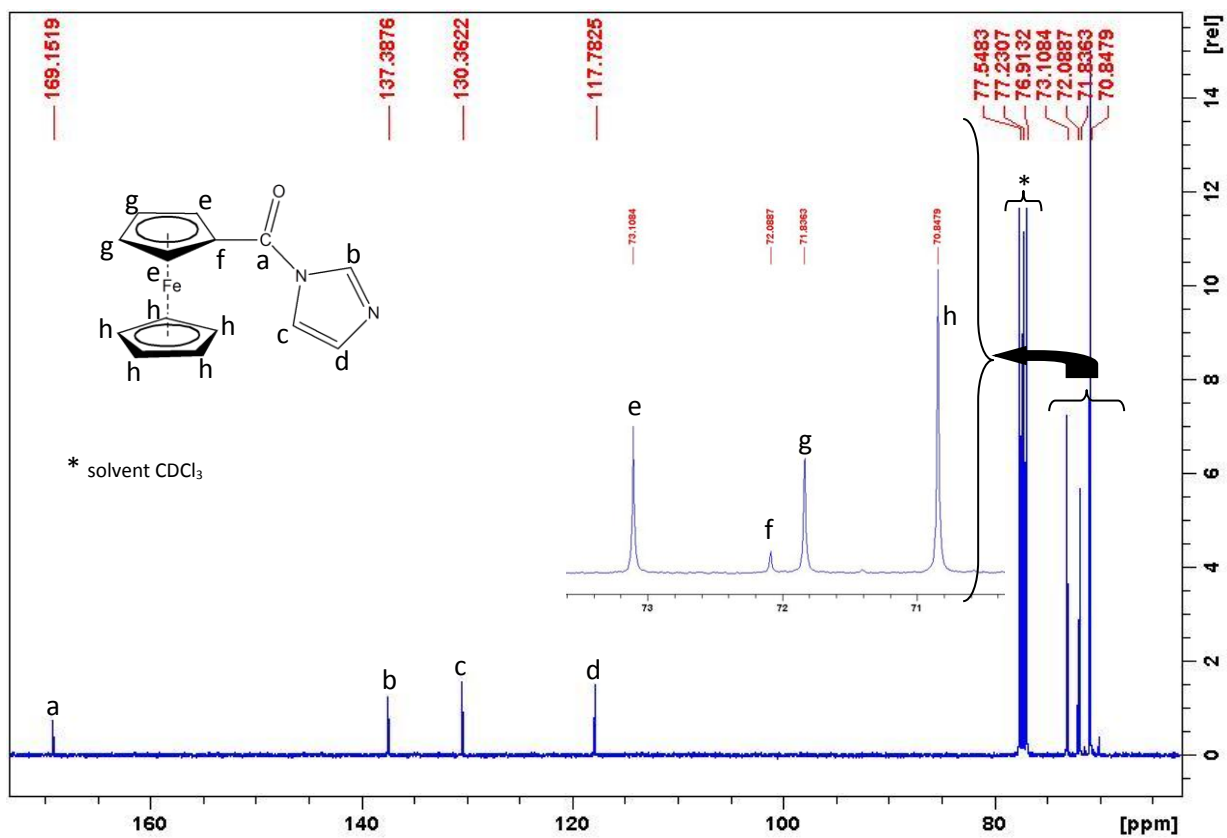
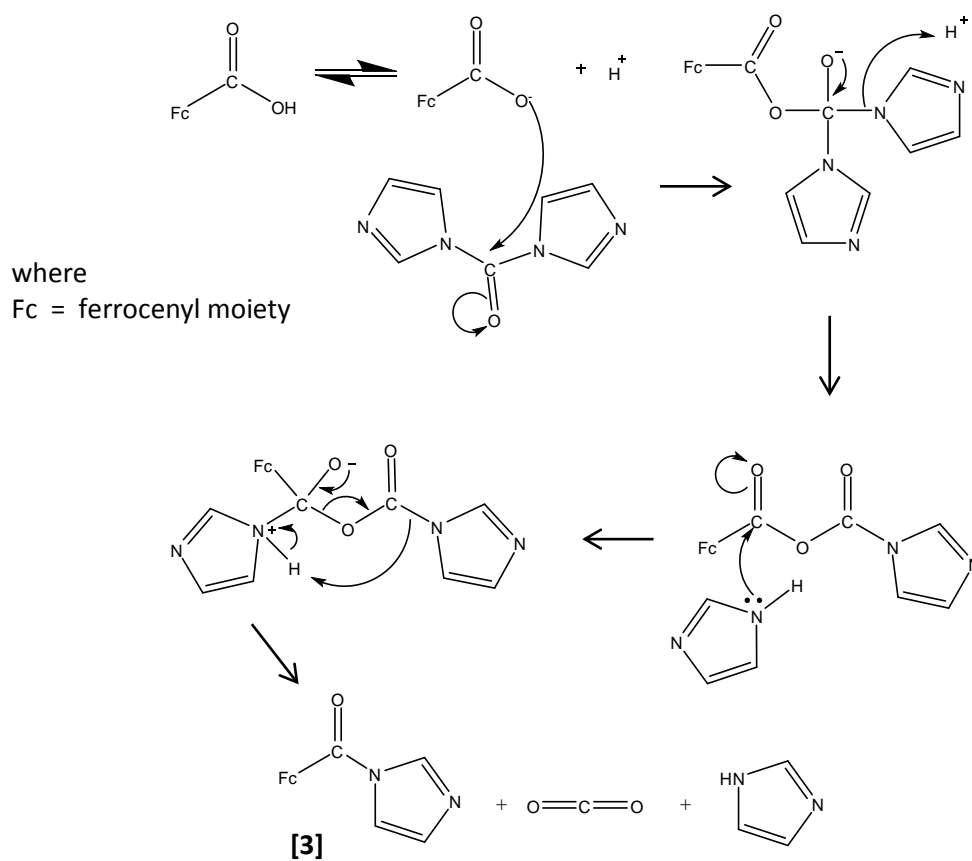


Figure 4.8 ^{13}C -NMR spectrum of compound [3].



Scheme 4.5 Plausible mechanism for the formation of compound [3].

4.6.3 (*N*-Phenylcarbamoyl)ferrocene [4]

The IR spectrum of compound [4] contained a peak at 3293 cm^{-1} (lit.¹⁵ 3294 cm^{-1}) assigned to an N-H stretch. (See **Appendix C, Figure C.3**.) Two prominent, sharp absorption peaks also occurred at 1639 and 1595 cm^{-1} (lit.¹⁵ 1643 and 1596 cm^{-1} respectively). The former was assigned to the carbonyl group of the amide moiety, while the latter was due to the aromatic carbon-carbon double bond vibration. This, coupled with the other characterization data in **Section 4.5.4**, and the XRD results following this, suggests that the compound exists as an amide in the solid state. Since it was deduced that this compound is a secondary amide, it is logical to assume it can undergo keto-enol type tautomerism in solution (see **Figure 4.9**). Also, the peak at 168.80 ppm in the ^{13}C -NMR spectrum (see **Appendix B, Figure B.3**) could be due to an imine carbon and the literature reports this for similar compounds.³⁰ Typically carbonyl carbons appear more downfield, but may produce signals near 168 ppm . Thus, solution IR studies would be beneficial in determining whether the amide or imine form (see **Figure 4.9**) predominates in solution, or whether a mixture exists.

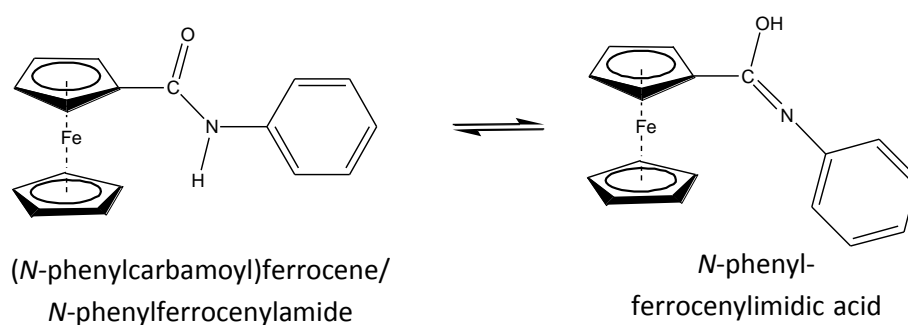


Figure 4.9 The resonance structures of compound [4] in solution.

The XRD results confirm that the compound exists as an amide in the solid crystalline state (see **Figure 4.10**). (For crystal structure data see **Table 4.2** at the end of this section.) In terms of intramolecular orientations, the cyclopentadienyl rings lie in an eclipsed conformation and are staggered at a small angle of 3.7° , the phenyl ring plane lies at 35.4° out of the plane of the amide group [N(1)-C(11)-O(1)-C(10)] and the amide group is twisted by 21.1° out of the plane of the C(6)-C(10) cyclopentadienyl ring. Bond lengths for this compound are consistent with literature.³¹ Refer to **Table 4.1**.

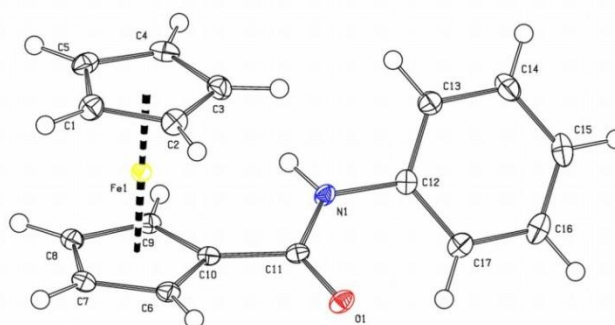
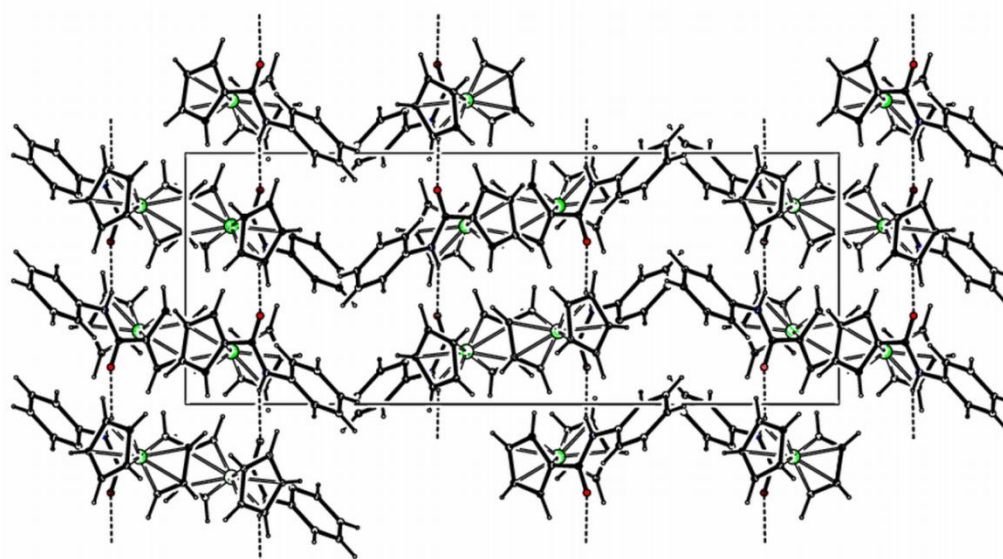


Figure 4.10 The ORTEP3 structure of compound [4].

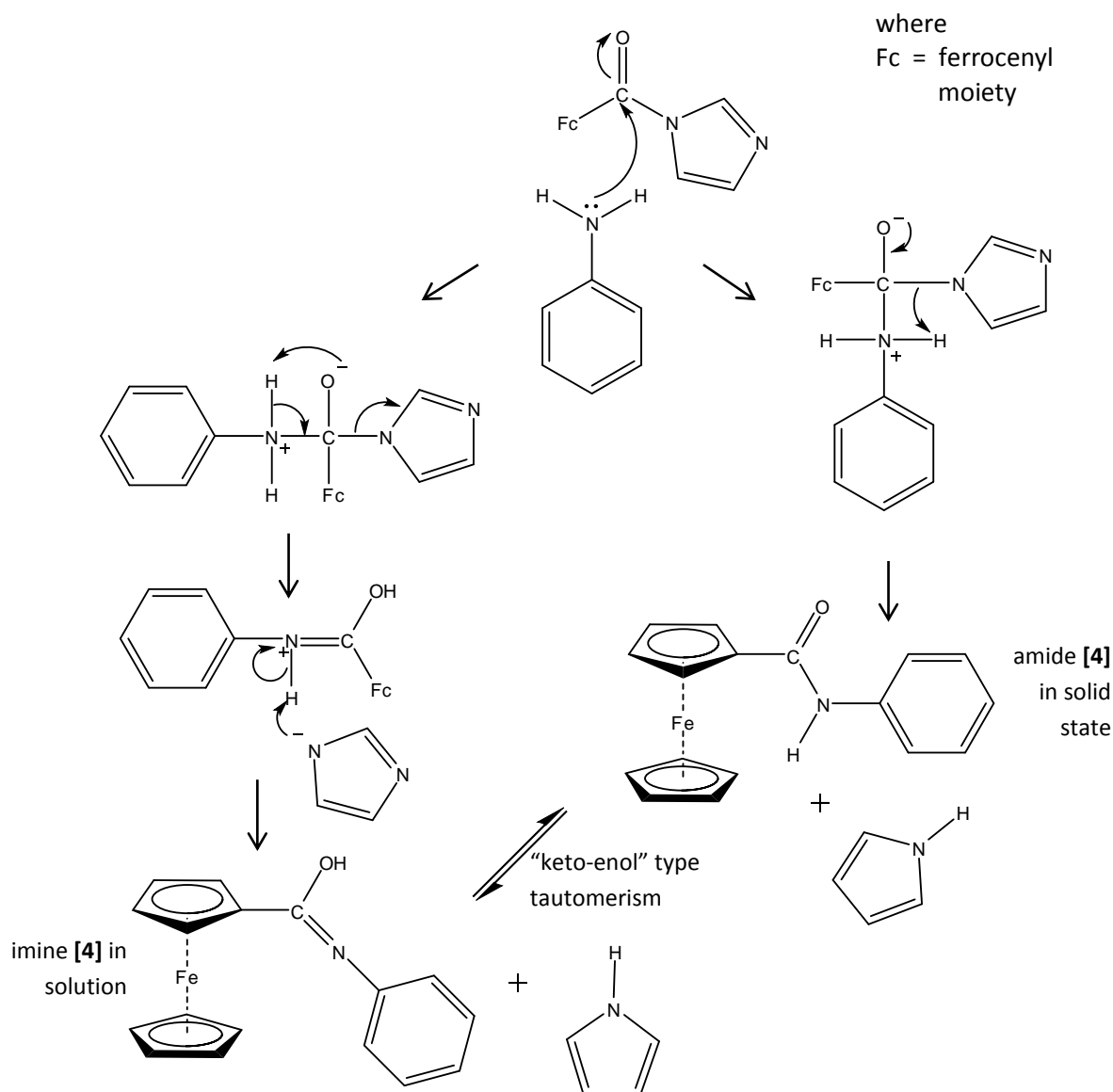
Table 4.1 Selected bond lengths and bond angles which are consistent with literature:³¹

Bond lengths (Å)		Bond angles (°)	
C(12)-N(1)	1.419 (17)	C(12)-N(1)-C(11)	126.33 (11)
C(11)-N(1)	1.363 (17)	C(10)-C(11)-O(1)	121.5 (12)
C(11)-O(1)	1.234 (16)	O(1)-C(11)-N(1)	123.7 (12)
C(10)-C(11)	1.482 (19)		
Fe(1)-C(10)	2.030 (14)		

In terms of intermolecular orientations and interactions, hydrogen bonds exist between O(1) and the H atom attached to N(1) of an adjacent molecule. The molecules are arranged head-to-tail forming chains along the *c*-axis while the packing of individual molecules to form a unit cell is shown in **Figure 4.11**. The hydrogen bond distance between N(1)-H(1A)...O(1) is 2.19 Å.

**Figure 4.11** The packing structure and unit cell (shown in the rectangle) of compound [4].

The most plausible mechanism for the formation of the imine derivative of compound [3] is shown in **Scheme 4.6**. The reaction begins with the electrophilic carbonyl carbon on the ferrocenoyl imidazolide compound being “attacked” by the lone pair of electrons on the nucleophilic nitrogen of the aniline. Two possible pathways can then be followed. Firstly, the nitrogen quaternary cation then loses its extra proton to the imidazole leaving group with the result that an amide and an imidazole form, with both products being neutral. Alternatively, a series of rearrangements and a proton transfer produces a neutral imine and an imidazole. The products can be interconverted by a “keto-enol” type tautomerism in solution.



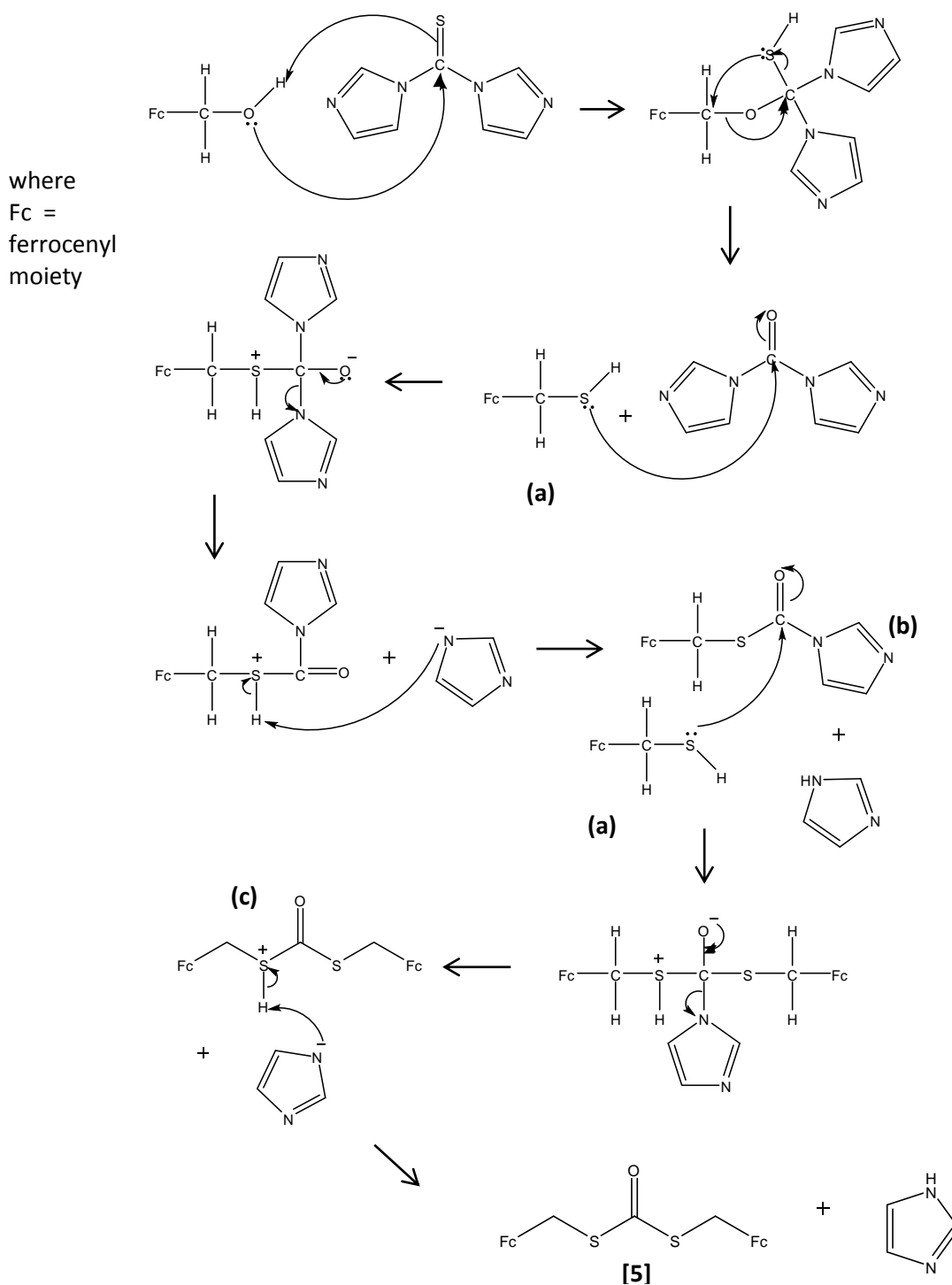
Scheme 4.6 Plausible mechanism for the formation of compound [4].

Table 4.2 Crystal structure data for [4], which was consistent with literature³¹.

Empirical formula	C ₁₇ H ₁₅ FeNO	Formula weight	305.15
Temperature	100(2) K	Wavelength	0.71073 Å
Crystal system	Orthorhombic	Space group	Pccn
Unit cell dimensions	a = 10.3640(2) Å α = 90° b = 25.9190(5) Å β = 90° c = 9.9441(2) Å γ = 90°	Volume	2671.23(9) Å ³
Absorption coefficient	1.122 mm ⁻¹	Density (calculated)	1.518 mg/m ³
Crystal size	0.63 x 0.04 x 0.04 mm ³	F(000)	1264
θ range for data collection	2.12 to 28.34°	Absorption correction	Semi-empirical from equivalents
Reflections collected	42976	Max. and min. transmission	0.9565 and 0.5383
Independent reflections	3333 [R(int) = 0.0254]	Refinement method	Full-matrix least-squares on F ²
Completeness to θ = 28.34°	99.9 %	Data / restraints / parameters	3333 / 0 / 181
Z	8	Goodness-of-fit on F ²	1.083
Largest diff. peak and hole	0.426 and -0.305 e.Å ⁻³	Final R indices [I > 2σ(I)]	R1 = 0.0250, wR2 = 0.0599
		R indices (all data)	R1 = 0.0310, wR2 = 0.0634
		Index ranges	-13 < h < 13, -34 < k < 32, -13 < l < 13

4.6.4 *S,S*-Bis(ferrocenylmethyl)dithiocarbonate [5]

A mechanism for the formation of compound [5] from ferrocenylmethanol and *N,N'*-thiocarbonyldiimidazole was proposed by Onyancha *et al.*²¹ (Refer to **Scheme 4.7**.) A simultaneous nucleophilic addition by a lone pair of electrons from oxygen on the ferrocenylmethanol with the carbon of the thiol group on the diimidazole, and a lone pair of the thiol sulfur on the alcohol's hydroxyl hydrogen occurs.



Scheme 4.7 A likely mechanism for compound [5].²¹

Rearrangement yields carbonyldiimidazole and the intermediate **(a)**. A second nucleophilic addition occurs between the sulfur lone pair on **(a)** with the carbonyl of the diimidazole. An imidazole ion is released and this accepts a proton from the sulfur cation to become neutral. In the process compound **(b)** is formed. Compound **(b)** reacts with compound **(a)** to give a bis-ferrocenyl compound **(c)**. Electron rearrangement again releases an imidazole ion which accepts a proton from the sulfur cation. The final products are compound **[5]** and an imidazole as a by-product, which are thermodynamically stable.

The IR spectrum of compound **[5]** contained a prominent absorption peak at 1634 cm^{-1} (lit²¹ 1635 cm^{-1}) assigned to a carbonyl stretch while the $^1\text{H-NMR}$ spectrum contained only four signals – corresponding to the four proton environments (see **Section 4.5.5**). This result is expected for this symmetrical molecule. Moreover, no aldehyde proton or carboxylic acid proton was evident in the spectra, hence the molecule is symmetrical.

Note that solvent-free methods usually yield higher percentages of product compared to solvent methods.³² Comparing the yields for the solvent-free and solvent synthesis of compound **[5]**, it can be seen that the former has a lower yield. In this case it may be as a result of the inability to scrape out all of the reaction mixture from the Pyrex[®] tubes (with solvent methods the remnant product particles can be easily washed out of the reaction vessel and included with the bulk of the product). Nevertheless, the advantages of solvent-free methods include the simplicity (reaction setup), time-efficiency (shorter reaction time) and minimal energy consumption.³³ Moreover, no solvent pre-drying or distillation is necessary. High purity solvents can be costly and thus solvent-free techniques are also desirable from an economic point of view.³³ Also, trends in both industry and in legislation the world-over are leaning towards greener processes. Solvent-free processes eliminate the use of toxic solvents such as aromatics and chlorine-based solvents. In turn, the need to dispose or recycle waste solvent is removed. In terms of possibly increasing yields, an alternative is to supply at least a 1:2 mole equivalents of ferrocenylmethanol:*N,N'*-thiocarbonyldiimidazole, this would supply double the amount of sulfur and may increase the yield of the product which contains two atoms of sulfur per molecule, depending on the reaction mechanism.

4.7 Conclusions

Three catalysts were successfully synthesized, characterized and purified. All contain heteroatoms and thus should be interesting as catalysts for the synthesis of MWCNTs and other SCNMs. Their use as catalysts for this purpose and their effects are discussed in **Chapter 6**, while that of ferrocene will be discussed in **Chapter 5**.

References

- 1 “Automotive Fuel Requirements – Current and Future”, presentation slides by J. Bennett, International Conference on Automotive Technology, Istanbul, 2004

- 2 S. Top, A. Vessières, G. Leclercq, J. Quivy, J. Tang, J. Vaissermann, M. Huchè and G. Jaouen, *Chem. Eur. J.*, 2003, **9**, 5223
- 3 G. Masson, A. J. Lough and I. Manners, *Macromolecules*, 2008, **41**, 539
- 4 W. A. Amer, L. Wang, A. M. Amin, L. Ma and H. Yu, *J. Inorg. Organomet. Polym.*, 2010, **20**, 605
- 5 R. C. J. Atkinson and N. J. Long, in *Ferrocenes; Ligands, Materials and Biomolecules*, ed. P. Štěpnička, John Wiley and Sons Ltd, England, 2008, pp. 3-32
- 6 F. Rebiere, O. Samuel and H. B. Kagan, *Tetrahedron Lett.*, 1990, **31**, 3121
- 7 R. M. Nielson, G. E. McManis, L. K. Safford and M. J. Weaver, *J. Phys. Chem.*, 1989, **93**, 2152
- 8 Y. Gao, B. Twamley and J. M. Shreeve, *Inorg. Chem.*, 2004, **43**, 3406
- 9 H. Seo, B. Y. Kim, J. H. Lee, H.-J. Park, S. U. Son and Y. K. Chung, *Organometallics*, 2003, **22**, 4783
- 10 I. R. Butler, in *Inorganic Experiments*, 3rd edition, ed. J. D. Woollins, Wiley-VCH Verlag GmbH and Co., Weinheim, 2010, pp. 173-176
- 11 C. Imrie, L. Cook and D. C. Leventis, *J. Organomet. Chem.*, 2001, **637-639**, 266
- 12 C. Imrie, P. Engelbrecht, C. Loubser and C. W. McClelland, *Appl. Organometal. Chem.*, 2001, **15**, 1
- 13 E. I. Edwards, R. Epton and G. Marr, *J. Organomet. Chem.*, 1976, **107**, 351
- 14 E. I. Edwards, R. Epton and G. Marr, *J. Organomet. Chem.*, 1979, **168**, 259
- 15 M. Oberhoff, L. Duda, J. Karl, R. Mohr, G. Erker, R. Fröhlich and M. Grehl, *Organometallics*, 1996, **15**, 4005
- 16 C. Suksai, P. Leeladee, T. Tuntulani, V. Ruangpornvisuti and N. Chaichit, *J. Mol. Struct.*, 2009, **938**, 117
- 17 P. D. Beer and J. Cadman, *Coord. Chem. Rev.*, 2000, **205**, 131
- 18 P. D. Beer and E. J. Hayes, *Coord. Chem. Rev.*, 2003, **240**, 167
- 19 W. Liu, X. Li, M. Song and Y. Wu, *Sens. Actuators B*, 2007, **126**, 609
- 20 P. D. Beer, H. Sikanyika, A. M. Z. Slawin, D. J. Williams, *Polyhedron*, 1989, **8**, 879
- 21 D. Onyancha, V. O. Nyamori, C. W. McClelland, C. Imrie and T. I. A. Gerber, *J. Organomet. Chem.*, 2009, **694**, 207
- 22 J. R. Rasmussen, C. J. Slinger, R. J. Kordish and D. D. Newman-Evans, *J. Org. Chem.*, 1981, **46**, 4843
- 23 A. I. Vogel, B. S. Furnis, A. J. Hannaford, P. W. G. Smith and A. R. Tatchell, *Vogel's Textbook of Practical Organic Chemistry*, 5th edition, Longman Group UK Limited with John Wiley and Sons Inc., UK, 1989
- 24 <http://delloyd.50megs.com/moreinfo/drying.html> (accessed 9 May 2011)
- 25 <http://delloyd.50megs.com/moreinfo/drying2.html> (accessed 9 May 2011)
- 26 Online version of Encyclopaedia Britannica:
<http://www.britannica.com/EBchecked/topic/205107/ferrocene> (accessed 31 March 2011)
- 27 Bruker (2008). APEX2, SAINT-Plus, XPREP and SADABS. Bruker AXS Inc., Madison, Wisconsin, USA
- 28 L. J. Farrugia, *J. Appl. Cryst.*, 1997, **30**, 565
- 29 W. L. Davis, R. F. Shago, E. H. G. Langner and J. C. Swarts, *Polyhedron*, 2005, **24**, 1611
- 30 C. Imrie, P. Kleyi, V. O. Nyamori, T. I. A. Gerber, D. C. Leventis and J. Look, *J. Organomet. Chem.*, 2007, **692**, 3443
- 31 N. Malek-Saied, R. El Aissi, S. Ladeira and E. Benoist, *Appl. Organometal. Chem.*, 2011, **25**, 680
- 32 A. Loupy, *Solvent-free Reactions*, Springer, Berlin, Heidelberg, 2008
- 33 P. T. Anastas and J. C. Walker, *Green Chemistry; Theory and Practice*, Oxford University Press Inc., New York, 1998

CHAPTER 5

SYNTHESIS AND CHARACTERIZATION OF MWCNTs AND OTHER SCNMs USING FERROCENE AS A CATALYST

This chapter describes the synthesis of undoped MWCNTs and other SCNMs, as well as their characterization techniques. Ferrocene was used as the catalyst for these syntheses. The results of the variation of synthesis parameters (temperature and catalyst concentration) are discussed, after a brief discussion on general procedures, reagents and instrumentation.

5.1 General procedures

5.1.1 Cleaning of quartz reactor and glass apparatus

Quartz and glass apparatus were cleaned by first scraping off the black carbonaceous deposit from CVD, followed by gentle scrubbing in soapy water. After rinsing with tap water the apparatus was rinsed in acetone until the solvent colour turned from orange/yellow to colourless. Remaining black carbonaceous material was burnt off by heating at 750 °C in the presence of air for a minimum of 30 minutes. Occasionally it was necessary to soak the quartz apparatus and glass cold finger in *aqua regia* (HCl:HNO₃ 3:1 v/v) or a base bath (NaOH/ethanol/water) to dissolve accumulated iron and iron oxides. After many runs even such methods did not completely remove the orange “stain” that appeared on the inner wall of the quartz tube.

5.1.2 Preparation of anhydrous toluene

Toluene used in the synthesis of MWCNTs was used exclusively from one securely sealed bottle and was considered dry enough for the synthesis of CNTs. (Toluene is usually dried over sodium wire, CaH₂ or 5 Å molecular sieves.¹)

5.2 Common laboratory chemicals, reagents, solvents and gases

Reagents

- toluene (BDH Chemicals Ltd, England, ≥ 99.5% AR)
- sodium hydroxide pellets (Associated Chemical Enterprises (Pty) Ltd, South Africa, 97%)
- hydrochloric acid (Associated Chemical Enterprises (Pty) Ltd, South Africa, 32% w/w)
- nitric acid (Saarchem, Merck, South Africa, min. 55%)

Solvents

- methanol (BDH Chemicals Ltd, England, 99.8%)

Gases

- 10% H₂ in Ar (v/v) (Afrox, South Africa, certified 10.1% H₂)

5.3 Reactor design and setup

The setup of the reactor used was based on a similar design used in literature for the floating catalyst CVD injection method.² A quartz tube (inner diameter 27 mm, length 850 mm), used as the reactor vessel, was placed inside a muffle/tube furnace (Elite Thermal Systems Limited Model No. TSH12/50/610) fitted with a main zone furnace controller (Eurotherm 2416) and an overtemperature controller (Eurotherm 2116). Refer to **Figure 5.1** for a schematic diagram of the reactor design and **Figure 5.2** for photographs. At one end of the quartz reactor tube, a quartz water-cooled injection port was fitted, by using a ground glass joint, and at the other end a glass cold finger, also fitted with a ground glass joint. Both ends were secured firmly onto the reactor tube by a series of hooks and elastic bands. This securing mechanism ensured that if increases in pressure occurred in the reactor at elevated temperatures, the injection port and cold finger would not become detached from the quartz tube. In this way oxygen was prevented from entering the system from the surrounding atmosphere.

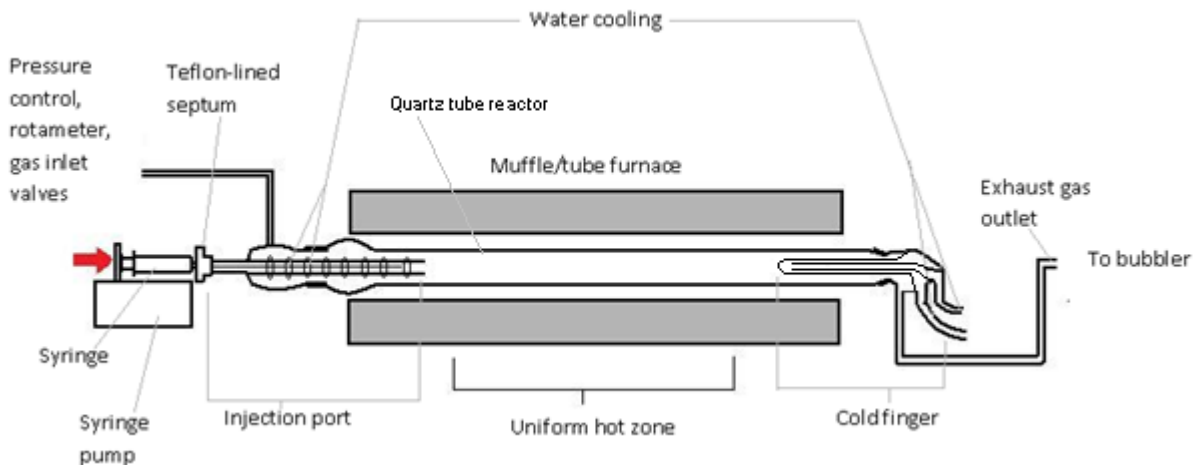


Figure 5.1 Schematic diagram of the reactor design and setup.

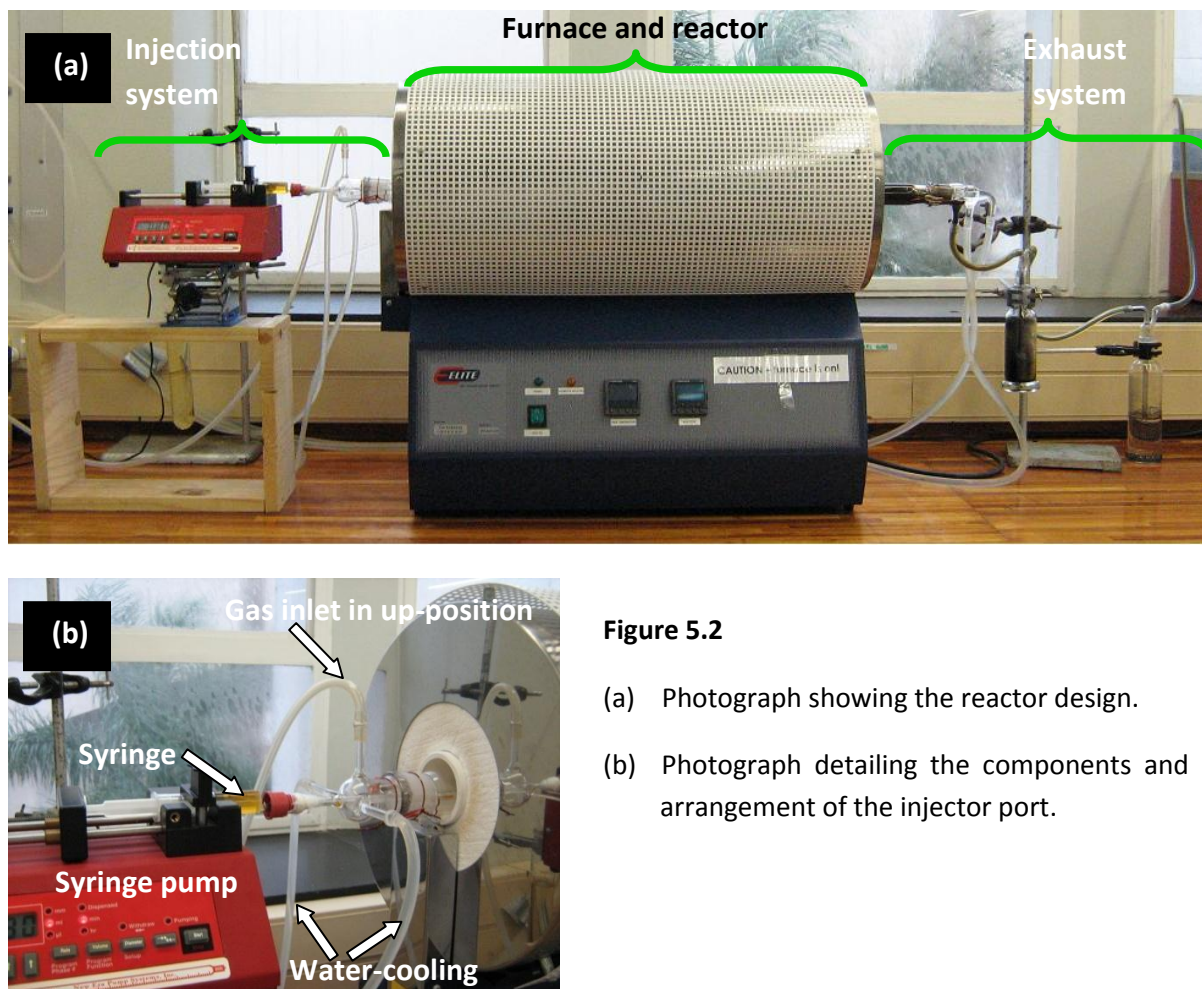


Figure 5.2

- (a) Photograph showing the reactor design.
- (b) Photograph detailing the components and arrangement of the injector port.

5.4 General procedure for synthesis and recovery of MWCNTs and other SCNMs from reactor

5.4.1 General synthesis method

The furnace was heated to the required temperature at a heating rate of 10 °C/min. Once the system was at the set temperature, the carrier gas and reducing agent, 10% hydrogen in argon (v/v), was supplied to the system *via* silicon tubing at a rate of 100 mL/min at 80 kPa for about 5 minutes to purge the system of oxygen-containing air. The carrier gas and reducing agent were set at a constant flow rate and pressure for the duration of the synthesis. It was found that the better orientation of the gas inlet was in the up-position rather than the down-position [see **Figure 5.2 (b)**]. The reason for this is that occasionally small amounts of the carbon source (toluene) and other vapours recondensed on the colder parts of the injection port, effectively blocking the gas inlet. This blockage resulted in an inconsistent flow rate and, thus, it was rectified by maintaining the gas inlet in the up-position. (Note that toluene

was chosen as a carbon source for all experiments in this project, since it has been shown to produce the highest yield of CNTs out of four aromatic hydrocarbons studied, namely, toluene, benzene, xylene and trimethylbenzene.³⁾

The injection port septum was lined with Teflon tape and fitted over the nozzle of the injection system. The septum was further secured to the nozzle with tightly wrapped strips of Parafilm® M.

Waste gases exiting the quartz reactor tube were allowed to pass through a water-trap and then vented to the exterior of the building.

A syringe pump was used to control the rate of injection, at 0.8 mL/min, of the catalyst-carbon source solution into the reactor. The injection pump employed was a New Era Pump Systems Inc. Syringe Pump Model No. NE-300.

The catalyst was weighed out and toluene added to produce either a 2.5 or a 5 wt.% solution, depending on the desired concentration. The total solution mass was 10.0 g. This solution was drawn into a disposable syringe attached to a SS 150 mm L non-boring 24 gauge bevelled-tip needle. Any air that entered the syringe during its filling was expelled before the needle was inserted into the septum of the injector port. After complete injection of the catalyst-carbon source solution, the needle was withdrawn from the system. In almost all runs a small volume (approximately 1.5 mL) of the solution remained pooled at the septum area. This volume was withdrawn from the system *via* the syringe and this approach was applied for all runs. Hence, in each case, almost the same volume (9.25 ± 0.75 mL) was injected to maintain the consistency of reaction solution volume.

The furnace was maintained at the maximum temperature (T_{\max}) for the duration of injection, after which the furnace was allowed to cool to ambient conditions.

5.4.1.1 Experiment 1

The five initial runs of the project were carried out for two purposes. Firstly, familiarization with the reactor design and operation was necessary to identify setup challenges which would need to be overcome before continuation with the project. Secondly, T_{\max} was varied in the first five runs (called Experiment 1), with other parameters held constant [$p = 80$ kPa, gas flow rate = 100 mL/min, injection rate 0.8 mL/min, reducing agent concentration 10% H₂ in Ar (v/v), 2.5 wt.% ferrocene in toluene], to evaluate its effects on the products (see **Table 5.1**).

5.4.1.2 Experiment 2

The three temperatures (900, 850 and 800 °C) from Experiment 1, which yielded the cleanest and highest percentage of CNTs, were used in Experiment 2. The purpose of these three subsequent runs was to investigate the effect of doubling the concentration of the catalyst, i.e. 5 wt.% ferrocene in toluene (see **Table 5.1**).

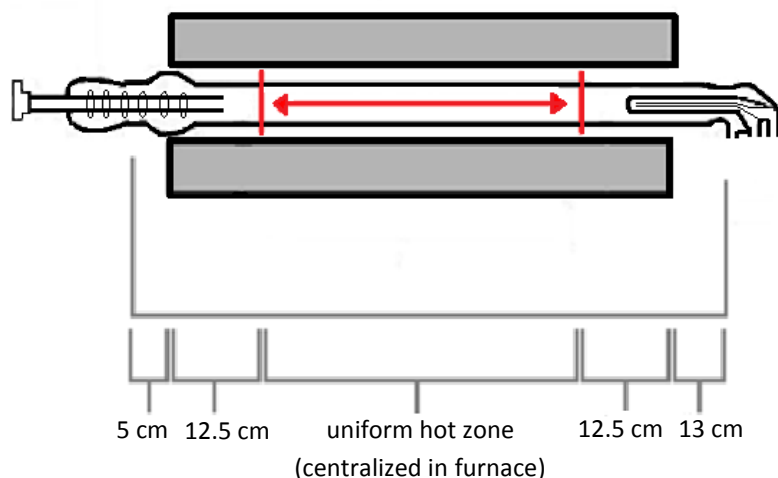
Table 5.1 Reaction parameters for Experiments 1 and 2 with ferrocene as the catalyst.

Exp. run	Primary variable	T _{max} * (°C)	Catalyst concentration (wt.%)
1.1	effect of temperature	950	2.5
1.2		900	
1.3		850	
1.4		800	
1.5		750	
2.1	effect of concentration	900	5
2.2		850	
2.3		800	

* Note that CNTs and other SCNMs may continue to grow even when the temperature under investigation drops as the system cools to room temperature. Thus “T_{max}” is perhaps a better way in which to describe the temperature parameter.

5.4.2 Recovery of MWCNTs and other SCNMs from reactor

When the system had cooled to about 350 °C the gas was switched off, but the reactor ends were not removed until room temperature was reached. The quartz components were then dismantled and the carbonaceous product scraped out of the quartz tube with a long stainless steel spatula. Deposition position of CVD products in a horizontal reactor has been studied by Chaisitsak *et al.*⁴ They showed, by atomizing a mixture of ferrocene and ethanol into an Ar stream, that variation in SCNM structure (specifically SWCNTs in their studies) can occur at different parts of the reactor. Morphologies of the products obtained from SEM imaging were significantly different between the hot zone and the cooler zones. Thus, for consistency and comparative validity of results, only the product which was deposited in the uniform hot zone was collected and weighed. The uniform hot zone was determined by placing of the quartz tube in the furnace as shown in **Figure 5.3**. On the “exhaust” side of the CVD reactor a trap and a water-trap were placed. These traps and the piping did indeed trap material but this material was



not analyzed. For consistency, only CVD products from the “uniform hot zone” were harvested. A ‘raw percentage yield of SCNMs’ value was calculated by finding the mass of collected CVD products as a percentage of the total mass of catalyst-carbon source solution injected into the reactor, i.e. the mass as a percentage of 10.0 g.

Figure 5.3 Placement of the quartz reactor tube in the furnace.

5.5 Purification methods

Three different purification procedures were tested on material obtained from the 900 °C run of Experiment 1. The purpose was to remove Fe and amorphous C impurities from the CNTs.

Method 1

Ground CNTs (0.050 g) were placed into a round-bottomed flask with approximately 20 cm³ of a 3:1 H₂SO₄:HNO₃ (98%:55%) solution. The mixture was heated to 120 °C and refluxed for 30 min at this temperature. The suspension was then diluted with distilled water and centrifuged. The supernatant was decanted off. The last two steps were repeated approximately six times. Finally, the mixture was filtered through a sintered glass disc (Pyrex® porosity grade 4) and the MWCNTs were washed with distilled water until the filtrate was colourless and neutral as tested by universal indicator paper. CNTs were removed from the sintered glass disc by washing off with acetone. The CNTs were dried in an oven at 120 °C for at least 1 h. The recovered material was 49%.

Method 2

Ground CNTs (0.050 g) were sonicated in approximately 50 cm³ of 30% HNO₃ for 30 min. This dispersion was then mechanically stirred for five days at room temperature. The mixture was subsequently diluted with distilled water and filtered under vacuum through Macherey Nagel 615 (MN 615) filter paper. The CNTs were washed with distilled water until the filtrate was colourless and universal indicator paper showed the solution pH to be neutral. Three methanol rinses were used to remove water and the product was then dried at 120 °C in an oven for 12 h. Finally, the purified CNTs were left under vacuum at room temperature overnight and then weighed. The recovered material was 90%.

Method 3

Ground CNTs (0.144 g) were placed in a round-bottomed flask with approximately 20 cm³ of 3 M HNO₃ solution. The mixture was heated to 105 °C and refluxed for 24 h at this temperature. The suspension was then diluted with distilled water.⁵ A solution of 1.25 M NaOH (8 cm³) was then added by Pasteur pipette and the mixture was then filtered under vacuum through MN 615 filter paper. The CNTs were washed over vacuum with distilled water until universal indicator paper showed the filtrate pH to be neutral. The solid was then dried in an oven for 12 h at 120 °C. The recovered material was 92%.

The next section is dedicated to the instrumentation used in characterization of the as-synthesized and purified CVD products, followed by the results of these analyses.

5.6 Characterization of MWCNTs and other SCNMs: Instrumentation and techniques

All CVD products, being mostly relatives of the graphite family, were black in colour, with both dull and shiny particles depending on the T_{\max} (see **Figure 5.4**). SCNMs that formed directly on the smooth surfaces of the quartz tube usually formed shiny flakes. Before any characterization was carried out, the products were thoroughly ground in a mortar and pestle to homogenise the sample as much as possible.



Figure 5.4

Representative image of a typical as-synthesized CVD product showing both dull and powdery particles, and shiny flakes.

5.6.1 Transmission electron microscopy (TEM)

Transmission electron microscopy (TEM) was performed on a JEOL JEM 1010 transmission electron microscope at 80 kV, by using copper grids with a carbon formovar layer or, at times, a holey carbon or lacy carbon layer. A match-head full amount of ground product was dispersed in dried ethanol in a sonicator for approximately 15 minutes to improve homogeneity of the suspension. Following this, 20 μL of the dispersion was transferred to a copper grid (routinely 150 or 200 mesh) covered with a thin formovar layer and the alcohol allowed to evaporate. The grid was inserted into the specimen chamber of the TEM instrument and viewed under a variety of magnifications at different locations on the specimen. Images were captured with a Megaview 3 camera. Data, such as magnification and scale bars, were embedded electronically into the images by using ITEM software on an attached computer. Analysis of captured images was also done with this same software package.

For the purposes of this project, it is worth noting that the electron beam was not placed on structures for an unnecessarily long period of time, which is known to damage CNT walls,⁶ and thus outer diameter measurements are considered representative of the actual values.

Low magnification images were captured and studied to get a broad view of the types and distribution of materials in each sample. Note that the determination of the distribution of SCNMs and amorphous carbon can be a subjective measurement as the software used cannot extract the distribution information from images. Nevertheless, the SCNMs which contribute to the bulk of a sample, and those which do not, can be estimated by observation. A rough estimate of the percentage distributions can be done by comparing samples.

TEM images displayed the 2D morphologies produced from different reaction conditions. These images were analyzed for average OD, ID and length of tubes. (Low magnification TEM images were used to fit

the entire length of individual CNTs in the field of view for length measurements.) Approximate maximum lengths were measured with the help of iTEM software. Three measurements of ID and OD were made per measured nanotube, with approximately 100 tubes being randomly measured. Tubes which displayed significantly obvious diameter variations were measured at thicker, average and narrower regions. Those tubes which appeared uniform in diameter were measured in three random locations. The sum of all three hundred measurements was divided by three hundred to give an approximate average value. The formulae used to determine the overall average IDs and ODs are shown in **equations (4)** and **(5)**. A sample image is shown in **Figure 5.5** with measurements of the CNT ODs.

$$100 \text{ tubes} \times 3 \text{ measurements per tube} = 300 \text{ measurements} \quad (4)$$

$$\Sigma(\text{all measurements}) \div 300 = \text{average diameter (nm) per sample} \quad (5)$$

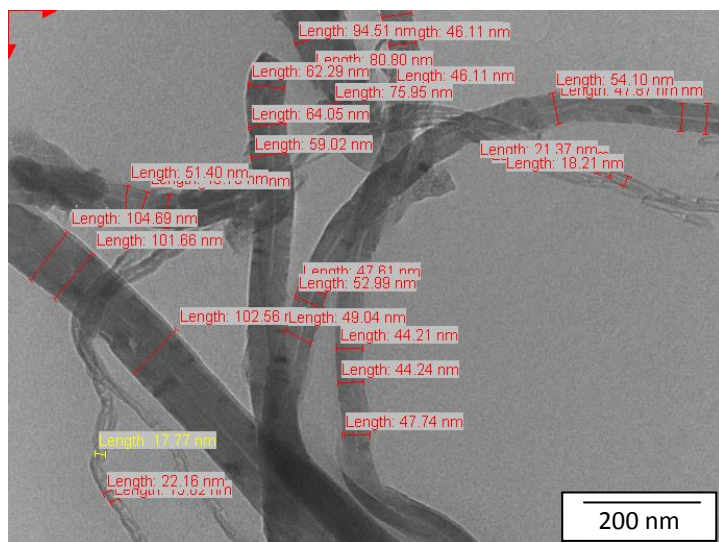


Figure 5.5

A sample image of how ODs were measured.

In terms of sphere diameter measurements, a minimum of 30 random measurements were taken.

The following three characterization techniques were used to study MWCNTs and SCNMs produced from heteroatom containing catalysts (**Chapter 6**) and Pd/MWCNTs (**Chapter 7**): High resolution transmission electron microscopy (HRTEM), high resolution scanning transmission electron microscopy (HRSTEM), high angle annular dark field microscopy (HAADF) and elemental mapping was done for selected materials only. This was done by using a JEOL 2100 instrument at 200 kV accelerating voltage and a LaB₆ gun. A minimum of 100 000 counts per sample was used while generating elemental maps. Gatan Digital Micrograph Software was used for high resolution work.

Please note that the order in which the runs were performed do not correspond with the order in which analyses are named and reported here, hence in SEM images the naming given is not consistent with the naming used in this report. Please, therefore, ignore the embedded text regarding the name of each run.

5.6.2 Scanning electron microscopy (SEM)

Three dimensional topographical information was obtained from two scanning electron microscopes – the JEOL JSM 6100 or LEO 1450 depending on the availability of the instruments. Typically an accelerating voltage of 10 to 20 kV was used for both instruments, although higher magnification images required a value from 10 to 15 kV to obtain a suitable image contrast. Optimal working distance for the LEO 1450 ranged between 4 and 6 mm with probe currents between 3 and 5 pA. Because the JEOL JSM 6100 was used in conjunction with EDX during imaging sessions, the working distance was set at around 25 mm, which is suitable for EDX measurements. The software employed was Bruker Esprit 1.8 for the JEOL JSM 6100 SEM and Zeiss SmartSEM Ver. 5.03.06. for the LEO 1450 SEM. Sample preparation was as for the TEM studies, except that instead of a known volume of the CNT-ethanol dispersion being used, an aluminium stub with sticky carbon tape was dipped into the dispersion. CNTs became attached to the carbon tape and the ethanol was allowed to volatilize off.

5.6.3 Electron dispersive X-ray spectroscopy (EDX)

A Bruker X-ray spectrometer, attached to the JEOL JSM 6100 SEM instrument, or at times the LEO 1450 instrument, was used to scan selected areas of samples to generate EDX spectra. An optimum working distance of about 25 mm was used. Scans lasted 3 minutes at a rate of between 5 and 10 kilo counts per second. Bruker Esprit 1.8 software was used to generate EDX spectra and convert the data in spectra directly into tables of normalized weight percent for selected elements. The accelerating voltage used was between 10 and 20 kV. Elemental mapping was performed on the JEOL 2100 (see **Section 5.6.1**).

Note that this analysis technique is more reliable for quantifying heavier elements, such as Fe, but less so for lighter elements, such as carbon, and is considered poorly reliable for elements lighter than boron. Also, EDX accuracy is influenced by a variety of factors.⁷ These include fluctuating numbers of electrons bombarding a sample, noise interference, variations in the number of backscattered electrons and the number of X-rays generated by sample electron bombardment. For these reasons, amongst others, precision, or repeatability, is not always high in such experiments. Nevertheless, EDX was used in this study in conjunction with more reliable, more accurate techniques, such as thermogravimetric analysis. Two EDX spectra, per material, were studied, hence error bars are shown. Qualitative analysis was more crucial in these EDX studies than the quantitative results.

5.6.4 Thermogravimetric analysis (TGA)

Analysis of the degradation of MWCNTs (and other SCNMs) was carried out by using a TA Instruments Q Series™ Thermal Analyzer DSC/TGA (Q600). A small (≈ 5 mg) homogenised sample was heated in air (50 mL/min) from room temperature to 900 or 1500 °C. For the first three TGA analyses, a heating rate of 20 °C/min was used. However, because 10 °C/min gives more detailed information over time, subsequent analyses were done employing the lower rate. TA Instruments Universal Analysis 2000 software was used to analyze and manipulate the thermograms generated from temperature and

weight changes. Some TGA curves were run at the University of the Witwatersrand on a Perkin Elmer Thermogravimetric Analyzer (TGA 4000) under the same conditions as above.

5.6.5 Brunauer, Emmett and Teller (BET) analysis

Degassing of ground and homogenized samples, of similar sample size, was done at 200 °C in N₂ overnight, and was followed by surface area determination on a Micromeritics Gemini BET instrument at 77 K.

5.6.6 Raman spectroscopy

Crystallinity of products from CVD was determined with a DeltaNu Advantage 532TM Raman spectrometer. The excitation source was a Nd:YAG solid state crystal in a class 3b diode laser. The excitation wavelength was 532 nm. The grating had 1800 lines per mm. A 2D CCD detector was used. NuSpecTM (2009) software was used to manipulate the scan durations, which typically ranged between 10 to 59 seconds. Manipulation of generated spectra was done by using GRAMS AI software.

5.7 Results and discussion of Experiment 1 – Effect of temperature

The first five sets of products collected from the synthesis of SCNMs by CVD from ferrocene [1] at 2.5 wt.%, were products synthesized under the same conditions, except for a variation in temperature. Temperatures at fifty degree Celsius intervals over the range 750 - 950 °C were chosen so as to correspond, for comparison, with common literature ranges. An in-depth and systematic discussion of each run of Experiment 1 based on the TEM, SEM and EDX analyses is initially given. This is followed by a comparative discussion of the runs, where trends are identified. In the comparative discussion, TGA, BET and Raman results are also considered. For subsequent experiments a systematic discussion of each temperature will not necessarily be given, but rather a comparative discussion from the start.

5.7.1 Experimental challenges, modifications and raw yields

Experiment 1 runs 1-5 (called 1.1, 1.2, 1.3, 1.4 and 1.5 respectively) were identical in terms of reaction conditions and parameters, except for changes in temperature. The purpose of this was to systematically identify the most suitable temperature band in which the maximum percentage of high purity MWCNTs is formed. **Table 5.2** shows the observations, challenges and the modifications of the experimental set-up and method for the first set of runs as well as the raw yields. Approximately the same volume of reaction solution was injected in each run so the yields are considered comparable. The table also shows a general trend of decreasing raw yield of SCNMs with decreasing T_{max} . This result is expected.⁸ At higher temperatures (900 and 950 °C), the exhaust hole of the cold finger sometimes became partially blocked by a build-up of carbonaceous product. The supposition is that at higher

temperatures the autogeneous pressure increases. This in turn increases the gas flow rate, carrying more carbon materials to the exhaust end of the tube. Ultimately this results in a higher carbonaceous build-up than for lower temperatures. Qiu *et al.* used coal gas as the carbon source, with no carrier gas, and found that at high flow rates (150 mL/min) the end of the tube became blocked.⁹ Though the gas flow rate was controlled in this project, (100 mL/min), it was only controlled from the front end of the reactor, i.e. the flow rate of the exhausting gases was not controlled. However, the rate at which the gas vented from the system as bubbles, through the bubbler, was monitored by observation. The higher the temperature the faster the bubbles formed and, simultaneously, the more product was pushed to the cold finger end of the tube and the more “jamming” occurred, as was just described. Also, Cheng *et al.* found that, depending on the temperature and the rate of flow of the carrier gas, products can be carried out of the reaction zone (the T_{\max} zone).¹⁰ This may be a reason for the unexpectedly low yields (< 20% in **Table 5.2**).

Table 5.2 Summary of the first five initial experimental runs (2.5 wt.% ferrocene in toluene) showing T_{\max} problems encountered and the intervention measures taken to correct or minimize these, as well as yields and product description.

Exp. run	T_{\max} (°C)	Challenges	Measures used to overcome challenges	Experimental error (specifically unreacted injection solution)	Volume injected (mL)	Results		
						Description of product	Raw yield from uniform hot zone (g)	Percentage raw yield of SCNMs (%)
1.1	950	pooling of injection solution at septum, approx. 1.5 mL did not enter system	withdrew the 1.5 mL pooled solution by syringe	≈ 1.5 mL unreacted injection solution	≈ 8.5	black shiny flakes and some dull black powder	1.429	14.3
1.2	900	pooling of injection solution at septum, approx. 1 mL did not enter system	-	≈ 1 mL unreacted injection solution	≈ 9	black shiny flakes and some dull black powder	1.780	17.8
1.3	850	pooling of injection solution at septum, approx. 0.5 mL did not enter system	withdrew the 0.5 mL pooled solution by syringe	≈ 0.5 mL unreacted injection solution	≈ 9.5	black shiny flakes and dull black powder	0.914	9.1
1.4	800	pooling of injection solution at septum, approx. 1 mL did not enter system	after this run a new form of septum was used	≈ 1 mL unreacted injection solution	≈ 9	black flakes, dull with some shiny surfaces	0.694	6.9
1.5	750	small amount of white vapours seen exiting system from ground glass joint of injection port	tightened elastic bands	-	10	black flakes, dull	0.478	4.8

At lower temperatures (< 850 °C) liquid remained in the system even after the reactor cooled to room temperature. This liquid was most probably an oil of polyaromatic hydrocarbons, formed by radical addition, as proposed by Reilly *et al.*¹¹ They suggest that when the hydrocarbon concentration is above

an optimal level, the CNT growth is hindered or totally ceases due to the radical condensate layer being deep enough to “smother” CNTs or the carbon-catalyst interface. In addition, this thick oily layer hinders the diffusion of H₂ away from the carbon-catalyst surface. In turn, H₂ cannot escape at a fast enough rate into the gas phase to react with the surface of the radical oil layer. Thus, the radical layer cannot contribute to the growing CNT. The authors state that high temperatures, coupled with high hydrogen concentrations, provide the correct conditions for optimal CNT growth rates. In this project, some of this liquid moved down the gas inlet effectively rendering the gas flow inconsistent. This problem was overcome by moving the gas inlet into the up-position as in **Figure 5.2 (b)**. Hence, for all further runs, this position was used. At 750 °C and even 800 °C some radical condensates, as mentioned previously, moved out of the exhaust end of the furnace. A similar yellow liquid was observed leaving the reactor at 500 °C in other experiments with ferrocene dissolved in xylene or benzene.¹² It was suggested that at this temperature the catalyst solution can pass out of the reactor unreacted because the reactor length was not long enough, the temperature was not high enough or the droplets were too large. (However, a vertical-flow reactor was used, so naturally gravity will have more of an effect on this phenomenon.) The loss of reaction material in this way can account for the lower yield of carbonaceous product at the lower temperatures in this project. Also, high gas flow rates would carry small liquid droplets of reaction mixture or, more likely polyaromatic hydrocarbon oil droplets, to the exhaust end faster than slower flow rates. This may also cause a decrease in yield. Many authors use 100 mL/min as a flow rate and thus it was decided to continue with this rate for comparative purposes.¹³

An in-depth discussion of the results of the TEM and SEM analyses, and very briefly EDX, for Experiment 1 follows. After this general trends will be discussed.

5.7.2 Products obtained at 950 °C

The TEM image **A** and SEM image **B** in **Figure 5.6** show that almost no nanotubes (estimated to be 2% of the raw yield), were synthesized at 950 °C (see **Table 5.3** in **Section 5.7.7.1**). Even with the homogenizing process used prior to TEM analysis, the CNTs that were present on the TEM formvar for viewing, were not isolated enough to measure lengths and were too few and far between to measure and analyze for ID and OD values.

Predominantly groupings of fused spheres were synthesized. These were estimated to constitute 73% of the collected synthesized material. At this high T_{max} , naturally, frequent collisions of iron NPs would occur and consequently a high rate of coalescence occurs and larger iron NPs result, whose diameters are less suitable for CNT formation and growth. In the case of this investigation, it is proposed that carbon cannot grow off the metal catalyst particle as CNTs, but instead the metal NPs catalyze sphere formation. Alternatively, carbon quickly covers the surface of the metal NPs and forms spheres in the form of iron/carbon core-shells. Certain spheres selected by SEM-EDX were found to contain significant quantities of iron (see **Appendix F, Table F.1**). Accordingly, this high iron content is expected at elevated temperatures. These spheres ranged in diameter, and SEM images showed the existence of both nano- and microspheres. No fibres or polygon structures were apparent. Approximately a quarter of the material was amorphous carbon.

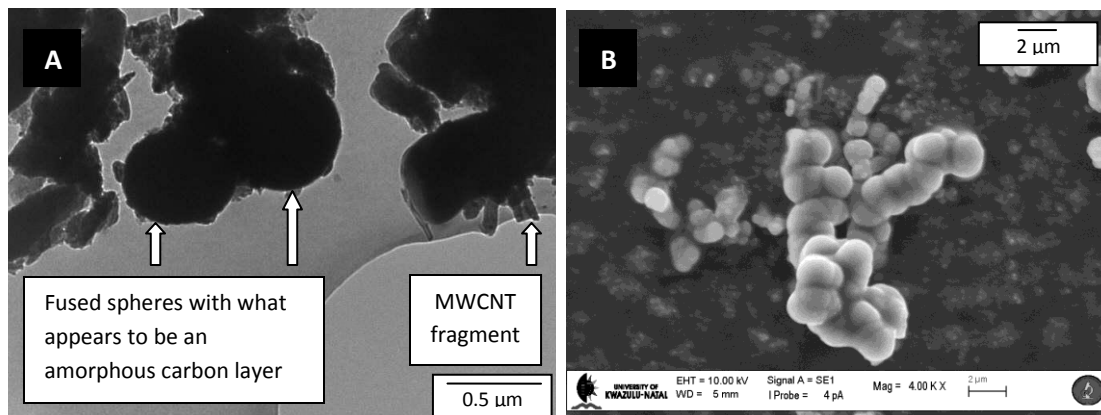


Figure 5.6 Representative images from (A) TEM and (B) SEM showing the formation of a large amount of carbon spheres relative to MWCNTs for the experiment conducted with 2.5 wt.% catalyst [1] at 950 °C.

5.7.3 Products obtained at 900 °C

From 900 °C to 750 °C significant quantities of carbon nanotubes were observed.

At 900 °C the TEM images (**Figure 5.7** image A) showed an estimated 92% of MWCNTs, in the raw yield, of good structure (see **Table 5.3** in **Section 5.7.7.1**). The representative longest MWCNTs were in the order of 10 μm. The tubes were mostly straight in nature with very few defective CNTs (few bends, kinks and other irregularities). A very high yield of CNTs, with regular structure, was also found in other studies under similar conditions.² SEM images showed well aligned tubes (see image B of **Figure 5.7**) even after homogenizing techniques were employed. A “stepped” effect on the bundle of aligned CNTs is apparent. Contrasting bands of light and dark are seen on the right hand side of the structure. This may be due to sudden bursts of ferrocene/toluene solution volatilizing from the injection port into the system. Although the injection rate was set at a predetermined value, at times bursts of vapourizing solution could be heard. Cao *et al.* observed similar bands when feeding a ferrocene/xylene solution into the system at intermittent stages.¹⁴ Some iron remains trapped in parts of some tubes. This can be determined from the darker areas on the TEM image. CNFs constituted approximately 2% of the collected material.

The average values for the ID and OD were 8.7 and 28.6 nm respectively (see **Table 5.3** in **Section 5.7.7.1**). The biggest proportion of MWCNTs had an ID value of 6 nm as seen from the highest bar in the ID histogram, and an OD of approximately 23 nm (see **Figure 5.8**). The histograms show a Gaussian-type distribution for the OD and ID as seen in much of the similar literature.¹⁵⁻¹⁷ Both histograms exhibit a tail for a small proportion of tubes with large IDs and ODs.

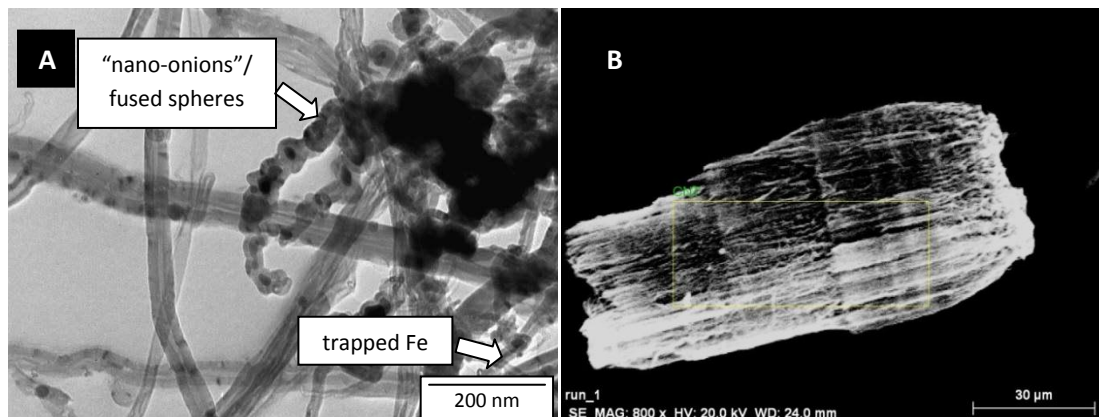


Figure 5.7 Representative images from (A) TEM and (B) SEM showing the formation of predominantly MWCNTs for the experiment conducted with 2.5 wt.% catalyst [1] at 900 °C.

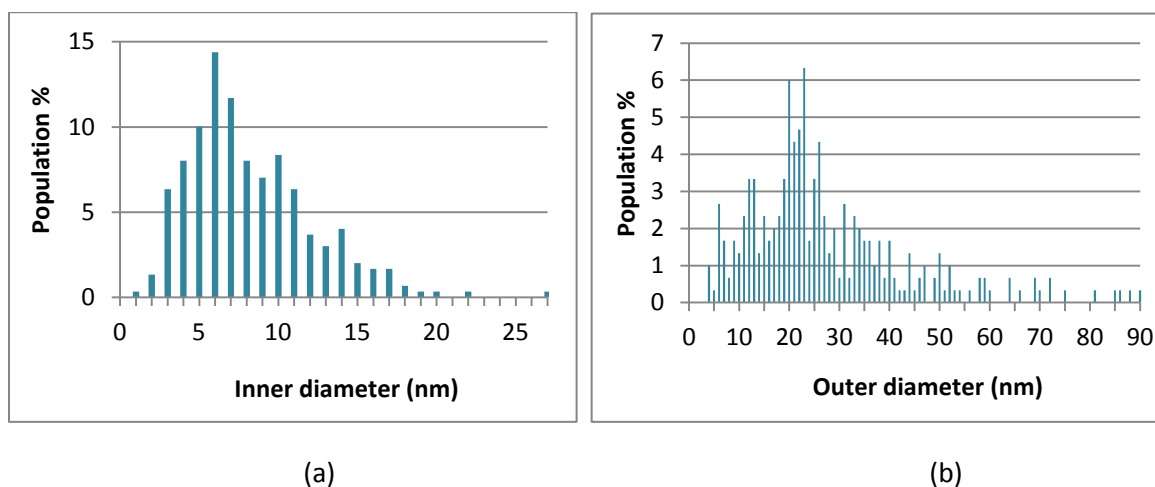


Figure 5.8 Histograms showing (a) ID and (b) OD distributions of MWCNTs obtained from 2.5 wt.% catalyst [1] at 900 °C.

There is a marked decrease in the percentage of spheres produced at this T_{\max} (900 °C) as compared to the previous run. Only 4% of the collected SCNMs are spheres. Some of the spheres consist of carbon only, while others consist of iron encased in a spherical carbon layer (iron/carbon core-shells). The former type of sphere may be hollow or solid, but this has not been determined. The TEM image **A** of **Figure 5.7** contains a structure which looks like fused nano-“onions”.¹⁸ No fused spheres were seen when the same material was observed under SEM at lower magnifications, presumably because of their small size.

This material is low in amorphous carbon and other SCNMs (see **Table 5.3** in **Section 5.7.7.1**). Very rarely were unusual structures, such as coils (see **Section 5.7.8**), seen, indeed too few to be worthy of statistical analysis.

5.7.4 Products obtained at 850 °C

TEM images taken from collected products at 850 °C indicate mostly tubes (93%) with almost no amorphous carbon ($\approx 1\%$) (image **A** in **Figure 5.9**). Spheres account for 3% (see **Table 5.3**). Many MWCNTs are straight and occasionally some are disordered. SEM image **B** in **Figure 5.9** indicates well aligned tubes. The average OD is about 10 nm larger than at 900 °C (39.1 *versus* 28.6 nm) and the average ID is about 1 nm different (9.6 *versus* 8.7 nm). An increase in temperature correlates with an increase in OD,⁴ although with these results this is not strictly the case. The supposition is that 850 °C is a more conducive temperature for CNT formation than 900 °C. Representative longest length increased, by approximately 3 μm , at this T_{max} relative to 900 °C. Again Gaussian-type distributions (**Figure 5.10**) for the MWCNT ODs and IDs were found, with a wider spread of ODs at this temperature than the previous. There appeared to be the same estimated proportion of fibres (2%) as at 900 °C.

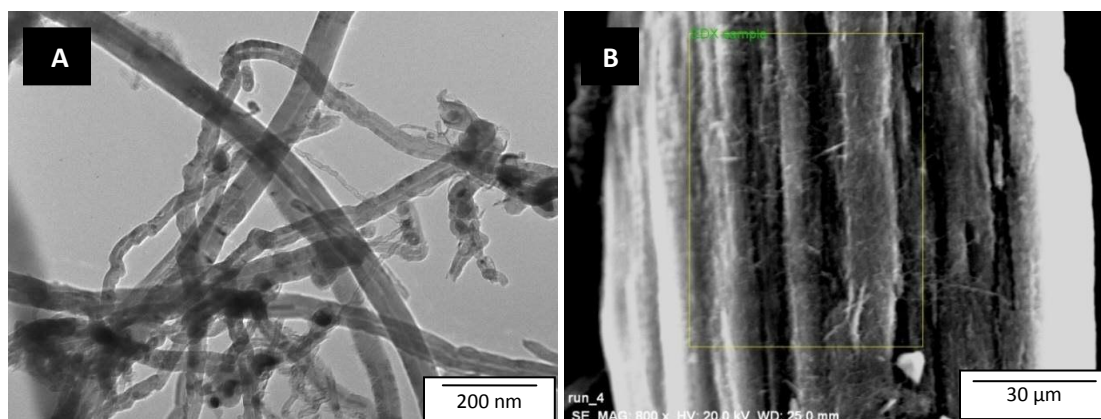


Figure 5.9 Representative images from (A) TEM and (B) SEM showing the formation of predominantly MWCNTs for the experiment conducted with 2.5 wt.% catalyst **[1]** at 850 °C.

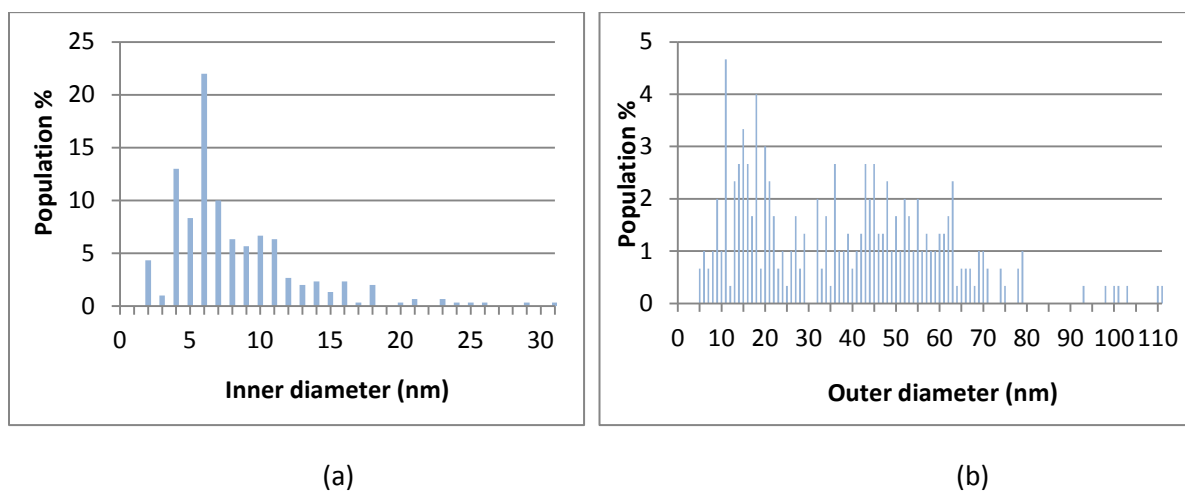


Figure 5.10 Histograms showing (a) ID and (b) OD distributions of MWCNTs obtained from 2.5 wt.% catalyst **[1]** at 850 °C.

Preliminary EDX investigations confirmed the presence of carbon and iron (refer to **Appendix F, Table F.1**).

5.7.5 Products obtained at 800 °C

At 800 °C a large proportion of high quality MWCNTs were found in the collected material (see the micrographs shown in **Figure 5.11**) as was the case in similar studies,² although the percentage of CNTs is marginally smaller than that obtained at 900 and 850 °C (91% *versus* 92 and 93% respectively – refer to **Table 5.3**). (Note these values are all approximately the same, but have been estimated to be these specific values based on comparison of micrographs and quantities of other SCNMs). The distributions of the ODs and IDs are given in **Figure 5.12**, again showing that a larger percentage of the population have smaller diameter values.

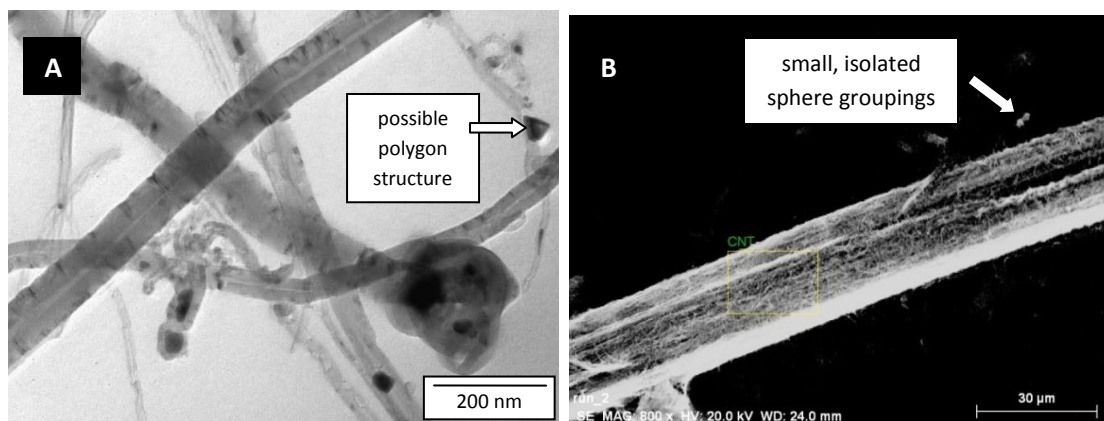


Figure 5.11 Representative images from (A) TEM and (B) SEM showing the formation of predominantly MWCNTs for the experiment conducted with 2.5 wt.% catalyst [1] at 800 °C.

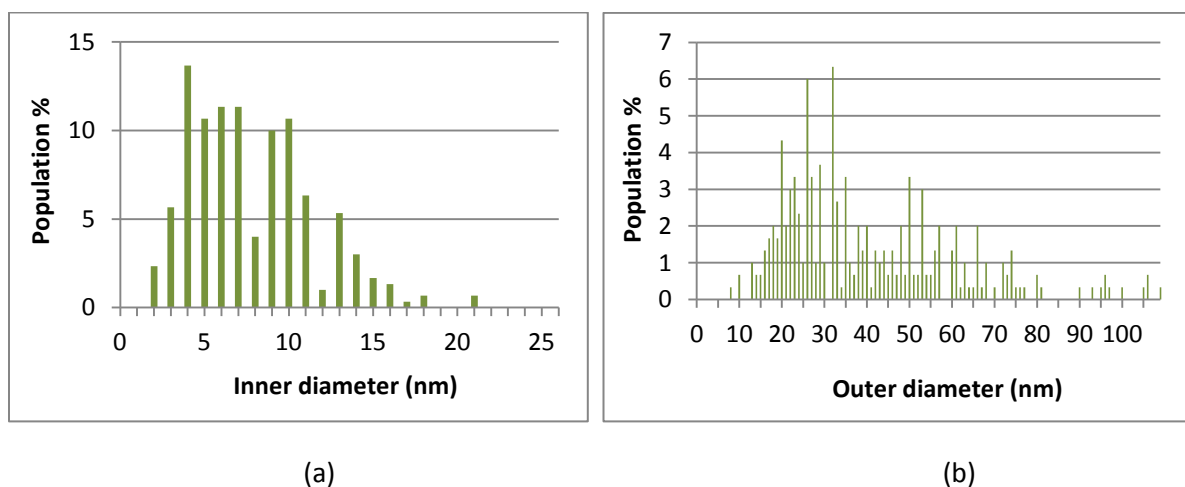


Figure 5.12 Histograms showing (a) ID and (b) OD distributions of MWCNTs obtained from 2.5 wt.% catalyst [1] at 800 °C.

This material contains relatively much longer tubes than at 850 °C (up to 17 μm) as observed in the TEM images (see **Table 5.3** for a comparison of representative longest length values). Note that in micrograph **B** of **Figure 5.11** one may be tempted to say that the CNTs were over 120 μm long, but such an image does not prove that single tubes reach from the beginning of the bundle to the end, although it shows the alignment of the tubes. It is interesting to note the regular shape of the bundle in the SEM micrograph. Fairly flat bundle surfaces may indicate high crystallinity of the component tubes. A possible explanation is that the straighter and less defective adjacent tubes are, the tighter the packing can be. Larger CNT surface areas can then interact by van der Waals interactions. This may lead to even tighter packing of tubes and, ultimately, “flat” surfaces on bundles. **Figure 5.13** is a simple graphical representation of **(a)** how straight, highly crystalline tubes would pack together more tightly resulting in flatter, more regular, bundle surfaces. In **(b)** the packing is looser due to more irregular CNTs.

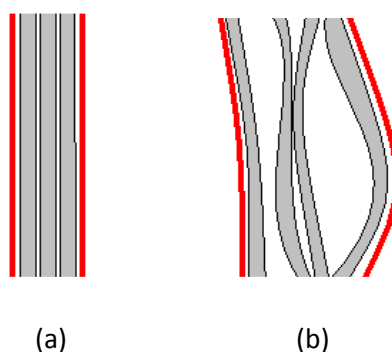


Figure 5.13 Diagram showing (a) straighter tubes in an ordered bundle, *versus* (b) more irregular CNTs in a less orderly bundle, as a result of differences in intermolecular and interparticle interactions.

However, although the tubes appear straighter (less deformation and defects) than those for other runs, and are bundled together uniformly, their crystallinity, as described by the I_D/I_G ratio in **Section 5.7.7.7**, shows that they are not as crystalline as those MWCNTs from the 900 and 850 °C runs. Thus the argument about crystallinity relating to bundle morphology is a very preliminary conjecture. Various parameters may influence bundle formation. These may include the substrate upon which the CNTs grow, the manner in which the metal catalyst particles deposit on a surface, and the metal particle size and its distribution, amongst others. Nevertheless, the regular shape and flat surfaces of the bundle in image **B** of **Figure 5.11** was striking and was not seen in other runs. This temperature also yielded tubes which were very consistent in structure, although “wavy” at one end (see **Appendix E, Figure E.1**). In this particular image the tubes appear “wavy” at one end. What causes this wave-like shape is a possible topic for future research.

Spheres were observed only in small fused groupings (see micrographs **A** and **B** of **Figure 5.11**). This material contained approximately the same percentage of spheres as at 850 °C.

Very little amorphous material was apparent ($\approx 3\%$) in the raw yield. The percentage of CNFs was the same as at 850 °C, and the amount of polygon structures was $\approx 1\%$ (for example, see **Figure 5.11** image **A**). The far right side of **Figure 5.11** image **A** contains what appears to be a triangular shape. TEM does

not reveal whether this is in fact a pyramidal structure in three dimensions or not, nor whether it is carbonaceous or metallic. The dark contrast suggests it may be an iron NP. However, it is interesting to note that Nyamori and Coville observed carbonaceous triangular structures in MWCNT syntheses performed using anthracene in sealed containers.¹⁹ Notably, these structures formed in runs without an iron catalyst. Perhaps, in this project, these structures formed in localized areas of the reactor where iron concentrations were low and, after sample preparation, were viewed alongside SCNMs formed from catalysis by iron. However, in this project, regular morphologies may merely be anomalies of a statistically meaningless nature due to their erratic appearance and low occurrence.

The material also contained some trapped iron in both tube hollows as well as in carbon spheres.

The average ID and OD (Table 5.3) are comparable with the previous run, i.e. 850 °C.

5.7.6 Products obtained at 750 °C

A T_{\max} of 750 °C afforded shorter, more disordered tubes as apparent from TEM imaging (see image A of Figure 5.14). The average ID and OD was lowest for this temperature (28.0 and 7.4 nm respectively), and the histograms show a smaller spread of the bulk of population groups (refer to Figure 5.15). The carbon content of tubes was comparable to that at 900 to 800 °C (see Appendix F, Table F.1).

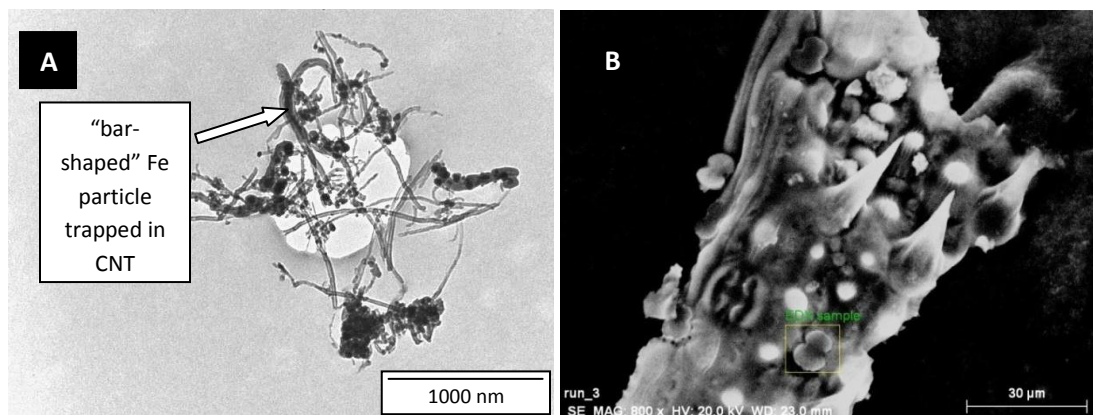


Figure 5.14 Representative images from (A) TEM and (B) SEM showing the formation of a highly heterogeneous mixture of irregular MWCNTs, carbon spheres and amorphous carbon from the experiment conducted with 2.5 wt.% catalyst [1] at 750 °C.

A much larger amount of spheres was found (15%) in the collected material. Accreted groupings such as clusters and strings of spheres were also synthesized. Higher magnifications revealed the material to be littered with small particles of amorphous carbon (30%). Image B of Figure 5.14 shows a highly heterogeneous mixture of structures relative to other runs. The strange morphology of the fused structures in this image is consistent with the wide distribution of SCNMs from Table 3, although why they are fused is not known. However, some images evidence the fact that this material does contain some isolated bundles of well aligned tubes. The yield of MWCNTs is an estimated 55%, almost half that of runs 1.2, 1.3 and 1.4.

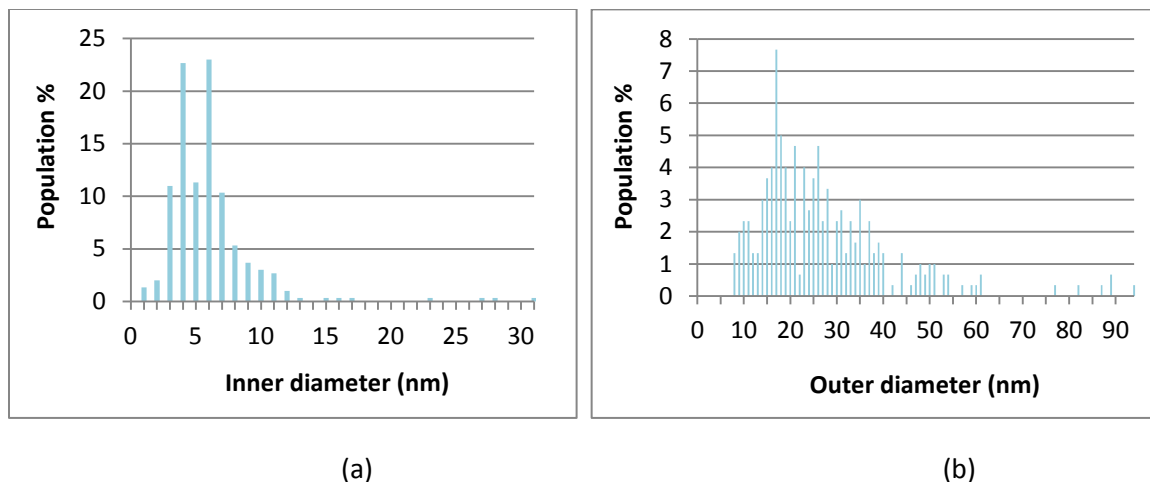


Figure 5.15 Histograms showing (a) ID and (b) OD distributions of MWCNTs obtained from 2.5 wt.% catalyst [1] at 750 °C.

“Bar-shaped” particles of iron trapped in CNTs, as seen in **Figure 5.14** image **A**, were suggested to be that shape due to mechanical stress during precipitation of graphitic carbon on large droplets of molten iron.²⁰ In the same paper it was suggested that two iron particles in a tube separated by a small distance may be the result of the collision of an iron particle in the tip of a tube colliding with another iron particle. The second particle is then responsible for all the further tube growth. Deck and Vecchio, however, stated that metal NPs inside CNTs may result from NP particles/atoms in the gas phase accumulating inside tubes to form larger particles.²¹ Snoeck *et al.* also describe how the metal NP is deformed from a sphere into an elongated shape.²²

A discussion of each product from Experiment 1 has just been given based on the TEM and SEM results with a brief mention of EDX results. A discussion on general trends will now be given, including the results derived from TGA, Raman, EDX and BET studies.

5.7.7 General trends from the effect of temperature

5.7.7.1 SCNMs formed

Varying the pyrolysis temperature has been shown to influence the structures which form from CVD and unusual structures can be formed, depending on the temperature. For example, Pradhan and Sharon used kerosene as a carbon source in supported catalyst CVD with nickel or iron as the catalyst and this yielded both straight and coiled CNTs respectively at 1000 °C.²³ Fused carbon spheres, with approximate diameters in the 600-900 nm range were formed at a temperature only 100 °C higher, 1100 °C, for both metal catalysts. Comparing the results of Pradhan and Sharon with those of this experiment shows a similar trend in terms of sphere formation. Namely, the general trend in this study was the preferential formation of fused spheres at the highest temperature (950 °C). The lowest temperature (750 °C) also yielded a fair percentage of spheres. The three intermediate temperatures

(800 to 900 °C) yielded predominantly MWCNTs. (Table 5.3 summarizes the effect of temperature on the SCNMs formed.) Nyamori *et al.* also found high yields of well-formed MWCNTs at 800 and 900 °C under similar conditions.² In their experiments they also tested 1000 °C and found no CNTs. A parabolic curve (Figure 5.16) was obtained when the yield of MWCNTs was plotted for each temperature, with the three inner temperatures forming the highest part of the curve. This shows visually the suitability of 800, 850 and 900 °C for the formation of high yields of MWCNTs (in the collected raw yields).

Table 5.3 Results of TEM analysis for Experiment 1.

Exp. run	T _{max} (°C)	Approximate percent distribution of morphologies					MWCNTs			C spheres
		% Carbon spheres	% Carbon fibres	% Polygon structures	% Amorphous carbon	% MWCNTs	Ave. OD (nm)	Ave. ID (nm)	Length (µm) [#]	Ave. OD (nm)
1.1	950	73	-	-	25	2 ^α	-	-	-	1349.4
1.2	900	4	-	-	4	92	28.6	8.7	≈ 10	-
1.3	850	3	2	1	1	93	39.1	9.6	≈ 13	-
1.4	800	3	2	1	3	91	41.5	9.2	≈ 17	-
1.5	750	15	-	-	30	55	28.0	7.4	≈ 15	1045.4

^α The very small percentage did not allow for measurement in terms of OD, ID or length. [#] Representative longest MWCNTs.

*Note that the polynomial line is a best fit curve for the data points, and as a result the maximum is over 100%. In reality over 100% MWCNTs cannot, obviously, be achieved. Thus this line is merely generated to graphically display the general trend in percentage MWCNTs with temperature.

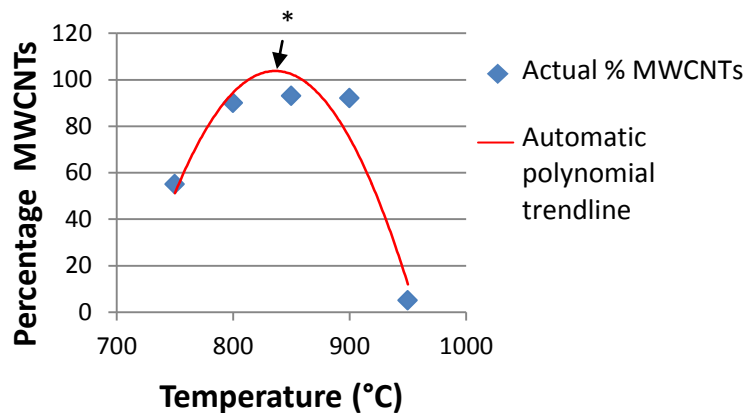


Figure 5.16

Parabolic curve showing the trend between temperature and percent MWCNT yield.

The quality of the MWCNTs, in the range 800 to 900 °C, was superior to that of MWCNTs obtained at the two outermost temperatures (750 and 950 °C). Specifically the MWCNTs tended to be straighter and “cleaner” (less amorphous material) between 800 and 900 °C. At 750 °C there are noticeably more defective tubes. These tubes are less straight and covered in a large amount of what appears to be amorphous material. The yield of amorphous carbon was also significant at the other extreme temperature (950 °C).

5.7.7.2 ID and OD of MWCNTs

Both the average OD and ID of MWCNTs values varied depending on the temperature and this will now be discussed. The average OD and ID values for this experiment are given in **Table 5.3** and are depicted graphically in **Figure 5.17** based on temperature variation. **Figures 5.18** and **5.19** show the spread of measurements used to generate the average values. Note that there are no values for the 950 °C material due to the very low MWCNT yield (2%).

The average ID values are similar for each T_{\max} , although the heights of the red bars in **Figure 5.17** do resemble a Gaussian-type shape which indicates that there is a maximum value. (The biggest average ID was found at 850 °C.) Nevertheless, it is both logical, and seen in the literature, that the ID of a growing MWCNT, at a specific temperature, does not vary as much over time as the OD.²⁴ (Note that where metal catalyst NPs remain trapped, the diameter of the tube can be altered at that specific point.¹²)

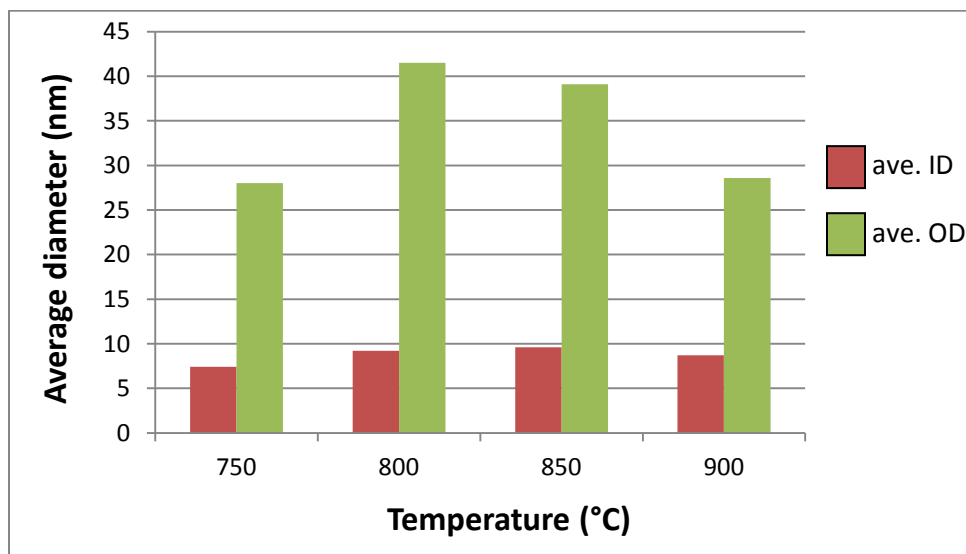


Figure 5.17 Histogram comparing the average inner and outer diameters of MWCNTs produced in Experiment 1 for all temperatures except 950 °C (which yielded too few MWCNTs to analyze for ID and OD).

Regarding ODs, carbon layers can grow on the outside of CNTs for long periods of time after the initial tube formation.²⁴ Indeed basic kinetics tells us that a higher temperature would cause a higher reaction rate. Thus, at higher temperature, the faster the rate of formation of additional walls onto CNTs, the faster the rate the OD increases. Thus, in the same period of time, OD values would be expected to be larger at higher temperatures. Indeed, in this experiment the average OD values differ significantly for each temperature and this is seen graphically in **Figure 5.17**. Literature also suggests that the higher the temperature, the more the iron particles collide and coalesce, forming larger catalyst particles and thus larger diameter CNTs.^{25,26} In one study, when furnace temperature was the only variable, and temperature was increased, CNT diameters increased as evidenced by RBM peaks in Raman studies shifting to lower frequencies.⁴ Interestingly, an inverse relationship is seen here in this project, with larger OD values for lower temperatures (in the range 900 to 800 °C). One initial explanation for this

may be, simply, that 800 °C, as compared to 850 and 900 °C, is more suitable for the formation of CNTs specifically. In other words, 800 °C is optimal for MWCNT formation. This notion, that temperature may not directly correlate in all cases with CNT diameter, gives some corroboration to the proposal by Nasibulin *et al.*²⁷ They investigated the idea that catalyst particle diameter determines the diameter of SWCNTs, and showed that they are not necessarily related to the experimental conditions. They state, “The ratio between catalyst particle and CNT diameters was close to 1.6 and independent of the experimental conditions”. They go on to say that the growth process is “universal”. In a similar study to Experiment 1, [2.5 wt.% ferrocene in toluene, at 0.8 mL/min injection rate, 100 mL/min gas flow rate, 5% H₂ in Ar (v/v), temperatures tested 800, 900 and 1000 °C] 800 °C also gave the largest average OD value² which supports the results of this work. Herein, the largest average OD value (41.5 nm) was obtained at 800 °C.

It is interesting to note that the histogram distributions of the OD and ID for different population groups for each T_{\max} are not symmetric because a small percentage of the population can have a wide range of IDs and especially OD values. This again confirms the idea that as time passes during MWCNT formation, so the OD can continue to grow to large sizes by further addition of layers, although this is only for a small percentage of the population.

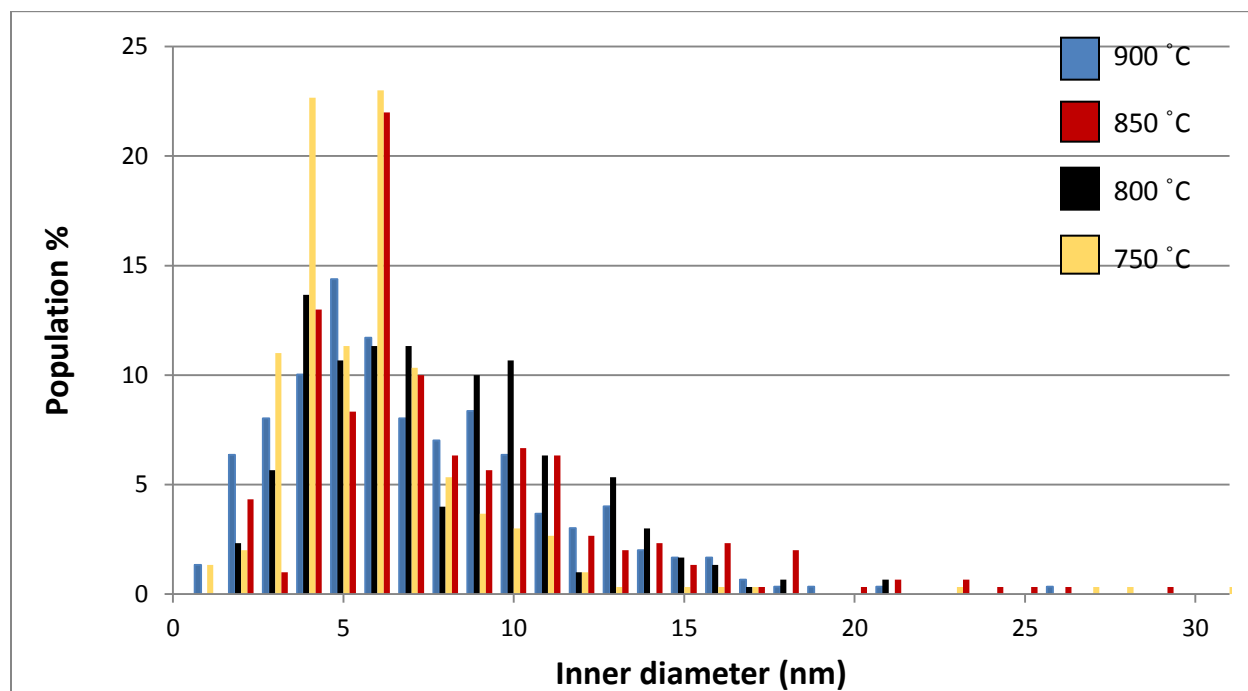


Figure 5.18 Histogram of the ID distribution for the MWCNTs obtained with 2.5 wt.% of catalyst [1] for $T_{\max} = 900$ to 750 °C.

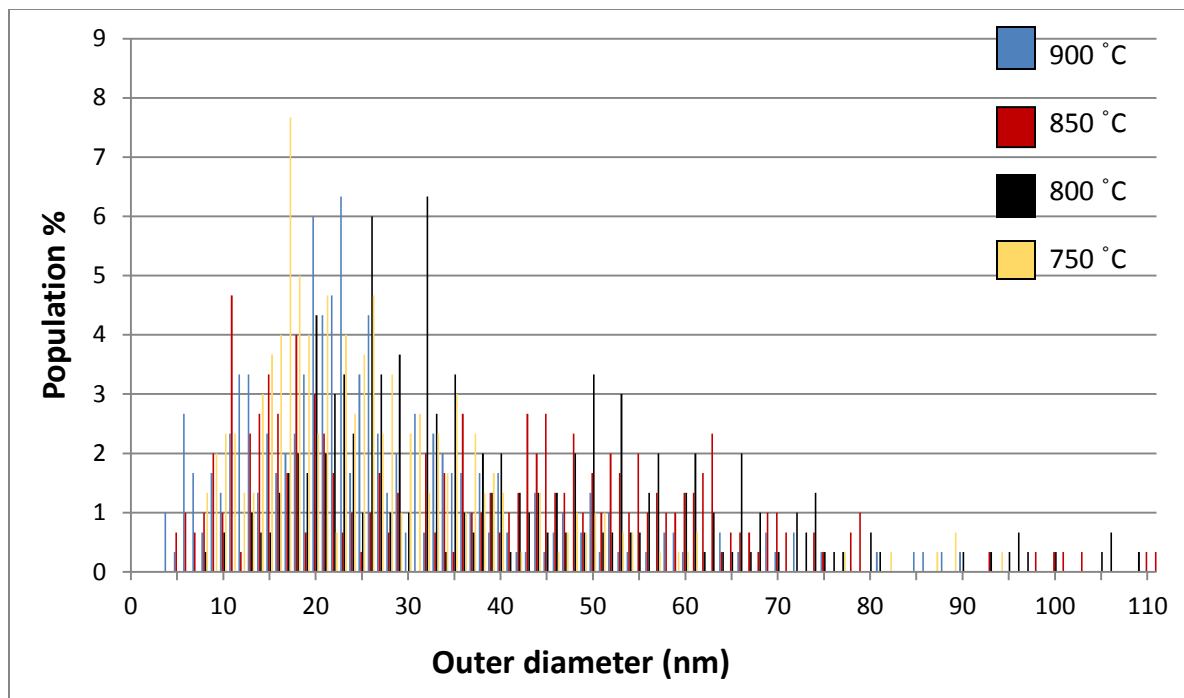


Figure 5.19 Histogram of the OD distribution for the MWCNTs obtained with 2.5 wt.% of catalyst [1] for $T_{\max} = 900$ to 750 °C.

5.7.7.3 Length of MWCNTs

The most conducive temperature for MWCNT growth, in terms of representative longest MWCNTs, from 2.5 wt.% [1] in toluene, is 800 °C, based on the data in **Table 5.3**. A trend of decreasing maximum length is apparent for temperatures decreasing from, or increasing from, 800 °C (see **Figure 5.20**). However, the length of the CNTs was correlated linearly to temperature by Lee *et al.*²⁸ However, several of their reaction parameters differed to those used here and thus we suggest that global reaction conditions, rather than individual parameters alone, affect product properties.

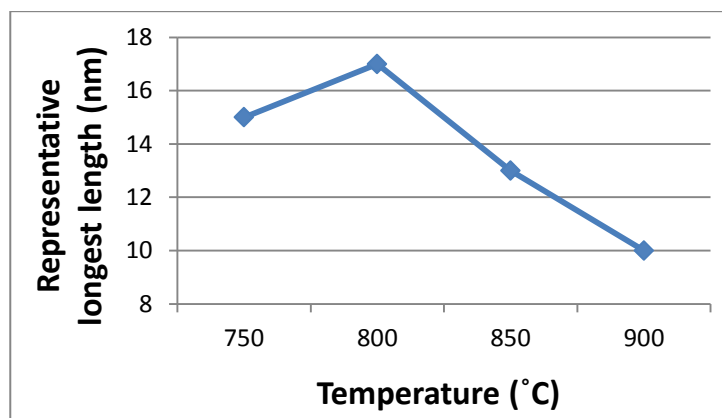


Figure 5.20 Graph showing the peak in representative longest MWCNT at 800 °C for Experiment 1.

5.7.7.4 Alignment of MWCNTs

All runs formed bundles of aligned CNTs [refer to **Figures 5.7, 5.9, 5.11 and 5.14 (B)**]. The product with the most well-aligned MWCNTs was the 800 °C material [**Figure 5.11 (B)**]. The 850 and 900 °C samples [**Figures 5.7 and 5.9 (B)**] also contain highly aligned MWCNTs, which is influenced by the low amount of amorphous carbon and few spheres (see **Table 5.3**). The high degree of alignment for the 800 °C material was discussed in **Section 5.7.5**. Well-aligned CNTs were also reported in the literature at 800 °C from ferrocene and xylene.¹⁴ Bundles at the extreme temperatures in the chosen range (950 and 750 °C) contained some bent and kinked CNTs as well as significantly larger amounts of amorphous carbon and spheres which would decrease CNT alignment. The results again confirm that temperatures in the range 800 to 900 °C are suitable for the growth of high quality MWCNTs. Deck and Vecchio explained how they believe “embryos” of CNTs pack onto a surface and force each other to grow in an aligned manner.²¹ If temperatures of 800, 850 and 900 °C are considered to be the most conducive for CNT growth based on percentage yields only, it is then logical to conclude that these large percentages of growing CNTs would correlate with alignment, according to the “embryo” model.

5.7.7.5 Size of spheres

The 950 and 750 °C runs produced significant quantities of spheres. Their size distributions are shown in **Figure 5.21**. The average sphere diameter (see **Table 5.3**) is larger for the higher of the two temperatures. This trend is thus: higher temperature correlates with larger sphere size.

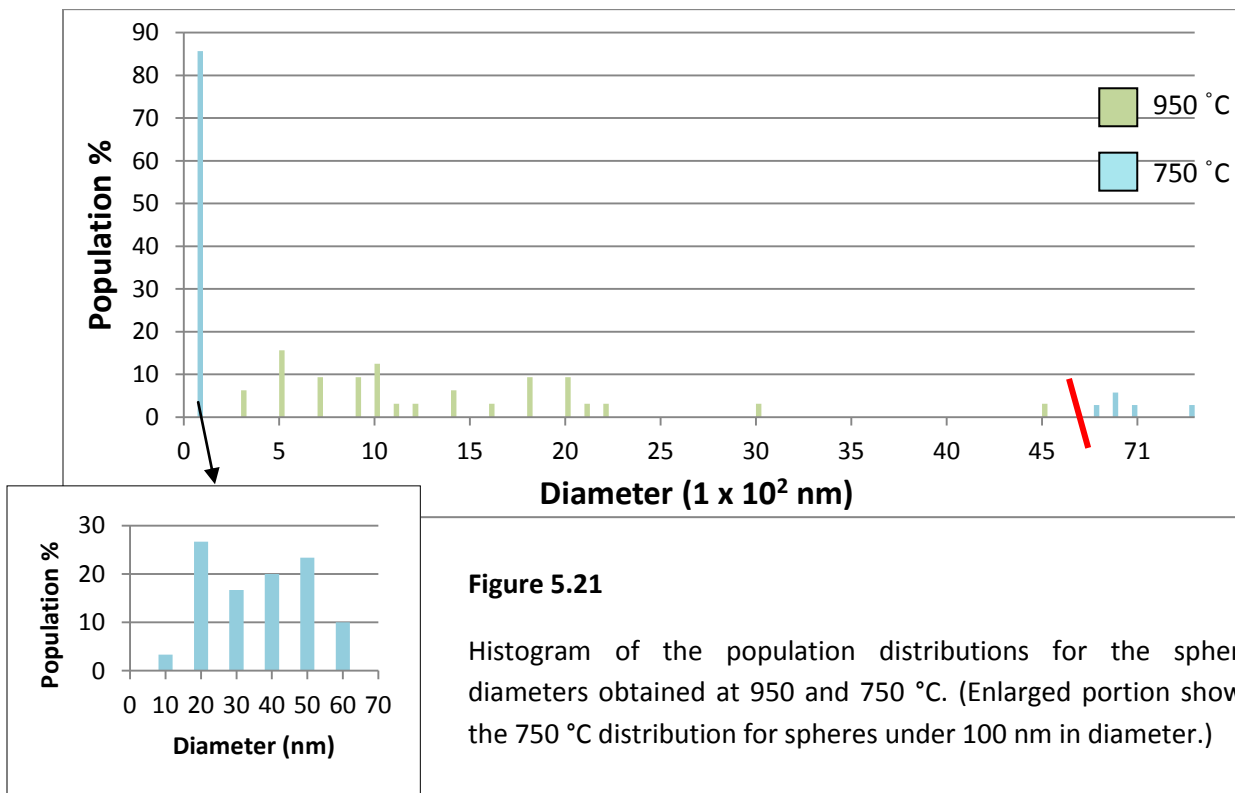


Figure 5.21

Histogram of the population distributions for the sphere diameters obtained at 950 and 750 °C. (Enlarged portion shows the 750 °C distribution for spheres under 100 nm in diameter.)

The most striking feature, perhaps, of the histogram in **Figure 5.21**, is that the bulk of the measurements from the 950 °C run lie dispersed up to about 2300 nm in diameter. In contrast, the 750 °C run yielded spheres in two major size groupings (0 - 70 nm, as shown in the insert, and 5000 - 10 000 nm approximately), with no intermediate diameters. (Note that the values to the right of the red line are not spaced at the same intervals as the values to the left of the line.) In other words, the 750 °C run conditions appear to be conducive for two sphere size groupings. No obvious relationship between temperature and sphere distribution is apparent from these results, although the two size groupings for the 750 °C run is of interest for further study.

5.7.7.6 Elemental composition (by EDX) of products

EDX was performed primarily to investigate CVD products qualitatively, although quantitative measurements were made as a preliminary investigation of elemental composition. Also, EDX is more suitable for thin layer or surface layer characterization, as it does not measure the whole sample, but only a small, unknown, volume of a material below the selected surface. Finally, quantitative EDX should be done against a standard sample for results to be truly meaningful. Such standards were not available at the time of this work. Thus, the quantitative data was merely used as a preliminary test for elements present. In terms of preliminary quantitative measurements, an average of two EDX spectra per SCNM type per temperature was recorded. (For more statistically reliable results many more structures per sample should be measured.) The percentages of carbon and iron present in CVD products, in terms of normalized weight percent, are summarized in **Appendix F, Table F.1**.

Occasionally, in the EDX spectra large Si, O or Al peaks were seen. The presence of Si and O were attributed to silica particles from the harsh product collection technique, namely the manual scraping of the CVD products off the quartz tube. This technique, which is at times vigorous, is the most plausible explanation of the existence of these element signals in the EDX spectra. However, confirmatory tests of Si:O ratios were not explored to confirm this theory. Also, an oxygen peak in the EDX spectra (as in **Appendix F, Figure F.1**) can be due to atmospheric O₂ which had adsorbed onto the CNTs.^{29,30} Al peaks can be attributed to the scattering of X-rays back from the aluminium stubs used to hold samples for SEM-EDX.

The preliminary EDX measurements, of those MWCNTs that were analyzed (see **Appendix F, Table F.1**), show that MWCNTs from runs 1.2 to 1.5 all contain approximately the same amount of carbon (\approx 95-97%) and iron (\approx 3-5%). Again, refer to the TGA results to be discussed in the next section since these are more conclusive and representative of the whole sample.

5.7.7.7 Crystallinity and thermal stability of products

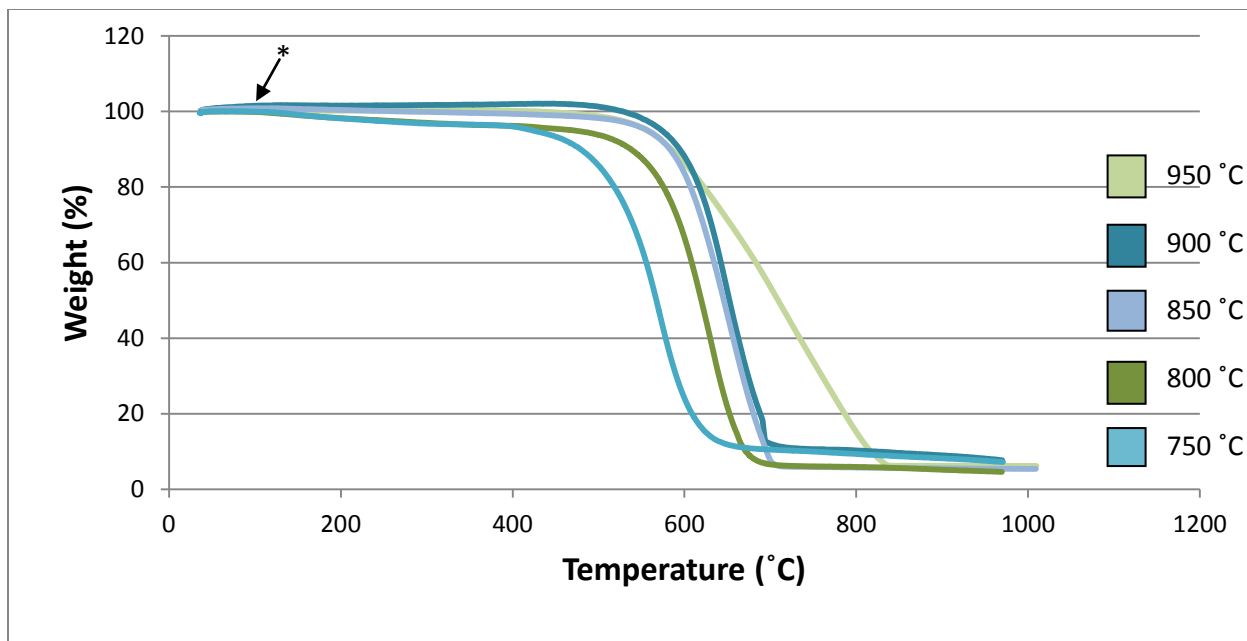
Table 5.4 shows the Raman spectroscopy data for Experiment 1. The intensity of the disorder and graphitic peaks (peaks characteristic of these types of materials) were compared as a I_D/I_G ratio. Lower ratios indicate samples which are less disordered and more crystalline (more graphitic). The three most

graphitized materials were those in the range 900 to 800 °C, which is the range containing very high yields of MWCNTs (> 90%) and very low percentages of spheres (< 5%). This supports the information in the TEM and SEM images in **Figures 5.7, 5.9 and 5.11** and the discussion in **Sections 5.7.7.1 and 5.7.7.4**, namely, the idea that this specific temperature range favours better quality MWCNTs. MWCNTs are, in general, more graphitic than spheres, but especially more so than large spheres. Deshmukh *et al.*, who reviewed carbon spheres, describe these structures as “layers of carbon that typically form broken concentric layers emanating from the core”.³¹ In other words, larger spheres tend to have short, broken (more disordered), overlapping “platelets” of graphite forming the outer shells. The 900 °C material had the lowest I_D/I_G ratio. Thus, this material is the most ordered. It was interesting to note that 800 °C, compared to 900 and 850 °C, was the least graphitic in nature (highest I_D/I_G ratio). As was discussed in **Section 5.7.5**, this material gave the most highly aligned CNTs. These two pieces of information seem to be contradictory and suggest that good alignment may not be a factor indicating high crystallinity. The trend for this temperature range (800 to 900 °C) is increasing crystallinity with increasing temperature (see also **Appendix G, Figure G.1**). This trend is in agreement with the trends found by Lee *et al.*²⁸ They also found an increase in crystallinity with increasing T_{max} in similar experiments (also within the range 800 to 900 °C). In this project the 750 °C material also obeys this trend, although its increased disorder can be easily explained by its larger sphere content. Notably, the most disordered material, from the data, was that which contained the most carbon spheres (950 °C) (see also **Table 5.3**). Literature has shown that spheres can give high I_D/I_G ratios which are indicative of disorder.³²

Table 5.4 Results from Raman spectroscopy analysis for Experiment 1 materials.

Catalyst conc. (wt.%)	T_{max} (°C)	“Disorder” D-band (cm^{-1})	“Graphitic” G-band (cm^{-1})	I_D/I_G ratio
2.5	950	1351	1595	0.882
	900	1353	1579	0.439
	850	1350	1581	0.738
	800	1353	1581	0.755
	750	1351	1557	0.764

TGA studies generated **Figure 5.22** (see also **Figure H.1** in **Appendix H**) for the decomposition of materials in air. Data from this figure is summarized in **Table 5.5**. All products have classic smooth decomposition curves characteristic of graphitic materials.



* Note: this region has a slightly increasing gradient, which indicates a slight gain in mass by the sample. Presumably this is iron in the samples combining with oxygen in the air to form solid iron oxides, thereby increasing the mass of the system.

Figure 5.22 TGA weight loss profiles obtained in air for the products produced in Experiment 1.

The TGA decomposition ranges, as will now be discussed, support the idea that the range 800 to 900 °C is best for high quality MWCNT formation. The 950 °C material decomposes over the largest temperature range (approximately 500 to 830 °C) indicating it is highly heterogeneous (this is supported by the large SCNM distribution data in **Table 5.3**). The residue weight percent was 6.2%. This remnant material is most probably iron oxides³³, which do not vapourize in this temperature range. For the 900 °C material, decomposition of the material in air began at approximately 500 °C, finishing just before 700 °C. This generated a decomposition range of approximately 200 °C. Remaining behind was a weight percent of 7.7%. The temperature range for decomposition and vapourization of the carbonaceous material for the 850 °C sample was also approximately 200 °C and the remnant weight percent of iron compounds about 5.4 wt.%. For the 800 °C material decomposition occurs between 490 and 680 °C and the temperature of maximum oxidation occurs at a slightly reduced temperature (as indicated by ϵ in **Figure H.1** in **Appendix H**) compared to the common temperature value for the 850 and 900 °C materials (indicated by ρ). This material (800 °C) had the lowest iron/iron oxide residue of approximately 5.2 wt.%. The 750 °C curve shows two significant weight loss events. Firstly, there is a sudden drop in the curve between 25 and 150 °C which is most likely due to the volatilization of liquid and volatile organometallic species. This liquid is most likely radical condensates,¹¹ some of which was observed to pass right out of the reaction zone. The second weight loss event, the decomposition of the CVD products, began at approximately 400 °C and ended at 630 °C. The 750 °C material contains remnant iron compounds constituting 7.2 wt.%.

The trends identified from the initial decomposition temperatures, the decomposition ranges and the residue percentages respectively are listed below.

- (i) The order of increasing thermal stability is $750\text{ }^{\circ}\text{C} < 800\text{ }^{\circ}\text{C} < 850\text{ }^{\circ}\text{C} \approx 900\text{ }^{\circ}\text{C} \approx 950\text{ }^{\circ}\text{C}$.
- (ii) The order of increasing heterogeneity (in terms of SCNM distribution) is $800\text{ }^{\circ}\text{C} \approx 850\text{ }^{\circ}\text{C} \approx 900\text{ }^{\circ}\text{C} < 750\text{ }^{\circ}\text{C} < 950\text{ }^{\circ}\text{C}$.
- (iii) The order of increasing purity (in terms of iron content) is $900\text{ }^{\circ}\text{C} < 750\text{ }^{\circ}\text{C} < 950\text{ }^{\circ}\text{C} < 850\text{ }^{\circ}\text{C} < 800\text{ }^{\circ}\text{C}$.

The gradients of the weight loss profiles for decomposition for the three intermediate temperatures are all similar, which suggests a similar degree of product distribution. And, it was shown in **Section 5.7.7.1** that these three samples are indeed very similar in terms of product distribution. The TGA curves for the three best temperatures (800, 850 and 900 °C) can be compared with the two extreme temperatures (750 and 950 °C). In this case the former curves all drop off at a steeper rate than the latter (the 950 °C gradient is particularly shallow). This sharper gradient, combined with a narrower decomposition temperature range, indicates that these three temperatures consist of a smaller range of structure types, i.e. they are purer samples. Again, the SCNM distribution in **Table 5.3** confirms this.

Table 5.5 Decomposition temperature and residue weight percent of the products from Experiment 1.

Exp. run	T _{max} (°C)	Main decomposition range (°C)	Temperature of max. decomposition (°C)	Residual mass percent (%)
1.1	950	≈ 500 to 830	729	6.2
1.2	900	≈ 500 to 700	649	7.7
1.3	850	≈ 500 to 700	650	5.4
1.4	800	≈ 490 to 680	634	5.2
1.5	750	≈ 400 to 630	571	7.2

5.7.7.8 Surface area of products

Results of BET analysis for Experiment 1 are shown in **Figure 5.23**. (Note that BET studies were not done for every experiment in this project due to very low yields obtained. Products of Experiment 1 were analyzed, however, to get a preliminary idea on the relationship between BET surface area and SCNM types in a material.)

No obvious trend is observed when the BET surface areas for the products from Experiment 1 are compared, unless the 850 °C value is considered as an anomaly. However, two important factors are noticeable. Firstly, large percentages of spheres lower the overall surface area of a material (see the very low surface area of about 3 m²/g for the 950 °C run), and higher percentages of MWCNTs give rise to larger surface area measurements (900 to 750 °C all have comparatively much higher surface areas – by an order of magnitude). Secondly, the 800 °C material has the highest BET surface area. This

indicates that this material is more suitable for use as a catalyst support, in terms of surface area, since high surface areas are favourable.

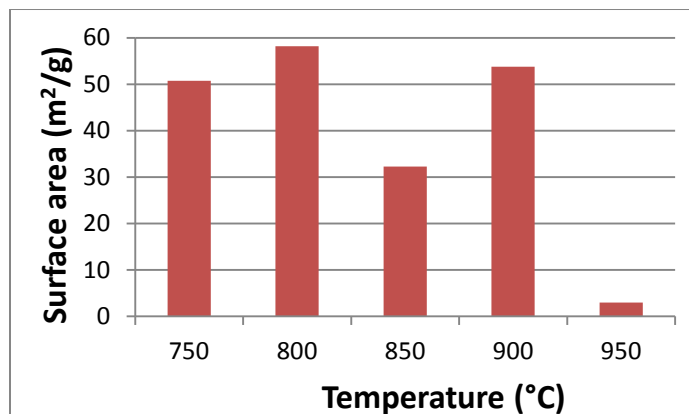


Figure 5.23

Histogram of the relative surface areas of the products synthesised for the temperature values of Experiment 1.

5.7.8 Anomalous structures

In all samples from all Experiments (1-6), very small percentages of anomalous structures were seen under TEM. Their very low occurrence makes these structures statistically insignificant. Nevertheless, some images, from various runs, were selected to display such structures. Refer to **Figure 5.24** for the following brief discussion on anomalous structures.

The thinner CNTs were, at times, twisted or buckled (image **A** and enlargement **B**), resulting in thinner diameters at these points.³⁴ Ends of CNTs tended to be closed, and fairly uniform in diameter, but occasionally the tips tapered (image **C**). Very rarely were coiled MWCNTs seen (image **D**). The highlighted section in image **E** shows a tube within a tube and a part of an exposed inner tube.

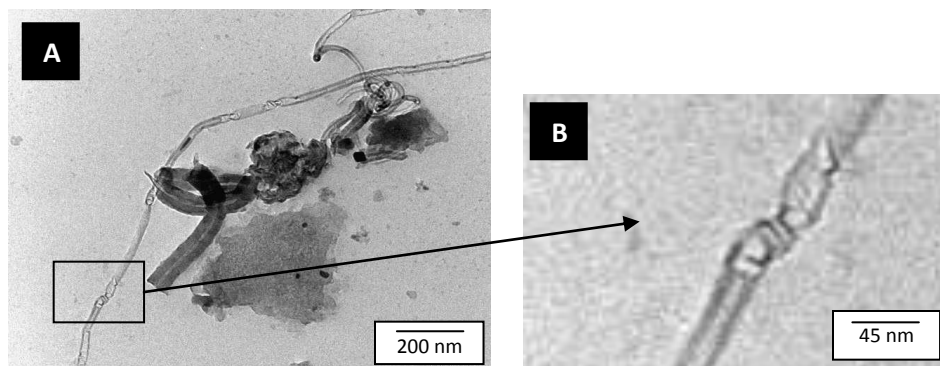


Figure 5.24 (continued on the next page).

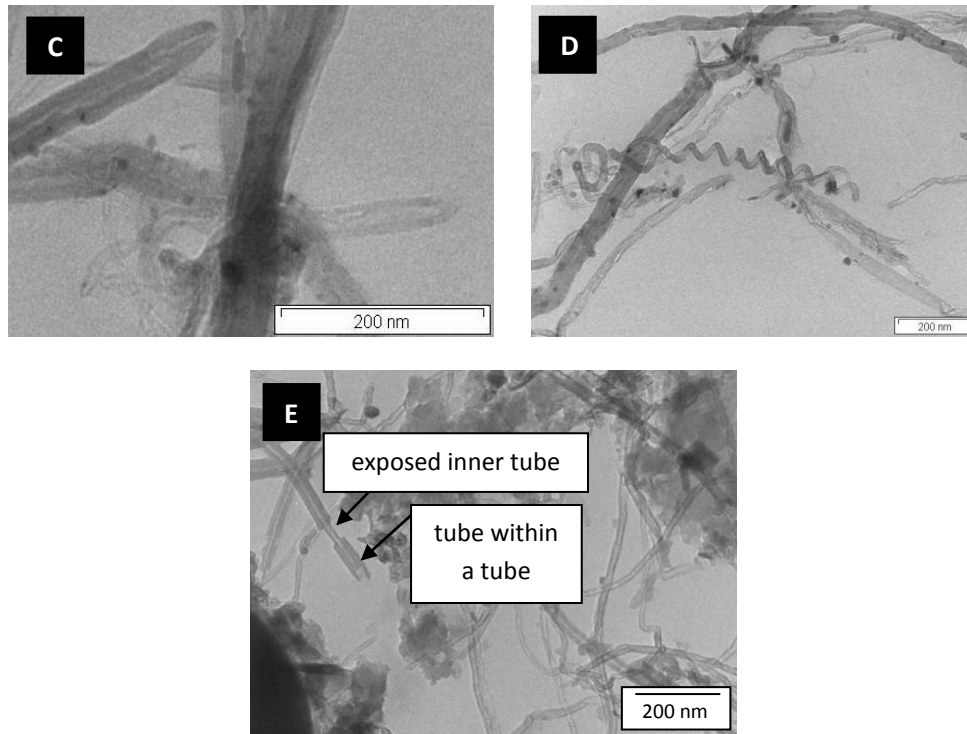


Figure 5.24 Selected images taken from various runs showing infrequently occurring structures.

(Such anomalous structures are unlikely to significantly affect the overall properties of the materials, because of their low occurrence. However, it is interesting and important to be aware of the existence of such structural differences when examining materials since, if they are prevalent in a material, these minor structural changes may affect the bulk properties.)

5.7.9 Conclusions from Experiment 1

- Ferrocene at 2.5 wt.% concentration is an effective catalyst for producing MWCNTs and micro- or nanospheres at all five chosen temperatures (950, 900, 850, 800 and 750 °C).
- Toluene is a suitable carbon source for the synthesis of SCNMs in the range 750 to 950 °C.
- In general, the higher the T_{\max} , the higher is the raw yield, although yields were low (< 20%).
- On either side of the range 800 to 900 °C sphere formation is favoured, especially above 900 °C.
- The lowest chosen temperature, 750 °C, gives an extremely heterogeneous material, although it is low in iron.
- TEM and SEM results indicate that MWCNTs are produced in the highest yield in the range $T_{\max} = 800$ to 900 °C, with greater alignment than at other temperatures.
- The highest average OD and ID values are for MWCNTs formed at a T_{\max} in the range 800 to 900 °C.
- The representative longest MWCNT was found to be 17 μm for a T_{\max} of 800 °C.

- Agreement between TEM, SEM and TGA analyses also showed that the samples in the range 800 to 900 °C are purest in terms of structure distribution, especially in the middle of this range (850 °C).
- Thermal stability was similar for $T_{\max} = 800$ to 950 °C (750 °C being the least thermally stable).
- Crystallinity is also highest in the range 800 to 900 °C, especially at the higher end of the range.
- Surface areas are highest in the range 800 to 900 °C (excluding 850 °C), making these materials better supports for metal catalysts than the extreme temperatures (950 and 750 °C).
- Irregularities in MWCNT structure (for example coiling and tapering of tips) were rare, and thus were not considered to have significant effects on bulk properties. For this reason such structural abnormalities were not studied further.

From the above summarized conclusions, it was decided that the best T_{\max} range, overall, was 800 to 900 °C, because of high yields of MWCNTs, long MWCNTs, larger surface areas, better thermal stability, low iron content (especially the 800 °C material) and high crystallinity. Experiment 2 was thus performed at these three temperatures, but at double the concentration of catalyst to investigate the effect of catalyst concentration.

Before Experiment 2 is discussed, a comparison of the three purification methods attempted is discussed.

5.8 Results and discussion of purified MWCNTs from Experiment 1

Three purification methods were compared by using samples from Experiment 1 ($T_{\max} = 900$ °C).

Method 1

This method made use of 0.050 g MWCNTs and 3:1 H_2SO_4 : HNO_3 (98%:55%) combined with heating at 120 °C for 30 minutes. TEM studies revealed that the harsh conditions of this purification method not only remove large quantities of iron (as evidenced by the decrease in dark areas between the micrographs in **Figure 5.25** and the image in **Figure 5.7**), but TEM images also showed that this method breaks CNTs into many shorter pieces. It is difficult to determine how much amorphous carbon has been removed as there was so little to begin with.

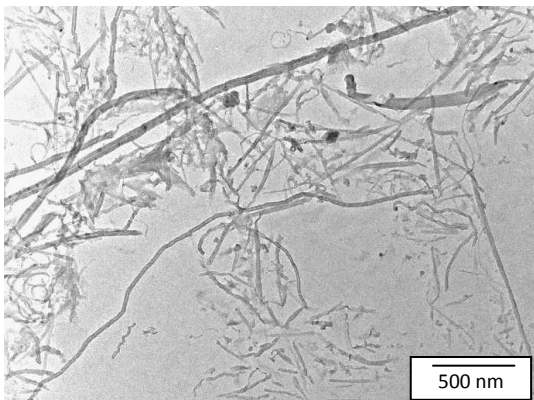


Figure 5.25

Micrograph of a sample from Experiment 1 (900 °C) purified by 3:1 H_2SO_4 : HNO_3 (98%:55%) at 120 °C for 30 minutes.

An advantage of this method is its time-efficiency, although the strong oxidizing conditions may cause roughening of tube walls and thereby decrease crystallinity.¹⁵ Roughening of the surfaces of MWCNTs is directly related to the acid conditions used, i.e. high concentration and longer time of acid treatment gave rougher tubes in the same experiments.¹⁵ Roughening may actually be an advantage, however, since this could increase the surface area and it has been shown that oxidizing acids provide more oxide groups for the attachment of metal palladium catalyst particles as was discussed in **Chapter 2**.^{35,36} Nevertheless, the disadvantages of this method, perhaps, outweigh the advantages. Firstly, CNTs are so much shorter and thinner after this purification method that most are lost through, or are compacted in, the sintered glass disc during filtration. This reduces the yield considerably. [An attempt was initially made to separate the MWCNTs by centrifugation at high speeds (30 000 rpm), for up to six times, but this did not sediment the CNTs sufficiently. Hence, decantation of the supernatant resulted in loss of product.]

Method 2

This method made use of milder conditions than Method 1, namely, sonication of 0.050 g MWCNTs in 30% HNO₃ followed by mechanical stirring in this acid solution for five days. There is also a marked difference between the products from this purification technique (see **Figure 5.26**) and those from Method 1 (see **Figure 5.25**), which indicates that this method is less harsh. When comparing **Figure 5.26** with **Figure 5.7**, it can be seen that this method, although time-consuming, is effective at removing much of the iron impurity, as evidenced by fewer dark areas. There still appears to be a small amount of amorphous carbon.

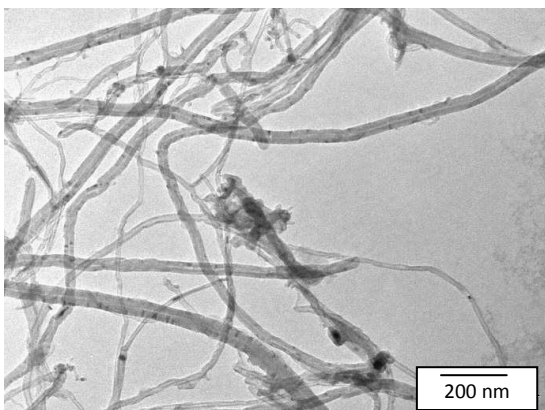


Figure 5.26

Micrograph of a sample from Experiment 1 (900 °C) purified by sonication in 50 cm³ of 30% HNO₃ for 30 minutes followed by stirring for five days at room temperature.

Method 3

The final method tested was also a comparatively mild approach. It consisted of refluxing 0.144 g of MWCNTs in 3 M HNO₃ for 24 h. The TEM image from this method (**Figure 5.27**) also shows a reduction in dark (Fe) areas compared to the unpurified sample (**Figure 5.7**).

In order to further assess the effectiveness of the three purification techniques, thermograms of the purified materials (**Figure 5.28**) were obtained and compared with that of the as-synthesized material.

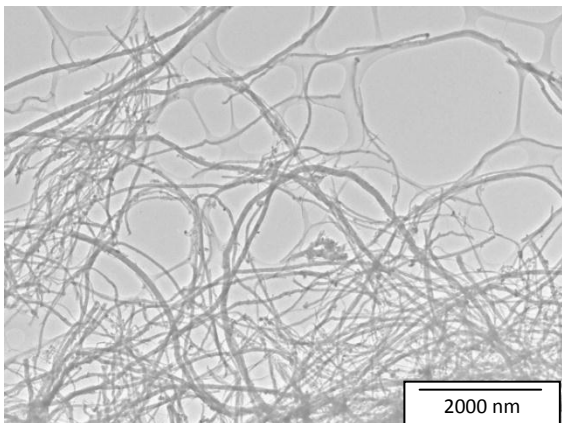
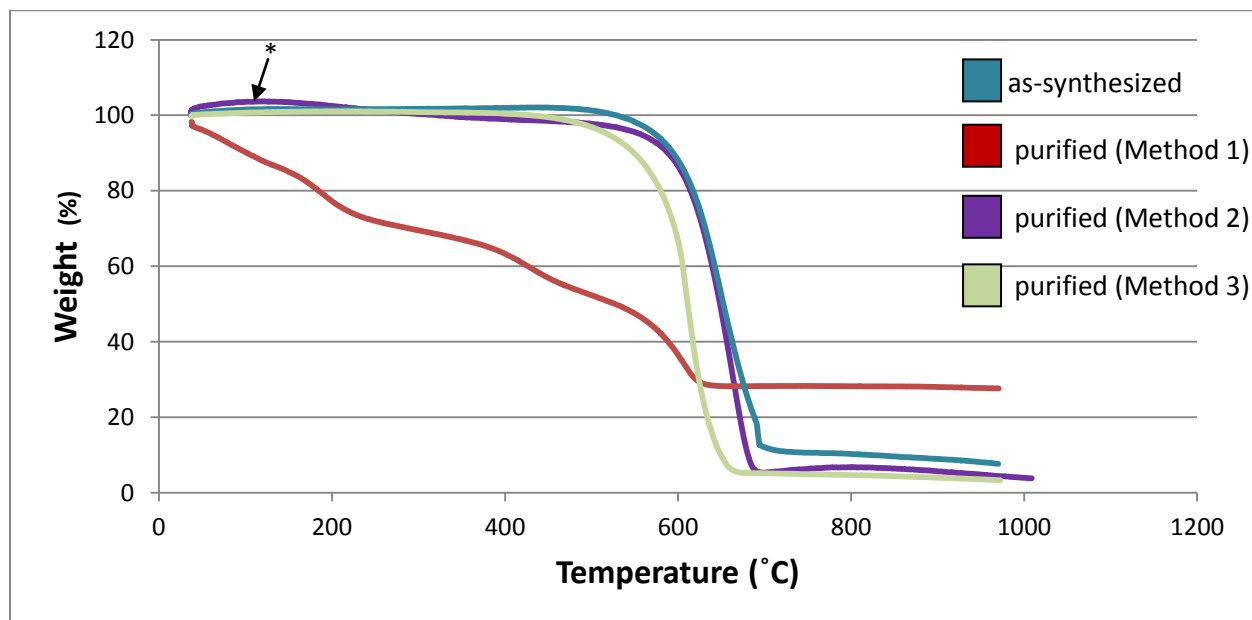


Figure 5.27

Micrograph of a sample from Experiment 1 (900 °C) purified by refluxing in 3 M HNO₃ for 24 h.



* Note: this region has a slightly increasing gradient, which indicates a slight gain in mass by the sample. Presumably this is iron in the samples combining with oxygen in the air to form solid iron oxides, thereby increasing the mass of the system.

Figure 5.28 TGA thermograms of samples obtained from Experiment 1 (900 °C) purified by the three purification methods *versus* the as-synthesized thermogram.

Method 1 was discarded as it was considered too harsh, resulting in low yields and low thermal stability. Regarding the thermal stability, **Figure 5.28** indicates that the sample purified by this method had several decomposition temperatures indicating that the purification procedure greatly altered the integrity of the MWCNTs. Harsh oxidizing conditions produce more oxide groups on the MWCNTs, which presumably lowers their thermal stability. Notably the sample decomposed rapidly even from room temperature. The relative percentage of iron residue approximates 28% as compared to 13% of the unpurified sample. This increased value indicates a significant loss of carbonaceous material from the crude product relative to the loss of iron in this purification technique. The larger relative percentage of iron after purification may have catalyzed the decomposition process, making it occur at

lower temperatures. Although annealing techniques could improve the crystallinity and thereby the thermal stability, the low yield remained a factor in discarding this method.

Methods 2 and 3 were milder techniques producing more thermally stable samples than from Method 1. Both techniques also gave larger yields than Method 1. Both decreased the relative percent of iron from 13% down to 5%. In other words, the purity (in terms of remnant iron) increased from 87% to 95%. The slight increase in the residual mass percent for Method 2 is most likely because of a further oxidation of iron. However, comparing these advantages of Methods 2 and 3, Method 3 was chosen for purification of other samples in this project since it has the added benefit of being less time-consuming. It was decided to use the Method 3-purified products without annealing processes, since it is known that the formation of defect sites and oxide groups on the CNTs aids metal NP deposition,³⁵ which is one of the aims of this project.

5.9 Results and discussion of Experiment 2 – Effect of temperature and concentration

Experiment 2 was carried out at the three best temperatures of Experiment 1 (800 to 900 °C), except that 5 wt.% catalyst [1] (ferrocene) was used (instead of 2.5 wt.% as in Experiment 1). All other reaction conditions were unchanged. A separate, in-depth discussion of each run of Experiment 2 will not be given as was done for Experiment 1. However, a comparative discussion of the results from Experiment 2 will be immediately commenced and contrasted and compared with the trends from Experiment 1.

5.9.1 Raw yields

The yields produced followed the expected trend reported in literature as mentioned previously, namely, higher temperatures yield more product (see **Table 5.6**).⁸

Table 5.6 Percentage raw yields of products from Experiment 2.

Exp. run	T _{max} (°C)	Percentage raw yield of SCNMs (%)
2.1	900	12.1
2.2	850	5.6
2.3	800	5.5

5.9.2 SCNMs formed

Each T_{max} in this experiment yielded a similar distribution of SCNM types (see **Table 5.7** for representative TEM and SEM images from each run of Experiment 2 and **Table 5.8** for the TEM analysis). Specifically all three temperatures yielded > 80% MWCNTs (with respect to the collected material, whose yields were low; < 13%).

When comparing the percentages of MWCNTs obtained in this experiment with those from Experiment 1 (see **Section 5.7.7.1**) a common trend is evident. Namely, the temperatures 800, 850 and 900 °C yield higher percentages of MWCNTs and lower percentages of spheres relative to other SCNM types in the collected material. This suggests that, for both Experiment 1 and 2, 800 to 900 °C is a conducive temperature range for MWCNT formation. Doubling the concentration of the catalyst (ferrocene) in this experiment did not seem to have a significantly large effect on the SCNM distribution, with only approximately a 10% decrease in MWCNT yields at all temperatures.

The quality of the MWCNTs in this experiment, in terms of bends, kinks and the like, appears to worsen as the temperature decreases. This will be discussed further in **Section 5.9.5**.

Table 5.7 TEM and SEM images of products from Experiment 2.

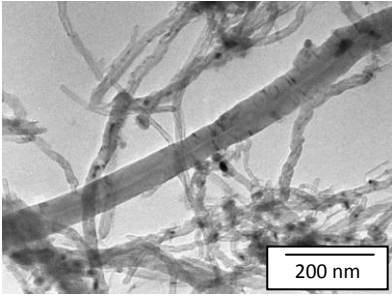
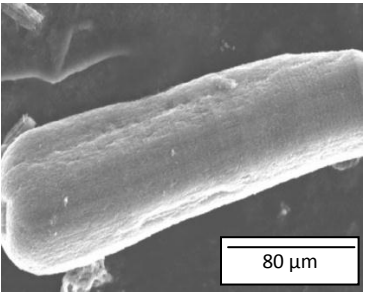
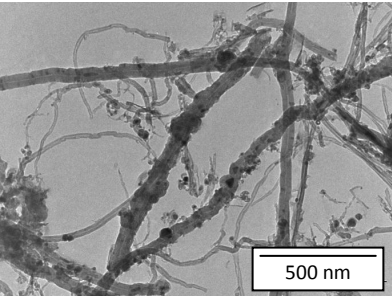
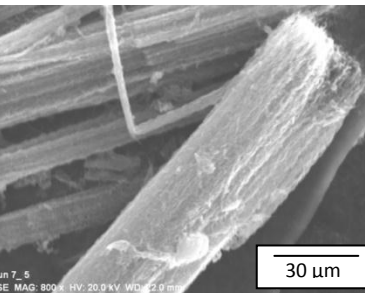
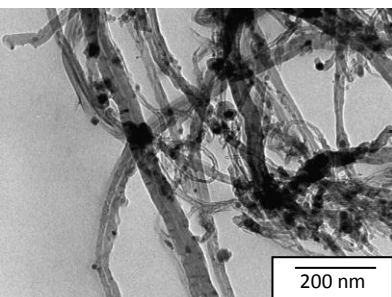
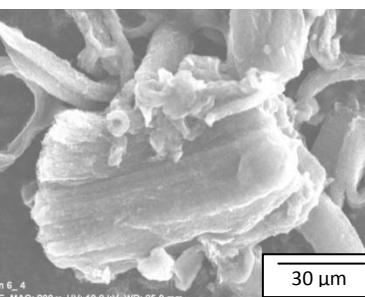
Exp. run	Cat- alyst	Cat. conc. (wt.%)	T _{max} (°C)	Representative TEM image	Representative SEM image
2.1	[1]	5	900		
2.2			850		
2.3			800		

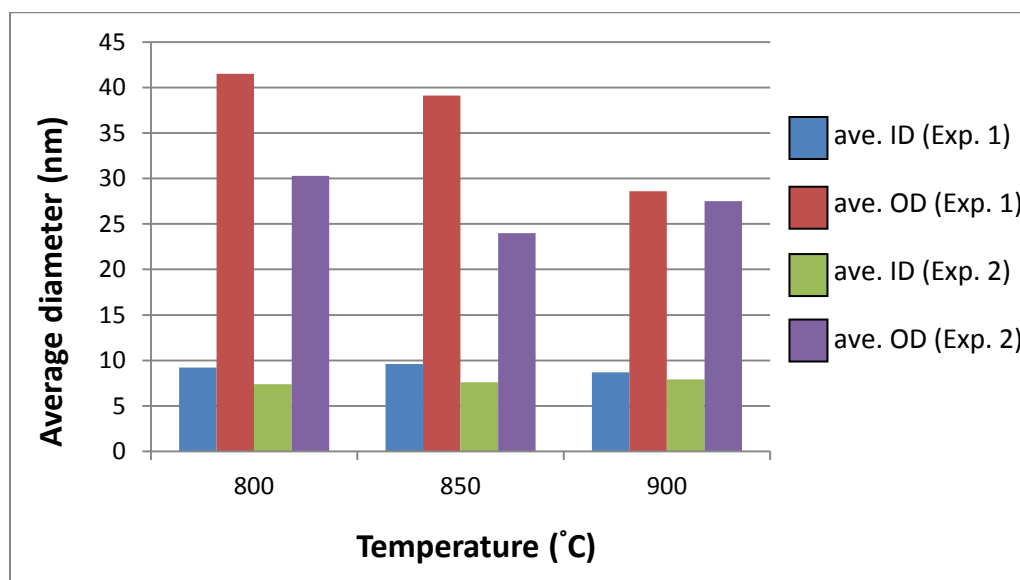
Table 5.8 Results of TEM analysis for Experiment 2.

Exp. run	T_{\max} (°C)	Approximate percent distribution of morphologies					MWCNTs		
		% Carbon spheres*	% Carbon fibres	% Polygon structures	% Amorphous carbon	% MWCNTs	Ave. OD (nm)	Ave. ID (nm)	Length (μm) [#]
2.1	900	9	-	-	9	82	27.5	7.9	≈ 7
2.2	850	6	1	1	8	84	24.0	7.6	≈ 8
2.3	800	3	-	-	11	86	30.6	7.4	≈ 4

* Note that sphere diameters were not measured in this experiment due to the low yields at all temperatures. [In experiments where the percentages of spheres is significant (> 10%), measurements were made.] [#]Representative longest MWCNTs.

5.9.3 ID and OD of MWCNTs

The average ID in this experiment decreased with a temperature decrease, from 7.9 nm at 900 °C to 7.4 nm at 800 °C (see **Table 5.8** and **Figure 5.29**). As was the case in Experiment 1, the ID values were not significantly different from each other. This was seen in the literature too.²⁴ However, comparing Experiments 1 and 2 average ID values, a trend is noticeable. Namely, Experiment 1 (2.5 wt.% catalyst) produced larger IDs than Experiment 2 (5 wt.% catalyst). This trend contradicts what is logically expected; that higher catalyst concentration would result in a higher rate of collision and coalescence of metal NPs in the CVD reactor, which would result in a wider ID.²² However, some of the literature contradicts this understanding that ID (or indeed OD) is related to the metal NP size,²⁷ as was discussed in **Chapter 1, Section 1.6.3**.

**Figure 5.29**

Histogram comparing the average OD and ID for MWCNTs from the 2.5 and 5 wt.% catalysts at 800, 850 and 900 °C.

The average ODs did differ significantly in this experiment. The outermost temperatures (900 and 800 °C), have higher values than at 850 °C (see **Figure 5.29**), i.e. no obvious trend of changing OD value with changing temperature, unless the OD value at 850 °C is not considered. In similar experiments, with ferrocene (5 wt.%) in toluene, at the same injection rate, the mean OD generally increased with increasing temperature in the range 800 to 1000 °C as may be expected according to the theory that increasing temperature increases the size of metal catalyst NPs.⁸ Singh *et al.* also found that higher ferrocene concentrations in toluene, in the CVD synthesis of CNTs, gave larger average ODs.²⁶ The OD results of this experiment were then compared with those from Experiment 1. This comparison showed that the average OD values in Experiment 1 (2.5 wt.% catalyst) are larger than in Experiment 2 (5 wt.% catalyst). (The same trend was found when comparing the average ID values as was just discussed.)

In summary, doubling the concentration of catalyst did influence both the average IDs and ODs as compared with the average IDs and ODs of Experiment 1, specifically, by decreasing these values. In experiments with ferrocene and toluene at 5 wt.% and 10 wt.% catalyst, the OD values of CNTs were also smaller at the higher concentration.⁸

Figures 5.30 and 5.31 show the ID and OD distribution histogram plots for the three T_{\max} values of Experiment 2. The tailing-off of both graphs again shows how the larger diameters vary widely for small groups of the population.

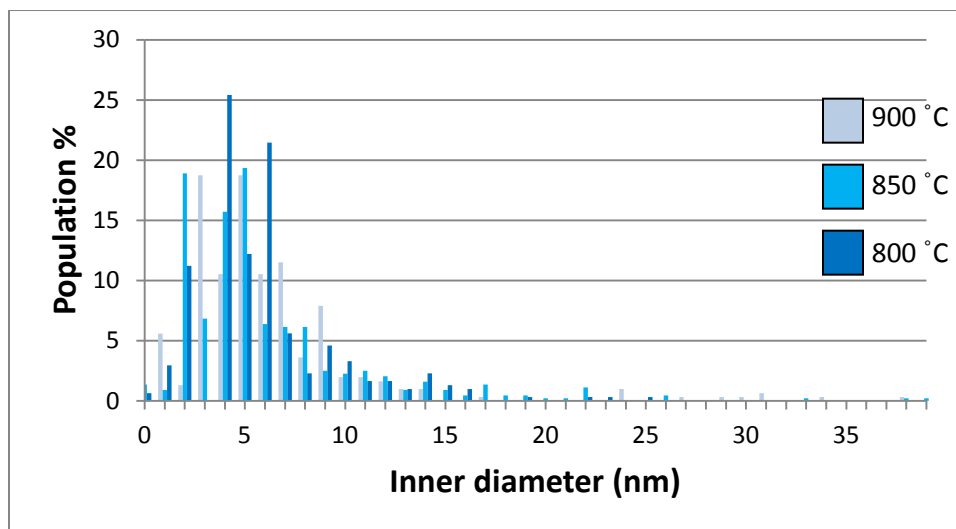


Figure 5.30 Histogram of the ID distribution for the MWCNTs obtained with 5 wt.% of catalyst [1].

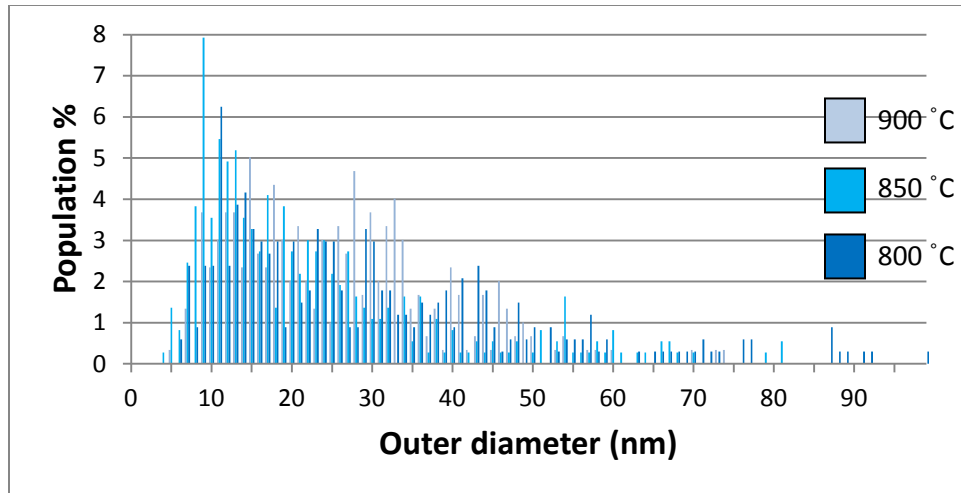


Figure 5.31 Histogram of the OD distribution for the MWCNTs obtained with 5 wt.% of catalyst [1].

5.9.4 Length of MWCNTs

The representative longest MWCNTs in Experiment 2 were found in the 850 °C sample (approximately 8 μm) (see **Table 5.8**). The 900 °C material had a value of 7 μm . These two values are considerably closer than that of the 800 °C material, whose value is noticeably smaller, namely 4 μm . Considering this, the general trend is an increasing length for an increasing temperature. However, the values from this experiment are significantly decreased as compared to those from Experiment 1 (see **Table 5.3** and **Figure 5.32**). This suggests that at a higher concentration (5 wt.%) the growth of MWCNTs is not as favourable as at the lower concentration (2.5 wt.%). These results may suggest again, that the effect of temperature does not work alone, but that a combined, nett, effect of temperature and concentration of catalyst may occur.

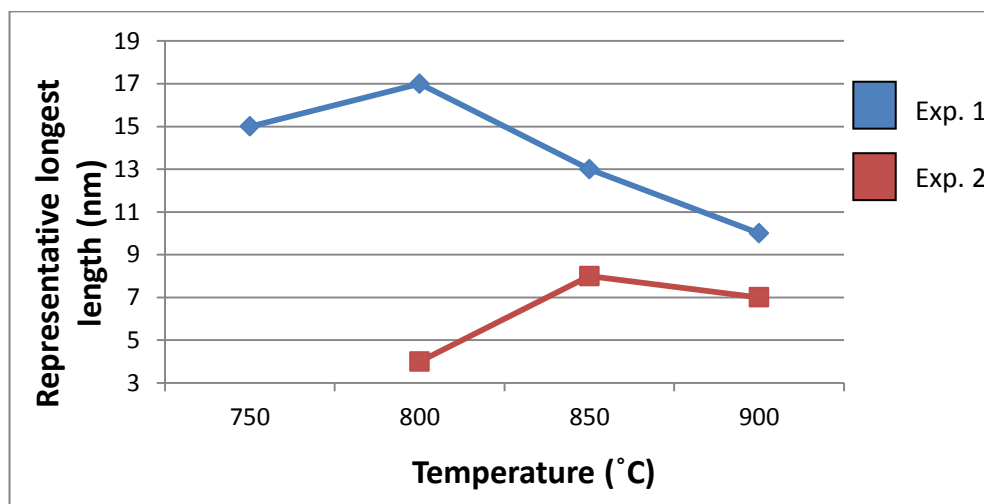


Figure 5.32 The representative longest MWCNTs at each temperature from Experiments 1 and 2.

5.9.5 Alignment of MWCNTs

As in Experiment 1, all runs yielded aligned CNTs. Ferrocene as the catalyst and toluene as the carbon source, under similar conditions, have produced “mats” of aligned CNTs in the literature.²⁶ The material with the most well-aligned MWCNTs (see **Table 5.7**) is difficult to distinguish, although the SEM images for the 900 and 850 °C materials show straight bundles suggesting well-aligned MWCNTs. These materials contain only slightly lower amounts of amorphous carbon than at 800 °C (see **Table 5.8**) and slightly more spheres which seem to not have had a significant effect on alignment due to their low abundance. However, the straightness of the CNTs in the main bundle in the SEM image in **Table 5.7** for the 800 °C material is poor, with the bundle “curling” at the ends. This suggests poorly ordered CNTs, or amorphous carbon-coated CNTs, which lead to the lack of good linearity of the bundle. In short, results suggest that the higher temperature (in the range 800 to 900 °C) at 5 wt.% catalyst concentration, favours enhanced alignment of MWCNTs.

In terms of concentration effects (Experiment 1 *versus* Experiment 2 results for the 800 to 900 °C materials), even a cursory glance at the SEM micrographs in **Figure 5.7** (900 °C) and **Figure 5.11** (800 °C) at 2.5 wt.% catalyst, appear to have better alignment of MWCNTs than the corresponding bundles at 5 wt.%. The bundles are more regular in shape at the lower catalyst concentration. The deduction is that the lower catalyst concentration (2.5 wt.% *versus* 5 wt.%) favours more highly aligned MWCNT bundle formation.

5.9.6 Crystallinity and thermal stability of products

The effect of temperature on crystallinity was investigated in this experiment as was done in Experiment 1. Chaisitsak *et al.* found that crystallinity was dependant on the temperature of the system.⁴ Raman spectroscopy analysis (**Table 5.9**) shows the 800 °C material to be the most graphitic in nature in this experiment (it has the smallest I_D/I_G ratio) while the 900 °C material was the most disordered. There is a definite trend of increasing disorder with increasing temperature seen in these results. This trend is opposite to what is found in some of the literature. For example, Singh *et al.* found higher crystallinity at higher temperatures.²⁶

Table 5.9 Results from Raman spectroscopy analysis of Experiment 2.

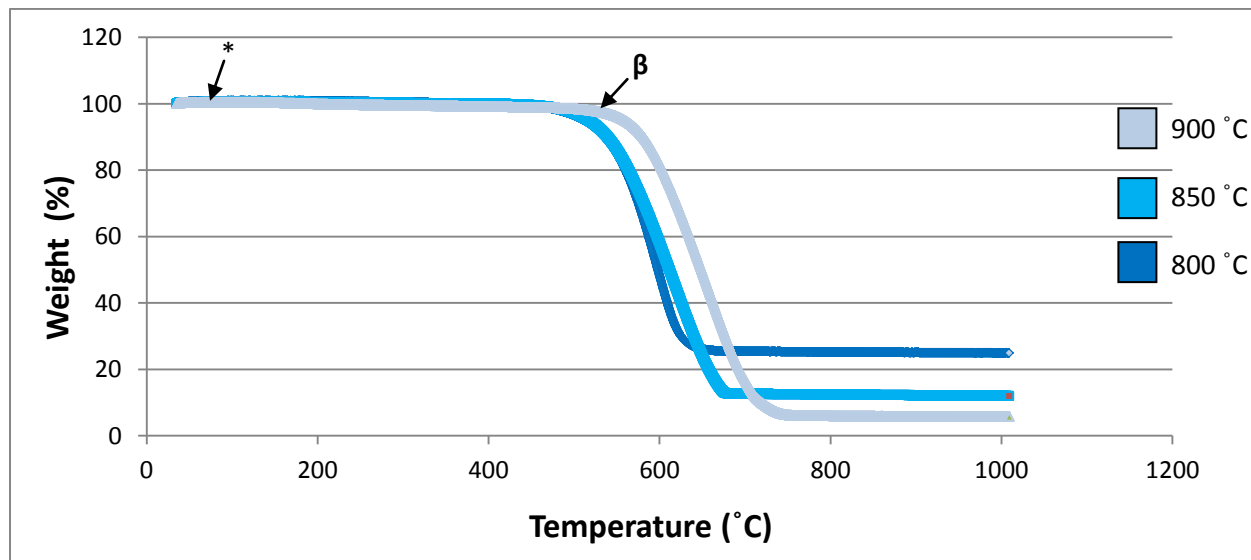
Catalyst conc. (wt.%)	T_{\max} (°C)	“Disorder” D-band (cm^{-1})	“Graphitic” G-band (cm^{-1})	I_D/I_G ratio
5	900	1350	1557	0.763
	850	1349	1579	0.732
	800	1350	1579	0.543

An inverse in the I_D/I_G ratio trend in Experiments 1 and 2 is observed – Experiment 1 favoured higher crystallinity at higher temperatures (in the range 900 to 800 °C) and Experiment 2 favoured higher

crystallinity at lower temperatures in this range. If the hypothesis that a net effect of temperature and concentration is true, i.e. temperature and concentration work in a co-dependent manner, it may be acceptable to say that in the range 800 to 900 °C, high crystallinity depends on both the concentration of catalyst and the temperature at which the material forms.

TGA results are shown in **Figures 5.33** and **Figure H.2** (the latter is in **Appendix H**). **Table 5.10** summarizes the important data from the thermograms. The 900 °C material is superior, having the highest temperature of onset of oxidation (highest thermal stability), at approximately 550 °C (see β in **Figure 5.33**), whereas the 850 and 800 °C materials begin decomposing at 500 °C. Also, the 900 °C material contains significantly less iron (5.8% versus 12.0% for 850 °C and 25.0% for 800 °C). However, the decomposition range for the 900 °C material is the largest, which indicates it has a bigger percentage spread of SCNM types (and lower percentage of MWCNTs relative to the other materials). This is supported by the data in **Table 5.8**. The smallest decomposition range is for the 800 °C material (see **Table 5.10**) which indicates that this material is more homogeneous in terms of SCNM types (containing the largest percentage of one type of SCNM, namely MWCNTs). This is confirmed in **Table 5.8**. The trends identified from the initial decomposition temperatures, the decomposition ranges and the residue percentages respectively follow.

- (i) The order of increasing thermal stability is 800 °C \approx 850 °C < 900 °C.
- (ii) The order of increasing heterogeneity (in terms of SCNM distribution) is 800 °C < 850 °C < 900 °C.
- (iii) The order of increasing purity (in terms of iron content) is 800 °C < 850 °C < 900 °C.



* Note: this region has a very slightly increasing gradient, which indicates a slight gain in mass by the sample. Presumably this is iron in the samples combining with oxygen in the air to form solid iron oxides, thereby increasing the mass of the system.

Figure 5.33 TGA weight loss profile in air for the products obtained from Experiment 2.

Thermal stability and purity (in terms of iron content) are perhaps the two most important pieces of information from the TGA studies. It is interesting to note that in both Experiments 1 and 2 the thermal stability increased with increasing T_{max} in general, for the range 800 to 900 °C. However, the trends for iron content are opposite for these experiments, with low iron content being favoured by low temperature at 2.5 wt.% catalyst and low iron content being favoured by high temperature at 5 wt.% catalyst concentration. Yet again the inference is that concentration and temperature cannot work independently in CVD experiments.

Table 5.10 Decomposition temperature and residue weight percent of the products from Experiment 2.

Exp. run	T_{max} (°C)	Main decomposition range (°C)	Temperature of max. decomposition (°C)	Residual mass percent (%)
2.1	900	≈ 550 to 775	653	5.8
2.2	850	≈ 500 to 680	617	12.0
2.3	800	≈ 500 to 620	594	25.0

5.10 Conclusions from Experiment 2

- The higher the T_{max} , the higher is the raw CVD yield, although yields were low (< 20%) which is a consistent trend regardless of catalyst concentration.
- Doubling the catalyst concentration decreased the percentage of MWCNTs produced, thus SCNM type must be dependent on catalyst concentration.
- A higher catalyst concentration (5 wt.% *versus* 2.5 wt.%) decreases the representative longest length the MWCNTs can reach.
- Alignment is poor at 800 °C when the 5 wt.% catalyst is used (but good for the 2.5 wt.% catalyst), showing that catalyst concentration directly affects alignment.
- Homogeneity (predominantly MWCNTs) increases as temperature decreases in the range 900 to 800 °C for the 5 wt.% catalyst.
- A higher concentration of catalyst results in smaller average OD and ID values.
- Crystallinity increases with decreasing temperature over the range investigated when the concentration is 5 wt.%, which therefore must be a catalyst concentration effect, as this trend is opposite at half the catalyst concentration.
- The highest thermal stability at this higher catalyst concentration is for the 900 °C material, which is also the purest in terms of trapped iron particles.

5.11 Summary of Experiments 1 and 2

Definite trends are seen in terms of temperature and concentration effects on the CVD products in Experiments 1 and 2. Nevertheless, at times the two parameters seem to work synergistically rather

than independently. In summary, 800 to 900 °C was found to be a suitable temperature range, with ferrocene being an efficient catalyst at both 2.5 and 5 wt.% concentration, for producing high yields (> 80%) of MWCNTs (with respect to the collected raw yields). Of the two catalyst concentrations, 2.5 wt.% produces the highest yields of MWCNTs with the longest lengths, best alignment and highest average OD values. MWCNTs were found to have a higher surface area than spheres. For both catalyst concentrations, low iron content seems to correlate with high disorder, although for the 2.5 wt.% concentration the highest disorder is for the 800 °C material, and for double the concentration, the 900 °C material.

In terms of purification techniques, Method 3 was chosen because it purifies the sample satisfactorily by decreasing the iron content to ≤ 5wt.% while yielding over 90% of product.

These results have shown that the material produced at 800 °C in Experiment 1 (2.5 wt.% ferrocene) is the most suitable material for use as a support for palladium, in terms of high percentage of well-structured MWCNTs, low iron content (even before purification), long length and relatively acceptable crystallinity. **Chapter 6** discusses the effect of heteroatoms in the catalyst on the CVD products and briefly evaluates their usefulness as potential catalyst supports.

References

- 1 A. I. Vogel, B. S. Furnis, A. J. Hannaford, P. W. G. Smith and A. R. Tatchell, *Vogel's Textbook of Practical Organic Chemistry*, 5th edition, Longman Group UK Limited with John Wiley and Sons Inc., UK, 1989, p 398
- 2 V. O. Nyamori, E. N. Nxumalo and N. J. Coville, *J. Organomet. Chem.*, 2009, **694**, 2222
- 3 N. Das, A. Dalai, J. S. S. Mohammadzadeh and J. Adjaye, *Carbon*, 2006, **44**, 2236
- 4 S. Chaisitsak, J. Nukeaw and A. Tuantranont, *Diamond Relat. Mater.*, 2007, **16**, 1958
- 5 H. Hu, B. Zhao, M. E. Itkis and R. C. Haddon, *J. Phys. Chem. B*, 2003, **107**, 13838
- 6 K. Mølhave, S. B. Gudnason, A. T. Pedersen, C. H. Clausen, A. Horsewell and P. Bøggild, *Ultramicroscopy*, 2007, **108**, 52
- 7 http://sbio.uct.ac.za/Webemu/SEM_school/EDX12.php (accessed 14 April 2011)
- 8 M. S. Mohlala, X.-Y. Liu and N. J. Coville, *J. Organomet. Chem.*, 2006, **691**, 4768
- 9 J. Qiu, Y. An, Z. Zhao, Y. Li and Y. Zhou, *Fuel Process. Technol.*, 2004, **85**, 913
- 10 H. M. Cheng, F. Li, G. Su, H. Y. Pan, L. L. He, X. Sun and M. S. Dresselhaus, *Appl. Phys. Lett.*, 1998, **72**, 3282
- 11 P. T. A. Reilly and W. B. Whitten, *Carbon*, 2006, **44**, 1653
- 12 H. Neumayer and R. Haubner, *Diamond Relat. Mater.*, 2004, **13**, 1191
- 13 V. O. Nyamori, S. D. Mhlanga and N. J. Coville, *J. Organomet. Chem.*, 2008, **693**, 2205
- 14 A. Cao, L. Ci, G. Wu, B. Wei, C. Xu, J. Liang and D. Wu, *Carbon*, 2001, **39**, 152
- 15 M. A. M. Motchelaho, H. Xiong, M. Moyo, L. L. Jewell and N. J. Coville, *J. Mol. Catal. A.: Chem.*, 2011, **335**, 189
- 16 P. Nikolaev, M. J. Bronikowski, R. K. Bradley, F. Rohmund, D. T. Colbert, K. A. Smith and R. E. Smalley, *Chem. Phys. Lett.*, 1999, **313**, 91
- 17 A. Leonhardt, S. Hampel, C. Müller, I. Mönch, R. Koseva, M. Ritschel, D. Elefant, K. Biedermann and B. Büchner, *Chem. Vap. Deposition*, 2006, **12**, 380
- 18 M. C. Schnitzler, M. M. Oliveira, D. Ugarte and A. J. G. Zarbin, *Chem. Phys. Lett.*, 2003, **381**, 541
- 19 V. O. Nyamori and N. J. Coville, *Organometallics*, 2007, **26**, 4083
- 20 L. Ci, B. Wei, J. Liang, C. Xu and D. Wu, *J. Mater. Sci. Lett.*, 1999, **18**, 797

- 21 C. P. Deck and K. Vecchio, *Carbon*, 2005, **43**, 2608
- 22 J.-W. Snoeck, G. F. Froment and M. Fowles, *J. Catal.*, 1997, **169**, 240
- 23 D. Pradhan and M. Sharon, *Mater. Sci. Eng. B96*, 2002, 24
- 24 M. Monthieux, H. Allouche and R. L. Jacobsen, *Carbon*, 2006, **44**, 3183
- 25 K. Kuwana and K. Saito, *Carbon*, 2005, **43**, 2088
- 26 C. Singh, M. S. P. Shaffer and A. H. Windle, *Carbon*, 2003, **41**, 359
- 27 A. G. Nasibulin, P. V. Pikhitsa, H. Jiang and E. I. Kauppinen, *Carbon*, 2005, **43**, 2251
- 28 Y. T. Lee, N. S. Kim, J. Park, J. B. Han, Y. S. Choi, H. Ryu and H. J. Lee, *Chem. Phys. Lett.*, 2003, **372**, 853
- 29 J. Hu, Y. Bando, J. Zhan, C. Zhi, F. Xu and D. Golberg, *Adv. Mater.*, 2006, **18**, 197
- 30 E. D. Dikio, F. T. Thema, C. W. Dikio and F. M. Mtunzi, *Int. J. Nanotech. Applica.*, 2010, **4**, 117
- 31 A. A. Deshmukh, S. D. Mhlanga and N. J. Coville, *Mat. Sci. Eng. R*, 2010, **70**, 1
- 32 H.-s. Qian, F.-m. Han, B. Zhang, Y.-c. Guo, J. Yue and B.-x. Peng, *Carbon*, 2004, **42**, 761
- 33 A. R. Harutyunyan, B. K. Pradhan, J. Chang, G. Chen and P. C. Eklund, *J. Phys. Chem. B*, 2002, **106**, 8671
- 34 Y.-F. Shi, H.-J. Quan, G.-B. Zheng, H. Sano and Y. Uchiyama, *Carbon*, 2002, **411**, 1674
- 35 C. Liang, W. Xia, M. van den Berg, Y. Wang, H. Soltani-Ahmadi, O. Schlüter, R. A. Fischer and M. Muhler, *Chem. Mater.*, 2009, **21**, 2360
- 36 Y. Suttisawat, P. Rangsunvigit, B. Kitiyanan, M. Williams, P. Ndungu, M. V. Lototskyy, A. Nechaev, V. Linkov and S. Kulprathipanja, *Int. J. Hydrogen Energy*, 2009, **34**, 6669

CHAPTER 6*

INFLUENCE OF HETEROATOMS (N, O AND S) ON THE SYNTHESIS OF MWCNTs AND OTHER SCNMs

This chapter discusses the results of the synthesis of MWCNTs and other SCNMs from catalysts [3], [4] and [5] (see Figure 6.1). These catalysts contain heteroatoms, namely nitrogen or sulfur and oxygen, and the effect of these heteroatoms on the SCNMs formed was investigated. The effect of temperature and concentration variation was also investigated. Catalysts [3] and [4] will be discussed together (Experiments 3, 4 and 5), since they contain the same heteroatoms (nitrogen and oxygen). Catalyst [5] will be discussed separately (Experiment 6) since it contains oxygen and a different heteroatom, namely sulfur. All reagents, instrumentation, synthesis, recovery and characterization methods were the same as those discussed in Chapter 5, Sections 5.1 to 5.4 and 5.6.

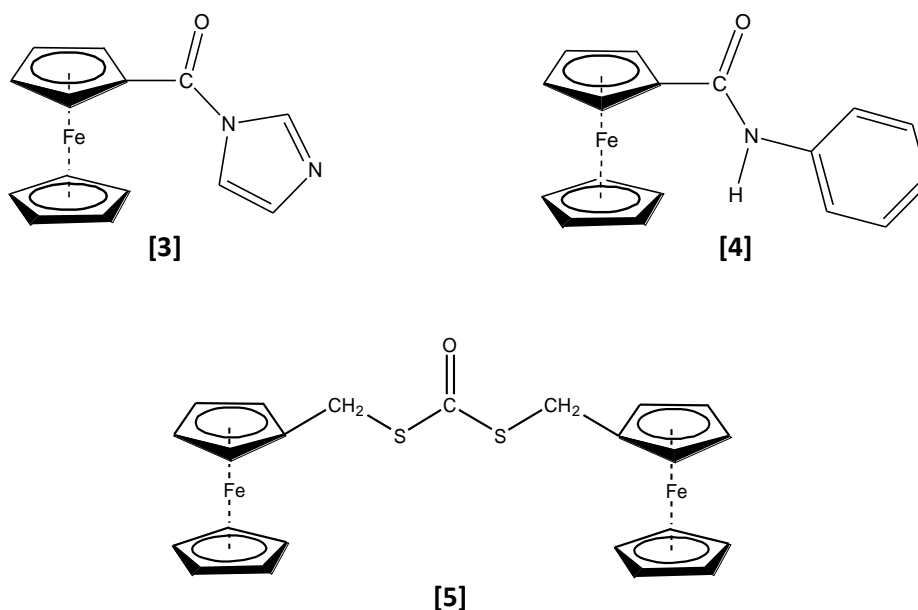


Figure 6.1 The structures of catalysts [3], [4] and [5].

6.1 Results and discussion of Experiments 3, 4 and 5 – Effect of the introduction of N and O

6.1.1 Reaction parameters and raw yields

Experiments 3 and 4 were performed with compound [3] as the catalyst (2.5 and 5 wt.%) at

*This chapter was revised and converted into a paper: R. S. Oosthuizen and V. O. Nyamori, *Appl. Organomet. Chem.*, 2012, (accepted for publication 11 June 2012, DOI 10.1002/aoc.2897).

the three best temperatures (900, 850 and 800 °C), i.e. based on the results from Experiments 1 and 2 (which were discussed in **Chapter 5**). Experiment 5 was carried out at the two outermost temperatures (900 and 800 °C) with catalyst **[4]**. However, catalyst **[4]** is poorly soluble in toluene. Thus, a catalyst concentration of 1.25 wt.% was used by injecting two lots of 0.125 g of catalyst dissolved in 10.0 g of toluene, giving a total solution mass of 20.0 g. Hence, with these conditions almost double the mass of carbon source was injected in Experiment 5 as compared to Experiment 3. Refer to **Table 6.1** for a summary of the parameters used and the raw percentage yield for Experiments 3, 4 and 5.

Table 6.1 Reaction parameters for Experiments 3 to 5 [toluene as C source, 10 % H₂ in Ar (v/v), gas flow rate 100 mL/min, injection rate 0.8 mL/min].

Catalyst	Primary variables	Catalyst concentration (wt.%)	Exp. run	T _{max} (°C)	Raw percentage yield of SCNMs (%)
[3]	effect of N & O source	2.5	3.1	900	6.45
			3.2	850	2.89
			3.3	800	0.18
	effect of concentration	5	4.1	900	5.97
			4.2	850	3.25
			4.3	800	0.30
[4]	effect of N & O source and concentration	1.25	5.1	900	19.53
			5.2	800	1.99

A trend of increasing yield with increasing T_{max} was seen in Experiments 3, 4 and 5 as expected from literature (although the catalysts used were different).¹ Just as with Experiments 1 and 2 in **Chapter 5**, all raw yields were low (< 20%) and this is not unusual for this kind of experiment. This is because most of the black powdered product passed out of the exhaust system in the gas stream, as was the case in Experiments 1 and 2 (**Chapter 5**).

6.1.2 SCNMs formed

As was mentioned in the previous chapter, varying the pyrolysis temperature has been shown to influence the structures which form in CVD experiments.² This section investigates this phenomenon further as well as the effect of differing catalysts and catalyst concentrations on the SCNMs produced. **Table 6.2** shows a representative TEM and SEM image of SCNMs formed for each run of Experiments 3 to 5. **Table 6.3** shows the results of TEM analysis for these same experiments. Refer to these two tables during the following discussion.

Experiment 3 (catalyst **[3]** at 2.5 wt.%) yielded very high percentages (≥ 80%), in the collected material, of well-formed MWCNTs at 800 and 850 °C. At 900 °C a significantly lower yield of MWCNTs was apparent (34%), with a corresponding increase in sphere production. (Indeed, masses of accreted spheres are visible in the SEM image in **Table 6.2** at 900 °C.) This was expected considering that higher temperatures promote sphere formation³. Experiment 4

(catalyst **[3]** at 5 wt.%), however, yielded primarily spheres ($\geq 68\%$), in the collected materials, at all temperatures. Experiment 5 (catalyst **[4]** at 1.25 wt.%) yielded very low percentages of MWCNTs ($\leq 10\%$), in the collected materials, and primarily spheres at both temperatures.

Table 6.2 TEM and SEM images of products from Experiments 3 to 5.

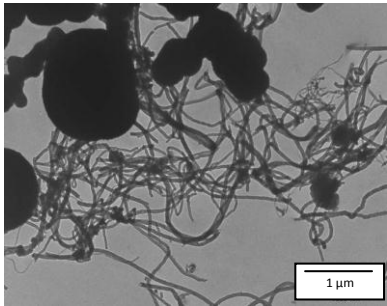
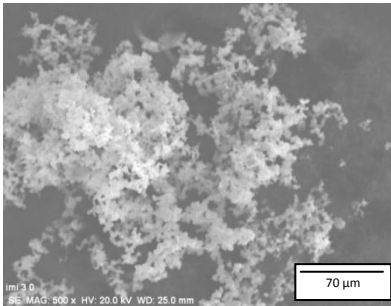
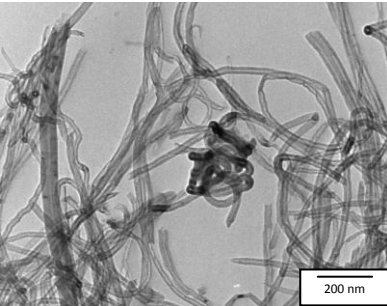
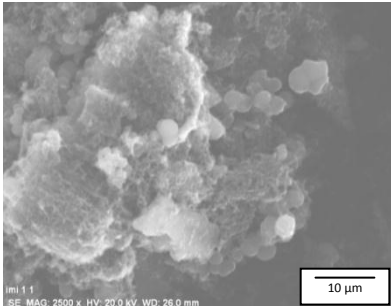
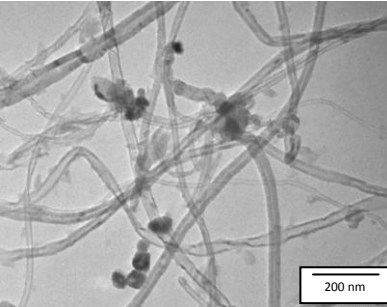
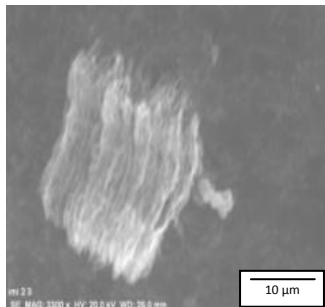
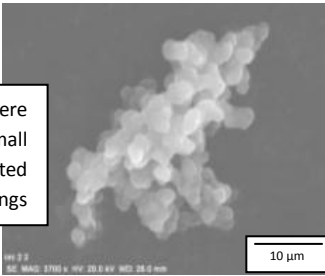
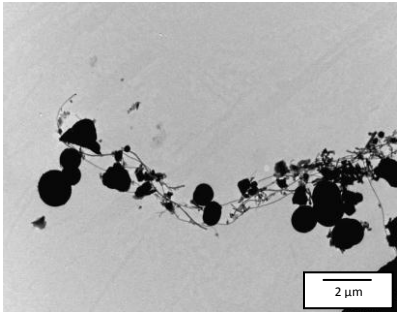
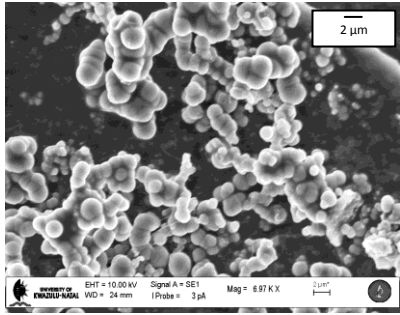
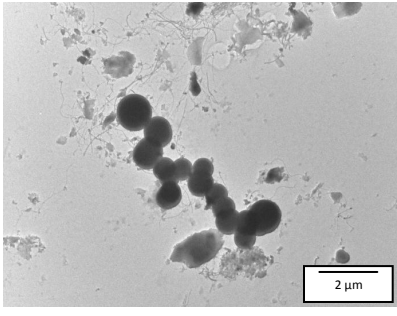
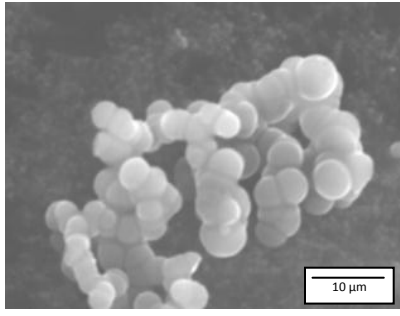
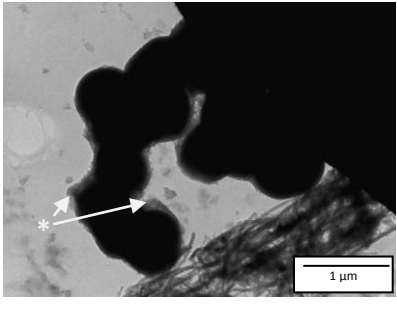
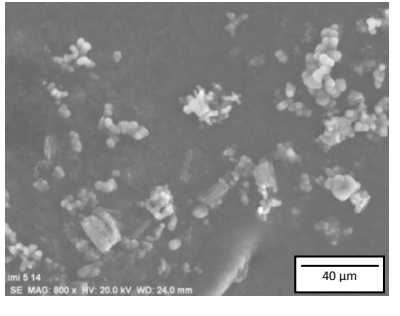
Exp. run	Cat.	Cat. conc. (wt.%)	T _{max} (°C)	Representative TEM image	Representative SEM image(s)
3.1	[3]	2.5	900		
3.2			850		
3.3			800		  <p>Spheres were found in small isolated groupings</p>

Table 6.2 cont...

Exp. run	Cat.	Cat. conc. (wt.%)	T _{max} (°C)	Representative TEM image	Representative SEM image
4.1	[3]	5	900		
4.2			850		
4.3			800		

*The grey areas are an amorphous carbon coating on the spheres (indicated by white arrows).

Table 6.2 cont...

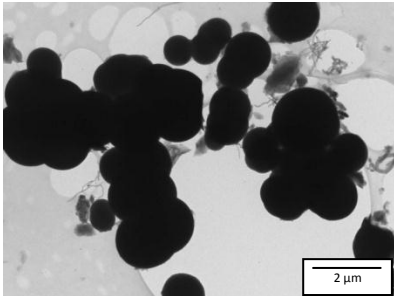
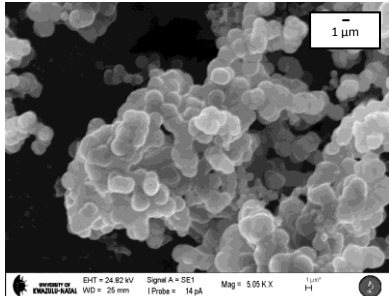
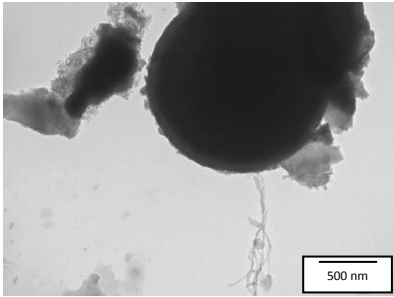
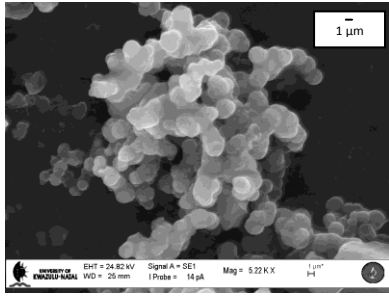
Exp. run	Cat.	Cat. conc. (wt.%)	T _{max} (°C)	Representative TEM image	Representative SEM image
5.1	[4]	1.25	900		
5.2			800		

Table 6.3 Results of TEM analysis for Experiments 3 to 5.

Exp. run	T _{max} (°C)	Approximate percent distribution of morphologies				MWCNTs			C spheres
		% Carbon spheres	% Carbon fibres	% Amorphous carbon	% MWCNTs	Ave. OD (nm)	Ave. ID (nm)	Length (μm) [#]	Ave. OD (nm)
3.1	900	60	4	2	34	53.3	10.2	≈2	733.6
3.2*	850	1.5	2	1.5	95	27.8	9.6	≈4	-
3.3	800	12	-	8	80	24.7	8.2	≈9	810.1
4.1	900	68	4	10	18	39.8	10.7	≈13	935.8
4.2	850	88	-	6	6	26.7	9.4	≈9	846.5
4.3	800	70	-	20	10	32.1	9.0	≈6	968.7
5.1	900	85	-	10	5	23.0	8.6	≈8	1135.6
5.2	800	70	-	20	10	25.1	7.8	≈7	1527.5

*The percentage of carbon spheres is so low (< 10%), thus sphere measurements are not included.

[#] Representative longest MWCNT.

Some interesting results were obtained in terms of trends of MWCNTs produced in Experiments 3 to 5. Firstly, an “inverted” trend for the percentage of MWCNTs produced, as temperature is increased, in Experiment 3 *versus* Experiment 4, is seen in the data in **Table 6.3** and as shown graphically in **Figure 6.2**. In other words, most MWCNTs were formed at 850 °C for Experiment 3, while the least were formed, at the same temperature, for Experiment 4. Secondly, **Figure 6.2** also shows that the percentage of MWCNTs from Experiments 4 and 5 are very similar, although these two experiments were performed with different catalysts and at significantly different catalyst concentrations (5 wt.% catalyst **[3]** and 1.25 wt.% catalyst **[4]** respectively).

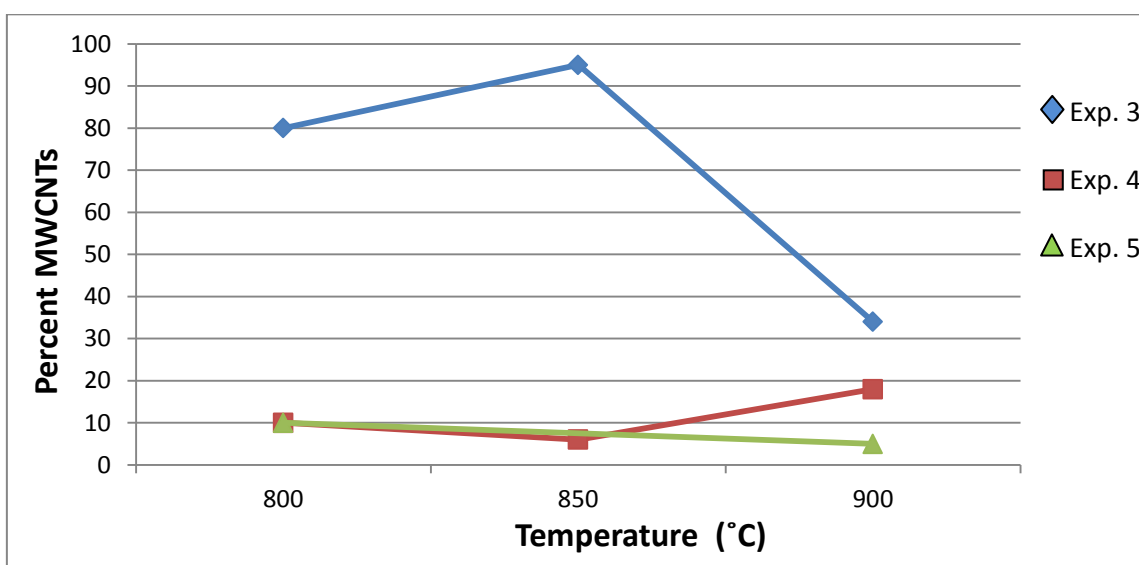


Figure 6.2 The relative percentages of MWCNTs formed for Experiments 3, 4 and 5.

The difference in the primary structures formed in Experiments 3 (2.5 wt.% catalyst **[3]**) and 4 (5 wt.% catalyst **[3]**) can be explained in the following way. Double the catalyst concentration (Experiment 4) produced a larger concentration of iron in the reaction system. This naturally led to more frequent collisions of iron NPs and more coalescence, resulting in larger iron NPs which are not favourable for MWCNT formation and, thus, the production of a larger percentage of spheres ($\geq 68\%$) relative to MWCNTs ($\leq 18\%$) occurred. However, in Experiment 3, especially at 800 and 850 °C, the percentages of MWCNTs were significantly larger ($\geq 80\%$) and the percentages of spheres significantly smaller ($\leq 12\%$). Again this can be attributed to smaller iron NPs that favoured MWCNT formation. Hence, when comparing the different predominant structures for Experiments 3 and 4, catalyst concentration must therefore have a significant influence on the type of SCNMs produced.

However, a different phenomenon was seen in **Chapter 5** when comparing Experiments 1 and 2 (see **Section 5.9.2**). (It is interesting to compare Experiments 1 and 2 with Experiments 3 and 4 respectively. Refer to **Table 6.4**. Experiments 1 and 3 have a catalyst concentration of 2.5 wt.% and Experiments 2 and 4 have a catalyst concentration of 5 wt.%, and so these respective pairs are comparable for concentration effects.) Both Experiments 1 and 2 yielded very high yields of MWCNTs, regardless of the ferrocene concentration. This is not the case for Experiments 3 and 4, which have significantly different product distributions. This suggests

that not only does catalyst concentration have an effect on SCNMs produced, as was the discussion for **Figure 6.2**, but that the product distribution is also dependent on the choice of catalyst. In other words, comparing SCNMs formed in Experiment 3 with Experiment 1 leads to the deduction that using the same temperatures and similar catalysts at the same concentration can yield similar products. However, this deduction does not hold when comparing SCNMs formed in Experiments 4 and 2 (**Table 6.4**). Thus, the best, overall deduction from these results, is that the choice of catalyst, or the ligand on the monosubstituted ferrocene catalyst (sometimes containing one or more heteroatoms), coupled with its concentration, significantly affects the type of SCNMs formed. This conclusion is in agreement with literature.³ The difference between the catalyst in Experiments 1 and 2 and that in Experiments 3 and 4 is the ligand on the ferrocene moiety. The catalyst in the latter two experiments contains a carbonyl group attached to an imidazole ring, thereby introducing oxygen and nitrogen into the system. Nxumalo *et al.* showed that the source of nitrogen atoms, and more importantly the quantity of nitrogen, affects the morphology of the products.⁴ And the quantity of nitrogen in Experiment 4 is double that of Experiment 3, producing significantly different SCNM distributions. Again it can be seen that reaction parameters do not work in isolation. Thus, one can build on a conclusion from **Chapter 5** about temperature and concentration acting together. Here in this section it can be seen that temperature, concentration and even catalyst (i.e. heteroatom) effects do not work independently.

Table 6.4 Comparison of the percentages of MWCNTs obtained in Experiments 1, 2, 3 and 4.

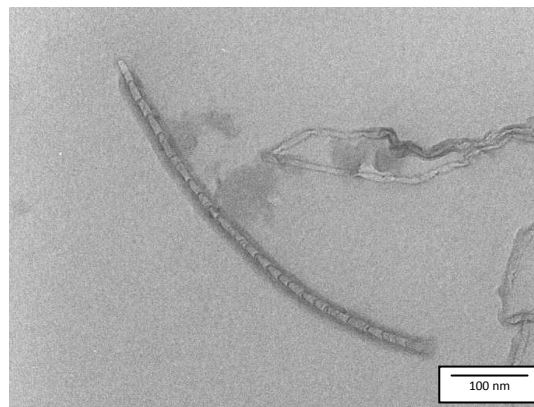
Exp.	Catalyst	Total mass of catalyst injected (g)	Cat. conc. (wt.%)	% MWCNTs produced
1	[1]	0.250	2.5	> 80 ^a
2		0.500	5	
3	[3]	0.250	2.5	≥ 80 ^b
4		0.500	5	≤ 20 ^a
5	[4]	0.250	1.25	≤ 10 ^a

a = at all temperatures investigated; b = 800 and 850 °C

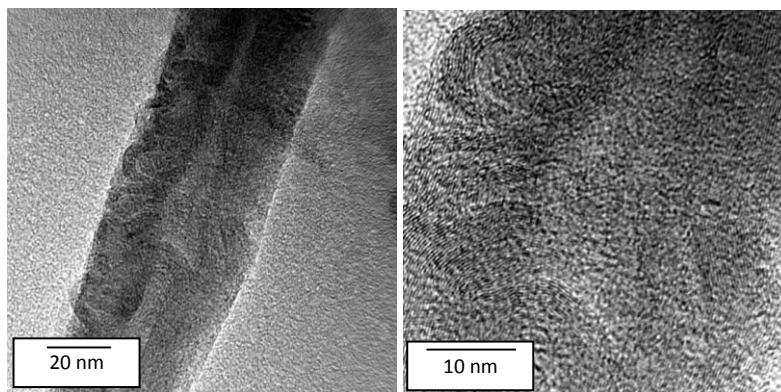
It is interesting to compare Experiment 3 and Experiment 5 since they both had the same mass of catalyst injected into the system. Nevertheless, it is difficult to compare Experiment 3 *versus* Experiment 5 thoroughly since more than one variable differed between the two; although the mass of catalyst injected was the same in these two experiments, the catalysts contained a different moiety on the ferrocene as well a different amount of carbon source. The most probable explanation for the low percentages of MWCNTs (≤ 10%) and high percentages of spheres (≥ 70%), in the collected material, in Experiment 5 *versus* an opposite trend in Experiment 3 (except for the 900 °C material in Experiment 3) is that spheres can form without a catalyst.⁵ To elaborate, in Experiment 5 the ratio of carbon source to catalyst was almost double that of Experiment 3. The higher carbon content (and much lower catalyst content) in Experiment 5 would promote sphere formation. Also, as was mentioned previously, differing ligands from N-containing catalysts influence SCNM distributions.⁴ Thus,

the combined effect of these two variables (carbon content in injected solution:catalyst content and catalyst ligand) needs further research.

As was mentioned, it is difficult to identify the effects of the heteroatoms in Experiments 3 to 5 in isolation because temperature, catalyst (and its ligand) and catalyst concentrations appear to work together. Nevertheless, two effects of heteroatoms can be easily studied, namely (i) the effect of N-doping on MWCNT structure and (ii) the effect of temperature and nitrogen concentration on MWCNT structure. With regards to the former, all runs produced pristine and “bamboo-shaped”^{6,7} MWCNTs. Bamboo-shaped MWCNTs occurred to a lesser extent and are typical of N-doped MWCNTs, see **Figure 6.3 (a)**, where incorporation of nitrogen atoms distorts the regular hexagon and pentagon ring structures in MWCNTs, resulting in cross-walls and tapering segments.⁸ **Figure 6.3 (b)** and **(c)** show high resolution TEM images of the walls of N-MWCNTs (from Experiment 5). The buckling and corrugation arise from incorporation of nitrogen.⁹



(a)



(b)

(c)

Figure 6.3 TEM images of (a) a “bamboo-shaped” MWCNT and HRTEM images of the (b) buckled walls of a N-MWCNT and (c) the same at higher magnification.

With regards to the effect of temperature and nitrogen concentration on MWCNT structure, the influence of these factors on the bamboo compartment length was measured (See **Table 6.5** and **Appendix I, Table I.1**). Specifically, a minimum of 30 MWCNTs with bamboo

compartments were measured. The average compartment length was shortest for the 800 °C sample for Experiment 3, indirectly suggesting that a higher nitrogen content was incorporated into the MWCNTs at this temperature. (This is also suggested by Raman and TGA data as will be discussed later in this chapter.) Jang *et al.*, who used NH₃ and C₂H₂ to produce N-CNTs, showed that nitrogen concentration is inversely proportional to the length of bamboo segments.¹⁰ The higher the concentration of nitrogen, the smaller the compartment lengths were. Their argument was that the more nitrogen that is available and incorporated during growth, the more disordered the tubes will be, giving rise to more compartmentalization. The results in this work are consistent with other literature^{11,12} where nitrogen content is decreased (as indicated by longer bamboo compartment lengths, in general) at higher reaction temperatures. However, Tetana *et al.*, who performed CVD experiments using acetonitrile and acetylene over a Fe-Co/CaCO₃ catalyst, found that higher temperatures resulted in a higher degree of N-doping.¹³ They attributed the difference to the particular reaction parameters, catalysts, reagents and methods used. (Indeed, if, as was discussed previously, factors such as temperature, catalyst and catalyst concentration work together, then it is logical to conclude that other reaction parameters, such as the unique set in the experiments of Tetana *et al.*, would influence the CVD products in a co-dependent manner.)

Table 6.5 Selected average bamboo compartment lengths.

Exp. run	T _{max} (°C)	Ave. bamboo compartment length (nm)	ratio of N : Fe in the catalyst
3.1	900	87.7	2:1
3.2	850	43.5	
3.3	800	33.5	
5.1	900	63.7	1:1
5.2	800	47.4	

In terms of amorphous carbon production in Experiments 3 to 5, both the temperature and oxygen heteroatom may have had an effect. Firstly, with regards to temperature effects, in Experiments 3, 4 and 5 the lower the temperature, the more amorphous carbon, in general, was produced (**Table 6.3** and **Figure 6.4**). Secondly, with regards to oxygen effects, some literature discusses how the presence of oxygen can remove amorphous carbon by oxidizing it into the gas phase more readily than MWCNTs. An example is where the hydroxyl radical from ethanol was shown to “clean” the MWCNTs of amorphous carbon.¹⁴ The MWCNTs formed in Experiment 3, compared to those of Experiment 4, appeared to be very “clean” and free of amorphous carbon (see **Tables 6.2** and **6.3** and **Figure 6.4**). However, doubling the catalyst concentration does not necessarily produce “cleaner” MWCNTs because of a higher oxygen concentration in the system. This deduction is confirmed when comparing the percentages of amorphous carbon in Experiment 5 with that of Experiments 3 and 4. In the former experiment the concentration of oxygen in the reaction system was lower than for the latter

two experiments. However, the same percentages of amorphous carbon were produced at this much lower oxygen concentration as compared to the highest concentration of Experiment 4. Also, in general, the percentages of amorphous carbon in Experiments 3 and 4 are higher than those of Experiments 1 and 2, where no oxygen was present in the catalyst. Thus, oxygen from catalysts [3] and [4] does not act as a system “cleanser”. In fact, the higher percentage of oxygen in Experiment 4, as compared to Experiment 3, may deactivate the iron catalyst by forming iron oxide(s). This would retard or prevent the iron NPs from catalyzing MWCNT growth. (This may explain why sphere percentages were so high in Experiment 4. As mentioned previously, spheres can grow without catalyst and if most of the iron NPs were deactivated, sphere formation would occur independently of the iron oxide particles.)

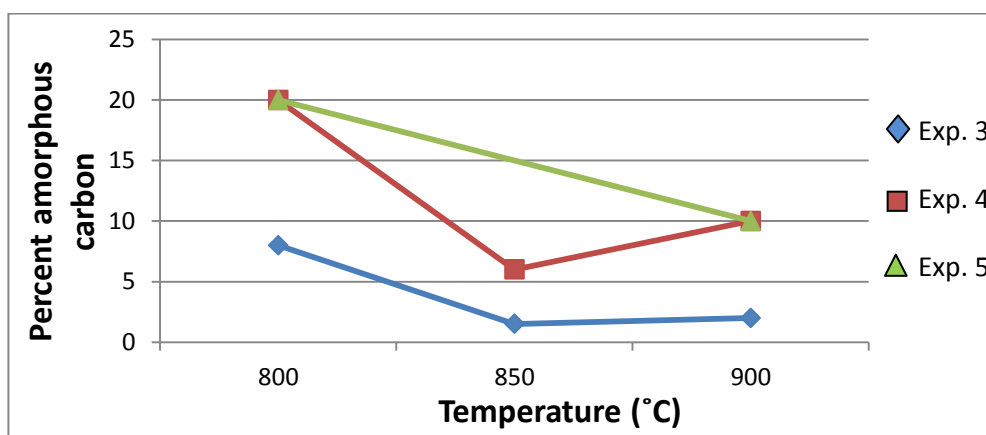


Figure 6.4 The relative percentages of amorphous carbon formed for Experiments 3, 4 and 5.

No polygon structures were seen in Experiments 3 to 5 as were seen in Experiment 1.

Although MWCNTs are the main focus of this project, since all catalysts produced some quantities of spheres it was decided to briefly study a few carbon spheres from Experiment 5, specifically, to look at the composition. Spheres can be solid, or containing another substance (core-shell) or hollow.¹⁵ **Figure 6.5** shows three different images of the same core-shell nanostructure. Image (a) is a HRTEM micrograph of a sphere. The centre is darker. Image (b), a high angle annular dark field (HAADF) image, shows the centre in a lighter tone confirming that the centre is indeed a heavier element. Image (c) is an EDX map of the same structure and shows that the centre is iron (indicated by red) while the rest of the sphere is carbon (indicated by green).

It was interesting to note that the occurrence and location of iron in and/or on the surface of spheres was not consistent. **Figure 6.6 (a)** shows this. **Figure 6.6 (b)** shows visually the agglomeration of iron NPs which favours sphere formation. Note that the diffuse red dots, which represent iron, spread to outside the core and even outside the sphere (as indicated by δ), indicating that scattering of the X-rays from the microscope beam has occurred. Iron, being a relatively heavy element, is a relatively heavy scatterer of electrons. Thus, iron signals far outside the core area are not considered representative of the actual location of iron NPs.¹⁶

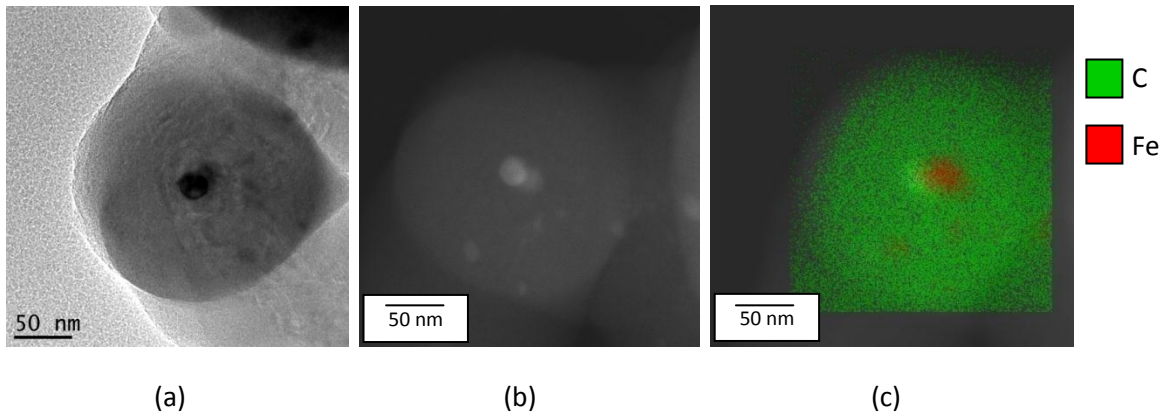


Figure 6.5 (a) HRTEM image, (b) dark field image and (c) elemental mapping image of an iron-core sphere from Experiment 5. (Note that the images are not in exactly the same orientation.)

A recent review on carbon nano- and microspheres discusses how the presence of a metal catalyst often produces solid carbon spheres. They hypothesize that the metal catalyst does not catalyze sphere formation, but rather that it assists in the decomposition of the carbon source.¹⁷

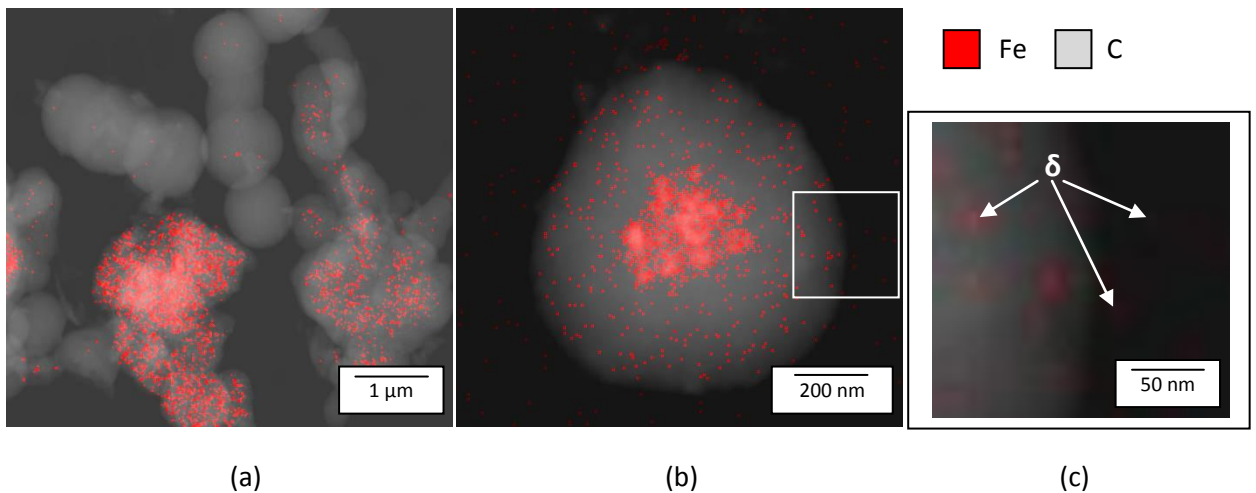


Figure 6.6 EDX maps for as-synthesized materials, showing (a) occurrence and position of iron NPs in/on spheres is not consistent in a sample and (b) that iron NPs occur near the centre of spheres and (c) scattered iron signals.

6.1.3 ID and OD of MWCNTs

Both the average OD and ID values for MWCNTs from Experiments 3 to 5 varied depending on the temperature, choice of catalyst and catalyst concentration, and this will now be discussed.

In Experiment 3 the average ID was largest at 900 °C and smallest at 800 °C (see **Table 6.3**). A definite trend of decreasing average ID with decreasing temperature is seen (see **Figure 6.7**). For Experiments 4 and 5 the same trend is seen. The average ODs, for Experiments 3 and 4,

were also largest at the highest temperature and, in general, follow the same trend as for the average IDs. The average ODs for Experiment 5 follow the opposite trend (increasing average OD with decreasing temperature), however, the two values are very similar, and thus this trend is not definitive. Further research is needed to confirm this preliminary trend for Experiment 5.

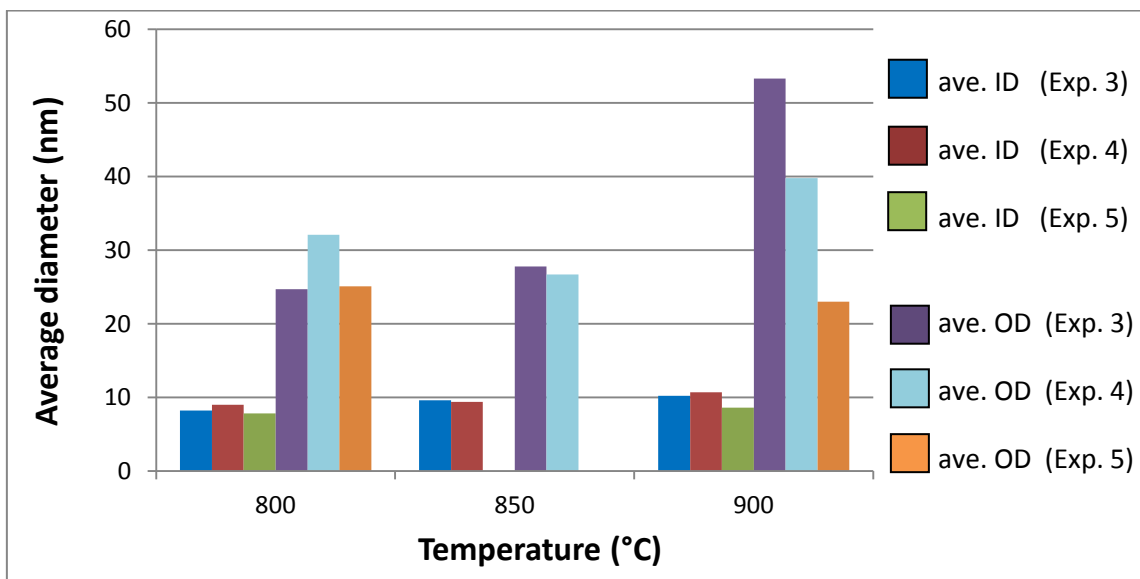


Figure 6.7 Histogram of the average IDs and ODs for Experiments 3, 4 and 5.

As was discussed in the previous chapter, the ID of a growing MWCNT, at a specific temperature, does not vary as much over time as the OD.¹⁸ This is also seen in Experiments 3 to 5 where the bars in **Figure 6.7** for average OD vary significantly in their height compared to the bars for the average IDs. The average OD value decreases, in general, as temperature decreases (except for Experiment 5). Thus, the same trend is evident for both the temperature-average ID and average OD relationships. As was discussed in **Chapter 5**, this is logical since the lower the temperature, the less frequently iron NPs would collide and coalesce in the reaction system, and thus the smaller the diameters of the CNTs.^{19,20}

When considering concentration effects, the average IDs and ODs of MWCNTs (shown in **Table 6.3** and **Figure 6.7**) for Experiment 4 (5 wt.% catalyst **[3]**), were expected to be larger than those of Experiment 3 (2.5 wt.% catalyst **[3]**) because of presumed larger iron NPs.²¹ Also, Chun *et al.* found that increasing the concentration of nitrogen in the system corresponded with larger CNT diameters.²² However, regarding the average OD values in this project, average ODs did not increase, in general, at the higher catalyst concentration, except for the 800 °C value. Panchakarla *et al.* showed that both the nitrogen source and reaction conditions determine the diameters of DWCNTs,²³ and perhaps the reaction conditions peculiar to Experiment 4 resulted in the unexpectedly low average ODs. Regarding the average ID values, when comparing Experiments 3 and 4, a general trend of larger average ID at higher concentrations is seen, except that the values for the average ID at 850 °C are so close that one cannot clearly distinguish between them.

When comparing Experiments 1 and 3, (different catalysts but same catalyst concentration) the trend for OD is inverted (see **Figure 6.8**), with a decreasing average OD for Experiment 1 and an increasing OD for Experiment 3 as temperature increases. However, when comparing Experiments 2 and 4 (also a situation of differing catalysts but same catalyst concentration), a trend of a minimum average OD at 850 °C with larger average ODs at 800 and 900 °C is observed. Thus, since the only difference in these respective experiment pairs was the catalyst (kind of ligand and presence or absence of heteroatoms), it can be seen that catalyst choice influences average OD and ID, but that the effect of temperature is not predictable when the catalyst concentration is 2.5 wt.%, but may follow similar trends when the concentration is 5 wt.%. Despite these preliminary conclusions, further research into the effects of using different catalysts at the same concentration is needed. One must bear in mind the significant effects different catalysts have on SCNMs (see the previous section) and thus the effects of different catalysts on the dimensions of MWCNTs are not necessarily predictable.

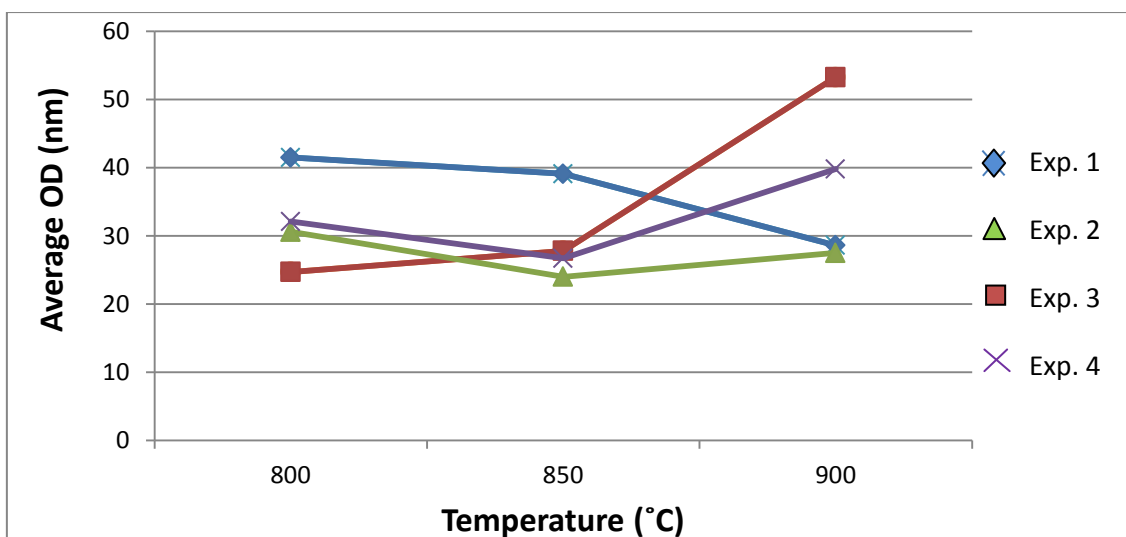


Figure 6.8 Variation in the average ODs at each temperature (in the range 800 to 900 °C) for Experiments 1 to 4.

Figures 6.9 and **6.10** show the distribution of the ID and OD values for Experiment 3 (2.5 wt.% catalyst), while **Figures 6.11** and **6.12** do the same for Experiment 4 (5 wt.% catalyst). For both experiments the ODs for each temperature span a wide range, i.e. the distributions of ODs for all temperatures of Experiments 3 and 4 are similar. This suggests that, with catalyst **[3]**, OD distribution may not be significantly influenced by catalyst concentration.

Figures 6.13 and **6.14** show the ID and OD distributions for MWCNTs obtained from Experiment 5 (catalyst **[4]** at 1.25 wt.%). Notably the distributions of both the IDs and ODs are narrower than those from Experiment 3. (Note that Experiment 5 was not performed at 850 °C.) Several factors may influence this difference in diameter distribution: (1) the different catalysts employed, (2) the different catalyst concentrations, and (3) the different sources of nitrogen. Regarding the last point, it has been shown that the diameter of N-CNTs is influenced by the source of nitrogen.²³ Considering that the Fe/C ratio of Experiment 3 was higher than that of Experiment 5, it is sensible that larger average ODs result. Literature has reported this previously.²¹

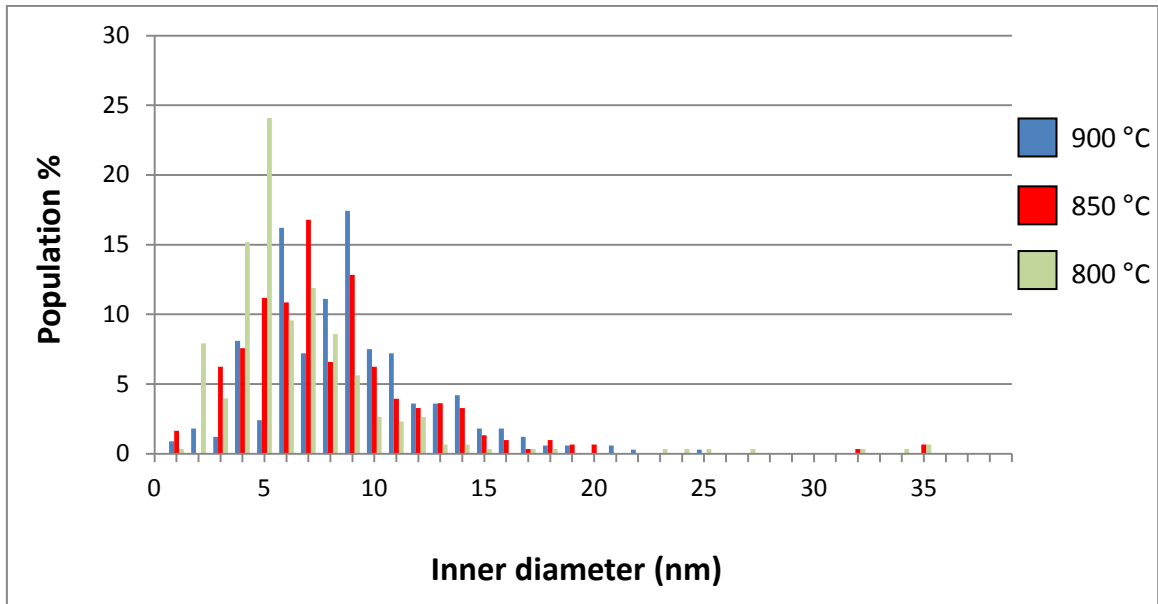
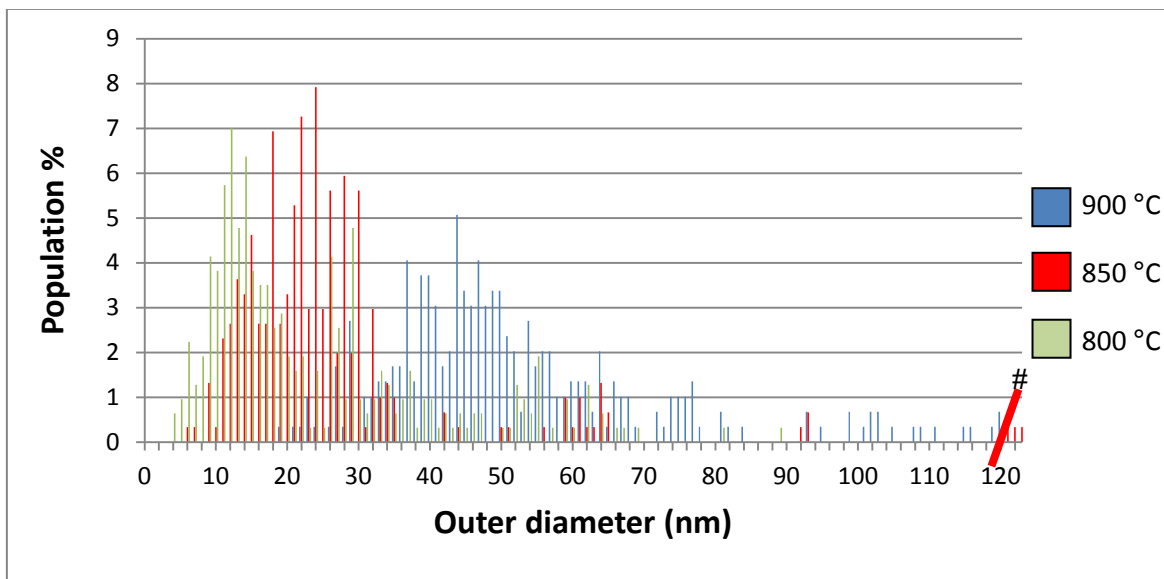


Figure 6.9 Histogram of the ID distribution for the MWCNTs obtained with 2.5 wt.% of catalyst [3].



The few measurements shown to the right of the red line are CNTs whose diameters are of the order 160 nm. (Since they are hollow, tubular structures they have been considered as CNTs here and not CNFs.)

Figure 6.10 Histogram of the OD distribution for the MWCNTs obtained with 2.5 wt.% of catalyst [3].

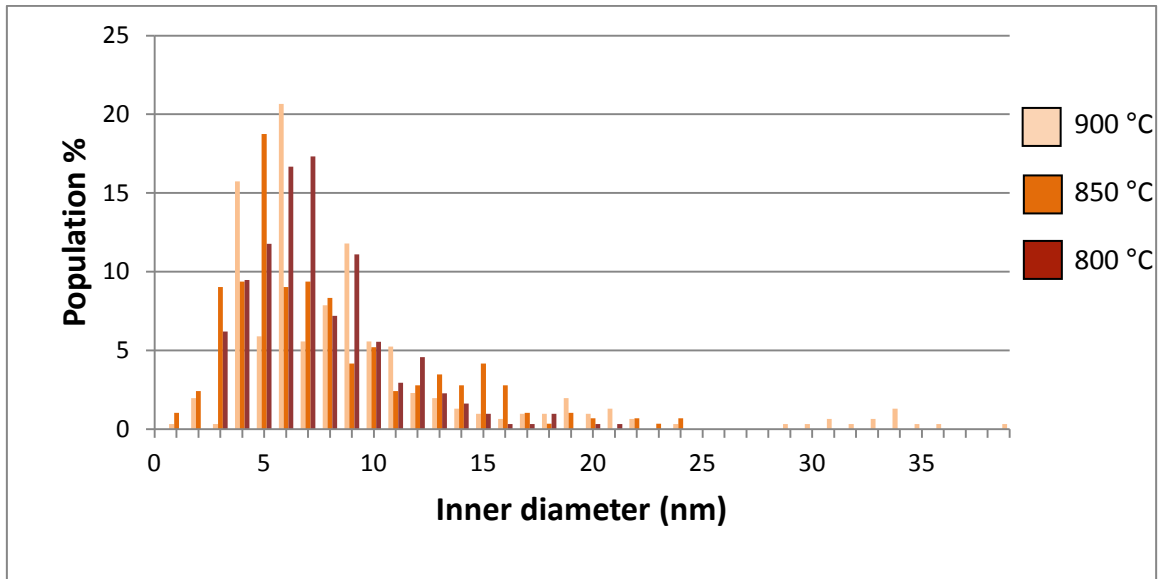


Figure 6.11 Histogram of the ID distribution for MWCNTs obtained with 5 wt.% of catalyst [3].

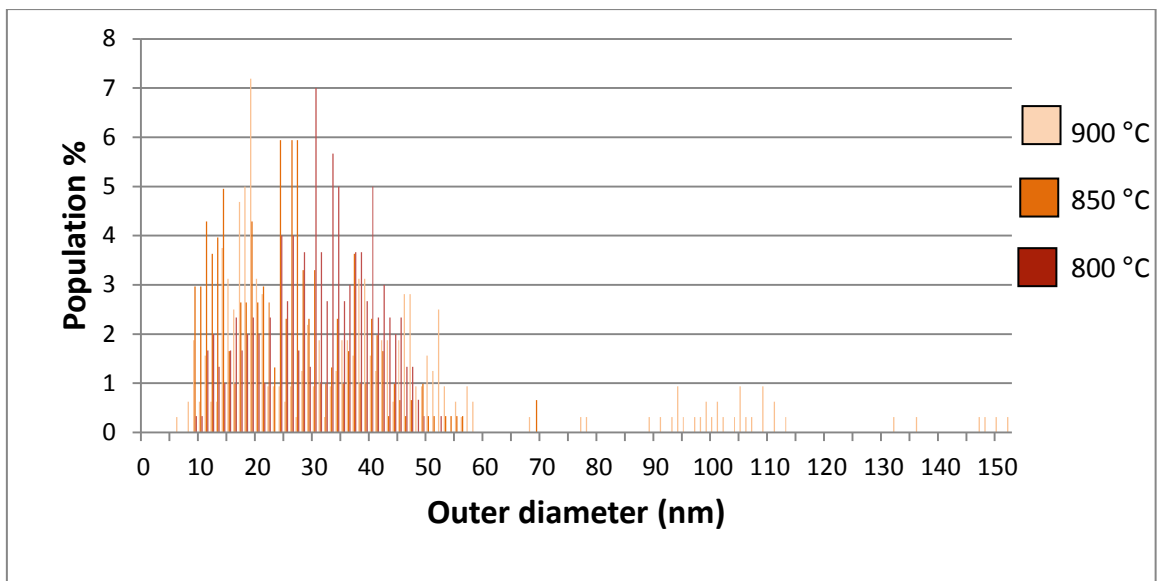


Figure 6.12 Histogram of the OD distribution for MWCNTs obtained with 5 wt.% of catalyst [3].

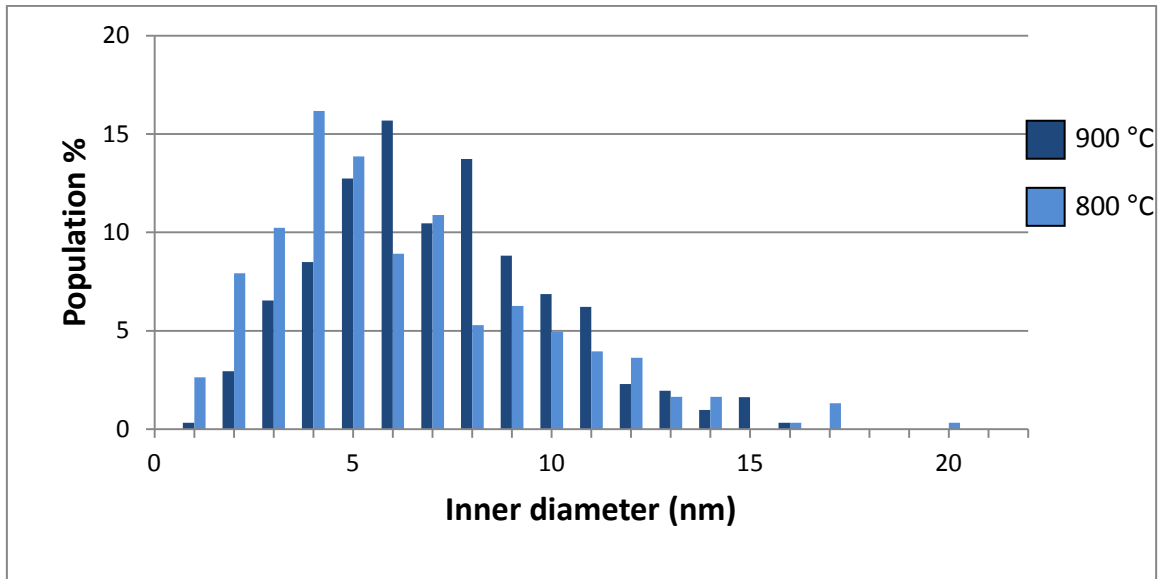


Figure 6.13 Histogram of the ID distribution for MWCNTs obtained with 1.25 wt.% of catalyst [4].

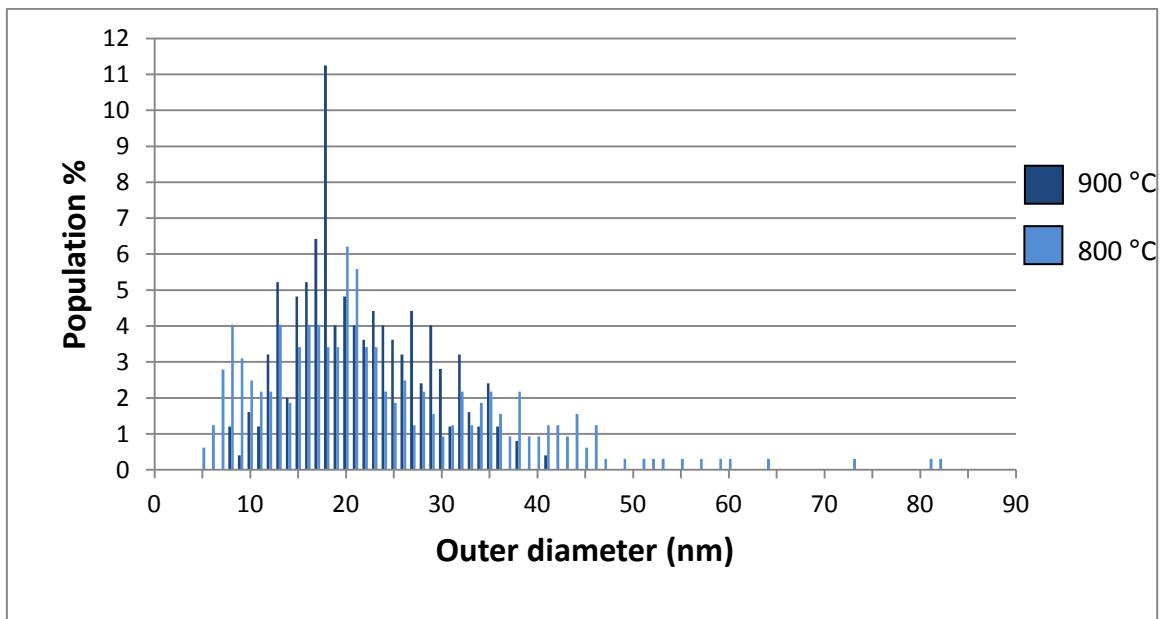


Figure 6.14 Histogram of the OD distribution for MWCNTs obtained with 1.25 wt.% of catalyst [4].

6.1.4 Length of MWCNTs

The representative longest MWCNTs from Experiment 3 (2.5 wt.% catalyst [3]) follow the same trend as those of Experiment 1 (2.5 wt.% catalyst [1]) for the 800 to 900 °C range. Specifically, the lower the temperature in the range 800 to 900 °C, the longer were these lengths of MWCNTs. The deduction is that 800 °C is the most conducive temperature, in the selected

temperature range and for the chosen parameters, for sustained growth of MWCNTs. Conversely, Experiment 2 (5 wt.% catalyst **[1]**) and Experiment 4 (5 wt.% catalyst **[3]**) both yielded the shortest CNTs, within their respective Experiments, at 800 °C. The results from Experiments 2 and 4 are, in general, consistent with the work of Khavrus *et al.* who synthesized N-doped CNTs.²⁴ They found that the T_{\max} value had a linear correlation with the CNT length, with higher temperatures (in range 800 to 900 °C) favouring longer lengths. Lee *et al.* also showed that the maximum length of CNTs is dependent on temperature, although in their experiments they used ferrocene and acetylene in the range 700 to 1000 °C.²⁵ They found a trend of longer length with higher temperature, although their CNTs weren't doped. The different trends found for the temperature-maximum length relationship for Experiments 1 and 3 *versus* 3 and 4 may suggest that, besides temperature, the concentration of catalyst is another factor affecting maximum length.

Comparing specific results from Experiments 1 (900 to 800 °C range) and 3, it can be seen that the N-doped MWCNTs from Experiment 3 are shorter than the undoped ones from Experiment 1. This was observed by Nxumalo *et al.* who showed that the length of CNTs becomes shorter with an increase in N-doping.⁴

The representative longest MWCNTs in the 900 and 800 °C materials from Experiment 5 are so close that one cannot distinguish between them and they differ from those of Experiments 3 and 4 at the same two temperatures. This can be explained in the following way. Firstly, a different catalyst was used in Experiment 5 *versus* that used in Experiments 3 and 4. Also, different catalyst concentrations were used in each of these Experiments. Different compounds decompose in different ways giving rise to different predominant fragments. Thus it is logical to conclude that the different catalysts, namely compounds **[3]** and **[4]**, will produce different radical and neutral species. These would react in different manners and at different rates ultimately influencing the SCNM final product. Length is thus one of the factors affected by the feedstock and its concentration.

6.1.5 Alignment of MWCNTs

All runs of Experiments 3, 4 and 5 showed small, infrequent, bundles of aligned MWCNTs at all temperatures. However, it is difficult to identify a relationship between temperature and alignment due to the low occurrence of bundles. Nevertheless, it was observable that the bundles of MWCNTs in Experiments 3 to 5 are not as regular in shape as those in Experiments 1 and 2 where ferrocene was used as a catalyst to obtain pristine non-doped MWCNTs. In general, in Experiments 3 to 5, the presence of a larger percentage of spheres, as well as an increase in the disorder of tubes (due to nitrogen and its effects) may well make these tubes less straight and thus the alignment decreases. The TEM images of CNTs in **Table 6.2**, especially at 850 °C, show some highly curled tubes. This may be due to distortion of the growing tube by the incorporation of nitrogen. This supposition is supported by the research of Kurt and Karimi who described their curled N-CNTs as having a vermicular (wormlike) shape.²⁶ They showed that the degree of N-doping influences the alignment of N-CNTs.

6.1.6 Size of spheres

Most runs of Experiments 3 and 4 yielded similar average sphere sizes (within the range 733.6 to 968.7 nm), i.e. micrometric-sized spheres, regardless of the T_{\max} and catalyst concentration. It was shown that temperature had little effect on sphere size²¹ as is the case in this work.

The average sphere sizes obtained in Experiment 5 were larger than those of Experiments 3 and 4. This is most likely due to the increased amount of carbon injected relative to catalyst.²¹

6.1.7 Crystallinity and thermal stability of products

The crystallinity of materials from Experiment 3 tended to increase with an increase in temperature, with the lowest I_D/I_G ratio occurring at the highest temperature (900 °C) (see **Table 6.6** and **Appendix G, Table G.1**). The Raman data for the 800 °C material for Experiment 3, which has 80% MWCNTs and 12% spheres, shows that it is more disordered than at 850 and 900 °C. The comparatively high I_D/I_G ratio for this material may suggest high N-doping in this sample relative to the other materials. This is supported by the shorter bamboo compartment lengths at this temperature than at 850 and 900 °C (**Table 6.5**). Studies in the literature showed that an increase in nitrogen concentration in the catalyst or in N-doping in MWCNTs was related to an increase in the degree of Raman disorder, with significant variations in the I_D/I_G ratio.^{4,22} The I_D/I_G values for Experiment 4 also decrease with increasing temperature. However, the bamboo compartment length (**Appendix I, Table I.1**), does not agree closely with the Raman data. Yet again the trend of increasing graphiticity with increasing temperature was seen in the Raman data for Experiment 5. The same crystallinity-temperature relationship was also seen in the literature by Lee *et al.*²⁵ and Liu *et al.*²⁷ Among other findings, the latter authors found that temperature affected the amount of nitrogen that was doped.

Table 6.6 Selected results from Raman analysis for Experiments 3 and 5.

Exp. run	T_{\max} (°C)	“Disorder” D-band (cm ⁻¹)	“Graphitic” G-band (cm ⁻¹)	I_D/I_G ratio
3.1	900	1329	1556	0.899
3.2	850	1342	1556	1.244
3.3	800	1337	1556	1.524
5.1	900	1341	1557	0.058
5.2	800	1333	1557	0.076

Comparing Experiment 3 with Experiments 4 and 5 shows that the trend in crystallinity may be independent of the choice of catalyst and its concentration, since all experiments (3, 4 and 5) had the same trend regardless of the catalyst used and its concentration. This suggests that temperature is the primary or predominant factor in determining crystallinity trends. It is

logical that the higher the temperature, regardless of the catalyst used or its concentration, would enhance annealing effects, thereby increasing crystallinity.

It is interesting to compare Experiments 3 and 5, since their catalyst concentrations are lower than that of Experiment 4. The I_D/I_G ratios (**Table 6.6**) for Experiment 5 are much smaller than for Experiment 3. This may suggest that the nanostructures in Experiment 5 (predominantly spheres of large size) are highly graphitic. Graphitic spheres have been reported in literature.^{28,29} **Figure 6.15** shows a small, highly graphitic sphere and **Figure 6.16** a highly graphitic MWCNT from Experiment 5. [Spheres are generally more graphitized the smaller they are,³⁰ although larger spheres can be graphitic too (see **Appendix E, Figure E.2**.)] Also, the concentration of nitrogen introduced into the reactor in Experiment 5 was much smaller than that of Experiment 3. It was expected that the lower nitrogen concentration would presumably lead to lower nitrogen incorporation in SCNMs and hence disorder would be lessened. In this way the I_D/I_G ratios would be lower for Experiment 5 than Experiment 3. The data in **Table 6.6** suggests this.

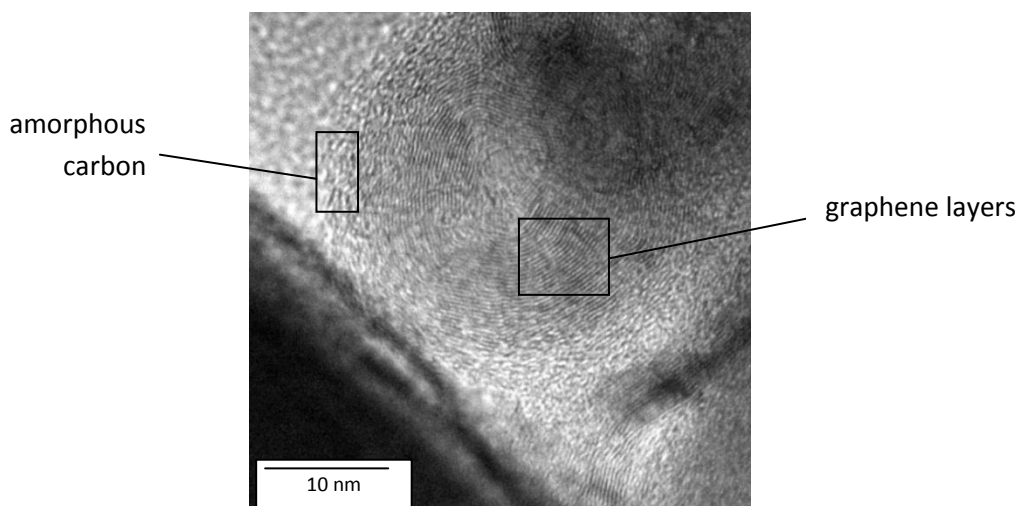


Figure 6.15 HRTEM image of a sphere with graphene layers.

When comparing the Raman spectroscopy data from Experiment 3 with that for Experiment 1 (for 800, 850 and 900 °C), the same graphiticity-temperature relationship is evident, namely improved graphiticity at higher temperatures. Because Experiments 1 and 3 differ only in catalysts used, the deduction is that temperature is a more important factor in determining crystallinity. Thus, the results from the comparison of Experiments 1 and 3 support the argument given above for Experiments 3, 4 and 5. However, this argument does not hold when comparing the Raman spectroscopy data from Experiment 4 with that for Experiment 2. Experiment 2 (of all experiments, including Experiment 6 which will be discussed in **Section 6.3**) is the only one that does not obey the graphiticity-temperature relationship. Thus, the hypothesis that temperature, predominantly, determines crystallinity needs further investigation.

Raman spectroscopy results and TGA results should correlate. Defect sites in graphene layers increase oxidative instability³¹ and, in contrast, highly crystalline sheets of graphite are more stable towards oxidation. **Figure 6.16** shows that MWCNTs can be highly graphitic with small

amounts of amorphous carbon, and, the higher the graphicity, the slower the onset of oxidation. The TGA results will now be discussed.

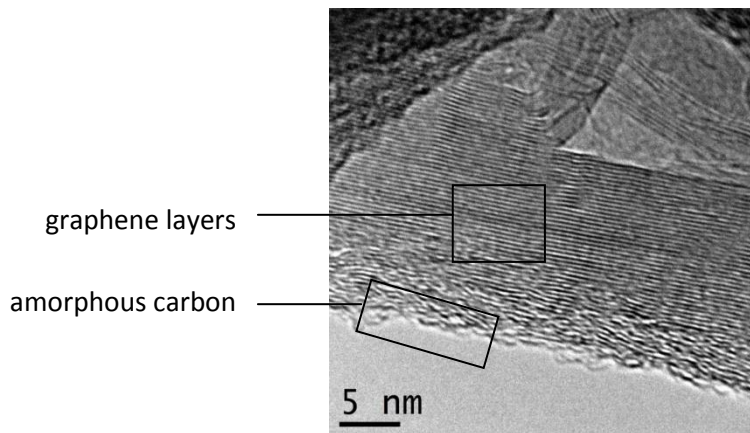


Figure 6.16

HRTEM image of a portion of a MWCNT from Experiment 5 (800 °C) showing graphene layers and an outer amorphous carbon layer.

TGA results, for the thermal decomposition of products from Experiments 3 and 4 in air, are shown in graphical form in **Figure 6.17**. The same is shown in **Figure 6.18** for Experiment 5. **Table 6.7** summarizes some important information extracted from these thermograms.

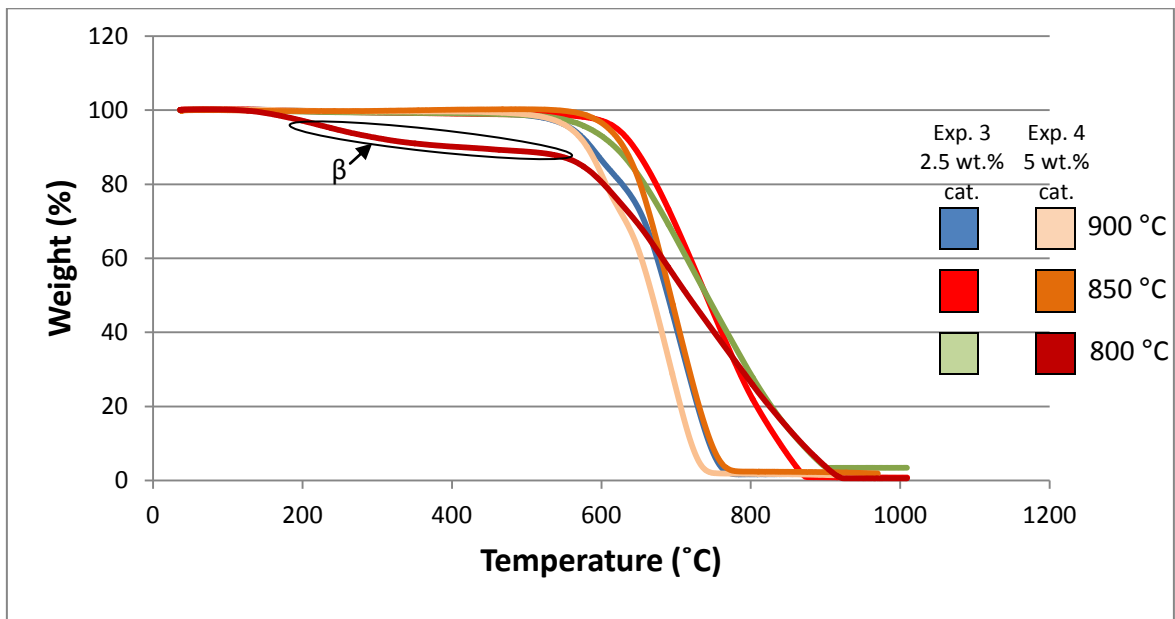


Figure 6.17 TGA weight loss percent curves obtained in air for Experiments 3 and 4 for the as-synthesized products at 2.5 and 5 wt.% catalyst respectively.

In Experiment 3 (2.5 wt.% catalyst **[3]**) both the 850 and 800 °C samples, which contain higher percentages of MWCNTs than the 900 °C sample, resisted decomposition for longer than the 900 °C sample, which has a significantly higher percentage of spheres. The deduction is that MWCNTs are more thermally stable than carbon spheres. In other words, thermal stability was decreased at the highest temperature since this temperature (900 °C) produced mostly spheres. However, comparing the 800 and 850 °C samples (see also **Appendix H, Figure H.3**) shows that the onset of oxidation for the 800 °C material occurs at a lower temperature. This supports the data in **Table 6.5** and **6.6**, which indicates that a higher degree of N-doping (in the

800 °C material) results in a more disordered and, thus, more thermally unstable material. Regarding weight loss gradients, the main weight loss gradient of the 900 °C material is steeper than for the 850 and 800 °C materials. This suggests that the abundant spheres (60%) in the collected material at 900 °C oxidize and decompose at a faster rate than do MWCNTs (which are significantly more abundant at the two lower T_{max} values of 800 and 850 °C). In terms of decomposition range, the 800 °C material had the largest decomposition range (\approx 510 to 900 °C). Defects can be caused by nitrogen incorporation. If the defects are not consistently spread amongst the SCNMs, it will lead to a shallower TGA gradient and, thus, a wider range of decomposition temperatures. The material with the smallest weight percent iron/iron oxide residue (0.8 wt.% as shown in **Table 6.7**) was that obtained at 850 °C and this is supported by the TEM image in **Table 6.2**, which shows very clean MWCNTs with no “dark spots”. However, all materials in this experiment were low in remnant iron.

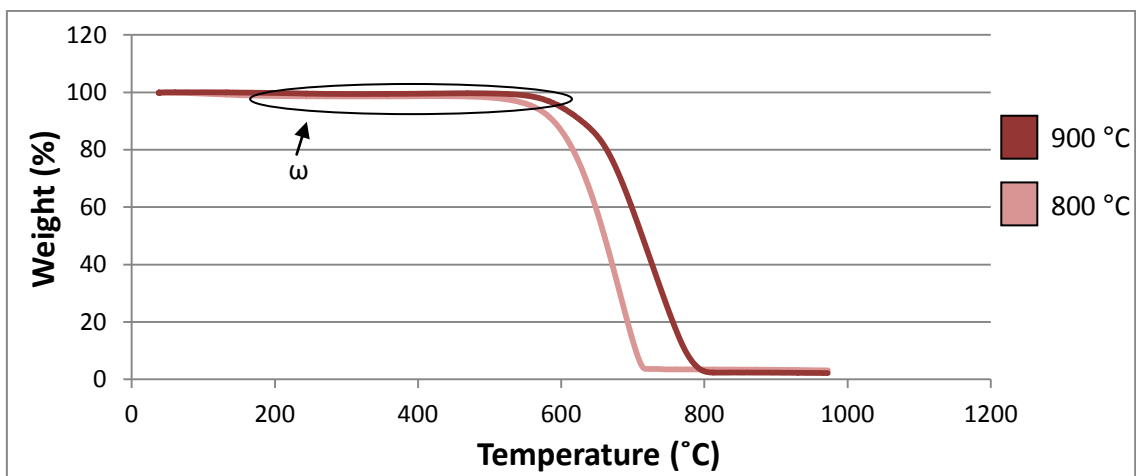


Figure 6.18 TGA weight loss percent curves obtained in air for Experiment 5 for the as-synthesized products at 1.25 wt.%.

Table 6.7 Decomposition temperature and weight percent residue from the products of Experiments 3, 4 and 5.

Exp. run	T_{max} (°C)	Initial decomposition temperature* (°C)	Main decomposition range (°C)	Temperature of max. decomposition (°C)	Residual mass percent (%)
3.1	900	\approx 480	\approx 480 to 770	706	1.7
3.2	850	\approx 550	\approx 550 to 870	740	0.8
3.3	800	\approx 510	\approx 510 to 900	724	3.4
4.1	900	\approx 480	\approx 480 to 740	689	1.1
4.2	850	\approx 550	\approx 550 to 770	701	1.9
4.3	800	\approx 510	\approx 510 to 910	681	0.6
5.1	900	\approx 550	\approx 550 to 800	716	2.2
5.2	800	\approx 500	\approx 500 to 710	678	3.1

*The temperature of oxidation onset was used primarily in determining “thermal stability”, rather than the main decomposition range.

Regarding Experiment 4 (5 wt.% catalyst [3]), again the 850 and 800 °C samples resisted oxidation for slightly longer than the 900 °C sample as was the case in Experiment 3. The best

temperature in this experiment, in terms of highest thermal stability, was observed for the material synthesized at 850 °C, since it began decomposing at the highest temperature (≈ 550 °C). This material also had the steepest weight loss gradient, which indicates a fast-decomposing material or a highly homogeneous material. The distribution values in **Table 6.3** confirm that the 850 °C material is the most homogeneous material from Experiment 4. As was the case for Experiment 3, all materials in this experiment were low in remnant iron (< 2 wt.%). The significant drop in gradient for Experiment 4 for the 800 °C material (β on **Figure 6.17**) suggests a combination of significant loss of moisture and groups such as $-\text{OH}$ and $-\text{COOH}$, as well as amorphous carbon decomposition. (Amorphous carbon usually decomposes in air in the region of approximately 320 °C.³²) Indeed this sample had the most amorphous carbon compared to other runs in this experiment (see **Table 6.3**).

For Experiment 5, there was a marked difference between the 900 and 800 °C curves in terms of the initial decomposition temperature (see **Figure 6.18**). Unlike Experiments 3 and 4, the onset of oxidation for the 900 °C sample occurs at a higher temperature than the 800 °C sample (≈ 550 versus ≈ 500 °C respectively). This shows the 900 °C sample to be more thermally stable. This is supported by the lower I_D/I_G ratio for this material (see **Table 6.6**). The gradient of the 800 °C curve drops slightly below the 900 °C curve in the temperature range between approximately 200 and 600 °C (ω on **Figure 6.18**). This may be indicative of more amorphous carbon as was shown in the TEM images in **Table 6.2** and the data in **Table 6.3**. The best material of the two in this experiment is the 900 °C material in terms of high thermal stability, high crystallinity, low amount of amorphous carbon and lowest iron remnant.

Experiments 3 and 4, when compared, do not show obvious concentration effects in the TGA results. What is interesting though, is that the 850 °C material, in both experiments, is the most thermally stable, although the SCNM distributions in these experiments are quite different. Of the two, Experiment 3 at 850 °C is the best candidate for future MWCNT catalyst support studies.

Experiments 1 and 3 (which have different catalysts but the same catalyst concentration) were then compared. In Experiment 1 a general trend of increasing thermal stability with increasing temperature (from 800 to 900 °C) was observed (although the 800 and 850 °C samples are very close in terms of initial decomposition temperature). In Experiment 3 no obvious trend was found for thermal stability with changing T_{max} . The best overall temperature from Experiment 1 (800 °C) was then compared with the 800 °C material from Experiment 3. It was interesting to note that the onset of oxidation occurred at a lower temperature for the undoped sample (Experiment 1) (**Figure 5.22** in **Chapter 5**) compared to the doped sample (**Figure 6.17** in this chapter). This was unexpected since Panchakarla *et al.* showed that undoped DWCNTs begin thermal decomposition at a slightly higher temperature than the doped version.²³ A possible explanation for this is that the undoped version has a higher weight percentage of iron [as determined by the remnant iron oxide(s) mass percent]. More iron may have catalyzed the earlier onset of oxidation.

Experiments 2 and 4 (which also have different catalysts but the same catalyst concentration) were then compared. As was the case for Experiment 1 versus 3, there is a general trend of

increasing thermal stability with increasing T_{\max} in Experiment 2, whereas no obvious trend is evident in Experiment 4 for thermal stability.

The TGA results of Experiments 3 and 5 were then briefly compared since the concentrations of catalysts are lowest in these two experiments. It was interesting to note that in both Experiments 3 and 5 the 800 °C materials had the highest content of remnant iron in their respective experiments and yet had relatively lower catalyst concentration than Experiment 4. In general, no obvious deduction can be made from the residual iron percentage data with respect to catalyst used (catalyst **[3]** versus **[4]**) or catalyst concentration (1.25 versus 2.5 wt.%), however.

The trends identified from the initial decomposition temperatures and the residue percentages respectively for Experiment 3 follow.

- (i) The order of increasing thermal stability is 900 °C < 800 °C < 850 °C.
- (ii) The order of increasing purity (in terms of iron content) is 800 °C < 900 °C < 850 °C.

The trends identified from the initial decomposition temperatures and the residue percentages respectively for Experiment 4 follow.

- (i) The order of increasing thermal stability is 900 °C < 800 °C < 850 °C.
- (ii) The order of increasing purity (in terms of iron content) is 850 °C < 900 °C < 800 °C.

The trends identified from the initial decomposition temperatures and the residue percentages respectively for Experiment 5 follow.

- (i) The order of increasing thermal stability is 800 °C < 900 °C.
- (ii) The order of increasing purity (in terms of iron content) is 800 °C < 900 °C.

6.2 Conclusions from Experiments 3, 4 and 5

- The higher the T_{\max} , the higher was the raw yield, however, low yields (< 20%) were obtained for Experiments 3 to 5.
- Ferrocenoyl imidazolide (catalyst **[3]**) is suitable for forming large percentages of MWCNTs (with respect to the collected material) at 2.5 wt.%, but at 5 wt.% produces mostly spheres, i.e. catalyst concentration influences the SCNMs formed.
- The best temperature for producing the largest percentage of MWCNTs, for catalyst **[3]** at 2.5 wt.%, is 800 °C.
- The oxygen concentration in Experiment 4 may be sufficiently large to deactivate the iron catalyst thereby increasing the sphere population.
- A comparison of the SCNMs formed in Experiments 1 and 2 with those in 3 and 4, shows that the choice of catalyst (or the ligand on ferrocene) influences the SCNMs produced.

- A comparison of the SCNMs from Experiments 3 and 5 showed that the ratio of Fe:C influences the SCNMs formed, although different catalysts were used in these experiments. Also, catalyst [4] produces bigger spheres than catalyst [3] due to the smaller Fe:C ratio.
- The introduction of nitrogen in the catalyst produces bamboo-shaped CNTs.
- For catalyst [3], the lower the temperature, in general, in the range 900 to 800 °C, the more amorphous carbon is produced.
- The widest average OD for MWCNTs was formed in Experiment [3] (2.5 wt.% catalyst [3]) at 900 °C.
- The OD distribution is not significantly influenced by the catalyst concentration (when comparing Experiments 3 and 4).
- Temperature and catalyst concentration may work together to influence the length of MWCNTs; with 800 °C, at 2.5 wt.% catalyst [1] or [3] producing some of the longer tubes. However, the 900 °C material, at 5 wt.% catalyst [3], gave the longest representative tubes of Experiments 3 to 5.
- N-CNTs are shorter, generally, than pristine CNTs at the same catalyst concentration.
- N-doping decreases the alignment of MWCNTs in bundles.
- Raman spectroscopy studies showed that higher temperatures correlate with higher crystallinity.
- Experiment 5 gave small I_D/I_G values indicating that the products are more crystalline than for Experiment 3.
- In both Experiments 3 and 4 the same trend of increasing thermal stability from 900 to 800 to 850 °C is seen (i.e. the 850 °C materials are the most thermally stable). And in both experiments the 800 °C samples had the largest decomposition range which corresponded to more Raman disorder.
- In Experiment 3 spheres decomposed at a faster rate than MWCNTs as seen from the 900 °C weight loss curve.
- The most suitable material from Experiments 3 to 5, in general, for use as a catalyst support, is the 850 °C material synthesized in Experiment 3. One reason for this is its very high yield of MWCNTs (95%) in the raw yield. Thus, this material is expected to have a higher surface area than other materials in Experiment 3, this deduction is based on the results in **Section 5.7.7.8 in Chapter 5** (although problems with scaling up prevented the collection of enough material for BET analysis after other analyses had consumed some of the material, i.e. TGA). High surface areas are considered desirable when choosing catalyst supports. Also, this material has a relatively high thermal stability and purity in terms of iron content. The low iron content, which can be further reduced by purification techniques, is desirable since the presence of iron must be minimized so that it does not interfere with, or deactivate, other metal catalysts which are loaded onto the MWCNTs.

6.3 Results and discussion of Experiment 6 – Effect of the introduction of S and O

6.3.1 Reaction parameters and raw yields

A catalyst concentration of 2.5 wt.% (Experiments 1 and 3) consistently yielded high percentages of MWCNTs (except for the 900 °C material in Experiment 3) in the raw yields. Thus, the same concentration was used in Experiment 6 for catalyst [5]. The temperatures chosen to investigate were 900 and 800 °C. The reaction parameters and raw yields for Experiment 6 are given in **Table 6.8**. A larger yield was found at the higher temperature, as expected.¹ Again, the yields were low (< 20%) as usual and this is mostly due to loss of product as a fine black powder in the gas flow of the exhaust system.

Table 6.8 Reaction parameters for Experiment 6 [toluene as C source, 10 % H₂ in Ar (v/v), gas flow rate 100 mL/min, injection rate 0.8 mL/min].

Exp. run	Primary variable	Catalyst	T _{max} (°C)	Catalyst concentration (wt.%)	Percentage raw yield of SCNMs (%)
6.1	effect of S & O	[5]	900	2.5	8.31
6.2			800		0.69

6.3.2 SCNMs formed

Literature reports that the presence of small amounts of sulfur can both promote³³ the growth of MWCNTs and produce Y-junction or branched CNTs.^{34,35} This was not observed in this work. However, it has also been shown that the form in which sulfur exists in the system, or the form in which it is added to the system, influences the products which are produced, and the presence of sulfur does not necessarily produce Y-junction CNTs.³⁶ In this work no observable MWCNTs were produced, nor CNFs nor polygon structures. Carbon spheres were the primary product, with 800 °C producing almost solely carbon spheres (see **Tables 6.9** and **6.10**). In the previous experiments, with similar reaction conditions to Experiment 6, more spheres were produced at higher temperatures depending on the reaction conditions and catalyst used. The opposite trend is seen here (see **Table 6.10**).

Table 6.9 TEM and SEM images of products from Experiment 6.

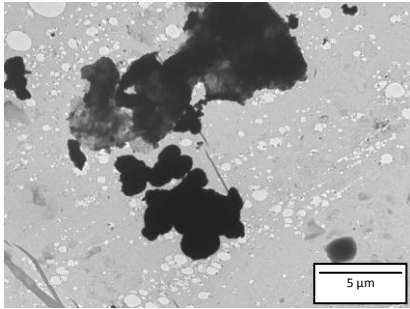
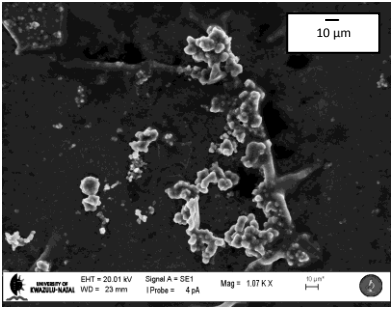
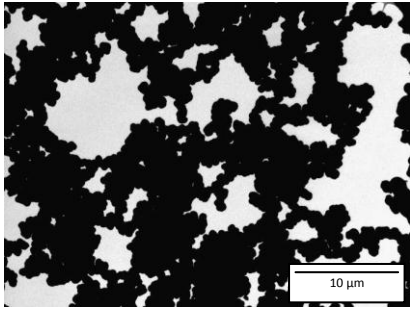
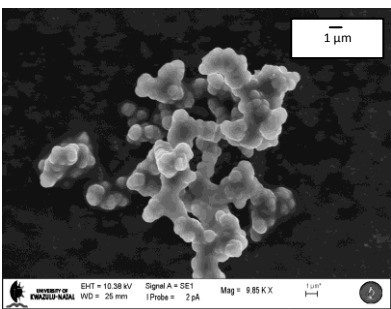
Exp. run	Cat.	Cat. conc (wt.%)	T _{max} (°C)	Representative TEM image	Representative SEM image
6.1	[5]	2.5	900		
6.2			800		

Table 6.10 Results of TEM analysis for Experiment 6.

Exp. run	T _{max} (°C)	Approximate percent distribution of morphologies		C spheres
		% Carbon spheres	% Amorphous carbon	Ave. OD (nm)
6.1	900	65	35	902.7
6.2	800	95	5	755.5

Preliminary EDX studies showed that sulfur was incorporated into the products (see **Appendix F, Table F.3**), although whether this sulfur was incorporated into the SCNM graphene structure or bonded to iron metal, or otherwise, was not studied. This is a topic for further research.

6.3.3 Size of spheres

Figure 6.19 shows the distribution of carbon nano- and microsphere diameters at T_{max} = 900 and 800 °C. The histogram for 900 °C (shown in blue) shows two major ranges, rather than a

smooth Gaussian type distribution, from approximately 200 to 500 and then 600 to 1300 nm. (This same trend is not conclusively seen for the red histogram for the 800 °C run.) This may suggest that the 900 °C catalyst, along with the other reaction parameters, is suitable for producing spheres in two distinct size categories. In other words, sphere growth is halted within two diameter ranges, depending on the T_{\max} of the system. **Appendix F, Table F.3** confirms the presence of sulfur in the products of this experiment.

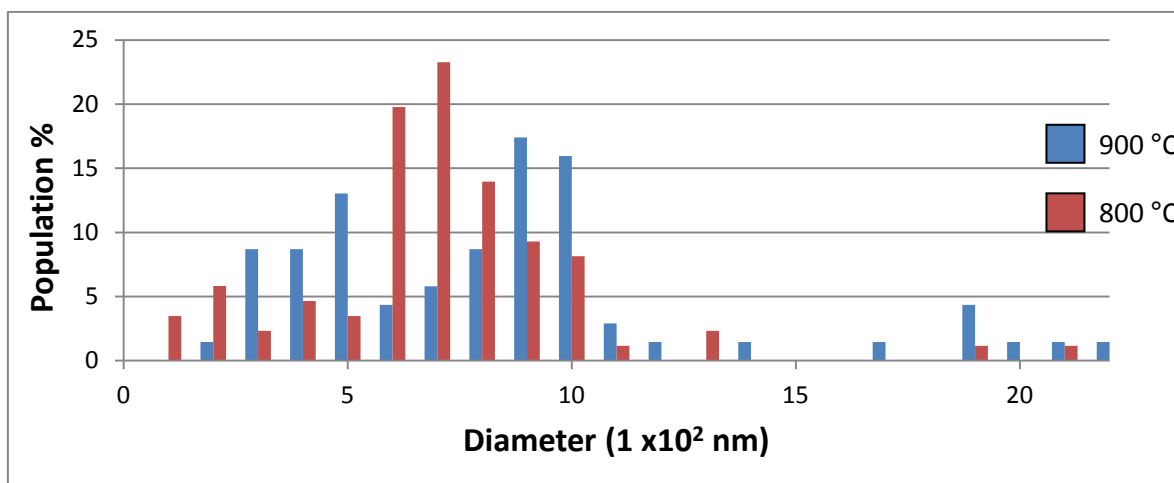


Figure 6.19 Histogram of the distribution of sphere diameters for 900 and 800 °C for catalyst [5].

6.3.4 Crystallinity and thermal stability of products

The Raman spectroscopy data (**Table 6.11**) shows a lower I_D/I_G ratio for the 900 °C material. This indicates that this sample is more graphitic in nature than the 800 °C material. This result is in disagreement with the data in **Table 6.10** where it can be seen that the 900 °C material has a significantly larger proportion of amorphous carbon than the 800 °C material. Hence, this would suggest that the greater percentage of the carbon spheres for the 800 °C material were not very graphitic.

Table 6.11 Results from the Raman spectroscopic analysis of Experiment 6.

Exp. run	T_{\max} (°C)	“Disorder” D-band (cm ⁻¹)	“Graphitic” G-band (cm ⁻¹)	I_D/I_G ratio
6.1	900	1372	1556	0.100
6.2	800	1372	1557	0.225

For the products of Experiment 6, there was a significant difference in the temperature of the onset of oxidation as seen in **Figure 6.20**. The 900 °C sample began oxidizing at approximately 200 °C (see the sudden, though slight, gradient decline at θ) and then more rapidly at approximately 400 °C. The former temperature is attributed to amorphous carbon oxidation (see the large amount of amorphous carbon in the TEM image in **Table 6.9** which supports this

deduction) and the latter to the beginnings of SCNM (spheres) oxidation. In contrast, the 800 °C sample appeared to have significantly less amorphous carbon since the first sign of noticeable decomposition began above the amorphous carbon decomposition temperature range, i.e. decomposition only began near 550 °C. This supports the lower amount of amorphous carbon seen in the TEM image in **Table 6.9** and the value in **Table 6.10**. Also, the 800 °C sample has a lower range of decomposition temperatures as indicated by the steeper gradient on the weight loss profile. This indicates that this sample decomposes more rapidly, and can indicate that this sample is more homogeneous in terms of SCNM distribution, which is the case (see **Table 6.10**). The 800 °C material had a significant weight percent of iron (7.2 wt.%) compared to the 900 °C material (2.8 wt.%). **Table 6.12** shows selected important information from the TGA thermogram.

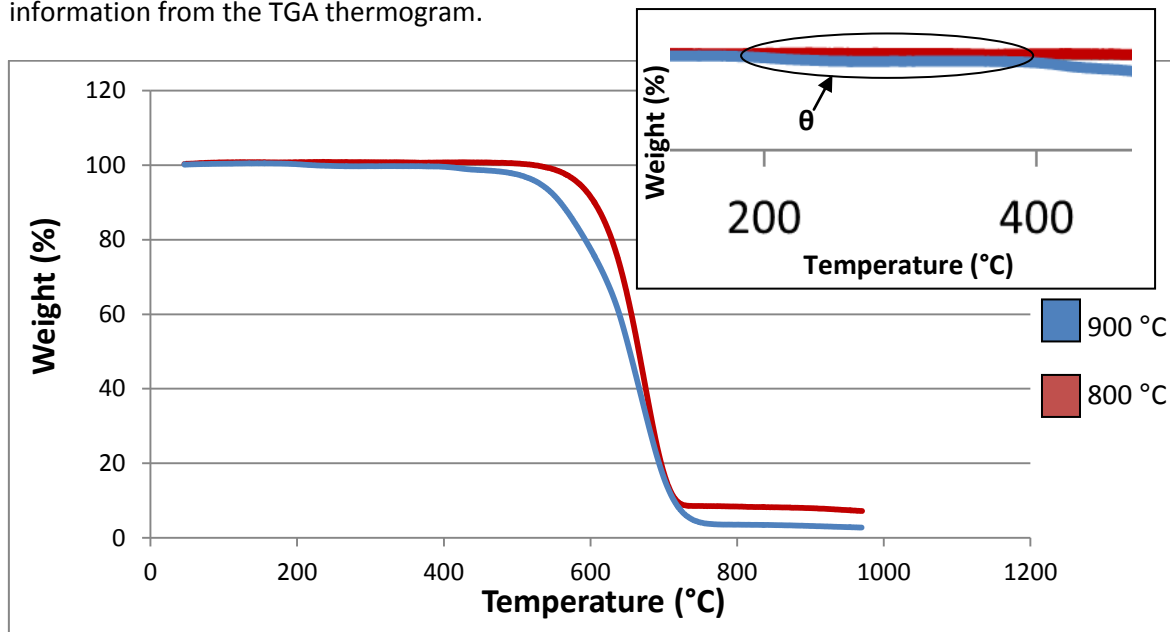


Figure 6.20 TGA weight loss percent curves obtained in air for the products from Experiment 6 with enlarged portion inserted to show θ more clearly.

Table 6.12 Decomposition temperature and residue weight percent of the products from Experiment 6.

Exp. run	T_{\max} (°C)	Main decomposition range (°C)	Temperature of max. decomposition (°C)	Residual mass percent (%)
6.1	900	≈ 400 to 730	659	2.8
6.2	800	≈ 550 to 710	673	7.2

The trends identified from the initial decomposition temperatures, the decomposition ranges and the residue percentages respectively follow.

- (i) The order of increasing thermal stability is 900 °C < 800 °C.
- (ii) The order of increasing heterogeneity (in terms of SCNM distribution) is 800 °C < 900 °C.
- (iii) The order of increasing purity (in terms of iron content) is 800 °C < 900 °C.

6.4 Conclusions from Experiment 6

- The higher the T_{\max} the higher the raw yield, however more amorphous carbon was produced at higher temperature.
- Catalyst [5] (relative to catalysts [3] and [4]) is suitable for the synthesis of spheres, especially at 800 °C where the yield of spheres, in the collected material, is very high.
- The presence of sulfur, at a catalyst concentration of 2.5 wt.%, did not promote MWCNT formation nor Y-junction MWCNT formation.
- The average sphere size is micrometric at both temperature values.
- In the 900 °C sample TGA studies confirm the presence of more amorphous carbon and more heterogeneity of SCNM types, although the Raman spectroscopy data does not support this.

6.5 Summary of Experiments 3 to 6

Of Experiments 3 to 6, Experiment 3 proved to be the only one suitable for producing high yields of MWCNTs (except for the 900 °C material), while other experiments produced primarily spheres. In other words, catalyst [3] at a concentration of 2.5 wt.% is preferred for MWCNT formation, especially at lower temperatures in the range 800 to 900 °C. Nitrogen was successfully doped into some MWCNTs in all runs, giving rise to “bamboo-shaped” compartments in these MWCNTs.

References

- 1 M. S. Mohlala, X.-Y. Liu and N. J. Coville, *J. Organomet. Chem.*, 2006, **691**, 4768
- 2 D. Pradhan and M. Sharon, *Mater. Sci. Eng.*, 2002, **B96**, 24
- 3 V. O. Nyamori, E. N. Nxumalo and N. J. Coville, *J. Organomet. Chem.*, 2009, **694**, 2222
- 4 E. N. Nxumalo, P. J. Letsoalo, L. M. Cele and N. J. Coville, *J. Organomet. Chem.*, 2010, **695**, 2596
- 5 H.-s. Qian, F.-m. Han, B. Zhang, Y.-c. Guo, J. Yue and B.-x. Peng, *Carbon*, 2004, **42**, 761
- 6 Y. Chai, Q. F. Zhang and J. L. Wu, *Carbon*, 2006, **44**, 687
- 7 X. Wang, W. Hu, Y. Liu, C. Long, Y. Xu, S. Zhou, D. Zhu and L. Dai, *Carbon*, 2001, **39**, 1533
- 8 C.-L. Sun, H.-W. Wang, M. Hayashi, L.-C. Chen and K.-H. Chen, *J. Am. Chem. Soc.*, 2006, **128**, 8368
- 9 C. P. Ewels and M. Glerup, *J. Nanosci. Nanotech.*, 2005, **5**, 1345
- 10 J. W. Jang, C. E. Lee, S. C. Lyu, T. J. Lee and C. J. Lee, *Apply. Phys. Lett.*, 2004, **84**, 2877
- 11 R. M. Yadav, P. S. Dobal, T. Shripathi, R. S. Katiyar and O. N. Srivastava, *Nanoscale Res. Lett.*, 2009, **4**, 197
- 12 P. Ghosh, M. Zamri, M. Subramanian, T. Soga, T. Jimbo, R. Katoh and M. Tanemura, *J. Phys. D: Appl. Phys.*, 2008, **41**, 155405
- 13 Z. N. Tetana, S. D. Mhlanga, G. Bepete, R. W. M. Krause and N. J. Coville, *S. Afr. J. Chem.*, 2012, **65**, 39
- 14 S. Maruyama, R. Kojima, Y. Miyauchi, S. Chiashi and M. Kohno, *Chem. Phys. Lett.*, 2002, **360**, 229
- 15 Y. Xia, B. Gates, Y. Yin and Y. Lu, *Adv. Mater.*, 2000, **12**, 693

- 16 Private communication with Dr Paul Franklyn (University of the Witwatersrand), at a HRTEM training program held at the University of KwaZulu-Natal, September 2011
- 17 A. A. Deshmukh, S. D. Mhlanga and N. J. Coville, *Mater. Sci. Eng., R*, 2010, **70**, 1
- 18 M. Monthieux, H. Allouche and R. L. Jacobsen, *Carbon*, 2006, **44**, 3183
- 19 K. Kuwana and K. Saito, *Carbon*, 2005, **43**, 2088
- 20 C. Singh, M. S. P. Shaffer and A. H. Windle, *Carbon*, 2003, **41**, 359
- 21 V. O. Nyamori and N. J. Coville, *Organometallics*, 2007, **26**, 4083
- 22 K.-Y. Chun, H. S. Lee and C. J. Lee, *Carbon*, 2009, **47**, 169
- 23 L. S. Panchakarla, A. Govindaraj and C. N. R. Rao, *ACS Nano*, 2007, **1**, 494
- 24 V. O. Khavrus, A. Leonhardt, S. Hampel, C. Täschner, C. Müller, W. Gruner, S. Oswald, P. E. Strizhak and B. Büchner, *Carbon*, 2007, **45**, 2889
- 25 Y. T. Lee, N. S. Kim, J. Park, J. B. Han, Y. S. Choi, H. Ryu and H. J. Lee, *Chem. Phys. Lett.*, 2003, **372**, 853
- 26 R. Kurt and A. Karimi, *ChemPhysChem.*, 2001, **2**, 388
- 27 J. Liu, S. Webster and D. L. Carroll, *J. Phys. Chem. B*, 2005, **109**, 15769
- 28 Z. L. Wang and Z. C. Kang, *J. Phys. Chem.*, 1996, **100**, 17725
- 29 Z. L. Wang and Z. C. Kang, *Carbon*, 1997, **35**, 419
- 30 Ph. Serp., R. Feurer, Ph. Kalck, Y. Kihn, J. L. Faria and J. L. Figueiredo, *Carbon*, 2001, **39**, 621
- 31 N. Yao, V. Lordi, S. X. C. Ma, E. Dujardin, A. Krishnan, M. M. J. Treacy and T. W. Ebbesen, *J. Mater. Res.*, 1998, **13**, 2432
- 32 A. Shahverdi, K. S. Kim, Y. Alinejad, G. Soucy and J. Mostaghimi, *Selective oxidation of excess amorphous carbon during single-walled carbon nanotubes synthesis by induction thermal plasma process*, Proceedings of the 2009 Conference of the International Plasma Chemistry Society, Bochum, Germany, 26-31 July 2009, paper 649
<http://www.ispc-conference.org/ispcproc/papers/649.pdf> (accessed 28 June 2012)
- 33 Y. Chen, Z. Sun, Y. N. Li and B. K. Tay, *Mater. Chem. Phys.*, 2006, **98**, 256
- 34 H. Zhu, L. Ci, C. Xu, J. Liang and D. Wu, *Diamond Relat. Mater.*, 2002, **11**, 1349
- 35 F. L. Deepak, A. Govindaraj and C. N. R. Rao, *Chem. Phys. Lett.*, 2001, **345**, 5
- 36 H. M. Cheng, F. Li, G. Su, H. Y. Pan, L. L. He, X. Sun and M. S. Dresselhaus, *Appl. Phys. Lett.*, 1998, **72**, 3282

CHAPTER 7

PREPARATION OF Pd/MWCNTs

7.1 Introduction to MOCVD

It was as far back as 1890 that the deposition of a metal, namely nickel, by the CVD process from a metal-organic substance was reported.¹ More than half a century later Marboe, in 1947, first reported platinum deposition.² However, it took almost three more decades before Rand published literature on platinum film deposition without a carrier gas.^{3,4} In 1988, the first report of the selection of palladium and platinum organometallic precursors for the deposition of thin metal films was published.⁵ Since then metal-organic chemical vapour deposition (MOCVD) processes have gained more interest and importance since they lead to many applications⁶ such as the formation of thin films of metals on various supports for electronic devices⁷ and in the formation of finely dispersed metal particles on supports for heterogeneous catalysis⁸ or hydrogen storage applications.⁹ In commonly used loading techniques, such as wet impregnation, the impregnation step is followed by tedious washing, drying, calcination and finally reduction.¹⁰ An important advantage of the MOCVD technique over more traditionally used methods, such as the one just mentioned, is its simplicity. When the metal is loaded, further treatment steps are not always necessary.

The MOCVD method can be employed to load pure metals including Fe, Co, Ni, Pd, Pt, Cu and Rh, as well as alloys, metal nitrides, metal oxides amongst other metal compounds.^{6,11,12} In general, MOCVD methods maintain the support integrity – for example, its structure and porosity.¹³ MOCVD reactor design varies. Some consist of a single chamber which is evacuated and placed under high pressure with a self-regulated reduction of the metal ion from the precursor on the support as is the case in this work. Others make use of inert gases to flush out air.¹⁴ Alternatively a reducing gas can be used to convert the metal cation to the zero valent state. Just as with the CVD synthesis of CNTs, it is logical that the parameters (for example flow rate, deposition temperature, deposition time and the like) employed determine the size and structure of the products.

Organometallic compounds and complexes are generally fairly volatile and consequently find use as MOCVD precursors in the same way as in the synthesis of SCNMs by CVD. The volatility is influenced by the nature of the ligands on the metal. Some metal NPs can be deposited at temperatures as low as 150 °C depending on the precursor compound and the presence of other gases in the system.^{14,15} Allyl, $\text{H}_2\text{C}=\text{CHCH}_2\text{R}$ ($\eta^3\text{-C}_3\text{H}_5$), and acetylacetonate, $\text{CH}_3\text{COCH}_2\text{COCH}_3$ (acac), groups can act as ligands and have been shown to increase volatility, and hence are commonly employed in such complexes.^{16,17} Besides high volatility, other fundamental requirements of the metal precursors in the MOCVD process include decomposition in such a manner as to not induce the formation of fragments which could poison the metal (typically chlorine and sulfur species can do this), and high levels of deposition.¹⁶ Volatile complexes of palladium, platinum and rhodium were reviewed as

precursor substances for the deposition of these metals by MOCVD,¹⁶ as well as other metal complexes and compounds.¹⁸

The importance of palladium, specifically, as a metal catalyst, and the enhanced catalytic properties it displays when supported on carbon nanotubes, has been reviewed in **Chapter 2**. Some commonly used palladium complexes for MOCVD include (η^3 -allyl)palladium complexes, or complexes with β -diketonate or dimethyl ligands [see **Figures 7.1 (a), (b) and (c)** respectively].¹⁶

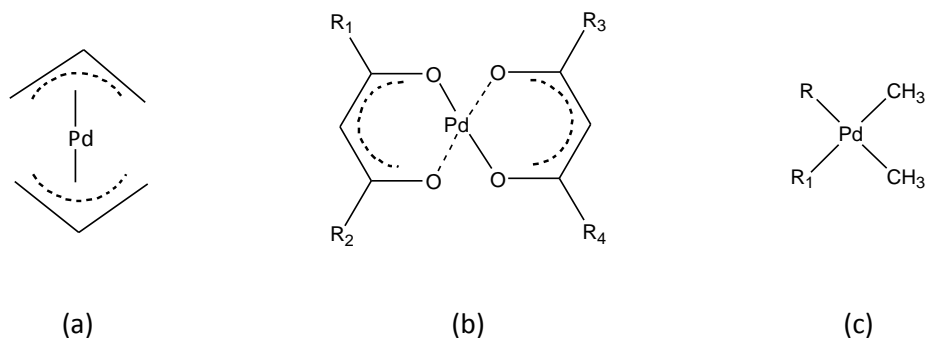


Figure 7.1 The basic structures of palladium complexes commonly used in MOCVD, specifically (a) (η^3 -allyl) palladium complexes, (b) β -diketonate palladium complexes and (c) palladium complexes with two methyl ligands.

The MOCVD of palladium to produce finely dispersed particles has been done using a variety of palladium precursors and a variety of support materials. These include Pd(Cp)(η^3 -allyl) and Pd(η^3 -allyl)(hfa) (where hfa is hexafluoroacetylacetonate) on powdered silica by a fluidized-bed reactor-modified MOCVD process^{13,17} and Pd(Cp)(η^3 -allyl) on nitric acid-treated CNFs¹⁹ and Pd(acac)₂ on γ -Al₂O₃/corderite.¹⁴

The structure of Pd(acac)₂, whose IUPAC name is palladium(II) 2,4-pentanedionate, and whose alternative name is palladium(II) *bis*-acetylacetonate [Pd(acac)₂], is shown in **Figure 7.2**. This compound has been patented for CVD use.²⁰ It decomposes and deposits under conditions below 300 °C and pressures below 10⁻⁴ Torr. Other studies, using TGA techniques, have shown that this palladium precursor complex decomposes at low temperatures (100-160 °C in an inert atmosphere).²¹ It is now commercially available and is air-stable at room temperature. Semyannikov *et al.* described a plausible mechanism by which gaseous Pd(acac)₂ decomposes.²²

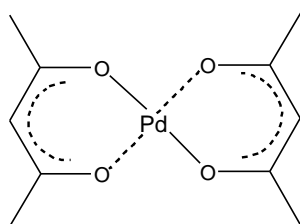


Figure 7.2 The structure of Pd(acac)₂.

Besides its use in MOCVD, there are also reports of the use of Pd(acac)₂ as a reagent for various organic syntheses such as acid and base hydrolysis and halide substitution.²³

Pd²⁺ salts, or complexes, can act as sources of Pd⁰.²⁴ In the case of Pd(acac)₂, the Pd²⁺ ions are reduced on the surface of CNTs after nucleation.

Pd(acac)₂ was chosen as a source of palladium in this project. The best overall support in this project, in terms of yield of MWCNTs, good thermal stability and low residual iron content, was the 800 °C material produced in Experiment 1 (catalyst **[1]** at 2.5 wt.%). (Refer to **Chapter 5**.) For comparison, an undoped commercial material was purchased. These two materials will be referred to as syn-MWCNTs (which is the synthesized material) and com-MWCNTs (the commercial material), respectively.

Note that, as was discussed in **Chapter 2**, MWCNTs that contain few defects attain only low metal NP loadings. Metals anchor better when the MWCNT surface has been pre-functionalized or when there are more surface defects for nucleation of metal NPs. With regards to palladium specifically, Liang *et al.* found no deposited palladium NPs on pristine CNFs.¹⁹ When the support was first treated with 5 M nitric acid, TEM revealed highly dispersed palladium NPs on the CNFs and inductively coupled plasma-optical emission spectroscopy (ICP-OES) results showed that the degree of loading was dependent on the degree of functionalization (as well as the amount of precursor compound in the deposition apparatus). Suttisawat *et al.*, who investigated the H₂ storage capacity of Pd- or V-MWCNTs, found that defect sites on re-crystallized MWCNTs resulted in a lowered interaction of palladium NPs with CNTs.⁹ This shows again that defect sites are necessary for higher palladium loading. Oxyacid treatment was thus performed prior to palladium loading and the method will be discussed in **Section 7.4.1**.

A discussion of the instrumentation, reagents for functionalization and loading techniques as well as the characterization processes and instrumentation follow in **Sections 7.2 to 7.5**.

7.2 Instrumentation – The MOCVD apparatus

The MOCVD apparatus [see **Figures 7.3 (a) and (b)**] consisted of a cylindrical stainless steel reaction chamber (140 mm x 10 mm) sealed at one end with a Swagelok® face seal fitting with a blind gasket. The other end was fitted with a fritted disc to minimize loss of solid materials, and after this was connected to a stainless steel 1/8 inch diameter vacuum line. This design is advantageous since it allows sublimation of the metal precursor and deposition to occur in the same vessel, thereby preventing loss of the precursor which may occur if the two processes occurred in separate regions.¹⁴ The system was attached to a rotary pump and the vacuum pressure maintained between 0.1 and 2 mbar. The vacuum pressure was monitored by means of a Thyracont VD84/1 Pirani vacuum gauge which measures absolute pressure rather than relative pressure. **Figure 7.3** shows both a schematic and photographic form of the MOCVD reactor.

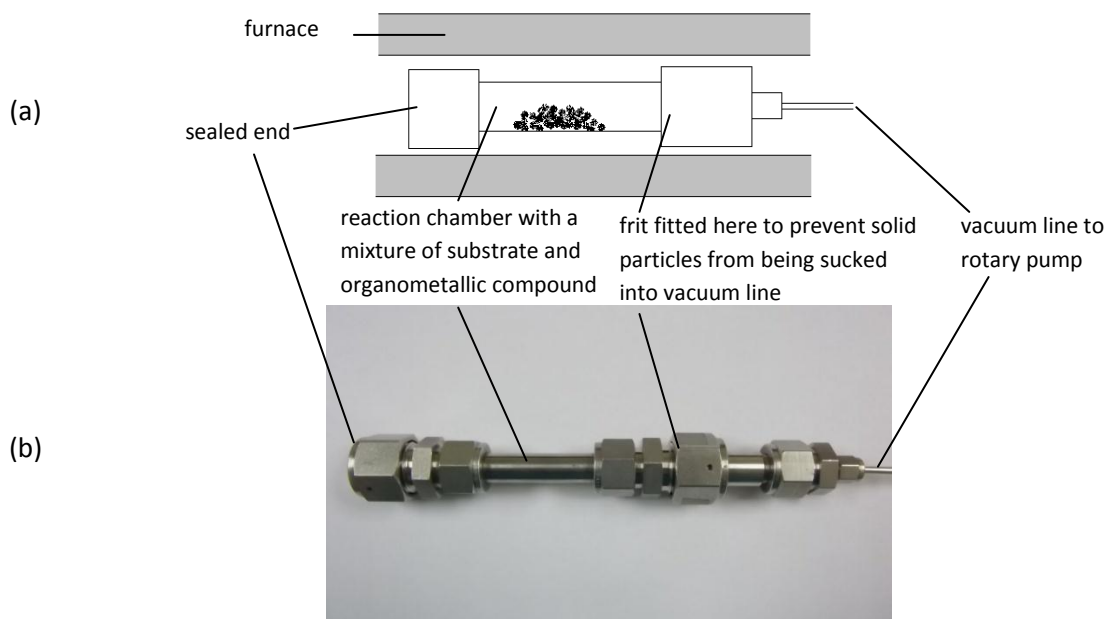


Figure 7.3 The MOCVD reactor in (a) schematic form and (b) photographic form.

7.3 Laboratory chemicals, reagents, solvents and gases

Reagents

- as-synthesized MWCNTs (produced in Experiment 1 at 800 °C)
- commercial MWCNTs (Cheap Tubes, USA, > 95 wt.%) purified by 2 M HCl
- Pd(acac)₂ (Merck, Germany, synthesis grade)
- Palladium ICP standard solution (Johnson Matthey, prepared in South Africa, guaranteed to be 1000 ppm ± 0.2% Pd in 0.5 M HNO₃)
- nitric acid ≥ 69% (Sigma-Aldrich, Germany, ACS reagent)
- hydrochloric acid, fuming 37% (Merck, Germany, ACS, ISO Reag, Ph Eur.)
- Pd on activated carbon (Sigma-Aldrich, USA, 10 wt.%)
- Pd on activated carbon (Sigma-Aldrich, USA, 5 wt.%)

Solvents

- in-house prepared doubled-distilled water

Gases

- N₂ (Afrox, South Africa, HP) for degassing in the Brunauer, Emmett and Teller analysis of surface area

7.4 General procedure

7.4.1 Surface functionalization of the chosen supports

MWCNTs in this project were acid treated prior to MOCVD. Note that although the commercially synthesized MWCNTs (also produced by CVD) were treated in dilute HCl(aq), by the manufacturer, to reduce metal content, it was decided to still treat this material in oxidizing acid to attach the oxide functional groups. The prefix “*f*–” will be used to denote functionalized/purified MWCNTs. Refer to **Chapter 5, Sections 5.5 and 5.8** for the conditions of acid treatment (Yield: *f*-com-MWCNTs = 97%; *f*-syn-MWCNTs = 97%). Acid-functionalized MWCNTs were characterized by TEM, SEM, TGA and BET (see **Section 7.6**).

7.4.2 Deposition of Pd by MOCVD

Pd(acac)₂ (0.072 g) was ground and mixed together in a mortar and pestle with *f*-com-MWCNTs (0.475 g) to attain approximately 5 wt.% palladium. The resulting homogeneous mixture was placed inside the MOCVD reactor and the reactor components sealed. The reactor, which was under vacuum (between 0.1 and 2 mbar), was then placed in the middle of a muffle furnace and the temperature allowed to reach 120 °C at a rate of 5 °C/min. The system was maintained at 120 °C for 30 minutes to remove any water from the system which may otherwise have interfered with the MOCVD process. The furnace was then heated to 400 °C at a rate of 8 °C/min and thereafter maintained at 400 °C for 45 minutes. (Temperatures above 400 °C can induce migration of particles over the support surfaces and agglomeration of metal particles,²⁵ thereby decreasing the available surface area of the metal for substrate molecules. However, Suttisawat *et al.* used a temperature of 450 °C for vanadium metal loading by MOCVD and their work did not mention agglomeration.⁹) The system was then allowed to cool to ambient conditions, still under vacuum. Lastly, the contents of the reactor were removed by scraping with a spatula, weighed and characterized. Cleaning of the reactor was done by scraping out solid residues and passing short bursts of air into the chamber.

This procedure and quantities were repeated for the *f*-syn-MWCNTs to obtain 5 wt.% Pd and then again for both supports at 10 wt.% Pd using the masses indicated in **Table 7.1**.

Table 7.1 Conditions varied for MOCVD.

Support	Mass precursor : mass support	
	5 wt.%	10 wt.%
<i>f</i> -syn-MWCNTs	0.072 g : 0.475 g	0.143 g : 0.450 g
<i>f</i> -com-MWCNTs		

7.5 Characterization of Pd/MWCNTs: Instrumentation and techniques

The presence of palladium was confirmed by using EDX and ICP-OES, and the latter technique was also used to determine the actual palladium loading. The average diameters and distributions of palladium NPs were determined by using TEM and SEM (a minimum of 100 palladium NPs per sample were measured). The BET surface areas of the loaded supports were also measured. The methodology for TEM, SEM, EDX and BET studies was discussed in **Chapter 5**, while that of ICP-OES will be discussed now.

7.5.1 Inductively coupled plasma-optical emission spectroscopy (ICP-OES)

ICP-OES involves the use of a plasma, usually argon, which is used to excite atoms and ions in a sample which then release energy at characteristic wavelengths. In this way this method allows elements to be identified. Also, the intensity of the emitted radiation is proportional to the quantity of the element and thus this method is both qualitative and quantitative.

A sample of Pd-MWCNTs from each deposition (0.05 g) was separately digested in *aqua regia* (10 cm³) in a closed vessel microwave system (CEM Mars Xpress) by ramping the temperature to 195 °C over a period of 15 minutes, and then holding the temperature constant for a further 15 minutes. After that the system was allowed to cool to room temperature. The resulting mixture was filtered and the vessel washed through MN 615 filter paper with double-distilled water. The filtrate was then diluted to 25 cm³ with double-distilled water. This solution was subsequently filtered through a 0.45 µm PVDF syringe filter to ensure the complete removal of fine particulates. The sample solution was aspirated into the ICP spectrometer (Perkin Elmer Optima 5300 DV) and the samples measured radially. (For instrumental conditions for ICP-OES see **Table 7.2**.) Two replicate samples of each material were analyzed. Quantification was by means of an external calibration line. The calibration standards were prepared in acid solution as were the samples with palladium, at concentrations of 0, 50, 100, 150, 200 and 250 ppm. This provided a suitable range to measure samples of 5 and 10 wt.% palladium since their corresponding concentrations, after digestion and dilution, were approximately 100 and 200 ppm respectively. ICP-OES measurements were done in triplicate for each sample. The software used to analyze the results was WinLab 32.

Since no certified reference material was available for validation of results, similar Pd/C materials were purchased and used as “reference” materials to verify that the digestion method chosen was suitable for complete digestion of the carbonaceous-metal-loaded materials. These reference materials were 5 wt.% palladium on activated carbon and 10 wt.% palladium on activated carbon. Their digestion and ICP-OES analysis was done prior to that of the MOCVD materials in this project, and results confirmed the digestions of palladium from the materials to be complete.

Table 7.2 Instrumental conditions for ICP-OES.

Power (W)	1300
Plasma gas flow rate (L/min)	15
Auxiliary gas flow rate (L/min)	0.2
Carrier gas flow rate in nebulizer (L/min)	0.80
Integration time (s)	60
Wavelength (nm)	324.270

7.5.2 Scanning electron microscopy (SEM)

Scanning electron microscopy using a field emission gun (FEG SEM) was performed on Pd-MWCNTs using a Zeiss Ultra Plus Field Emission SEM with v 05.04.05.00 software at 2 to 10 kV and a working distance of approximately 3 mm. Sample preparation for this was the same as described in **Chapter 5, Section 5.6.2**. Two types of images were taken – normal high magnification SEM images and backscattered images. The purpose of the latter was to give better contrast between the MWCNTs and the palladium NPs. In backscattered imaging, elements with a higher atomic number scatter electrons to a greater degree than those elements with a lower atomic number. Hence, the heavier elements appear brighter and thus backscattered imaging allows one to easily identify the position of heavier elements (in this case palladium).

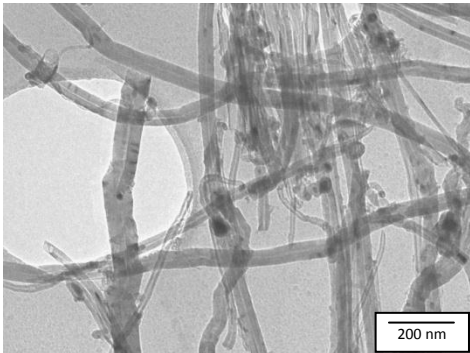
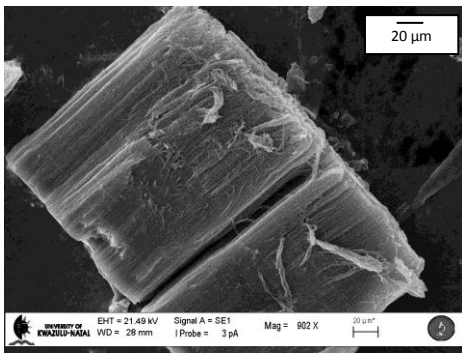
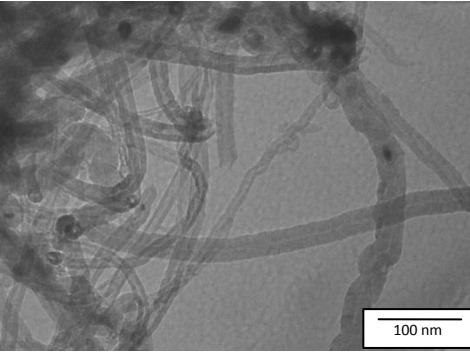
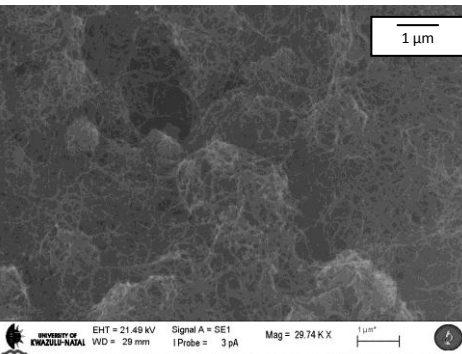
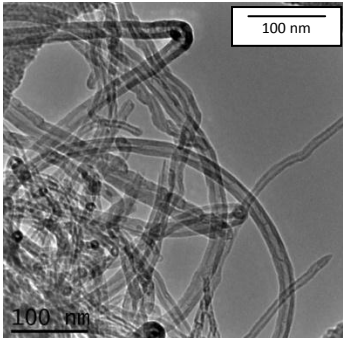
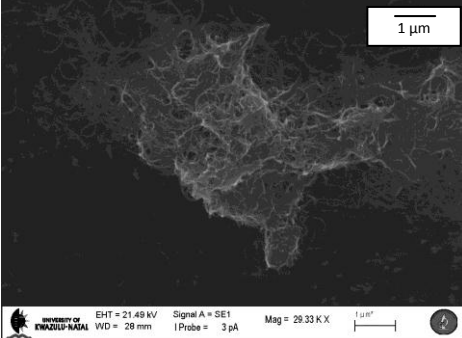
7.6 Results and discussion of oxyacid functionalization of supports

7.6.1 TEM and SEM analysis

Table 7.3 shows selected representative TEM and SEM images of the chosen supports before and after purification and oxyacid functionalization. (Note that images of the syn-MWCNTs can be found in **Chapter 5, Section 5.7**.) It was interesting to note that the TEM and SEM images of the *f*-syn-MWCNTs look very much like those of the pristine, unfunctionalized version. There still remain a few iron particles trapped inside MWCNTs (as seen by the dark areas in the TEM images). Also, even after grinding and acid treatment, a few bundles of aligned MWCNTs still existed. There was no significant difference between the TEM and SEM appearance of the supports before and after acid treatment, however in **Appendix E, Figure E.3** small, if not negligible, amounts of very short *f*-com-MWCNTs are visible. The acid is considered to have “cut” or fragmented the long tubes, even though the acid treatment regime is considered to be mild. What was interesting to note is the very small proportion of dark areas in the TEM for the pristine commercial MWCNTs, indicating the low iron content to begin with (2.1 wt.%), see **Table 7.4**. Also, it was interesting to note that the commercially bought MWCNTs were “fluffy” in appearance (in bulk). This is evident in the SEM image where it can be seen that MWCNTs were in no way aligned, hence the low density of the bulk material. The EDX results, in **Appendix F, Table F.4**, show the presence of small amounts of

iron, especially in the commercially bought material, although, the EDX results were primarily useful for qualitative use, as mentioned previously.

Table 7.3 TEM and SEM images of the pristine (commercial) material and both acid-functionalized supports.

	Representative TEM image	Representative SEM image
f -syn-MWCNTs ^π		
com-MWCNTs		
f -com-MWCNTs ^{δ,ω}		

^π See **Chapter 5, Section 5.7**, for images of the pristine version of these MWCNTs.

^ω The first image is an HRTEM image.

^δ See also **Appendix E, Figure E.2**.

7.6.2 TGA results

Figure 7.4 shows the thermograms of each support in air before and after oxyacid treatment. There is very little difference between the as-synthesized supports and their purified/functionalized versions. However, the iron residue percent is lower for the two purified versions. Specifically the iron content in the syn-MWCNTs dropped from 5.2 wt.% to

4.9 wt.% after purification and functionalization with oxide groups (see **Table 7.4**) and the content in the com-MWCNTs dropped from 2.1 wt.% to 1.8 wt.%, indicating that the purification technique was successful in removing some iron.

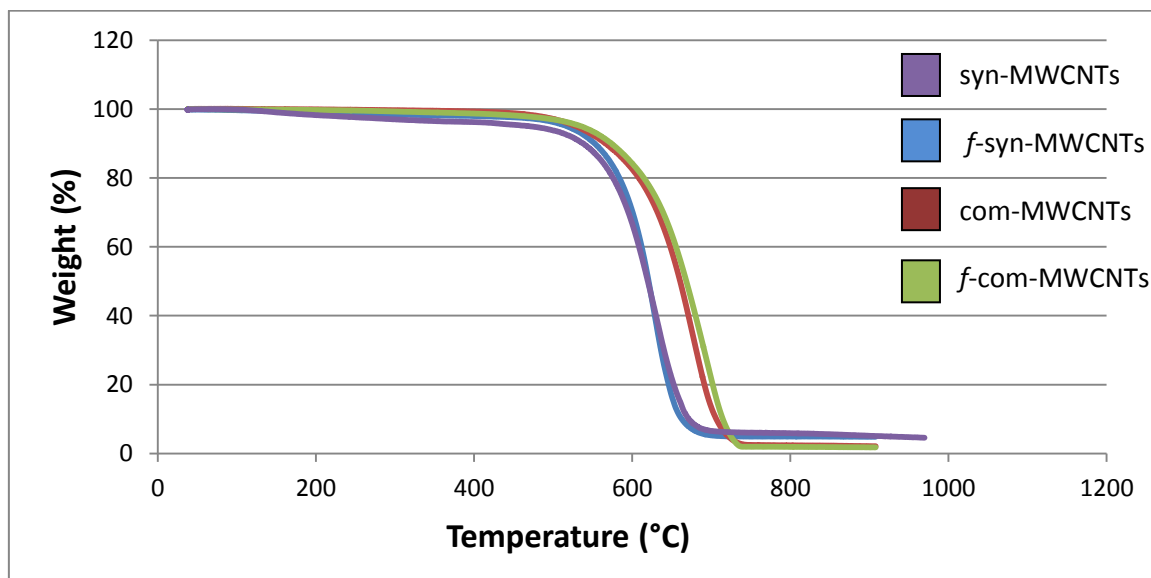


Figure 7.4 Thermograms obtained in air of the pristine chosen supports and the purified versions.

Table 7.4 Decomposition temperature and residue weight percent of the supports before and after oxyacid treatment.

Support	Main decomposition range (°C)	Temperature of max. decomposition (°C)	Residual mass percent (%)
syn-MWCNTs	≈ 500 to 680	634	5.2
<i>f</i> -syn-MWCNTs	≈ 500 to 650	627	4.9
com-MWCNTs	≈ 500 to 725	674	2.1*
<i>f</i> -com-MWCNTs	≈ 500 to 725	697	1.8

*Note that the manufacturer's packaging states < 1.5 wt.% ash, which is not consistent with this value.

The order of increasing purity (in terms of iron content) is syn-MWCNTs < *f*-syn-MWCNTs < com-MWCNTs < *f*-com-MWCNTs.

7.6.3 BET analysis

The BET surface area of the pristine and functionalized MWCNTs (**Table 7.5**) was determined as per the discussion in **Chapter 5, Section 5.6.5**.

Table 7.5 The BET surface areas of the functionalized chosen supports.

	BET surface area (m ² /g)
syn-MWCNTs	58.20
<i>f</i> -syn-MWCNTs	53.10
com-MWCNTs	146.35
<i>f</i> -com-MWCNTs	152.27

The surface area of the commercial MWCNTs is significantly higher than the synthesized ones, most likely due to their much smaller diameters (see **Table 7.8**). Also, it was interesting to note that the surface area of the functionalized supports is lower, rather than higher, for the synthesized material. This result was unexpected. The assumption is that the oxide groups on the *f*-syn-MWCNTs can lead to a lowered surface area by stronger interaction of individual MWCNTs which are now more chemically active. In other words, unfunctionalized MWCNTs are more inert and attract each other by weak van der Waals forces. In the *f*-syn-MWCNTs MWCNTs, dipole-dipole interactions, as a result of the oxide groups, may enhance the clustering of MWCNTs, thereby decreasing surface area. However, this is a preliminary supposition and was not observed for the commercial material. The surface area of the commercial material increased after functionalization as expected.

7.7 Results and discussion of the deposition of Pd onto supports

7.7.1 Raw yields

Small amounts of material were lost during deposition of palladium, although yields remained high (> 81%). Deviations from 100% yield may be due to several factors, the two main ones being: (1) the loss of very fine particles through the fritted disc during evacuation of the reactor and (2) deposition of palladium on the walls of the reactor rather than the support.

Table 7.6 shows the raw yields of MOCVD products.

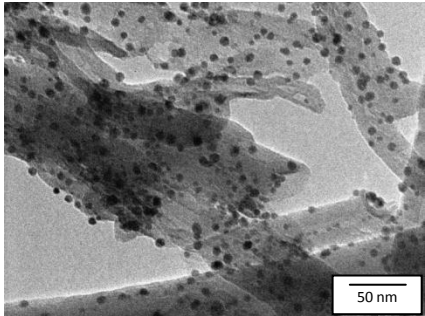
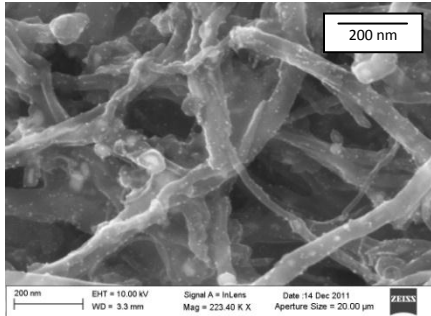
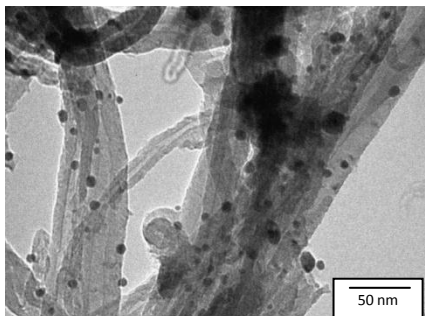
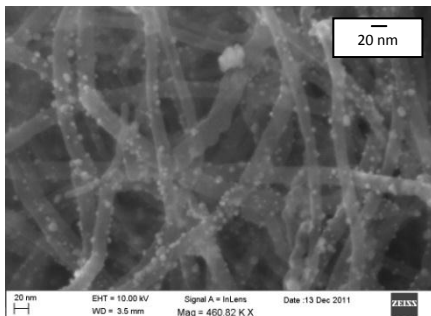
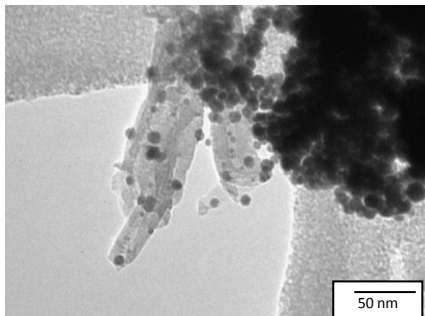
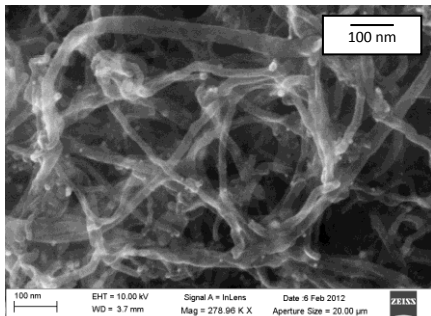
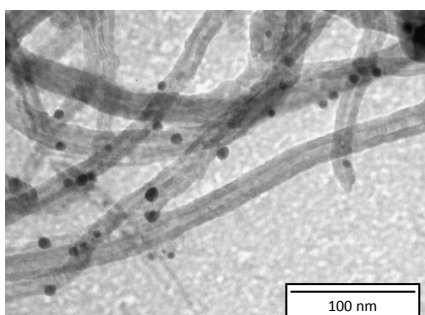
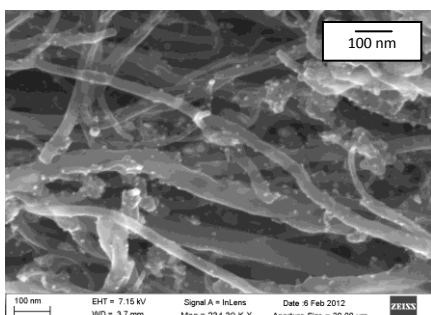
Table 7.6 Raw yields of each catalyst after acid purification and Pd-loading.

Catalyst	Approx. loading of Pd (wt.%)	Percent raw yield (%)
Pd- <i>f</i> -syn-MWCNTs	≈ 5	89.6
	≈ 10	81.8
Pd- <i>f</i> -com-MWCNTs	≈ 5	85.8
	≈ 10	81.3

7.7.2 TEM and SEM analysis

TEM images (**Table 7.7**) show discrete palladium NPs fairly evenly distributed on the supports.

Table 7.7 TEM and SEM images of the loaded supports.

Catalyst	Pd loading (wt.%)	Representative TEM image	Representative FEG SEM image
Pd- <i>f</i> -syn-MWCNTs	≈ 5		
Pd- <i>f</i> -com-MWCNTs			
Pd- <i>f</i> -syn-MWCNTs	≈ 10		
Pd- <i>f</i> -com-MWCNTs			

FEG SEM mainly enabled the viewing of lighter spots on MWCNTs, however, these could indicate palladium NPs, but this is not conclusive (see **Appendix E, Figure E.4** for an enlarged version of the *f*-syn-MWCNTs with a loading of 5 wt.% palladium). However, backscattered SEM images provide information of the composition of a sample by collection of high-energy electrons from elastic scattering. Heavier elements scatter electrons with a greater frequency and hence in backscattered SEM images the heavier elements appear much lighter in contrast to the lighter elements. Hence, backscattered SEM images were also taken to prove these lighter spots are indeed not carbon, but rather a heavier element (predominantly palladium). (Note that since TGA results in **Section 7.6.2** reveal minor percentages of residual iron, some, but very few, of the light spots may be due to iron.) Also, EDX confirmed the presence of palladium (see **Figure F.5** in **Appendix F**). **Appendix E, Figures E.5** and **E.6** show clearly where the palladium NPs are located on the MWCNTs for the 5 wt.% materials of both support types. **Figures E.7** and **E.8** do the same for the 10 wt.% loaded materials. Occasionally large clusters are apparent.

The size distribution of palladium NPs on each support is shown graphically in **Figure 7.5**. Noticeably, for all materials, the distribution is similar. Only the 10 wt.% Pd-*f*-syn-MWCNTs material had a few larger sized (> 17 nm) palladium NPs.

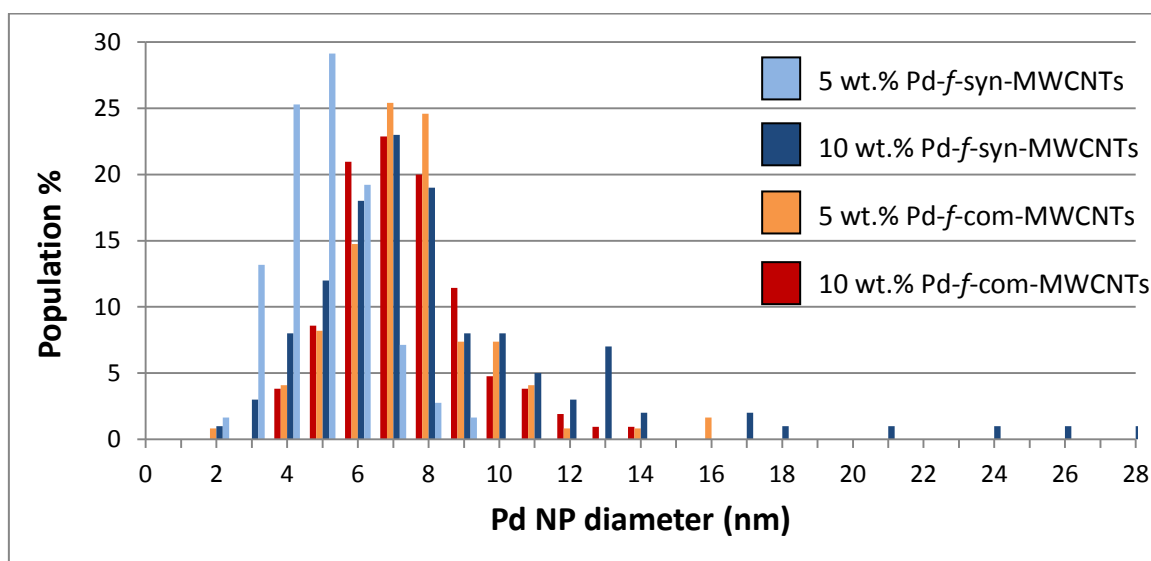


Figure 7.5 Histogram of the population distribution of Pd NP sizes for each catalyst.

The average diameter of palladium NPs is shown in **Table 7.8** and **Figure 7.6**. It was interesting to note that the average diameters hardly differ for the Pd-*f*-com-MWCNTs at both loadings, although they differ significantly for the Pd-*f*-syn-MWCNTs at both loadings. Why this is so is not known, but we suggest that the unique conditions in the Pd-*f*-syn-MWCNTs 10 wt.% experiment may have promoted agglomeration. Specifically, the low surface area (due to larger diameters) of the Pd-*f*-syn-MWCNTs, coupled with the relatively high concentration of palladium in the system for the loading at 10 wt.% experiment, may have significantly promoted agglomeration of palladium NPs. However, this effect would be minimal for the relatively narrow MWCNTs of the commercial material. Further research on the variation of palladium NP size with different supports and at different metal concentrations is necessary.

An average metal NP size of approximately 5 nm is considered to be low enough to achieve a high enough metal surface area suitable for viable catalytic activity.¹⁴ Khavrus *et al.* deposited noble metals (Pt, Ru or Pd) from the acetylacetonate salt(s) onto N-MWCNTs during MWCNT synthesis (using a simultaneous CVD method).²⁶ Their metal NP sizes ranged from 2 nm to 60 nm. This shows that the results in this project are competitive with, or even, superior to, this literature example since the maximum sizes of NPs here were far lower than those of Khavrus *et al.* However, they did not give average NP sizes.

Table 7.8 Average Pd NP size for each catalyst.

Catalyst	Ave. MWCNT OD (nm)	Approx. loading of Pd (wt.%)	Ave. Pd NP diameter (nm)
Pd- <i>f</i> -syn-MWCNTs	41.5*	≈ 5	5.4
		≈ 10	8.9
Pd- <i>f</i> -com-MWCNTs	8-15 [§]	≈ 5	8.0
		≈ 10	7.9

*It was considered that functionalization, being relatively mild, would not strip carbon layers off MWCNTs significantly. At the same time, the addition of functional groups would also not significantly increase the ODs of the MWCNTs. Hence, this value is the same as that of the syn-MWCNTs (see **Chapter 5, Section 5.7.7.1**).

[§]As determined by the manufacturer.

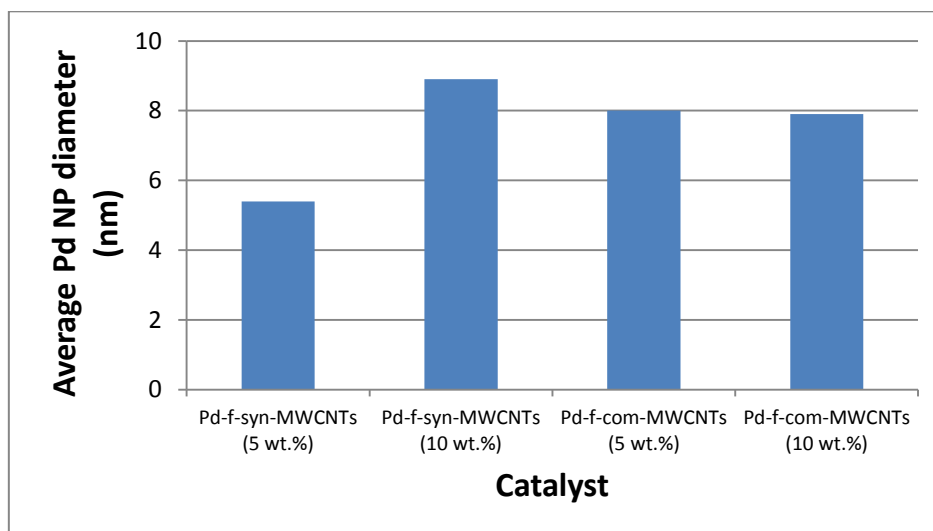


Figure 7.6 Histogram of the average Pd NP size for each catalyst.

Figure 7.7 shows two HRTEM images from the 5 wt.% Pd-*f*-syn-MWCNTs material. The first image, **Figure 7.7 (a)**, contained what looked like crystallites of palladium, i.e. regular-shaped palladium NPs. Higher magnification investigations revealed that palladium NPs were not crystalline, neither did they show any crystal fringes [see **Figure 7.7 (b)**]. In **Figure 7.7 (b)** a thin layer of carbon is apparent on the palladium NP labelled π . Very similar images were seen in a report by Khavrus *et al.*,²⁶ although their metal-MWCNTs hybrids were synthesized simultaneously with the MWCNT synthesis, which explains why graphene layers could easily

cover the metal NPs. The NPs in their report also did not show lattice fringes. Nhut *et al.* suggested that the manner in which metal NPs interact with a CNT surface may determine whether the NPs are crystalline or not.²⁷

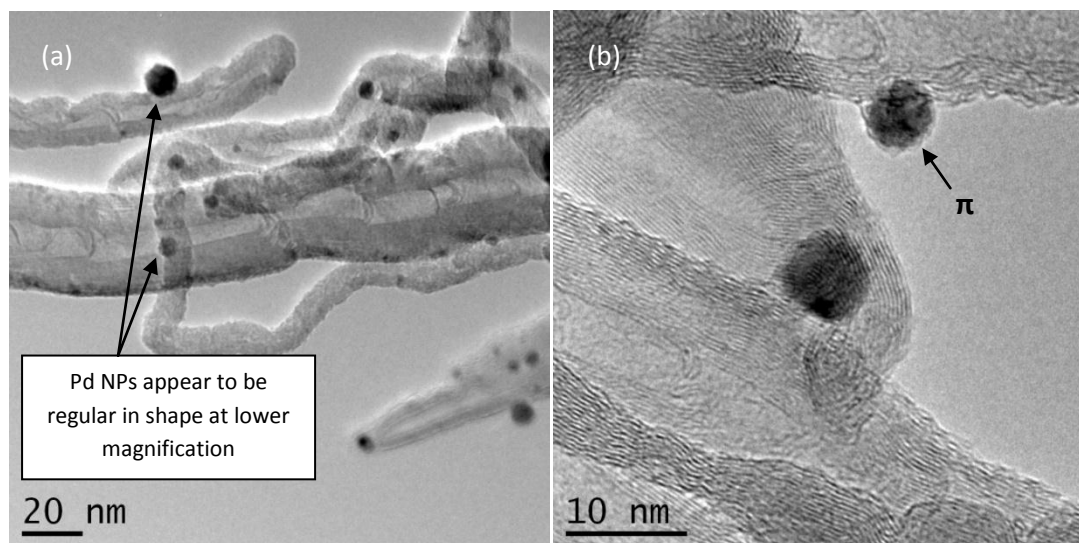


Figure 7.7 HRTEM images of 5 wt.% Pd-*f*-syn-MWCNTs where (a) contains metal NPs which appear to be regular in shape and (b) higher magnification (of another area of the sample) shows that Pd NPs were not regular but amorphous.

7.7.3 BET analysis

The BET surface area of each material was determined after palladium was loaded (see **Table 7.9**).

Table 7.9 BET surface area of each catalyst.

Catalyst	Approx. loading of Pd (wt.%)	BET surface area of Pd loaded support (m ² /g)
Pd- <i>f</i> -syn-MWCNTs	≈ 5	62.53
	≈ 10	58.35
Pd- <i>f</i> -com-MWCNTs	≈ 5	143.88
	≈ 10	141.14

The BET surface areas of the two Pd-loaded *f*-syn-MWCNT supports are similar and higher than those of the unloaded *f*-syn-MWCNTs (see **Table 7.5**). This could be due to the fact that metal NPs, being small relative to the large diameter of the *f*-syn-MWCNTs, increase the surface area. However, the Pd-loaded *f*-com-MWCNTs, have BET surface area values that are lower than the unloaded *f*-com-MWCNTs. It may be that the metal NPs are large relative to the diameter of the *f*-com-MWCNTs, and thus decrease the surface area overall. What is consistent though, is that the 5 wt.% hybrids have slightly higher BET surface areas (3 to 4

m²/g) than the corresponding 10 wt.% hybrids. This could be expected since the metal NP sizes are also smaller.

7.7.4 ICP-OES analysis

ICP-OES analysis was used to confirm quantitatively the loading of palladium on each support. (Refer to **Appendix J, Figure J.1** for the calibration curve.)

Table 7.10 The predicted and actual palladium loadings for each catalyst, with reference material values.

Catalyst	Predicted approximate loading according to Pd precursor mass used (wt.%)	Actual Pd loading (wt.%) (standard deviation, n=2)	Reference material loading (wt.%)
Pd- <i>f</i> -syn-MWCNTs	≈ 5	4.5 (0.0)	5.4
	≈ 10	10.2 (0.0)	10.3
Pd- <i>f</i> -com-MWCNTs	≈ 5	6.3 (0.1)	5.4
	≈ 10	11.4 (0.2)	10.3

The reference material loadings approximate 5 and 10 wt.% and indicate that the digestion was sufficiently good to digest all palladium. (Note, the manufacturer does not supply accurate weight percent loading values or error bars.)

For both supports, palladium was successfully loaded at the approximate desired weight percentages. The Pd-*f*-com-MWCNTs loadings were slightly higher than the approximate predicted loadings whereas the Pd-*f*-syn-MWCNTs values were closer to the approximate values. The standard deviations are relatively low for all catalysts indicating a fairly consistent loading throughout each material (samples were selected randomly from each catalyst). Note, however, that the standard deviation for the Pd-*f*-syn-MWCNTs at approximately 5 and 10 wt.% loadings was 0.0 indicating that both of the duplicate samples (each measured in triplicate), for each of these catalysts, had the same weight percent loading, (to one decimal place). This indicates that distribution of palladium NPs is more consistent throughout the materials containing the *f*-syn support.

7.8 Conclusions

- The chosen supports were successfully purified (in terms of reducing the iron content) as seen by the TGA studies.
- The chosen supports were successfully loaded with approximately 5 or 10 wt.% palladium by the MOCVD technique, with good yields (> 81%).

- Acid-treatment lowered the BET surface area for both supports and Pd-loading increased the surface area in the synthesized materials, but decreased the surface area in the commercial materials.
- The BET surface areas of the Pd-loaded materials were slightly higher for the 5 wt.% materials than the corresponding 10 wt.% materials.
- Palladium NPs were fairly evenly distributed on the supports and the average size values ranged between 5.4 and 8.9 nm in diameter.

References

- 1 L. Mond, C. Langer and F. Quincke, *J. Chem. Soc.*, 1890, **57**, 749
- 2 E. C. Marboe, US Patent. 2430520, 1947
- 3 M. J. Rand, *J. Electrochem. Soc.*, 1973, **120**, 686
- 4 M. J. Rand, *J. Electrochem. Soc.*, 1975, **122**, 811
- 5 J. E. Gozum, D. M. Pollina, J. A. Jensen and G. S. Girolami, *J. Am. Chem. Soc.*, 1988, **110**, 2688
- 6 A. C. Jones and M. L. Hitchman (eds), *Chemical vapour deposition: precursors, processes and applications*, 2009, Royal Society of Chemistry, Cambridge, UK
- 7 N. L. Jeon, W. Lin, M. K. Erhardt, G. S. Girolami and R. G. Nuzzo, *Langmuir*, 1997, **13**, 3833
- 8 P. Serp, R. Feurer, R. Morancho and P. Kalck, *J. Mol. Catal.*, 1995, **101**, L107
- 9 Y. Suttisawat, P. Rangsunvigit, B. Kitiyanan, M. Williams, P. Ndungu, M. V. Lototsky, A. Nechaev, V. Linkov and S. Kulprathipanja, *Int. J. Hydrogen Energy*, 2009, **34**, 6669
- 10 J. A. Schwarz, C. Contescu and A. Contescu, *Chem. Rev.*, 1995, **95**, 477
- 11 G. S. Girolami and J. E. Gozum, *Mater. Res. Soc. Symp. Proc.*, 1990, **168**, 319
- 12 D. C. Bradley, *Polyhedron*, 1994, **13**, 1111
- 13 J.-C. Hierso, R. Feurer and P. Kalck, *Chem. Mater.*, 2000, **12**, 390
- 14 V. Cominos and A. Gavriilidis, *Appl. Catal. A: Gen.*, 2001, **210**, 381
- 15 H. Lang and R. Buschbeck, in *The Chemistry of Metal Enolates*, ed. J. Zabicky, John Wiley and Sons Ltd, West Sussex, England, 2009, p 954
- 16 J.-C. Hierso, R. Feurer and P. Kalck, *Co-ord. Chem. Rev.*, 1998, **178-180**, 1811
- 17 J.-C. Hierso, P. Serp, R. Feurer and P. Kalck, *Appl. Organomet. Chem.*, 1998, **12**, 161
- 18 H. O. Pierson, *Handbook of Chemical Vapour Deposition*, 2nd ed., Noyes Publications/William Andrew Publishing, Norwich, USA, 1999, pp 84 – 107
- 19 C. Liang, W. Xia, M. van den Berg, Y. Wang, H. Soltani-Ahmadi, O. Schlüter, R. A. Fischer and M. Muhler, *Chem. Mater.*, 2009, **21**, 2360
- 20 T. Kudo and A. Yamaguchi, Jpn. Patent 62207868, 1987
- 21 V. Cominos and A. Gavriilidis, *Eur. Phys. J. AP*, 2001, **15**, 23
- 22 P. P. Semyannikov, V. M. Grankin, I. K. Igumenov and A. F. Bykov, *J. Phys. IV C5 (Suppl.)*, 1995, 205
- 23 R. G. Pearson and D. A. Johnson, *J. Am. Chem. Soc.*, 1964, **86**, 3983
- 24 J. Tsuji, *Palladium Reagents and Catalysts – New Perspectives for the 21st Century*, John Wiley and Sons Ltd, West Sussex, England, 2004, p 2
- 25 M. Che and C. O. Bennett, *Adv. Catal.*, 1985, 36, 55
- 26 V. O. Khavrus, A. Leonhardt, S. Hampel, C. Täschner, C. Müller, W. Gruner, S. Oswald, P. E. Strizhak and B. Büchner, *Carbon*, 2007, **45**, 2889
- 27 J.-M. Nhut, L. Pesant, J.-P. Tessonnier, G. Winé, J. Guille, C. Pham-Huu and M.-J. Ledoux, *Appl. Catal. A: Gen.*, 2003, **254**, 345

CHAPTER 8

CONCLUSIONS AND FUTURE WORK

8.1 Conclusions

MWCNTs possess unique properties such as toughness, flexibility, inertness, electrical conductivity and high surface area which are beneficial to the materials, electronics and catalysis industries. Much research into fine-tuning these properties is currently being carried out. At the nanoscale, properties are highly dependent on morphology and chemical composition. For this reason tailoring the morphology and composition is the starting point in developing MWCNT-related materials for industry.

This project focussed on the synthesis of MWCNTs, and other SCNMs, by the CVD floating catalyst method with a primary view to investigate the effects of variations in the physicochemical reaction parameters on these materials. The materials were synthesized using organometallic catalysts and toluene. The overall most suitable material containing a very large proportion of MWCNTs was then identified and loaded with palladium NPs and thus was used as a support, since MWCNTs are, generally, higher in surface area compared to some traditional catalyst supports. Palladium was the metal of choice since it is known to be an excellent catalyst in several industrial carbon-carbon bond and hydrogenation reactions. Hydrogenation reactions, specifically those carried out over Pd/MWCNTs *versus* other Pd/C systems, were reviewed. The literature indicated that, in general, Pd/MWCNT systems are superior to other Pd/C systems in terms of conversion and selectivity.

In terms of the first and main aim of the project, temperature, catalyst choice and catalyst concentration were varied to investigate the related effects. These main parameters and some of their primary effects are now briefly summarized.

- Ferrocene **[1]**, a commonly used CVD catalyst for MWCNT synthesis, was investigated at 2.5 and 5 wt.% under $T_{\max} = 950, 900, 850, 800$ and 750 °C (Experiment 1). It was found that the highest yields of MWCNTs, with relatively high thermal stabilities and high surface areas, in general, were produced at temperatures between 800 and 900 °C. [The two lower temperatures in the range (800 and 850 °C) also had the lowest remnant iron contents.] These three temperatures were chosen for the subsequent three experiments.
- Three purification methods were tested (on the material from 900 °C in Experiment 1) with Method 3 (treatment with 3 M HNO_3) proving to be both mild (thus maintaining MWCNT integrity) yet effective in reducing the iron content.
- Doubling the catalyst (**[1]**) concentration (Experiment 2) caused a decrease in the yields of MWCNTs, smaller diameters and shorter MWCNT lengths. Interestingly some property trends were completely reversed by the increased catalyst concentration, for example the crystallinity-temperature trend. It was shown that some properties depend on the combined effect of reaction parameters.
- Three ferrocene derivatives, i.e. ferrocenoyl imidazolide **[3]** (a source of nitrogen and oxygen), *N*-phenyl-carbamoylferrocene **[4]** (a source of nitrogen and oxygen) and *S,S*-bis(ferrocenylmethyl)dithiocarbonate **[5]** (a source of sulfur and oxygen), were then

successfully synthesized and characterized. The effect of the heteroatoms from these catalyst compounds on the CVD products was then investigated as is discussed in the next few points.

- Compound [3] was investigated at 2.5 and 5 wt.% at 900, 850 and 800 °C (Experiments 3 and 4). Very clean (low amorphous carbon and iron) but poorly aligned MWCNTs, of high yield (relative to the raw yields), were formed with 2.5 wt.% catalyst at 800 and 850 °C, while predominantly spheres were formed at all temperatures for the 5 wt.% catalyst. The “cleanliness” of the 2.5 wt.% runs was attributed to the removal of amorphous carbon by oxygen. All runs produced N-doped MWCNTs of the “bamboo” morphology. For the 2.5 wt.% catalyst, bamboo compartment length increased with increasing temperature and this corresponded with increasing crystallinity, thereby indicating a higher nitrogen incorporation.
- Compound [4], at 1.25 wt.% concentration and $T_{\max} = 900$ or 800 °C (Experiment 5), produced predominantly spheres of large size, presumably due to the increased relative concentration of carbon. Although it also contained oxygen, a significant amount of amorphous carbon was produced. It was found that the higher of the two temperatures formed a more thermally stable and graphitic material.
- Compound [5] did not produce any observable MWCNTs, but mostly spheres (Experiment 6).
- The best undoped and the best doped material from CVD synthesis, in terms of high MWCNT yield (relative to raw yield), purity (relatively low iron content) and good thermal stability were the products from Experiment 1 (800 °C) and Experiment 3 (850 °C) respectively. The former material was successfully scaled-up and purified to reduce the iron catalyst content.

In the second part of the project palladium was loaded onto the chosen supports, from $\text{Pd}(\text{acac})_2$ at approximately 5 and 10 wt.%, by using a vacuum MOCVD technique. Characterization by TEM, SEM, EDX, BET and ICP-OES revealed that palladium was successfully loaded and that palladium NPs, of average diameter 5.4 to 8.9 nm, were evenly dispersed. The palladium NPs were shown to influence the BET surface area of the materials.

Thus, all objectives (**Chapter 3**) were achieved. However, the results of this work have opened up a host of further research objectives, some of which will be discussed in the subsequent section, **Section 8.2**.

8.2 Future work

Many possible avenues of future research stemming from this work exist and they include the following:

- Investigate ways to minimize the CVD products which are vented through the exhaust system and, which, consequently decreases yields.
- Scale-up the material from Experiment 3 at 850 °C. Consequently, investigate the surface area of this material and load it with palladium (5 and 10 wt.%) by MOCVD to investigate the effect of N-doping on Pd-loading.
- Investigate the catalytic activity of this system on hydrogenation reactions *versus* that of the Pd-loaded *f*-syn-MWCNTs and Pd-loaded *f*-com-MWCNTs.

- Investigate how the surface energies of as-synthesized, acid-purified and Pd-loaded MWCNTs (doped and undoped) differ and investigate what this means in terms of reactivity and viability of each as a catalyst support or catalyst-support system, (to compare with the catalytic activity results from the previous point).
- Investigate whether MWCNTs grow in a “wavy” fashion at times, or whether this is a result of grinding and sample preparation for SEM analysis.
- Why spheres under certain conditions appear to form in two distinct size groupings.
- Investigate the combined effects of how catalyst ligand and catalyst content affects SCNM distributions.
- Determine why the carbon spheres produced under Experiment 5 conditions are so close in average OD and why the ones produced at the lower temperature are larger.
- Investigate whether having two equivalents of the sulfur-containing reactant for the synthesis of compound [5] improves yields.
- Do further investigations with other, different, catalysts at the same concentration to determine the prevalence of a phenomenon noticed this work, namely that temperature may not always have a predictable effect on the average OD and ID of MWCNTs, as is commonly found.
- It was suggested that choice of catalyst and its concentration are also factors determining crystallinity of SCNMs, and that temperature is not always an overriding factor in crystallinity. This needs to be studied further.
- Determine what form sulfur exists in in the carbon spheres produced in Experiment 6, namely, whether the sulphur is bonded to carbon, or iron, or merely trapped in or dissolved in carbon and iron respectively.
- A myriad of possible ferrocene derivatives can be studied as catalysts for MWCNT or other SCNM synthesis and the physicochemical reaction parameters can be increasingly fine-tuned to produce desirable CVD products.
- Doping is also known to be possible with other elements, for example boron. It would be interesting to dope MWCNTs with boron or nitrogen from catalysts differing only in terms of the heteroatom (boron or nitrogen) on the ligand.
- Loading weight percentages of palladium can be varied (< 5 wt.%, between 5 and 10 wt.%, > 10 wt.%) and its effect on catalytic activity investigated.
- Conditions for palladium loading can be varied (i.e. investigate temperature < 400 °C).
- Investigate the palladium catalysts on a variety of hydrogenation reaction types to see their effectiveness for different reactions, i.e. carbon-carbon double *versus* triple bond reductions, in terms of conversion and selectivity.
- Average palladium NP size may be a function of both the support and metal content in the MOCVD reactor. This could be further investigated.
- The simultaneous formation of Pd-N-MWCNTs (i.e. N-doping and Pd-loading occur at the same time in one reactor) is little studied in the literature and would be interesting to explore since it is a time-efficient process.

In general, apart from the possibilities mentioned here, there could be lots of other interesting investigations that would be noteworthy to explore in the future.

APPENDICES

APPENDIX A

$^1\text{H-NMR}$ SPECTRA

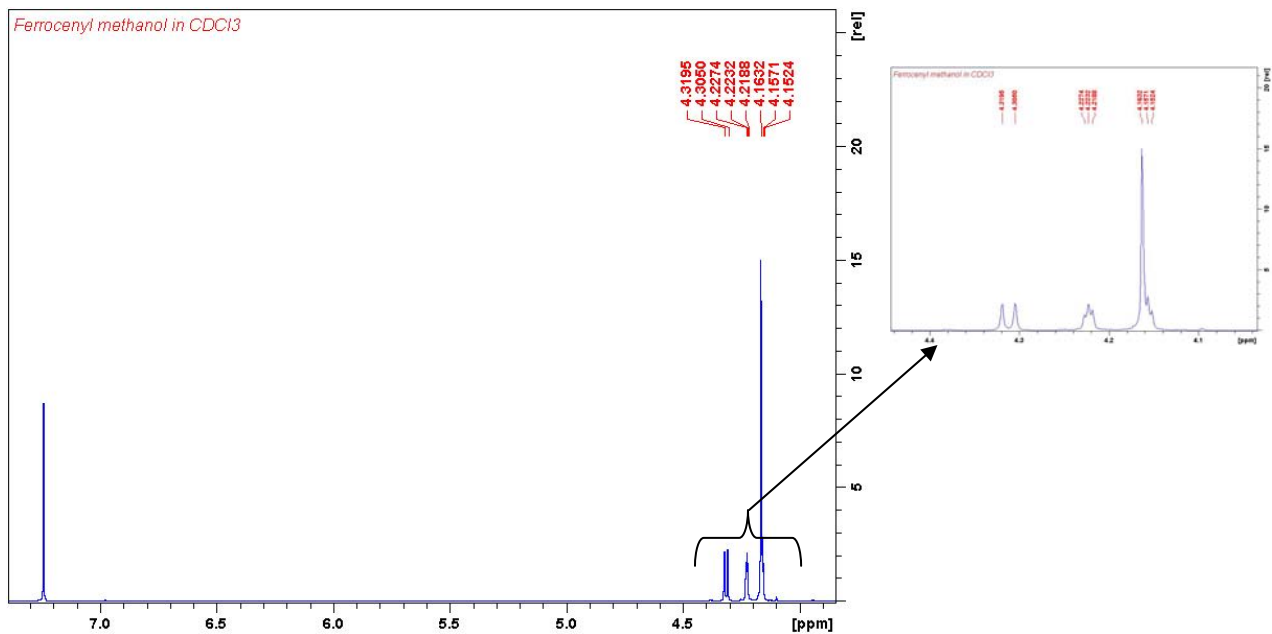


Figure A.1 $^1\text{H-NMR}$ spectrum of ferrocenylmethanol [2].

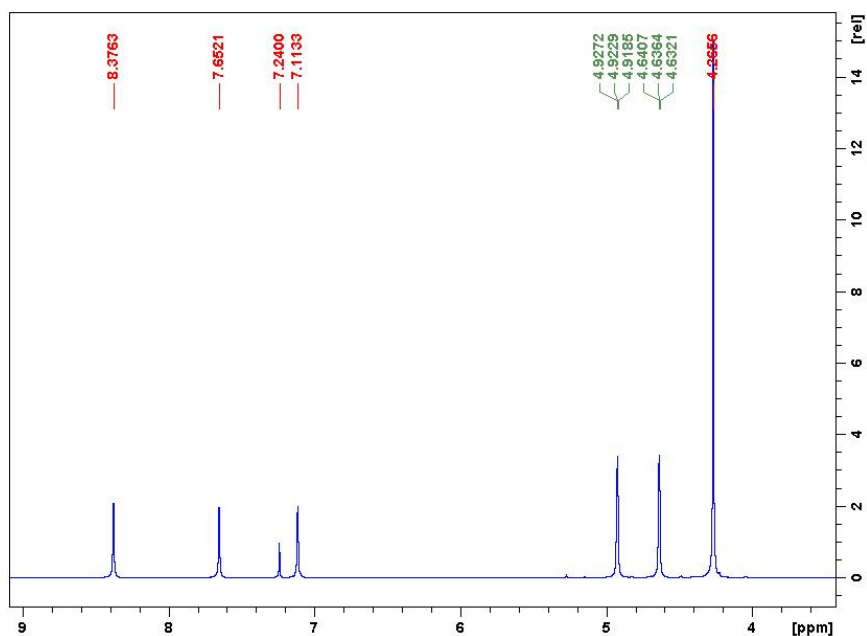


Figure A.2 $^1\text{H-NMR}$ spectrum of ferrocenoyl imidazolid [3].

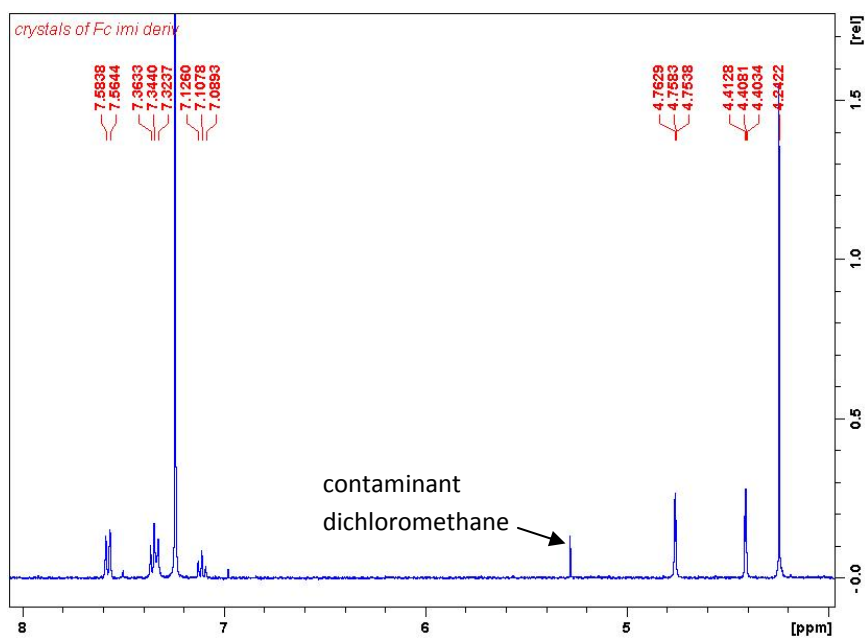


Figure A.3 $^1\text{H-NMR}$ spectrum of (*N*-phenylcarbamoyl)ferrocene [4].

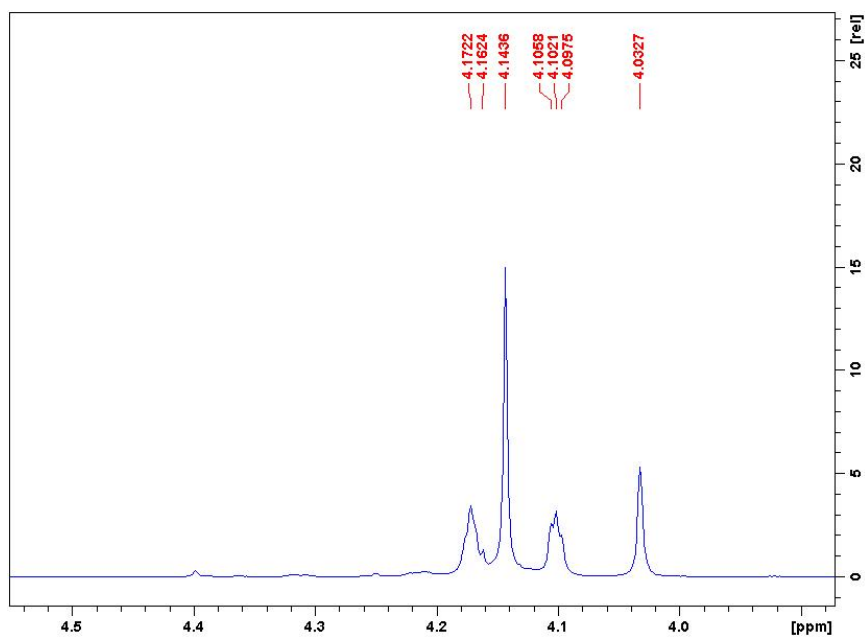


Figure A.4 $^1\text{H-NMR}$ spectrum of *S,S*-bis(ferrocenylmethyl)dithiocarbonate [5].

APPENDIX B

^{13}C -NMR SPECTRA

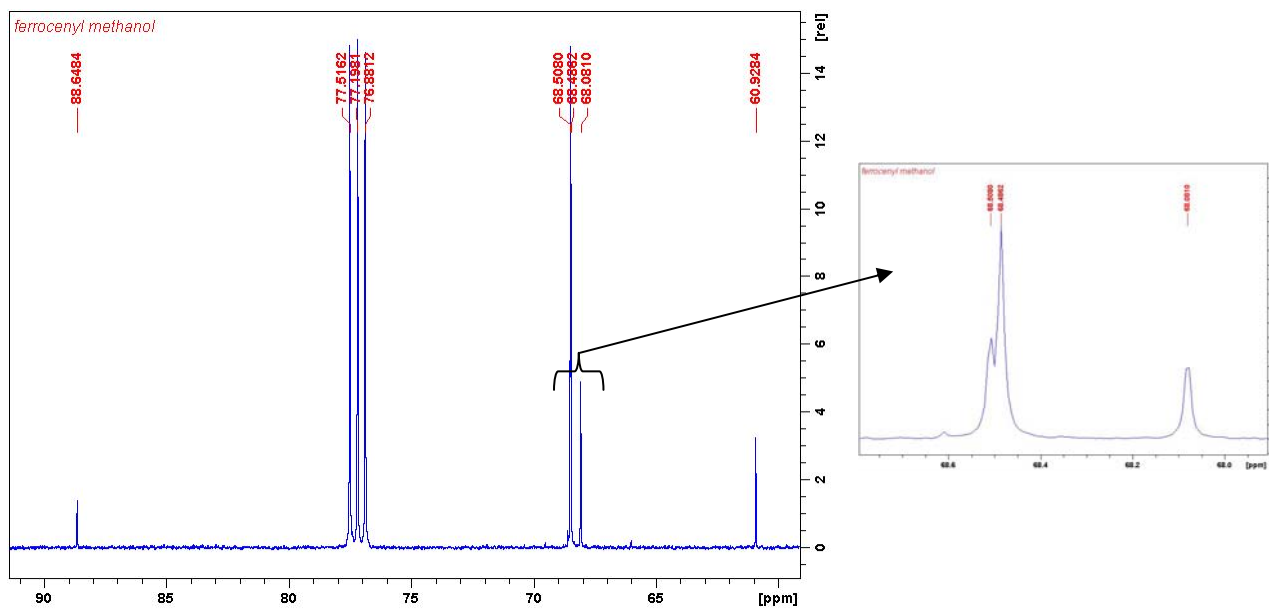


Figure B.1 ^{13}C -NMR spectrum of ferrocenylmethanol [2].

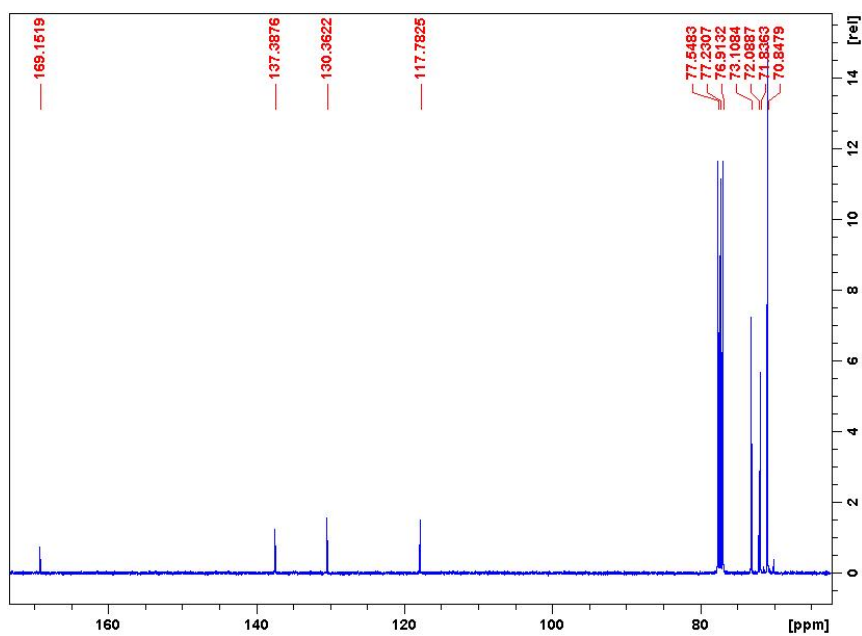


Figure B.2 ^{13}C -NMR spectrum of ferrocenoyl imidazolid [3].

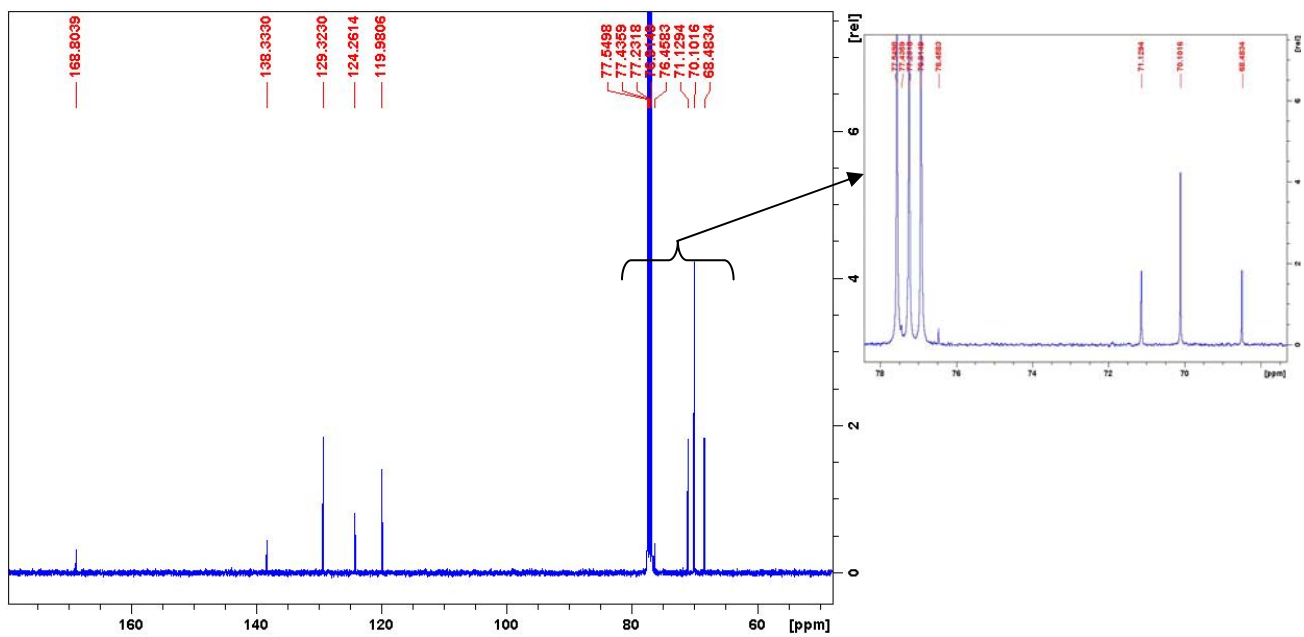


Figure B.3 ^{13}C -NMR spectrum of (*N*-phenylcarbamoyl)ferrocene [4].

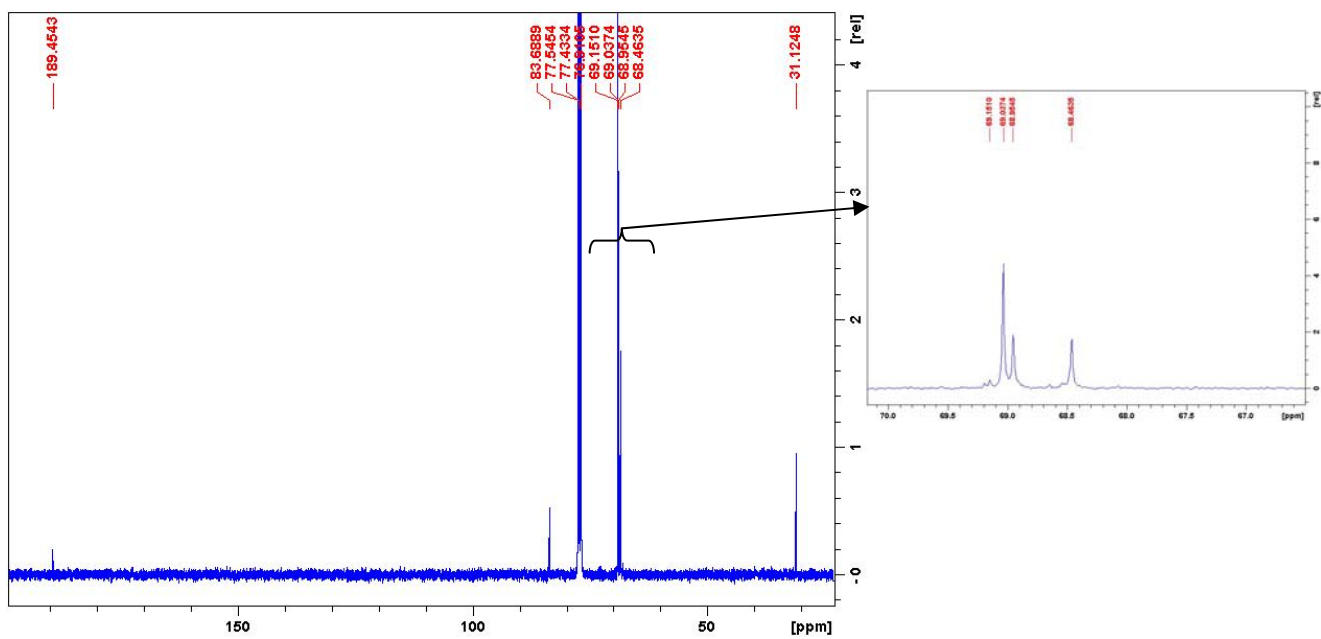


Figure B.4 ^{13}C -NMR spectrum of *S,S*-bis(ferrocenylmethyl)dithiocarbonate [5].

APPENDIX C

FTIR SPECTRA

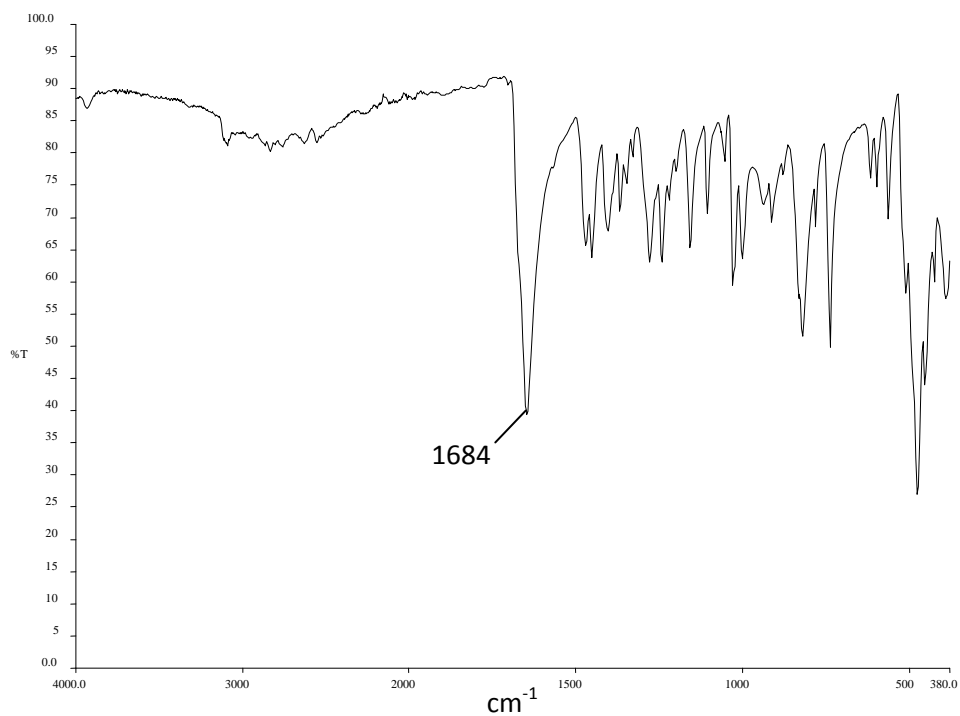


Figure C.1 (a) IR spectrum of ferrocenecarboxaldehyde.

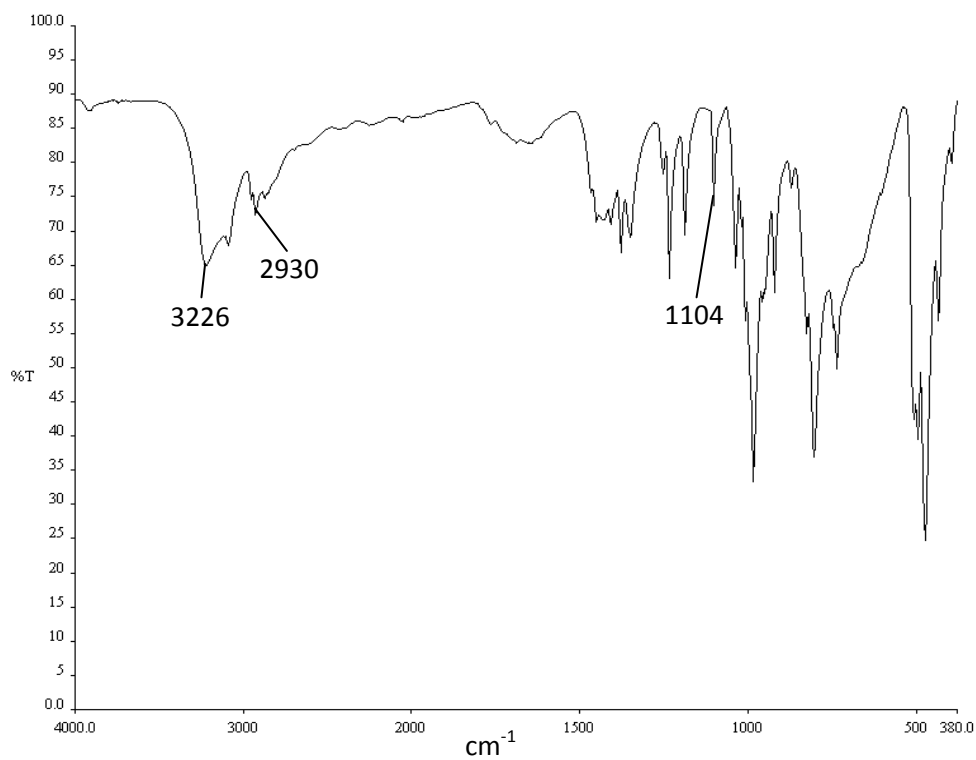


Figure C.1 (b) IR spectrum of ferrocenylmethanol [2].

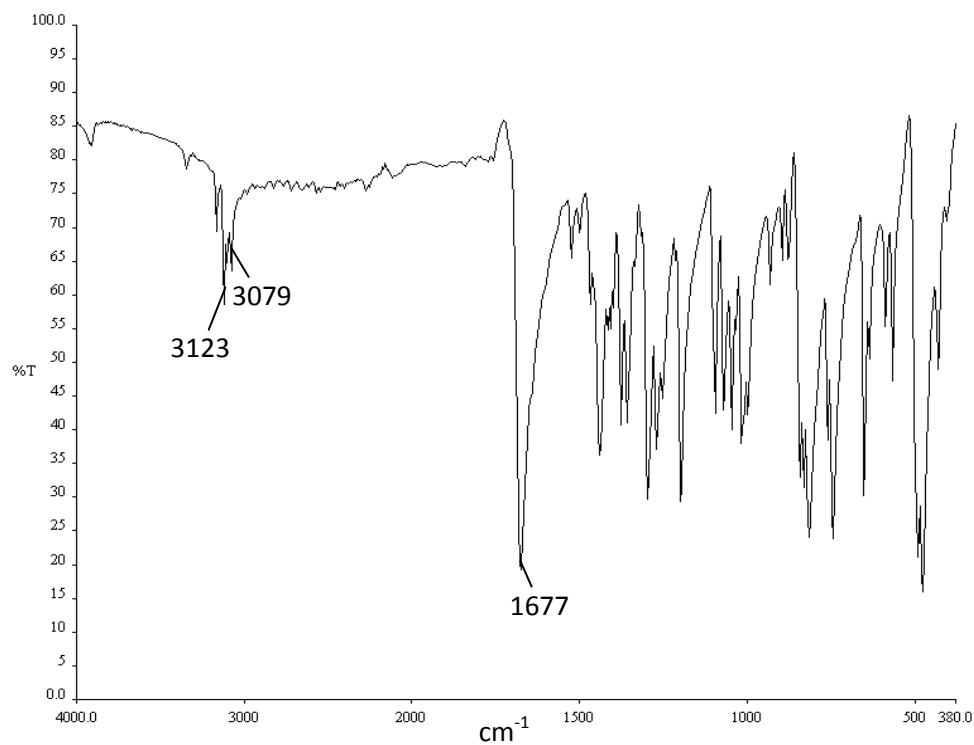


Figure C.2 IR spectrum of ferrocenoyl imidazolide [3].

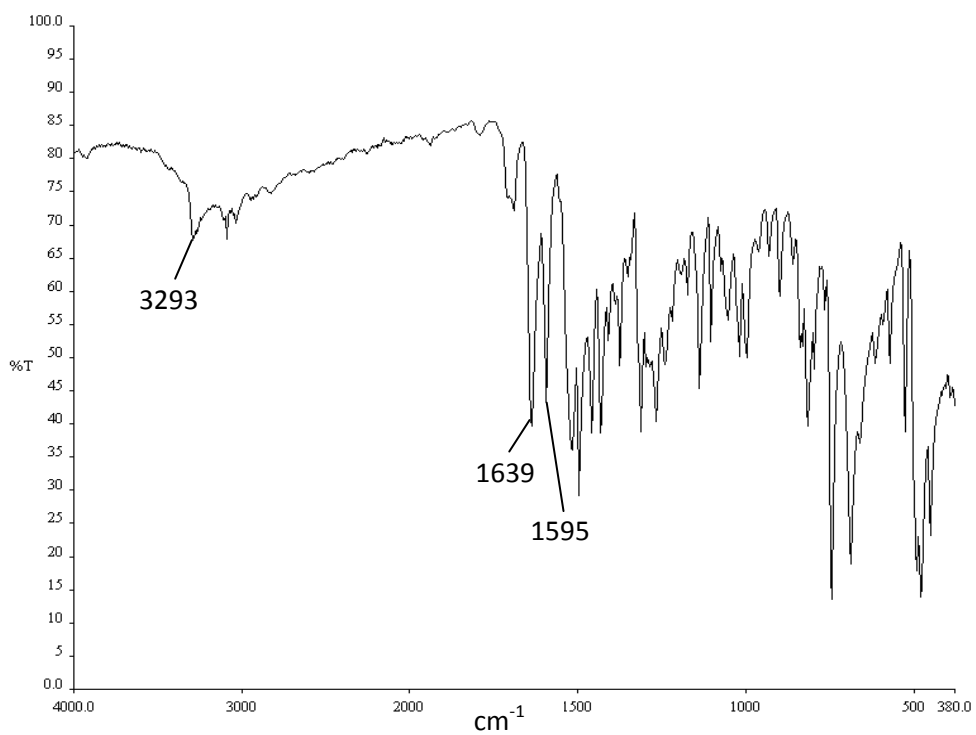


Figure C.3 IR spectrum of (*N*-phenylcarbamoyl)ferrocene [4].

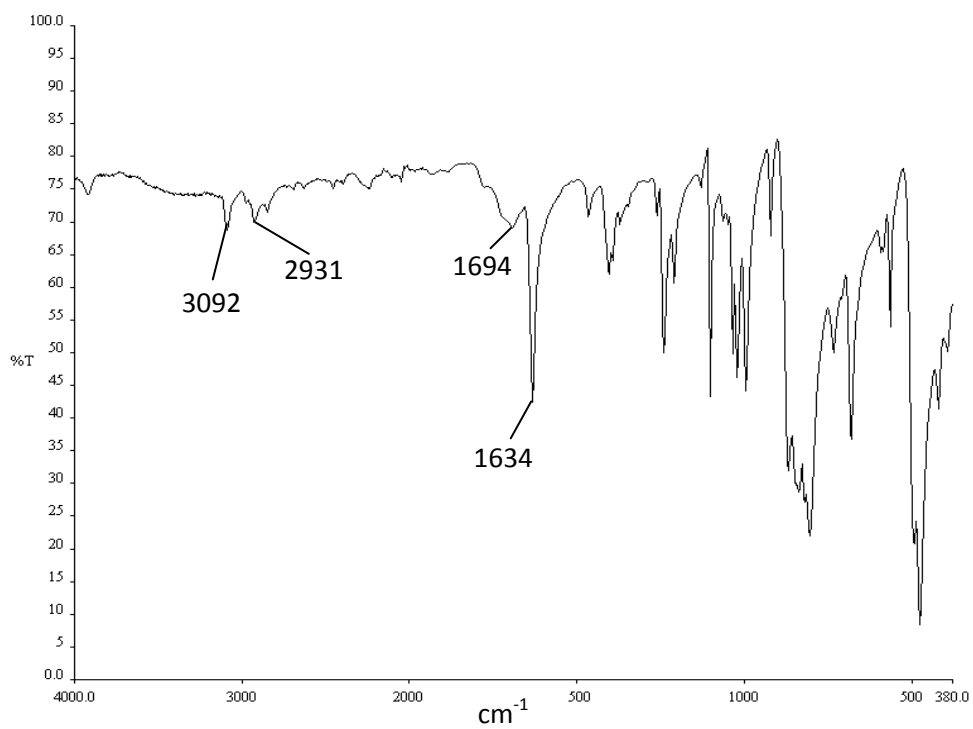


Figure C.4 IR spectrum of *S,S*-bis(ferrocenylmethyl)dithiocarbonate [5].

APPENDIX D

MASS SPECTRA

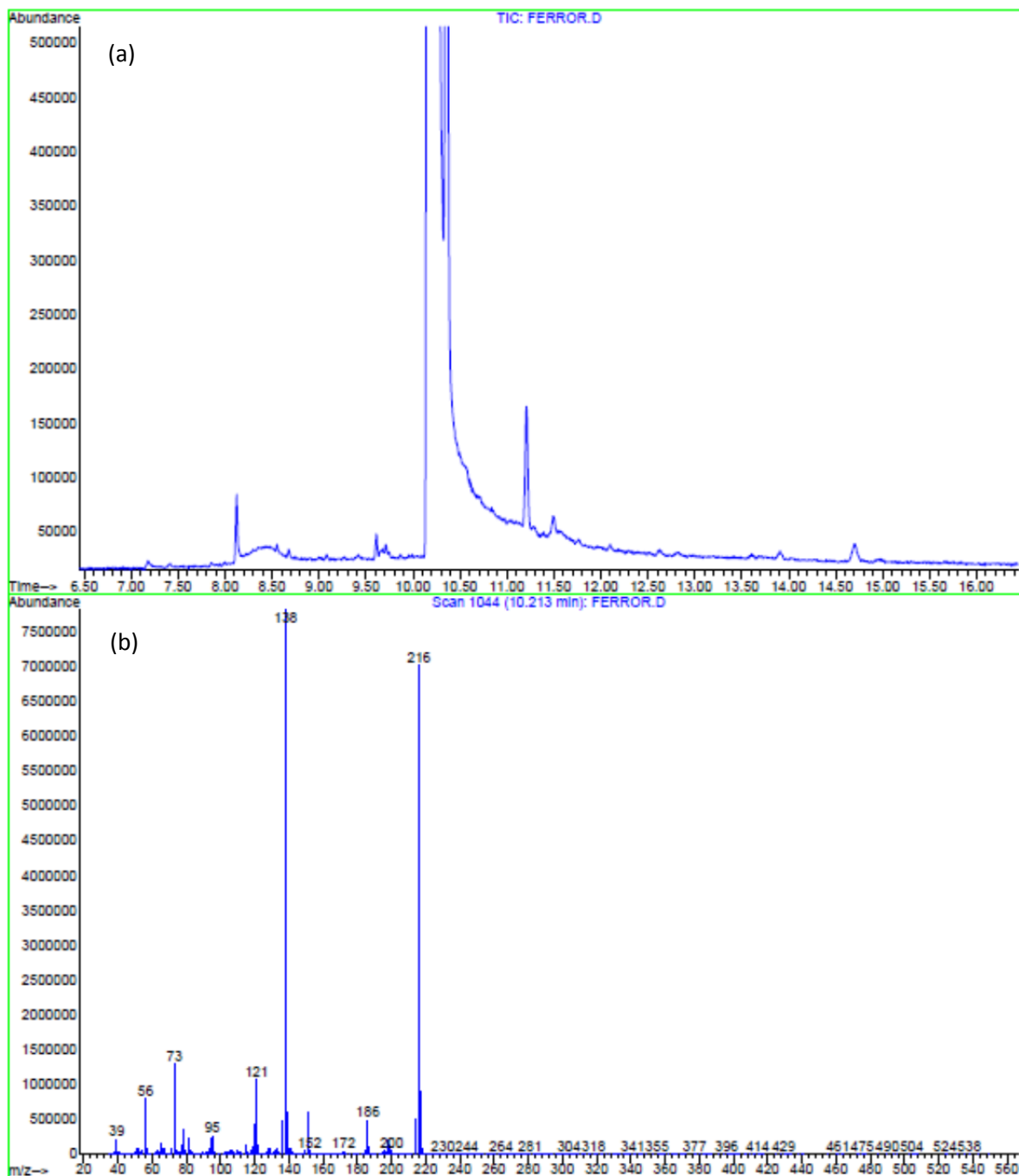


Figure D.1 (a) Total ion chromatogram of products from the synthesis of ferrocenylmethanol **[2]** and (b) the mass spectrum of ferrocenylmethanol **[2]** which eluted at 10.213 mins.

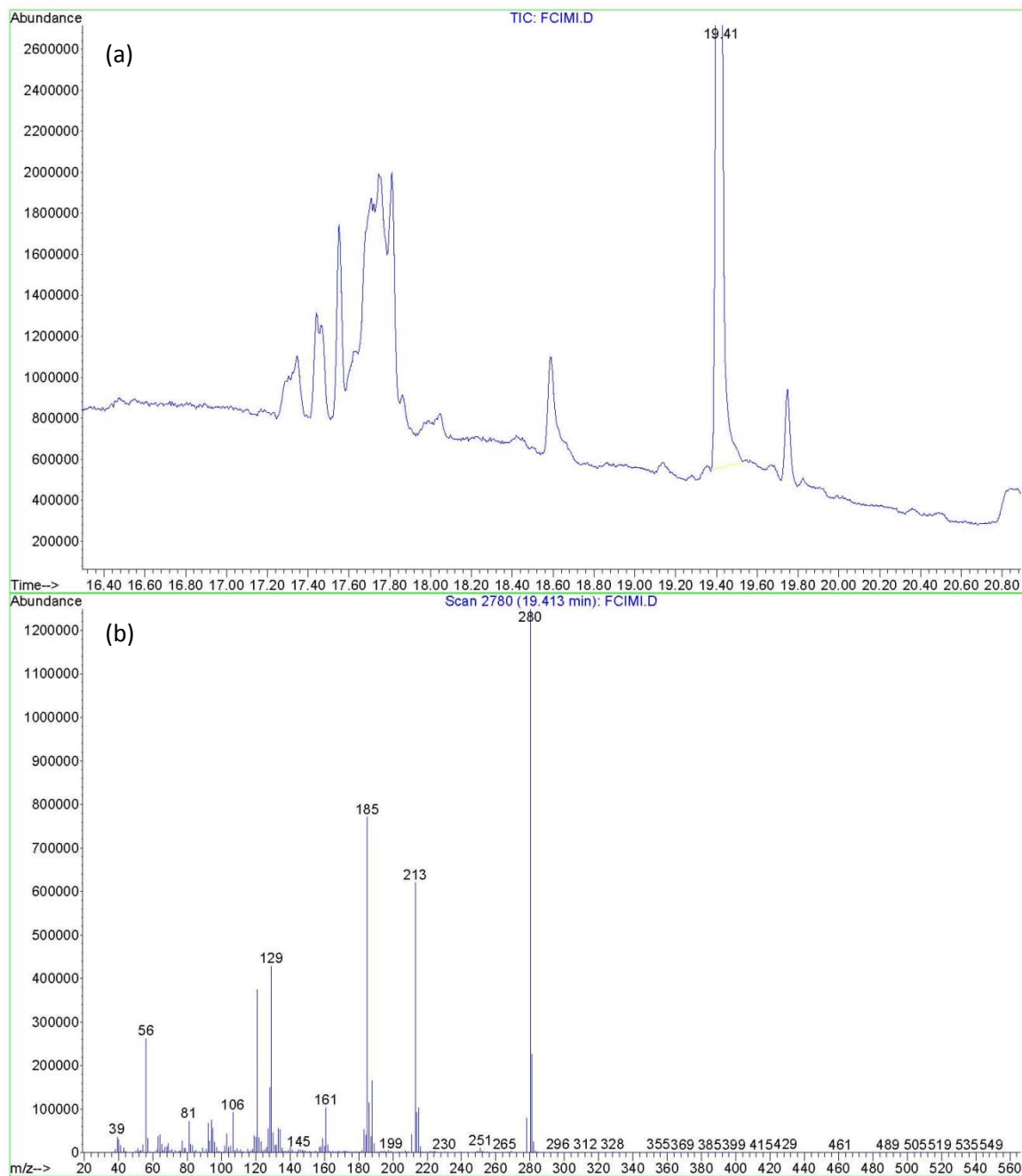


Figure D.2 (a) Total ion chromatogram of products from the synthesis of ferrocenoyl imidazolid **[3]** and (b) the mass spectrum of ferrocenoyl imidazolid **[3]** which eluted at 19.413 mins.

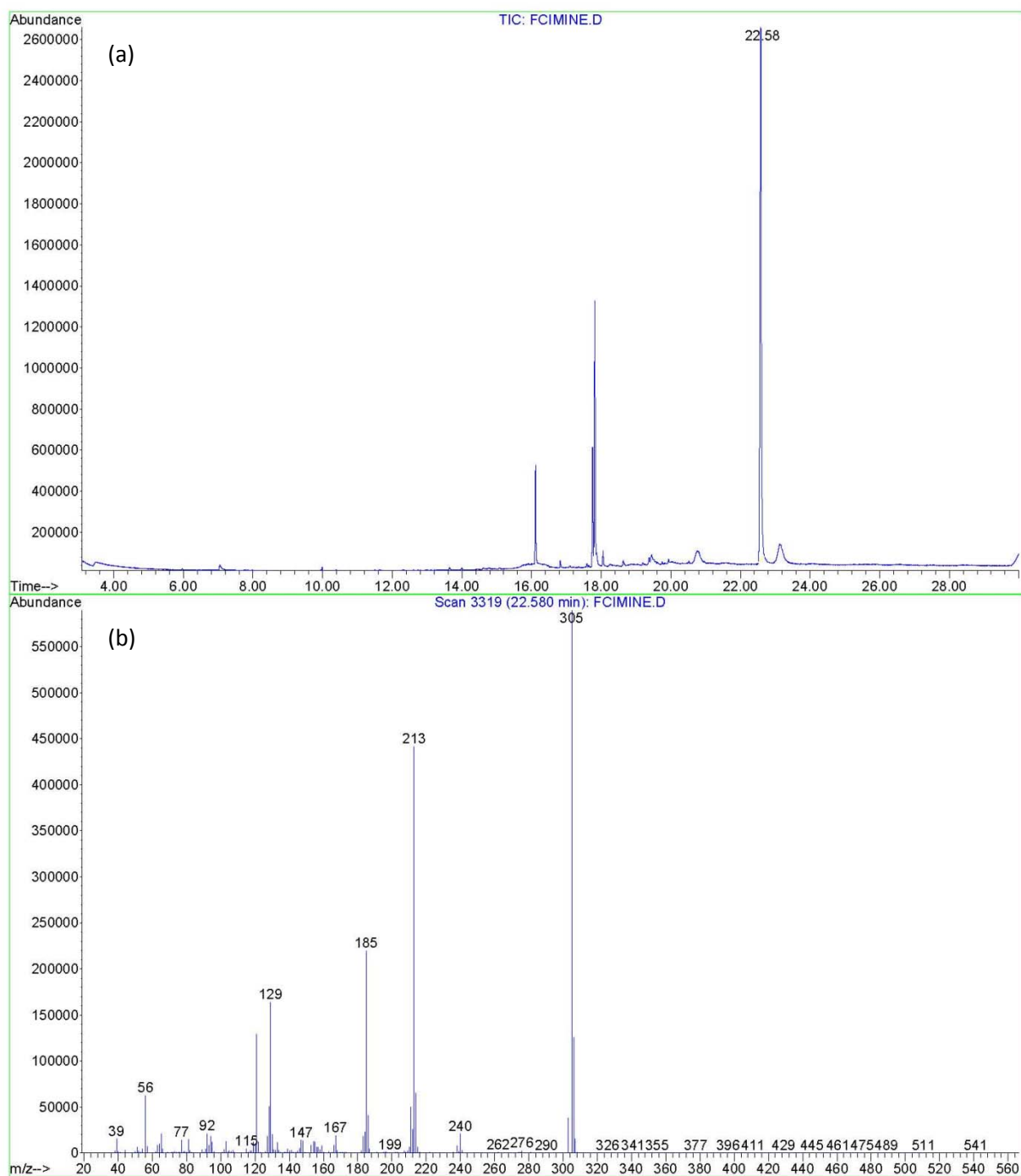
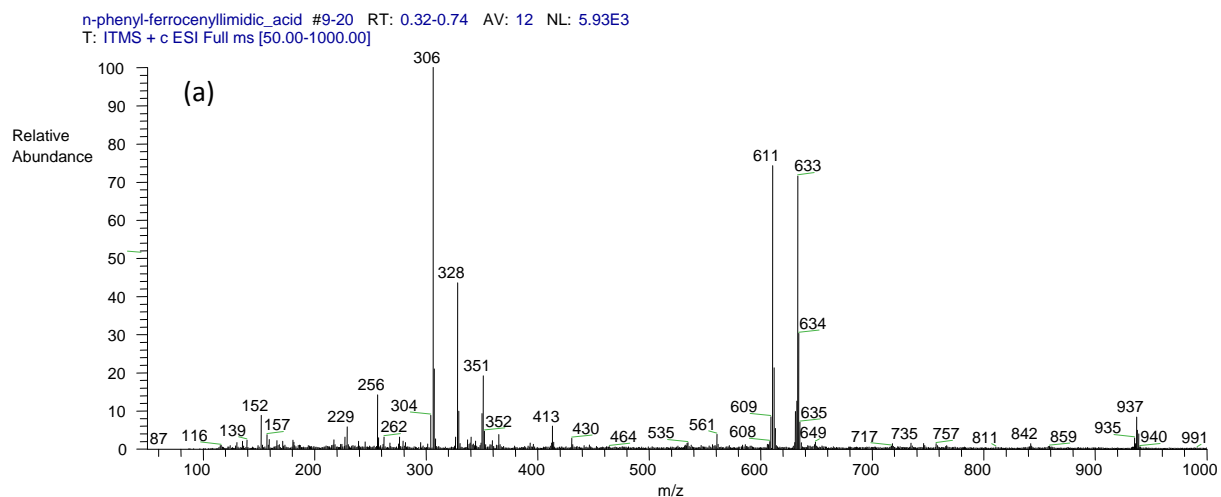


Figure D.3 (a) Total ion chromatogram of products from the synthesis of (*N*-phenylcarbamoyl)ferrocene **[4]** and (b) the low resolution electron ionization mass spectrum of (*N*-phenylcarbamoyl)ferrocene **[4]** which eluted at 22.580 mins.



RS01_2_HRESI-c1 #16 RT: 0.58 AV: 1 NL: 4.76E5
T: + c ESI Full ms [274.50-323.50]

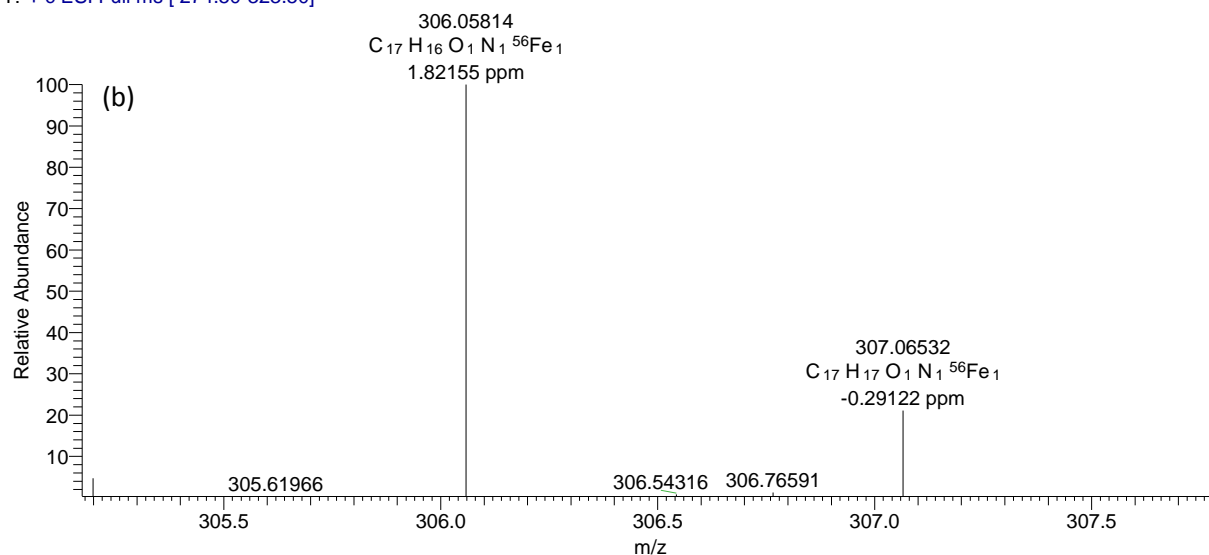


Figure D.4 High resolution electrospray ionization mass spectrum of (*N*-phenyl-carbamoyl)ferrocene **[4]** with (a) full spectrum showing peaks at 611 and 633 from the polyethylenimine as a reference solution and (b) characteristic iron splitting pattern for the most abundant peak.

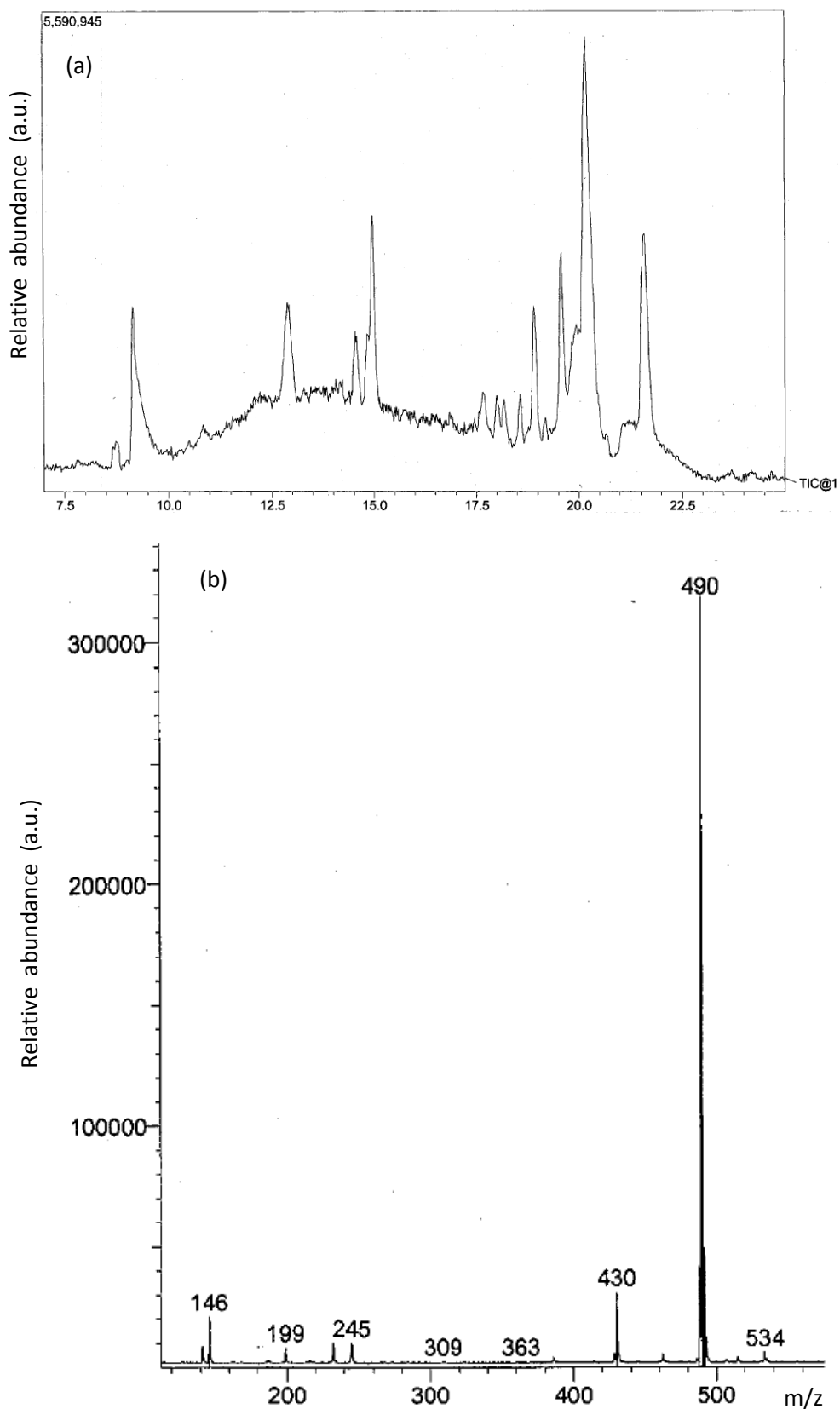


Figure D.5 (a) Total ion chromatogram of products from the synthesis of *S,S*-bis(ferrocenylmethyl)dithiocarbonate [5] and (b) the mass spectrum of *S,S*-bis(ferrocenylmethyl)dithiocarbonate [5] which eluted at 20.142 mins.

APPENDIX E

SELECTED SEM, TEM AND HRTEM IMAGES OF MWCNTs AND SCNMs

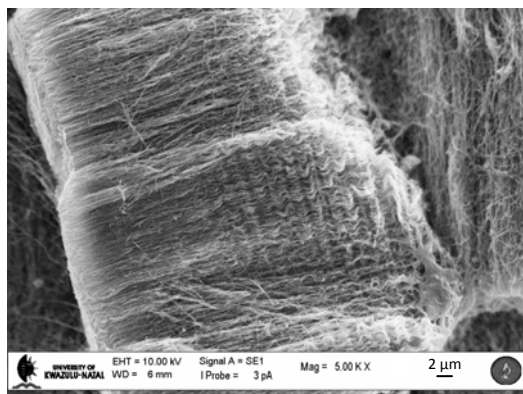


Figure E.1 SEM micrograph of a bundle of “wavy” MWCNTs (2.5 wt.% ferrocene, 800 °C).

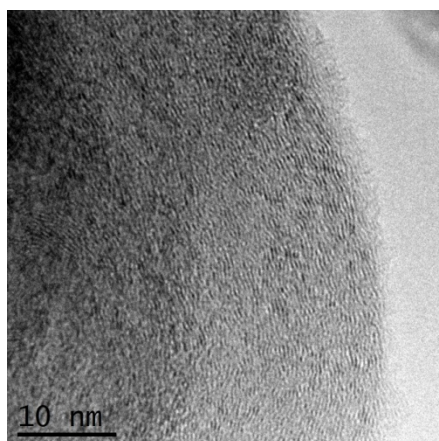


Figure E.2 HRTEM image of a mostly graphitic sphere (2.5 wt.% ferrocene, 800 °C).

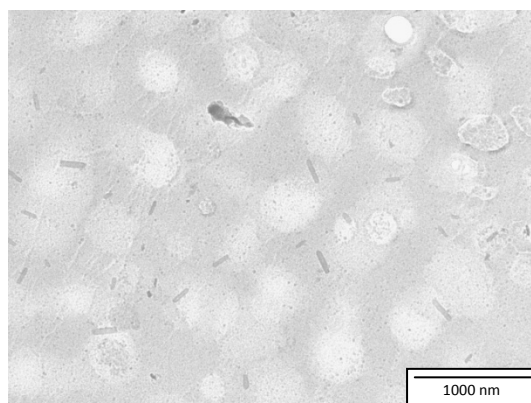


Figure E.3 TEM micrograph of small pieces of *f*-com-MWCNTs.

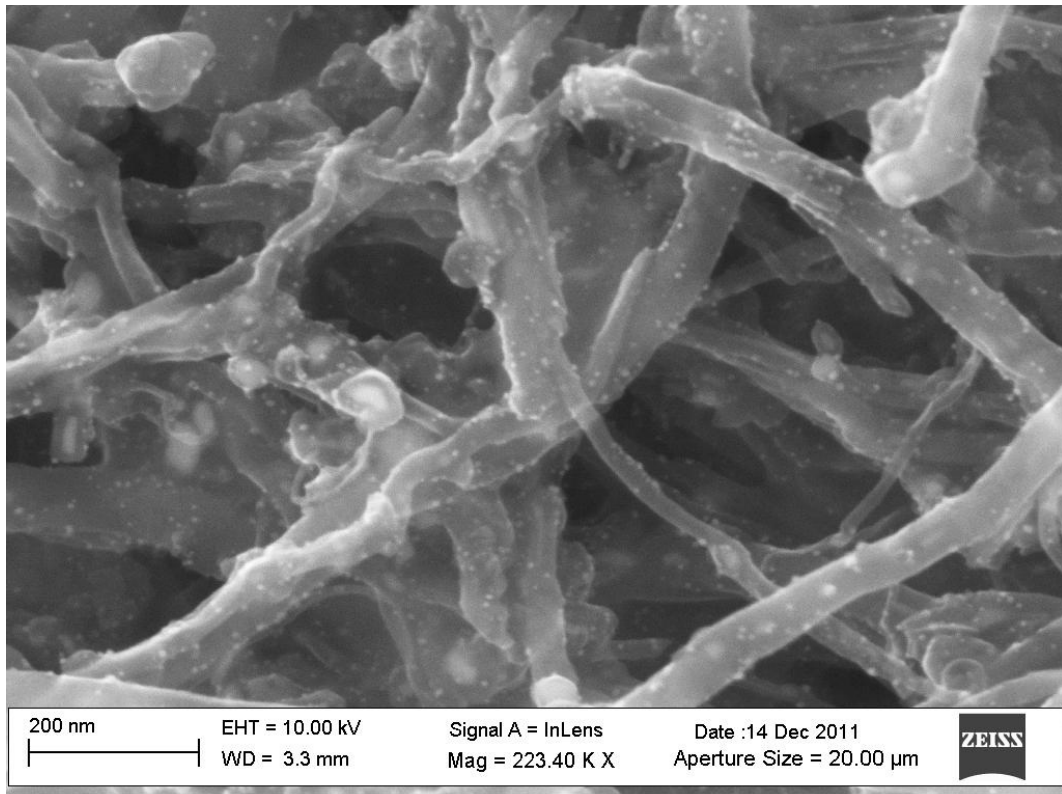


Figure E.4 Enlarged FEG SEM image of *f*-syn-MWCNTs with a loading of 5 wt.% Pd.

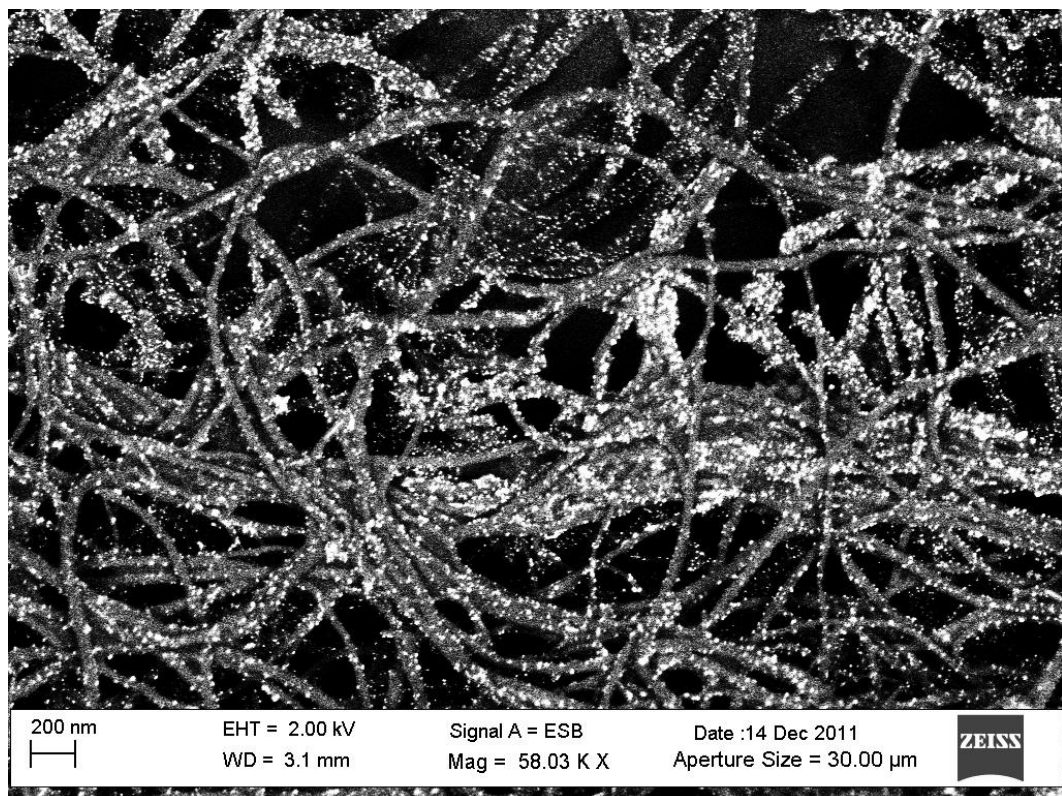


Figure E.5 FEG SEM backscattered image of *f*-syn-MWCNTs with a loading of 5 wt.% Pd.

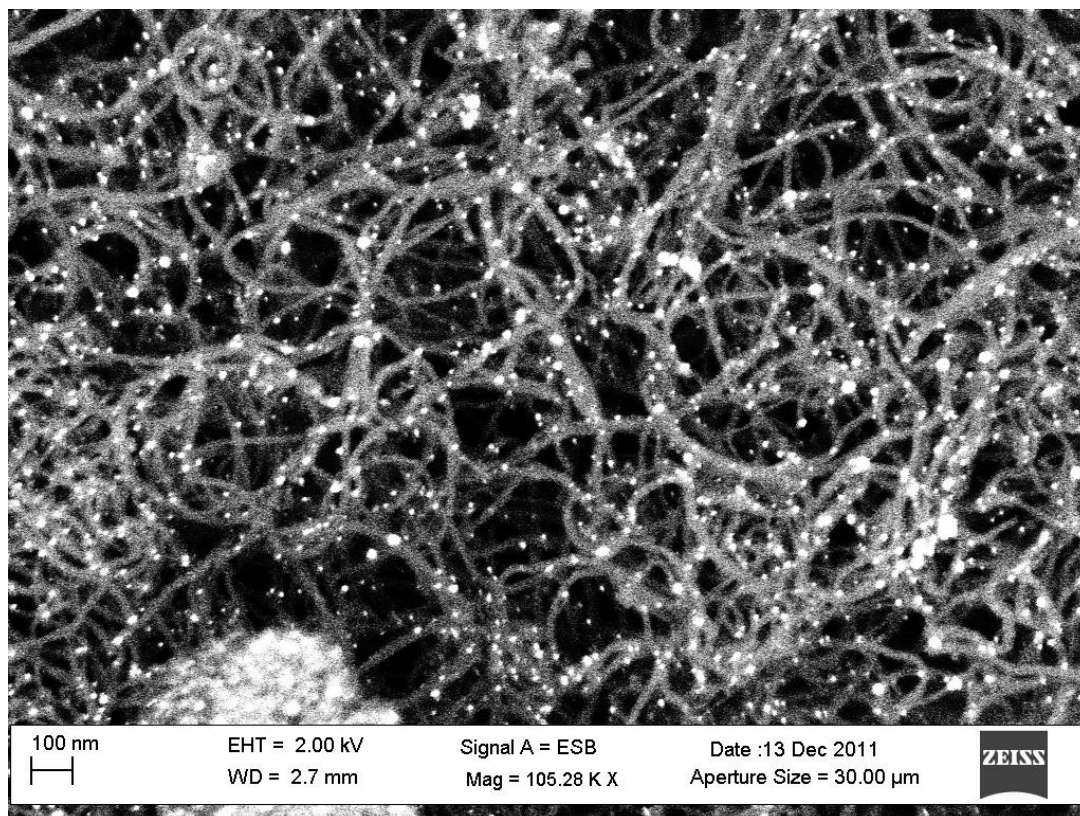


Figure E.6 FEG SEM backscattered image of *f*-com-MWCNTs with a loading of 5 wt.% Pd.

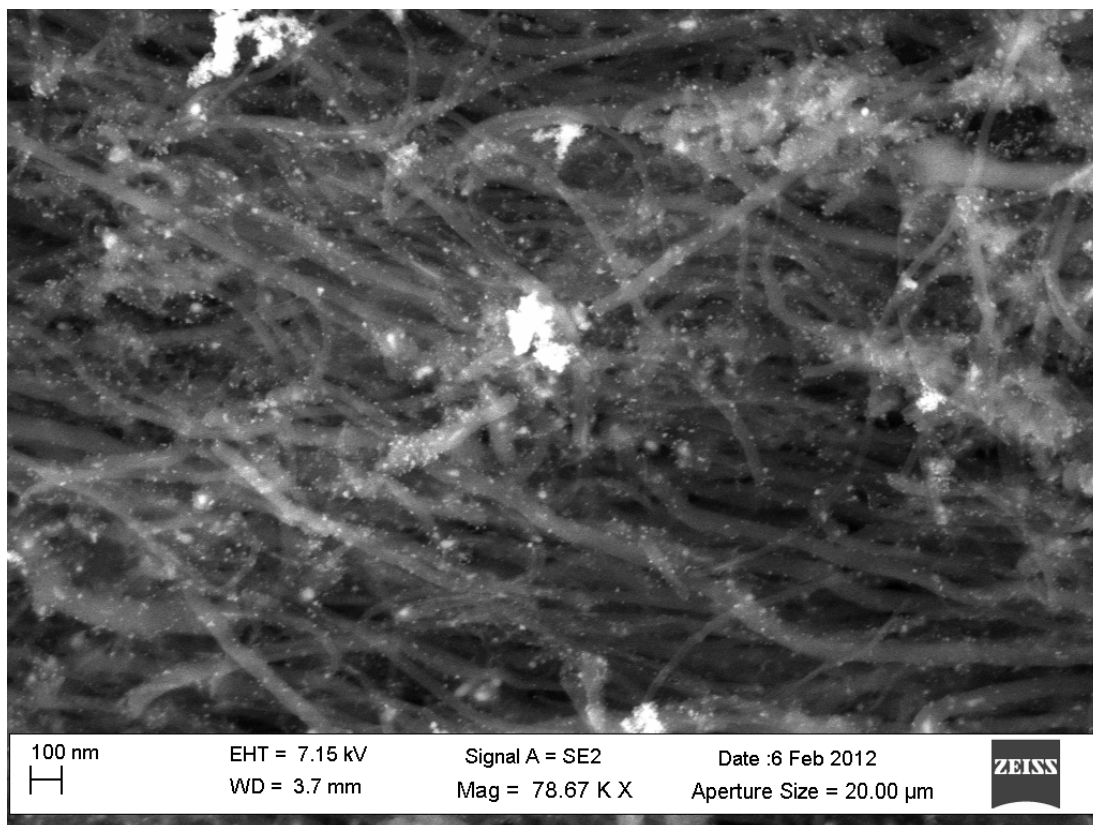


Figure E.7 FEG SEM backscattered image of *f*-syn-MWCNTs with a loading of 10 wt.% Pd.

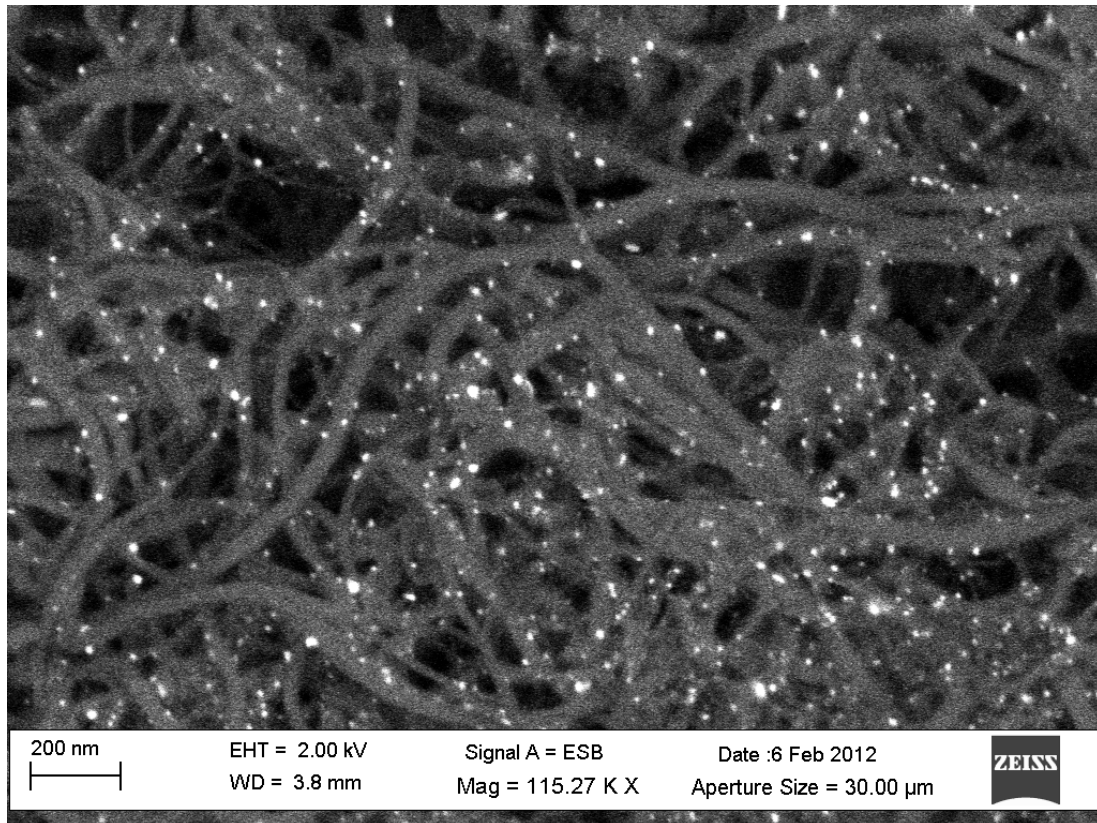


Figure E.8 FEG SEM backscattered image of *f*-com-MWCNTs with a loading of 10 wt.% Pd.

APPENDIX F

EDX RESULTS

Table F.1 EDX results from Experiments 1 and 2.

Exp. run	T _{max} (°C)	Structure	Normalized wt.%		
			C	Fe	Error
1.1	950	fused spheres	85.97	14.03	± 11.26
1.2	900	MWCNTs	97.70	2.30	± 1.19
1.3	850	MWCNTs	97.21	2.79	± 0.21
1.4	800*	MWCNTs	95.77	4.23	± 1.53
1.5	750	MWCNTs	95.68	4.32	± 1.42
		fused spheres	99.75	0.25	± 0.15
2.1	900	MWCNTs	96.89	3.11	± 2.09
2.2	850	MWCNTs	92.69	7.31	± 1.79
2.3	800	MWCNTs	68.20	31.80	± 29.99

*See also Table F.4.

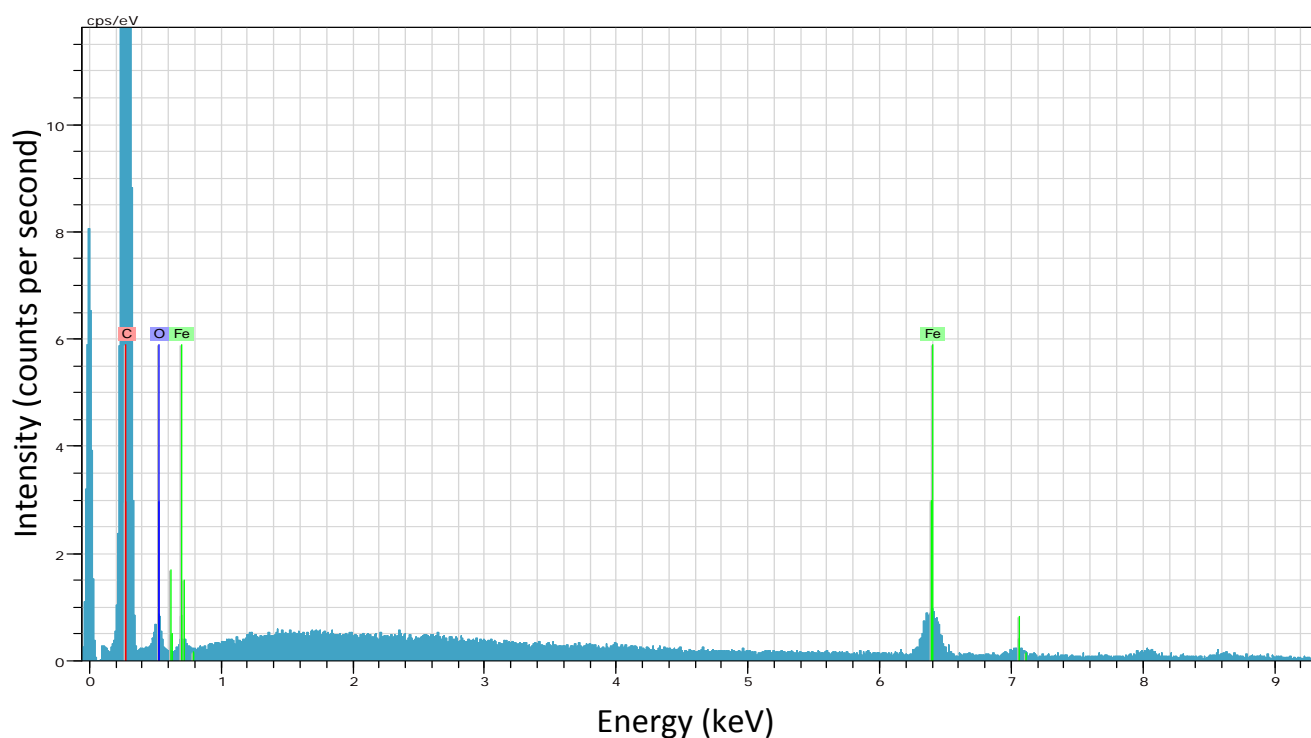


Figure F.1 EDX spectrum of MWCNTs from experiment 1 (2.5 wt.% ferrocene, 850 °C).

Table F.2 EDX results from Experiments 3, 4 and 5.

Exp. run	T _{max} (°C)	Structure	Normalized wt.% (±error)		
			C	Fe	N
3.1	900	fused spheres	92.62 (±0.19)	0.14 (±0.05)	7.24 (±0.23)
3.2	850	fused spheres	94.03 (±0.30)	0.05 (±0.01)	5.92 (±0.32)
		MWCNTs	93.20 (±2.01)	0.20 (±0.09)	6.60 (±2.10)
3.3	800	fused spheres	83.79 (±6.96)	0.04 (±0.02)	16.17 (±6.98)
		MWCNTs	93.36 (±0.69)	0.44 (±0.06)	6.20 (±0.64)
4.1	900	fused spheres	94.89 (±0.28)	0.06 (±0.02)	5.05 (±0.26)
4.2	850	fused spheres	72.39 (±19.10)	24.82 (±21.35)	2.79 (±2.25)
4.3	800	fused spheres	92.18 (±1.15)	0.27 (±0.01)	7.55 (±1.16)
		MWCNTs	93.34 (±0.15)	0.07 (±0.05)	6.59 (±0.11)
5.1	900	fused spheres	88.49 (±0.44)	0.20 (±0.08)	11.31 (±0.52)
5.2	800	fused spheres	85.49 (±0.93)	0.12 (±0.01)	14.39 (±0.94)

Table F.3 EDX results from Experiment 6.

Exp. run	T _{max} (°C)	Structure	Normalized wt.% (±error)		
			C	Fe	S
6.1	900	spheres	99.46 (±0.08)	0.38 (±0.06)	0.16 (±0.02)
6.2	800	spheres	99.10 (±0.11)	0.50 (±0.05)	0.40 (±0.05)

Table F.4 EDX results for the chosen supports.

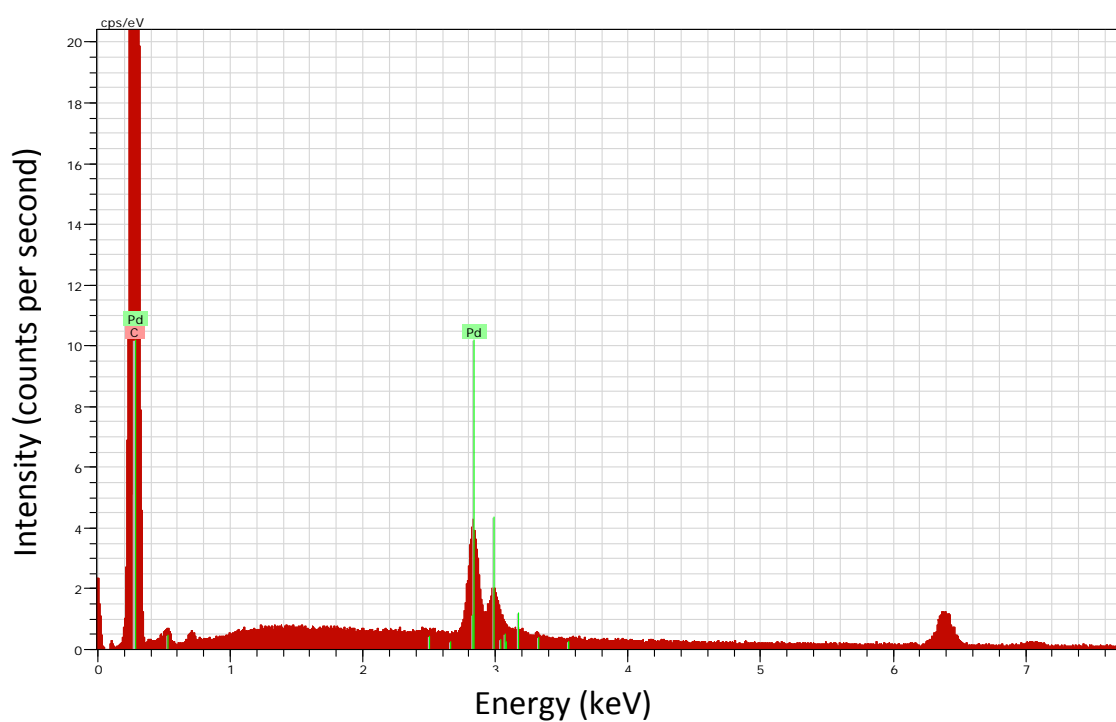
Sample	Normalized wt.%		
	C	Fe	Error
syn-MWCNTs*	95.77	4.23	± 1.53
<i>f</i> -syn-MWCNTs	97.04	2.96	± 0.005
com-MWCNTs	99.86	0.14	± 0.02
<i>f</i> -com-MWCNTs	99.84	0.16	± 0.045

*See **Table F.1** 800 °C.

Table F.5 EDX results for the Pd loaded supports.

Sample	Percent Pd loaded (wt.%)	Normalized wt.%*		
		C	Pd	Error
Pd- <i>f</i> -syn-MWCNTs	5	97.67	2.33	± 0.02
Pd- <i>f</i> -com-MWCNTs		93.64	6.36	± 0.54
Pd- <i>f</i> -syn-MWCNTs	10	95.58	4.42	± 0.30
Pd- <i>f</i> -com-MWCNTs		96.86	3.14	± 0.14

*Note that only C and Pd were considered here.

**Figure F.2** EDX spectrum of 10% Pd on *f*-syn-MWCNTs (2.5 wt.% ferrocene, 800 °C).

APPENDIX G

RAMAN RESULTS

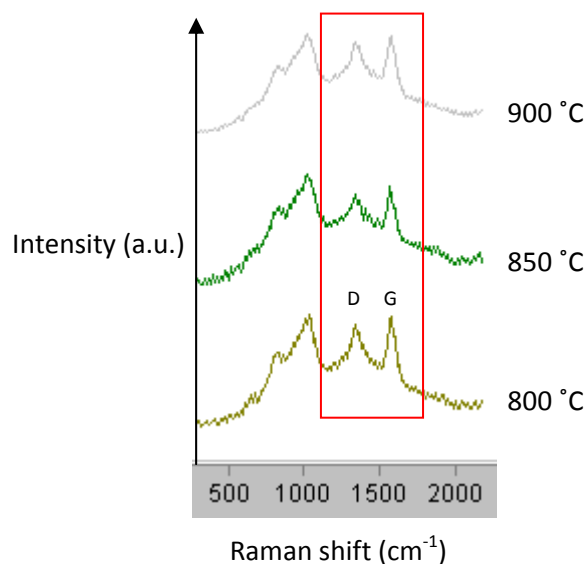


Figure G.1 Raman spectra of the best range, in terms of crystallinity, from Experiment 1 with red box highlighting peaks of interest.

Table G.1 Raman analysis for Experiments 3 to 5.

Exp. run	T _{max} (°C)	"Disorder" D-band (cm ⁻¹)	"Graphitic" G-band (cm ⁻¹)	I _D /I _G ratio
3.1	900	1329	1556	0.899
3.2	850	1342	1556	1.244
3.3	800	1337	1556	1.524
4.1	900	1367	1557	0.074
4.2	850	1381	1556	0.143
4.3	800	1375	1557	0.155
5.1	900	1341	1557	0.058
5.2	800	1333	1557	0.076

APPENDIX H

TGA DERIVATIVE CURVES

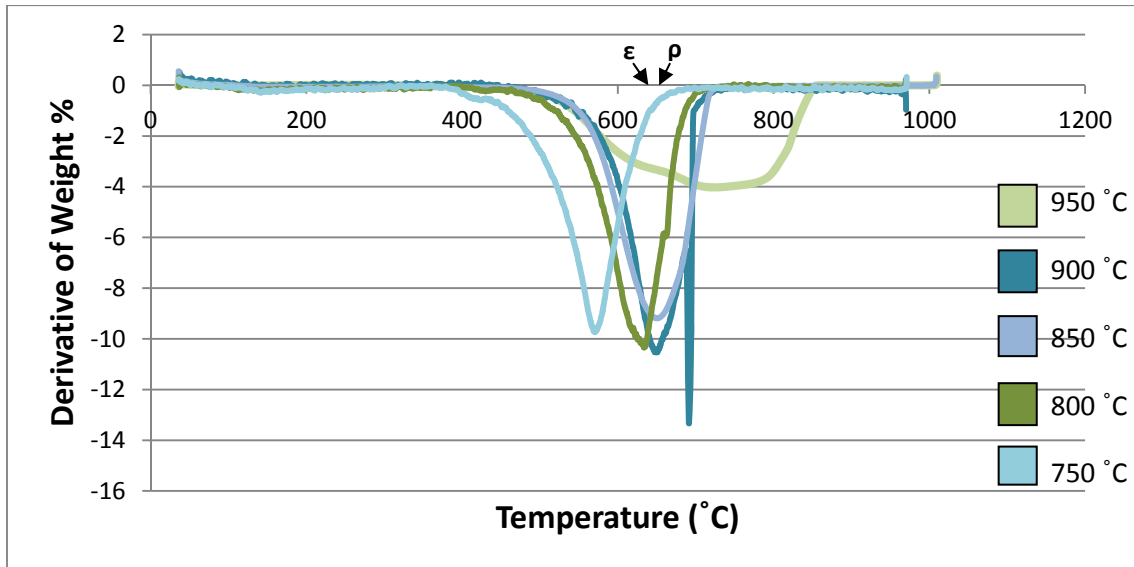


Figure H.1 TGA temperature derivative curves in air for the products obtained from Experiment 1.

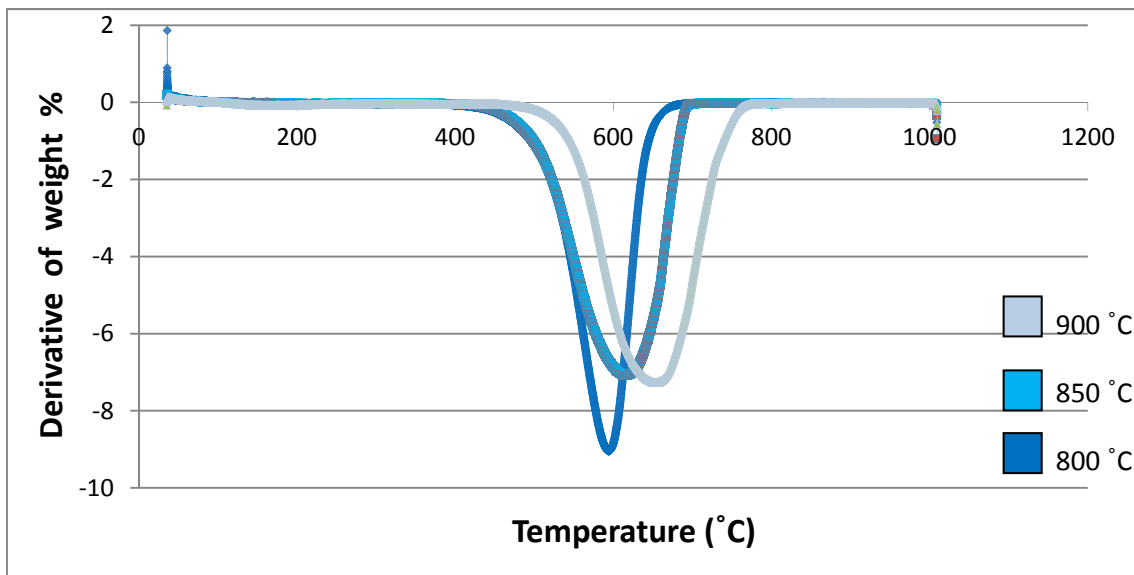


Figure H.2 TGA temperature derivative curves in air for the products obtained from Experiment 2.

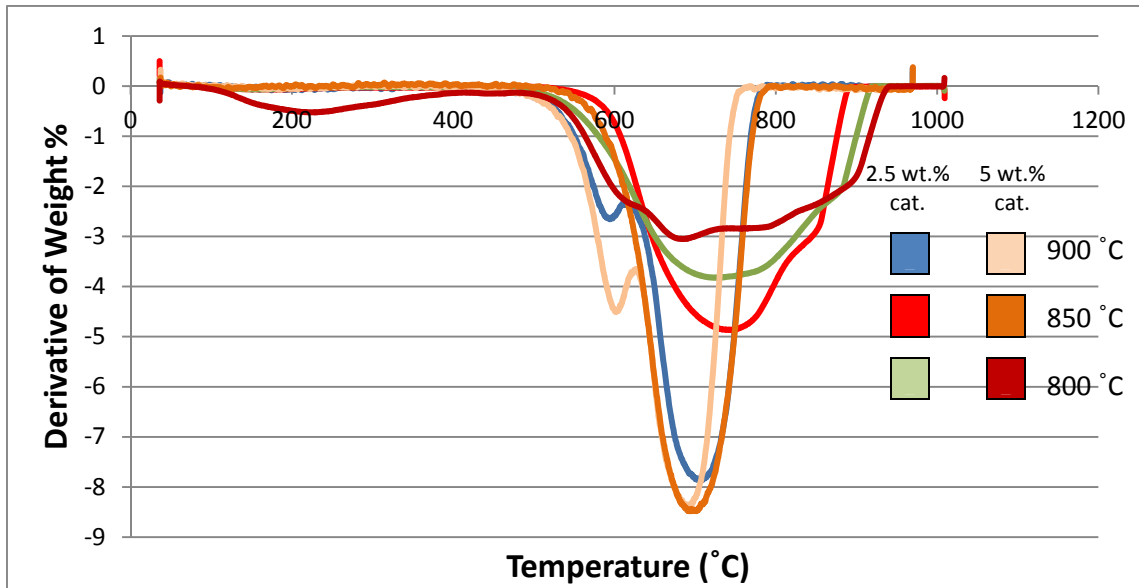


Figure H.3 TGA temperature derivative curves in air for the products obtained from Experiments 3 and 4.

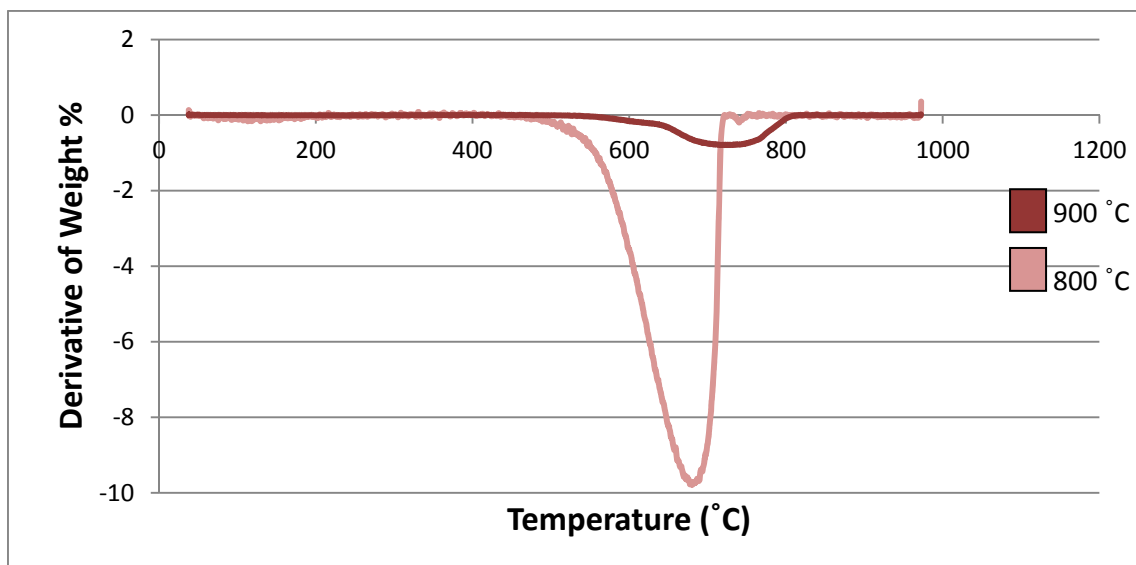


Figure H.4 TGA temperature derivative curves in air for the products obtained from Experiment 5.

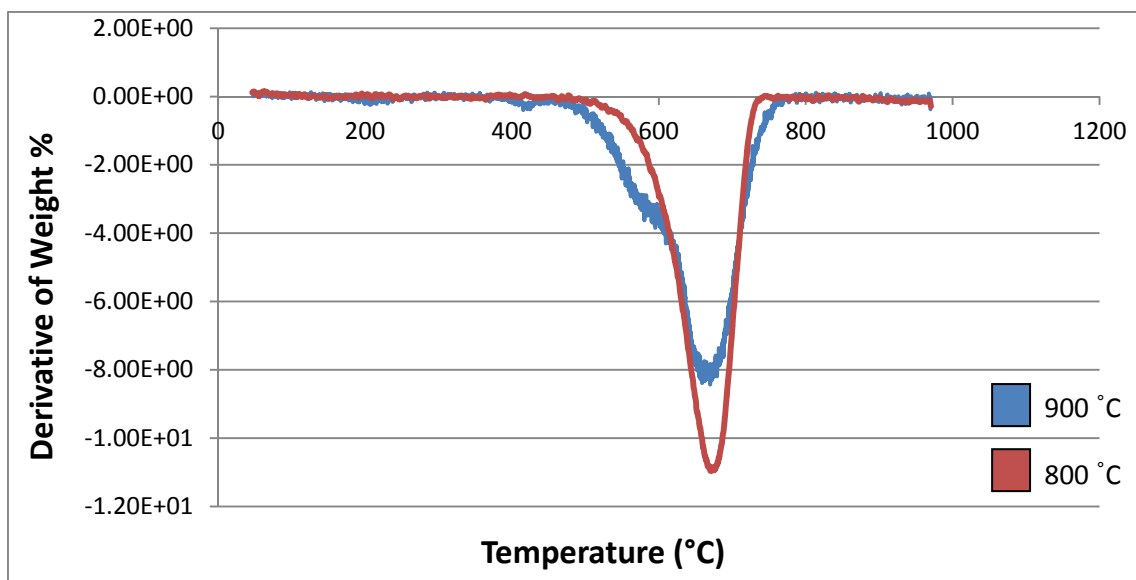


Figure H.5 TGA temperature derivative curves in air for the products obtained from Experiment 6.

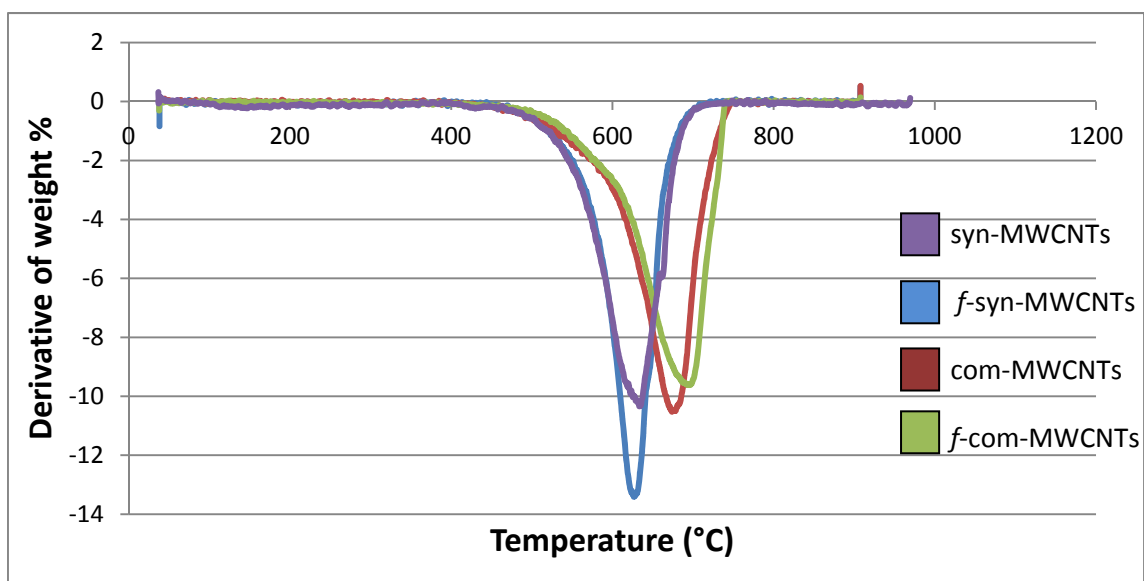


Figure H.6 TGA temperature derivative curves in air for the as-synthesized and functionalized supports for the loading of Pd.

APPENDIX I

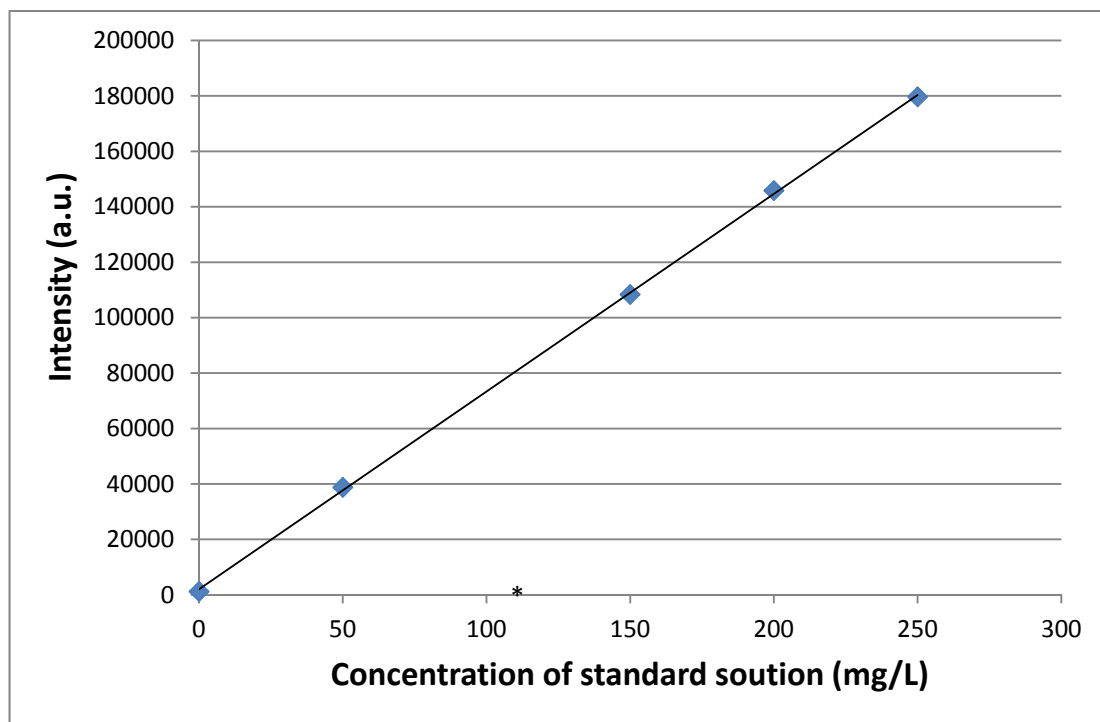
BAMBOO COMPARTMENT LENGTHS

Table I.1 Average bamboo compartment lengths.

Exp. run	T _{max} (°C)	Ave. bamboo compartment length (nm)	N : Fe (atomic ratio/empirical formula)
3.1	900	87.7	2:1
3.2	850	43.5	
3.3	800	33.5	
4.1	900	76.9	
4.2	850	43.6	
4.3	800	89.4	
5.1	900	63.7	1:1
5.2	800	47.4	

APPENDIX J

ICP-OES CALIBRATION CURVE



*The corresponding intensity value was an outlier and so was not included as part of the calibration curve.

Figure J.1 The ICP-OES calibration curve from the prepared Pd standard solutions.